

Institut für Immunologie
Medizinische Fakultät der
Ludwig-Maximilians-Universität München

Development of novel phosphatidylserine-binding reagents for research, diagnostics, and therapy



Kumulative Habilitationsschrift
zur Erlangung der *Venia Legendi*
im Fach Immunologie

vorgelegt von
Dr. sc. nat. Jan Kranich
München, 2024

Fachmentorat:

Prof. Dr. Thomas Brocker
Prof. Dr. Vigo Heissmeyer
Prof. Dr. Veit Hornung

Die in dieser Habilitationsschrift beschriebenen Arbeiten wurden von mir an folgenden Institutionen durchgeführt:

2004 bis 2009

Als Doktorand und Postdoc in der Arbeitsgruppe von Prof. Adriano Aguzzi, Universitätsspital Zürich, Zürich.

2012 bis 2023

Als Research Fellow in der Arbeitsgruppe von Prof. Thomas Brocker am Institut für Immunologie, Medizinische Fakultät, Ludwig-Maximilians-Universität München, München.

In der vorliegenden kumulativen Habilitationsschrift werden die folgenden fünf Publikationen zusammenfassend beschrieben und im Kontext diskutiert:

- 1.) Follicular dendritic cells control engulfment of apoptotic bodies by secreting Mfge8. **Kranich J**, Krautler NJ, Heinen E, Polymenidou M, Bridel C, Schildknecht A, Huber C, Kosco-Vilbois MH, Zinkernagel R, Miele G, Aguzzi A.; J Exp Med. 2008 Jun 9;205(6):1293-302.
- 2.) Engulfment of cerebral apoptotic bodies controls the course of prion disease in a mouse strain-dependent manner. **Kranich J**, Krautler NJ, Falsig J, Ballmer B, Li S, Hutter G, Schwarz P, Moos R, Julius C, Miele G, Aguzzi A. J Exp Med. 2010 Sep 27;207(10):2271-81.
- 3.) In vivo identification of apoptotic and extracellular vesicle-bound live cells using image-based deep learning. **Kranich J***, **, Chlis NK*, Rausch L, Latha A, Schifferer M, Kurz T, Foltyn-Arfa Kia A, Simons M, Theis FJ**, Brocker T**. J Extracell Vesicles. 2020 Jul 16;9(1):1792683. * equally contributed first author, ** corresponding author.
- 4.) Rausch L, Lutz K, Schifferer M, Winheim E, Gruber R, Oesterhaus EF, Rinke L, Hellmuth JC, Scherer C, Muenchhoff M, Mandel C, Bergwelt-Baildon M, Simons M, Straub T, Krug AB, **Kranich J***, Brocker T*. Binding of phosphatidylserine-positive microparticles by PBMCs classifies disease severity in COVID-19 patients. J Extracell Vesicles. 2021 Dec;10(14):e12173. * equally contributed last author.
- 5.) Rausch L, Flaskamp L, Ashokkumar A, Trefzer A, Ried C, Buchholz VR, Obst R, Straub T, Brocker T*, **Kranich J***. Phosphatidylserine-positive extracellular vesicles boost effector CD8⁺ T cell responses during viral infection. Proc Natl Acad Sci U S A. 2023 Apr 18;120(16):e2210047120. * equally contributed last author.

Table of contents

1. Summary	6
2. Zusammenfassung	8
3. Introduction	10
3.1 Phosphatidylserine – more than a marker for apoptotic cells.....	10
When and how is PS exposed?	11
The role of surface PS	12
3.2 Extracellular Vesicles (EVs)	14
Functions of EVs	16
The role of EVs in T cell priming	17
3.3 Milk-fat epidermal growth factor 8	18
4. Overview and discussion of research works	20
4.1 The role of Follicular dendritic cell (FDC)-produced MFG-E8.....	20
4.2 The role of MFG-E8 in prion disease	22
4.3 Using fluorescent MFG-E8 fusion proteins to stain PS ⁺ cells <i>in vivo</i>	24
4.4 Identification and characterization of PS ⁺ cells in COVID-19 patients.	27
4.5 How EVs modulate T-cell responses.....	29
5. Outlook	32
6. Literature	33
7. Publication Record	38
7.1 Publications as first or last author.....	38
7.2 Publications as co-author	39
7.3 Reviews.....	41
8. Acknowledgements	42
9. Appendix	44
9.1 Follicular dendritic cells control engulfment of apoptotic bodies by secreting Mfge8.	44
9.2 Engulfment of cerebral apoptotic bodies controls the course of prion disease in a mouse strain-dependent manner.	55
9.3 <i>In vivo</i> identification of apoptotic and extracellular vesicle-bound live cells using image-based deep learning.	67
9.4 Binding of phosphatidylserine-positive microparticles by PBMCs classifies disease severity in COVID-19 patients	88
9.5 Phosphatidylserine-positive extracellular vesicles boost effector CD8 ⁺ T cell responses during viral infection.....	107

1. Summary

The studies discussed here explore the multifaceted role of the phospholipid phosphatidylserine (PS) as both an “eat-me” signal for apoptotic cells and as a useful marker to study extracellular vesicles (EVs).

The works summarized here leverage the newly developed PS-binding reagents derived from the secreted glycoprotein MFG-E8, which functions as a bridging molecule between apoptotic cells and macrophages. Thereby MFG-E8 facilitates the engulfment of apoptotic cells by the phagocytosing macrophage.

In germinal centers MFG-E8 is solely produced by follicular dendritic cells (FDCs). By supplying MFG-E8 they license tingible body macrophages to efficiently clear dying B cells that occur during the germinal center reaction. Lack of FDC-produced MFG-E8 leads to accumulation of apoptotic cells on the surface of macrophages and impairs their degradation, ultimately promoting autoimmunity.

MFG-E8 also plays a pivotal role in the brain especially during pathological conditions, such as prion disease. Its absence leads to accumulation of dying cells and of infectious prions accelerating disease progression.

Detecting and studying dying cells in tissues presents challenges, due to their scarcity and due to the lack of suitable reagents. However, the development of novel fluorescent MFG-E8 fusion proteins for *in vivo* PS labeling allowed the identification of PS⁺ cells in their native microenvironment. Combined with cell analysis using imaging flow cytometry and deep-learning assisted image interpretation, this approach facilitates the precise detection and characterization of dying cells based on PS exposure. Surprisingly, it also revealed that only few PS⁺ cells are apoptotic. Unexpectedly, most PS⁺ cells were living cells decorated with PS⁺ extracellular vesicles (EVs) on their surface.

In vivo PS-labeling using fluorescent MFG-E8-based reagents has unlocked the possibility to investigate interactions of EVs with lymphocytes. During viral infections, such as lymphocytic choriomeningitis virus (LCMV) in mice and SARS-

CoV-2 in humans, T cells and particularly activated cytotoxic T cells displayed a pronounced increase in EV-binding. Notably, in SARS-CoV-2 infections, EV-binding by peripheral blood mononucleated cells (PBMCs) strongly correlates with disease severity and was highest in patients with severe disease. T cells decorated with PS⁺ platelet-derived microparticles show increased proliferation and a higher expression of effector cytokines.

In LCMV-infected mice, activated T cells bind exosomal EVs originating from antigen-presenting cells. These EVs trigger antigen-dependent stimulation in pre-activated T cells and cause clustering of the T-cell receptor complex, activation of the transcription factor NFAT, drive T cell proliferation and enhance expression of effector genes.

Collectively, these results underscore the importance of EVs in modulating T-cell responses making them an interesting therapeutic target for improving or inhibiting T-cell responses in viral infections, cancer, or autoimmunity.

2. Zusammenfassung

Die hier besprochenen Studien untersuchen die vielseitige Rolle des Phospholipids Phosphatidylserin (PS), das sowohl als "Eat me"-Signal für apoptotische Zellen, als auch als wertvoller Marker zur Untersuchung extrazellulärer Vesikel (EVs) fungiert.

Die hier präsentierten Arbeiten nutzen neu entwickelte PS-bindende Reagenzien, die von dem sezernierten Glykoprotein MFG-E8 abgeleitet sind. MFG-E8 agiert als Brückenmolekül zwischen apoptotischen Zellen und Makrophagen, wodurch die Phagozytose von apoptotischen Zellen durch Makrophagen erleichtert wird.

Im Keimzentrum wird MFG-E8 ausschließlich von folliculären dendritischen Zellen (FDCs) produziert. Durch die Produktion von MFG-E8 ermöglichen sie den Tingible-Body-Makrophagen die effiziente Beseitigung absterbender B-Zellen, die während der Keimzentrumsreaktion auftreten. Ein Fehlen von FDC-produziertem MFG-E8 führt zur Akkumulation apoptotischer Zellen auf der Oberfläche der Makrophagen und beeinträchtigt deren Abbau, was letztlich die Entstehung von Autoimmunerkrankungen begünstigt.

MFG-E8 spielt auch im Gehirn eine bedeutende Rolle, insbesondere bei pathologischen Zuständen wie Prionenerkrankungen. Im Mausmodell führt ein Mangel an MFG-E8 zu einer Akkumulierung absterbender Zellen und infektiöser Prionen, was den Krankheitsverlauf beschleunigt.

Die Detektion und die Untersuchung sterbender Zellen in Geweben sind aufgrund ihrer Seltenheit und des Mangels an geeigneten Reagenzien eine Herausforderung. Die Entwicklung neuer fluoreszierender MFG-E8-Fusionsproteine für die In-vivo-PS-Markierung ermöglicht die Identifizierung von PS⁺-Zellen in ihrer natürlichen Umgebung. In Kombination mit Zellanalyseverfahren wie Imaging Durchflusszytometrie und Deep-Learning-gestützter Bildinterpretation wird die präzise Detektion und Charakterisierung sterbender Zellen auf Grundlage der PS-Exposition erleichtert. Überraschenderweise ergab sich, dass die Mehrheit der PS⁺-Zellen nicht apoptotisch sind, sondern lebende Zellen, die PS⁺ extrazelluläre Vesikel (EVs) auf ihrer Oberfläche tragen.

Die In-vivo-PS-Markierung mit fluoreszierenden Reagenzien auf MFG-E8-Basis hat die Möglichkeit eröffnet, die Interaktionen von EVs mit Lymphozyten zu untersuchen. Während Virusinfektionen, wie dem lymphozytären Choriomeningitis-Virus (LCMV) bei Mäusen und SARS-CoV-2 beim Menschen zeigen T-Zellen, insbesondere aktivierte zytotoxische T-Zellen, eine ausgeprägte Zunahme der EV-Bindung. Bei SARS-CoV-2-Infektionen korrelierte die EV-Bindung durch mononukleäre Zellen im peripheren Blut (PBMCs) stark mit dem Schweregrad der Erkrankung und war bei Patienten mit schwerem Verlauf am höchsten. T-Zellen, die mit PS⁺-Mikropartikeln von Blutplättchen dekoriert waren, zeigten eine erhöhte Proliferation und eine stärkere Expression von Effektorzytokinen.

In LCMV-infizierten Mäusen binden aktivierte T-Zellen exosomale EVs, die von Antigen-präsentierenden Zellen stammen. Diese EVs lösen eine antigenabhängige Stimulation in voraktivierten T-Zellen aus, was zu einer Clusterbildung des T-Zell-Rezeptorkomplexes, zur Aktivierung des Transkriptionsfaktors NFAT, zur Förderung der T-Zellproliferation und zur Steigerung der Expression von Effektorgenen führt.

Zusammengenommen unterstreichen diese Erkenntnisse die bedeutende Rolle von EVs bei der Modulation von T-Zell-Antworten und machen sie zu einem vielversprechenden therapeutischen Ziel für die Verbesserung oder Inhibition von T-Zell-Antworten bei akuten oder chronischen Virusinfektionen, Krebserkrankungen oder Autoimmunität.

3. Introduction

3.1 Phosphatidylserine – more than a marker for apoptotic cells

The lipid bilayer of cell membranes from mammalian cells is predominated by four different phospholipids: sphingomyelin (SM), phosphatidylcholine (PC), phosphatidylethanolamine (PE) and phosphatidylserine (PS). These different phospholipids show an asymmetrical distribution. While in intact cells SM and PC are mainly on the outer side of the membrane, PE and PS are on the intracellular side (Bruce Alberts, 2002). The difference in the distribution of phospholipids between the intra- and extracellular leaflet of the membrane is an important discriminator of live and dying cells (Figure 1).

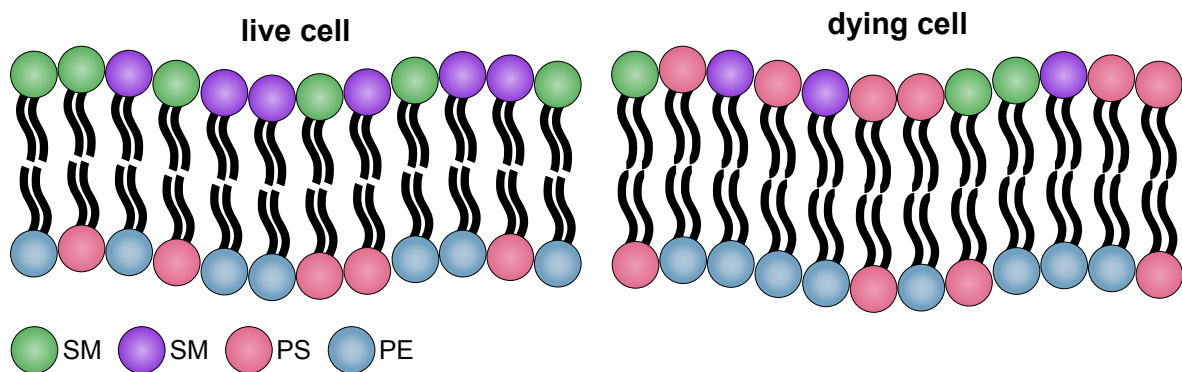


Figure 1. Schematic illustration of the assymetric distribution of the four main phospholipids in mammalian cell membranes in intact live (left) and apoptotic cells.

Among these phospholipids, especially PS has attracted a lot of research interest, especially due to its function as 'eat-me' signal that helps phagocytes to recognize and remove apoptotic cells, which display PS exposed on their surface (Segawa and Nagata, 2015). The structure of PS is displayed in Figure 2.

In the endoplasmatic reticulum two different PS synthases synthesize PS from PC and PE (Segawa and Nagata, 2015).

To be able to function as an 'eat-me' signal, PS has to be kept from the surface of live intact cells. ATP-dependent flippases are responsible for this. Flippases belong to the family of P-Type ATPases which has 15 and 14 family members in mouse and human, respectively (Palmgren and Nissen, 2011). ATP11C has been identified as an important flippase required for the intracellular retention of PS (Yabas et al., 2011). However, knocking out ATPC11 in mammalian cells was not sufficient to disturb the

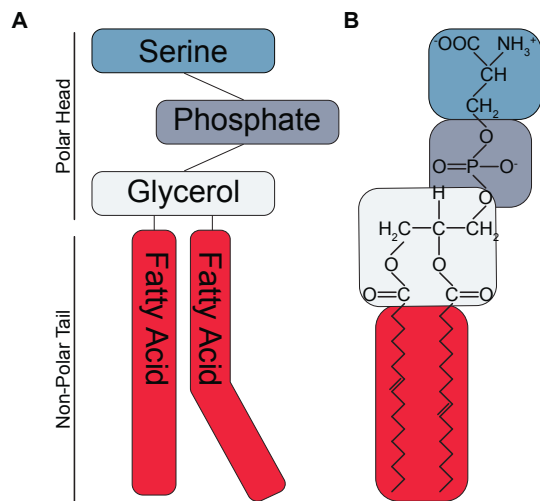


Figure 2. (A) Schematic representation and (B) structural formula of PS.

asymmetrical distribution of PS, although the flippase activity was strongly reduced, indicating that other flippases could compensate for the loss of ATPC11 (Segawa et al., 2014). Another important factor for holding up the asymmetry is ATP11C's chaperone CDC50A. In contrast to deleting ATPC11, knocking out CDC50A in cell lines was sufficient to constitutively expose PS on the surface. This indicates that CDC50A also functions as a chaperone

for other ATP-dependent flippases that have been suspected to compensate for the function of ATPC11, when it was removed (Segawa et al., 2014; Segawa and Nagata, 2015).

When and how is PS exposed?

PS exposure during cell death or platelet activation happens very rapidly (Obydenny et al., 2016; Sapor et al., 2018). However, studies showed that the passive diffusion of phospholipids is very slow with half-lives of several hours (Zachowski, 1993). The accelerated PS exposure during apoptosis can be explained by active transport mediated by aminophospholipid translocases, which are also called scramblases. This reduces the half-life of PS transport through the membrane to a few minutes (Bassé et al., 1996; Zachowski, 1993). Several of these scramblases have been identified, such as the caspase-dependent Xkr-related protein 8 (Xkr8) and the Ca^{2+} -dependent transmembrane protein 16F (TMEM16F; Suzuki et al., 2013; Suzuki et al., 2010).

During apoptotic cell death PS exposure is dependent on the action of caspases. Both, the flippase ATPC11 and the scramblase Xkr8 contain caspase-3 recognition sites. While cleavage by caspase-3 inactivates ATPC11, caspase-cleavage of Xkr8 is required for its activation (Segawa and Nagata, 2015).

Initially, it was thought that PS exposure was limited to apoptotic cell death, but PS exposure has now been found also in other forms of cell death, such as pyroptosis (de Vasconcelos et al., 2019), necroptosis (Shlomovitz et al., 2019) or necrosis. In these forms of cell death, PS exposure is independent of caspase activity (Furuta et al., 2021).

Furthermore, not only dying cells expose PS. It is also an important feature of platelet activation. There, PS exposure is also caspase-independent and requires Ca^{2+} and the scramblase TMEM16F. This scramblase is also involved in PS exposure during non-apoptotic cell death (Shlomovitz et al., 2019).

Extracellular vesicles (EVs), such as exosomes, microvesicles and apoptotic bodies also exhibit PS on the outer leaflet of the membrane. Whether all or only a subset of EVs have externalized PS is still a controversial matter (Matsumoto et al., 2021; Rausch et al., 2023; Yoshida and Hanayama, 2022). There is little known about the mechanisms of PS exposure in exosomes or microvesicles. However, as there will be no ATP production in most EVs, the absence of ATP will reduce flippase activity leading eventually to PS exposure. In addition to this, it has also been shown that TMEM16F is involved in the shedding of membrane vesicles from various cell types (Bricogne et al., 2019; Ehlen et al., 2013; Fujii et al., 2015). TMEM16F activity might therefore also contribute PS exposed on the surface of EVs.

The role of surface PS

As mentioned above, the role of exposed PS on dying cells is to facilitate their rapid removal by phagocytic cells. Phagocytes, such as macrophages can carry different receptors for direct or indirect PS-binding. A receptor that binds PS directly is Tim4. It is highly expressed on Kupfer cells, peritoneal and splenic red pulp macrophages (Kay and Fairn, 2019). Tim4-deficient macrophages show reduced binding and impaired uptake of apoptotic cells (Nishi et al., 2014). Receptors, that bind PS indirectly through bridging molecules are integrins, which bind to milk-fat globule epidermal growth factor 8 (MFG-E8, [see below](#)) and Mer tyrosine kinase (MerTK), which binds to the bridging molecule Gas6. Absence of any of these molecules will

strongly impair engulfment of apoptotic cells (Nakano et al., 1997; Nishi et al., 2014; Raymond et al., 2009).

PS on EVs will also facilitate their uptake by their target cells, probably using the same PS-binding receptors that are used to remove apoptotic cells. However, there are only few studies, that have investigated the uptake or binding mechanisms of EVs. But one study revealed that the PS is needed for the rapid clearance of EVs from the blood (Matsumoto et al., 2021).

One hallmark of activated platelets is the presence of PS on their surface. Surface PS is thought to be crucial for the proagulant activity of platelets (Zhao et al., 2016). Coagulation is initiated by endothelial damage. This leads to the polymerization of fibrin. Together with platelets, polymerized fibrin forms a plug closing the site of the wound. During the coagulation cascade different serine proteases and their glycoproteins become activated sequentially and activate the next factor in the cascade, eventually leading to formation of polymerized fibrin through the action of the proteases thrombin and fibrinogen (Figure 3, (Sang et al., 2021).

During the initiation phase of the coagulation cascade the phospholipids PS and PC drive the activation of serine proteases by providing a catalytic surface, which is strongly reduced in the absence of lipid membranes (Zwaal et al., 1998). Vitamin K-dependent coagulation factors can directly interact with PS through an N-terminal γ -carboxyglutamic acid (Gla) domain in a Ca^{2+} dependent manner. Removing the Gla domain from prothrombin reduced their affinity to PS 1000-fold (Zwaal et al., 1998).

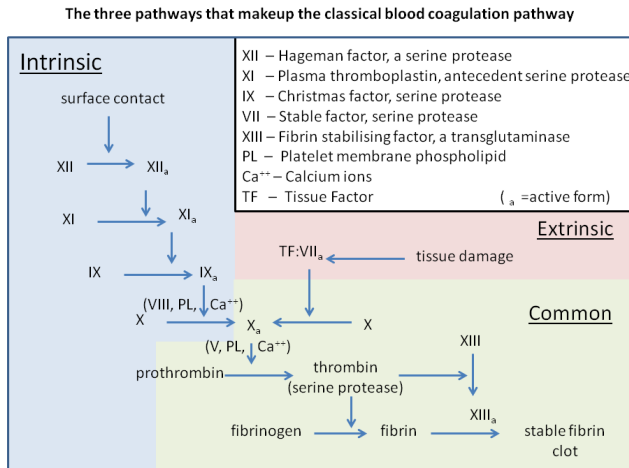


Figure 3. Factors involved in the coagulation cascade.
 (from "Classical blood coagulation pathway" By Dr Graham Beards, via [Commons Wikimedia](#)).

3.2 Extracellular Vesicles (EVs)

The term extracellular vesicles (EVs) comprises several different very heterogeneous small membrane particles. These particles can differ in size, origin, and function, but have in common that they are very small and hence difficult to separate and characterize individually. The three main groups of EVs are exosomes, microparticles or ectosomes and apoptotic bodies. The smallest EVs are the exosomes with sizes ranging from approx. 30-100nm (Figure 4). Exosomes are generated by invagination of endosomes. Prior to the release into the extracellular space from their mother cells, they are stored in multivesicular bodies (Yates et al., 2022). Microvesicles are larger than exosomes with a size range between 100-1000nm (Figure 4). Unlike exosomes, they are released directly by budding from the plasma membrane. It is assumed, that virtually any cell type produces and secretes exosomes and microvesicles (Yates et al., 2022). In contrast, apoptotic bodies are only released from cells undergoing apoptosis. They are the largest EVs with sizes ranging from 1000-5000nm (Figure 4). Similar to microvesicles, they are formed by budding from the cell membrane (Santavanond et al., 2021). Apart from these three main groups of EVs, there are additional, less well studied EV subsets, such as exomeres, which are non-membranous particles with a size of approx. 50nm (Anand et al., 2021).

It is very difficult to discriminate the different EV subtypes as there are no specific markers other than their size that can be used to define specific EV subtypes. However, certain membrane proteins, namely family members of the tetraspanin proteins, are strongly enriched in exosomes. Hence, the tetraspanin proteins CD81, CD9, CD63 are often used as exosome markers (György et al., 2011).

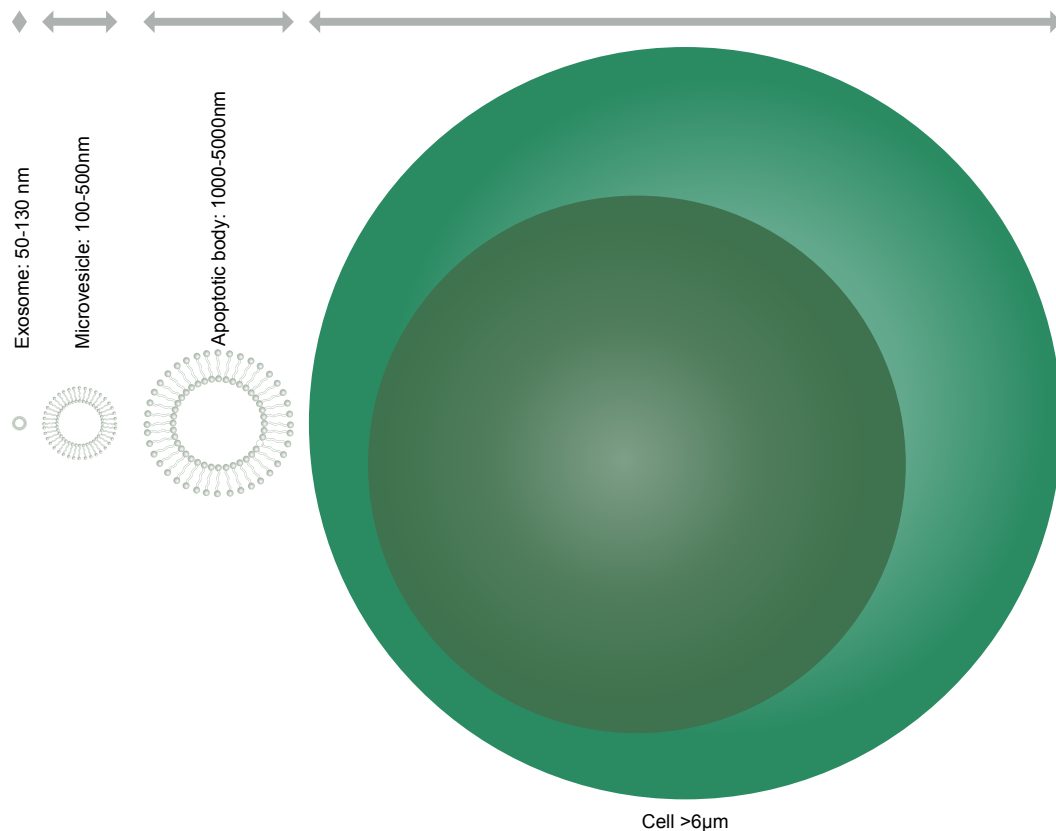


Figure 4. Illustration of the size of different EV subsets.

Differential ultracentrifugation can be used to separate EV subsets by size (Sidhom et al., 2020). In general, however, obtaining pure isolates of EVs can be challenging and a large variety of methods has been developed to obtain EVs from fluids. These methods comprise ultracentrifugation, ultrafiltration, immunoaffinity methods, precipitation, and size exclusion chromatography. All these methods have their advantages and disadvantages and lead to isolates with different EV compositions and impurities and contaminating proteins or lipids. For this reason, strict guidelines for the reporting of the isolation method and the analysis of the purified EVs have been put into place. These require thorough characterization of the isolated EV, by different methods, including nanoparticle tracking analysis (NTA), Western Blotting and electron microscopy (Théry et al., 2018).

Functions of EVs

It is believed that the main physiological role of EVs lies in the intercellular communication. EVs can carry different cargos, such as mRNA, miRNA, cytosolic and surface proteins, mitochondria, and other small organelles (Neven et al., 2017) and even telomers as a recent report describes. Telomer containing EVs from antigen-presenting cells were shown to have the ability to rescue T cells from senescence (Lanna et al., 2022).

There is great interest in EVs in the cancer field, as there is hope that EVs in liquid biopsies can be used as early non-invasive biomarker for cancer. Also, cancer cells constitutively produce and secrete EVs, hence their RNA and protein cargo could give valuable information about the disease stage. Although many promising studies about the usefulness of EVs as biomarkers have been published, there is currently no EV-based diagnostic test approved for clinical use (Urabe et al., 2020).

EVs are not only of diagnostic interest in the cancer field. EVs seem to play important roles in cancer pathology itself. Sung et al. showed that EVs from cancer cells were required for controlled movement of cancer cells (Sung et al., 2015). Another study showed that EVs contribute to the degradation of the extracellular matrix through microRNAs secreted via EVs. This allows tumor cells to invade different tissues and facilitates metastasis formation (Becker et al., 2016; Zhou et al., 2014). Metastasis formation and tumor growth is facilitated by increased angiogenesis. EVs containing epidermal growth factor receptor (EGFR) secreted from tumor cells are taken up by endothelial cells and can increase angiogenesis (Al-Nedawi et al., 2009).

In a mouse model of glioblastoma, transfer of the truncated and oncogenic form of EGFRvIII between glioma cells via EVs has been observed. Glioma cells lacking expression of the truncated form can acquire the oncogenic activity of the truncated receptor through these EVs promoting tumor growth (Al-Nedawi et al., 2008).

Tumor-derived EVs can not only promote cancer progression by transferring oncogenic activity, increasing angiogenesis or facilitating metastasis formation, they

have been shown to also be able to dampen anti-tumor immune responses. Programmed death-ligand 1 (PD-L1)-bearing EVs produced by tumor cells can bind to PD-1 expressing tumor specific CD8⁺ T cells (Chen et al., 2018). This EV-mediated

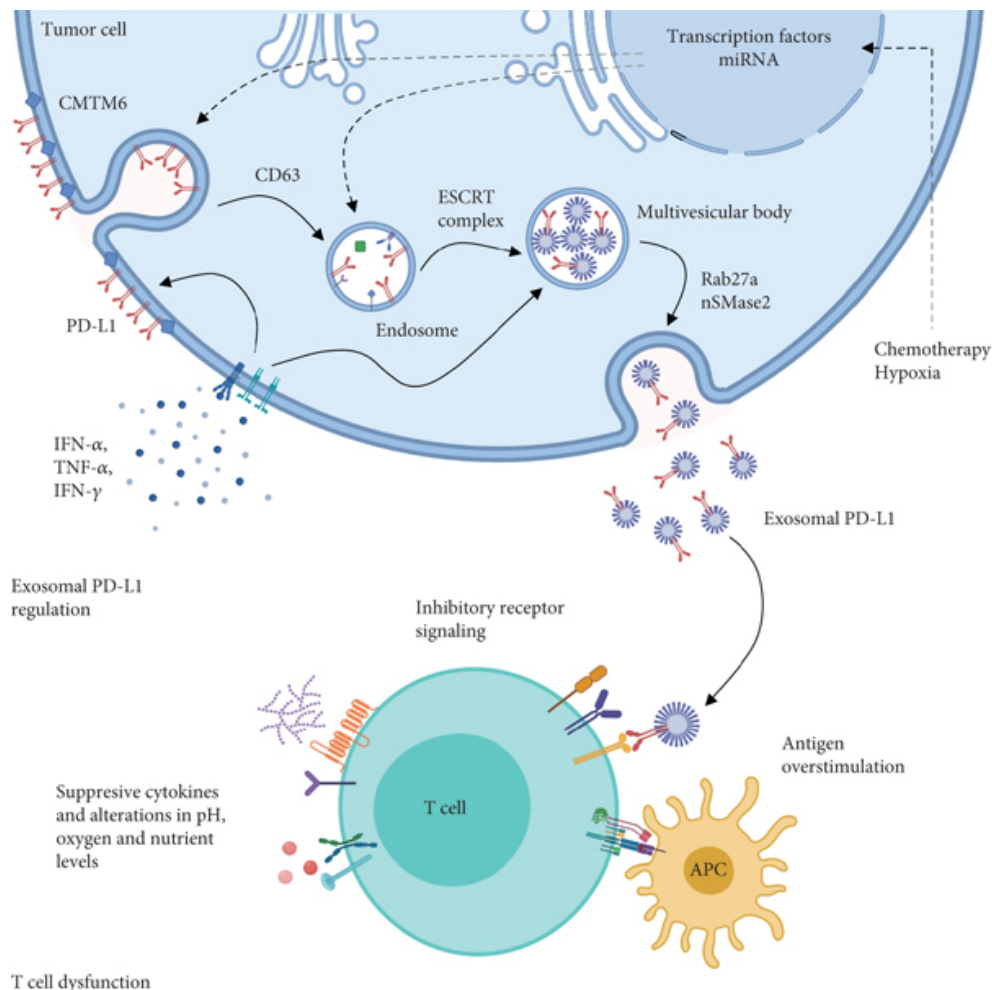


Figure 5. Illustration of T cell inhibition by tumor-derived PD-L1 carrying exosomes. From (Ayala-Mar et al., 2021).

PD-L1:PD-1 interaction leads to T-cell inactivation (Garcia-Diaz et al., 2017; Figure 5). Furthermore, these EVs have been shown to compete with anti-PD-1 antibodies that are given as immune checkpoint inhibitors to cancer patients to increase anti-cancer immune responses, mediating resistance to the therapy (Chen et al., 2022).

The role of EVs in T cell priming

Not only in the cancer field EVs have sparked great interest, also in the field of immunology EVs have received a lot of attention. Already in 1998 EVs derived from exosomes have been used to successfully immunize against tumors in mouse models (Zitvogel et al., 1998). However, the clinical trials using EVs to vaccinate against

cancers that followed were unfortunately all unsuccessful. It is well established that EVs carry MHC-I and MHC-II molecules (Raposo et al., 1996), co-stimulatory molecules like CD80 and CD86 (Kovar et al., 2006), and the integrin LFA-1 (Nolte't Hoen et al., 2009), hence EVs have everything they need to potentially prime naïve T cells. But it is unclear if EVs are indeed able to do so, albeit many studies have addressed this. What seems to be undisputed is that antigen-presenting cells (APCs) can take up antigen associated with EVs, and then use this EV-derived antigen to prime naïve T cells. This is considered indirect priming by EVs (Hao et al., 2007). If EVs can prime naïve T cells directly, without the presence of APCs is still a matter of debate. While direct priming of T cells has been achieved *in vitro* by adding large amounts of EVs to cultured T cells (Kovar et al., 2006; Raposo et al., 1996), an involvement of DCs in the priming of T cells in *in vivo* models, where exogenous EVs have been administered, cannot be ruled out (Zitvogel et al., 1998). Results from my own research, which will be discussed in [chapter 4.5](#), strongly argue against priming of naïve T cells, but clearly show stimulation of already activated T cells through EVs (Rausch et al., 2023).

3.3 Milk-fat epidermal growth factor 8 (MFG-E8)

MFG-E8, also known as lactadherin is a secreted PS-binding glycoprotein expressed by various phagocytic cells types, like immature dendritic cells (Miyasaka et al., 2004), activated peritoneal macrophages (Hanayama et al., 2002), but also by non-phagocytic cells like perivascular cells in the spleen (Krautler et al., 2012), epithelial cells in the mammary gland (Atabai et al., 2005), and follicular dendritic cells in germinal centers (Kranich et al., 2008).

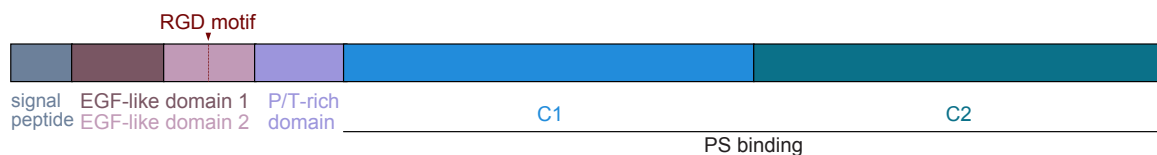


Figure 6. illustration of the functional domains of murine MFG-E8.

MFG-E8 has been shown to be important for the clearance of apoptotic cells. With its two PS-binding domains C1 and C2 (Figure 6) it binds to PS exposed on apoptotic cells. Macrophages then recognize MFG-E8 opsonized apoptotic cells through MFG-E8's RGD motif (Figure 6) and bind it via integrins. This interaction induces the

engulfment of the apoptotic cell (Hanayama et al., 2002; Hanayama et al., 2004; Zullig and Hengartner, 2004). Mice lacking MFG-E8 develop a lupus-like autoimmunity and show impaired clearance of apoptotic germinal center B cells (Hanayama et al., 2004).

Unlike many other PS-binding proteins, like e.g. Annexin V (Vermes et al., 1995) or Tim-4 (Miyanishi et al., 2007), MFG-E8 is able to bind PS Ca^{2+} -independently (Hanayama et al., 2002). This has made MFG-E8 an excellent tool to study PS⁺ cells in many of my studies as will be discussed in the following chapters.

4. Overview and discussion of research works

4.1 The role of Follicular dendritic cell (FDC)-produced MFG-E8

Follicular dendritic cells control engulfment of apoptotic bodies by secreting Mfge8. **Kranich J**, Krautler NJ, Heinen E, Polymenidou M, Bridel C, Schildknecht A, Huber C, Kosco-Vilbois MH, Zinkernagel R, Miele G, Aguzzi A.; *J Exp Med.* 2008 Jun 9;205(6):1293-302.

In this study the role of FDC-produced MFG-E8 was investigated. As FDCs play a major role in peripheral replication of prions, there was great interest in finding genes differentially expressed in these cells, to allow FDC-specific deletion or overexpression of genes suspected to be involved in prion propagation and replication. Huber et al. hence performed a transcriptomic screen of isolated FDC clusters and identified MFG-E8 as being differentially expressed by FDCs in the spleen (Huber et al., 2005).

We then investigated the role of MFG-E8 in FDCs and found that MFG-E8 is identical to the antigen identified by the FDC-specific antibody FDC-M1.

A previous study by Hanayama et al., claimed that MFG-E8 in the spleen was expressed by tingible body macrophages (TBMs). However, this was in contradiction with our findings that FDCs are the sole source of MFG-E8 in the spleen and that TBMs do not express *Mfge8*. We confirmed this using in situ hybridization combined with immunohistochemistry and bone marrow transfer between wild-type and *Mfge8*^{-/-} mice. In addition to this, we could further show that TBMs take up exogenously administered recombinant MFG-E8, leading to the conclusion that TBMs become MFG-E8 positive by taking up FDC-derived MFG-E8.

Mfge8^{-/-} mice develop a lupus-like autoimmune phenotype with autoantibodies against nuclear components (Hanayama et al., 2004). This was caused by impaired clearance of apoptotic B cells from the germinal center (GC). In these mice, apoptotic cells accumulate on the surface of TBMs, which are unable to engulf them in the absence of MFG-E8.

We observed the same phenotype in bone marrow transfer experiments where only FDCs lack expression of *Mfge8*. When we transferred *Mfge8*^{-/-} bone marrow into irradiated WT mice, bone marrow macrophages lack expression of *Mfge8*, FDCs in contrast express *Mfge8*, as they are of stromal origin. In this situation, clearance of apoptotic GC B cells is normal. In the opposite situation, where *Mfge8*^{-/-} mice receive wild-type bone marrow and their FDCs lack *Mfge8* expression, engulfment of apoptotic GC B cells was abolished (Figure 7).

From these experiments we concluded that FDCs license TBMs to phagocytose apoptotic GC B cells by providing MFG-E8. Hence, FDCs play an important role in preventing autoimmunity caused by impaired clearance of apoptotic cells. This we could further confirm by analyzing clearance of apoptotic GC B cells in various knock-out mouse strains that lack FDCs and develop severe systemic autoimmunity. All these strains show severely impaired phagocytosis of apoptotic cells from the GC.

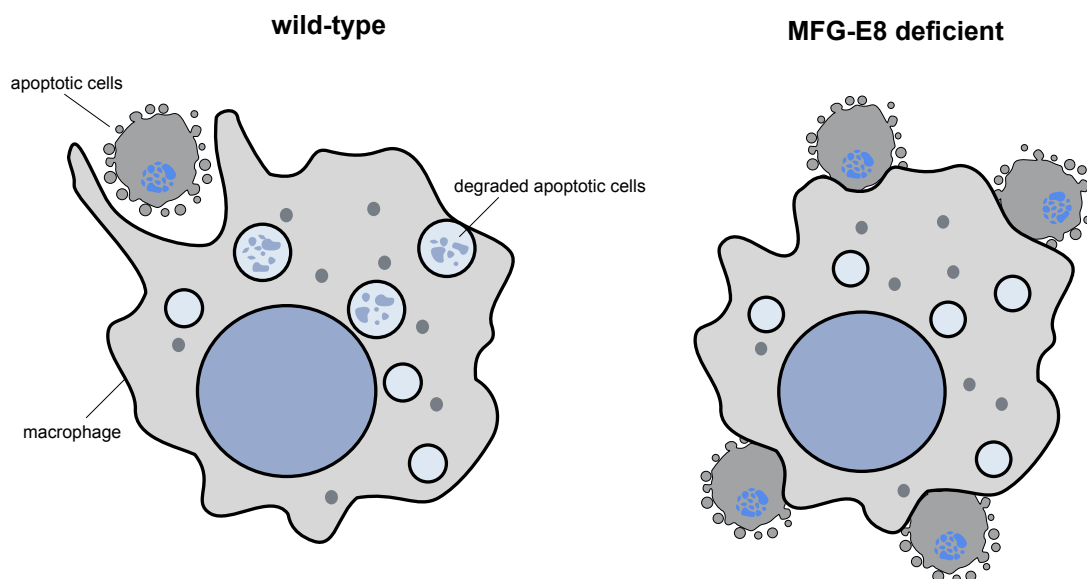


Figure 7. Impaired engulfment of apoptotic cells in the absence of MFG-E8.

Left: Macrophage engulfs apoptotic cell and has phagolysosomes with partially degraded apoptotic cells. Right: Impaired engulfment of apoptotic cells due to the lack of MFG-E8. Apoptotic cells accumulate on the surface of the macrophage.

4.2 The role of MFG-E8 in prion disease

Engulfment of cerebral apoptotic bodies controls the course of prion disease in a mouse strain-dependent manner. Kranich J, Krautler NJ, Falsig J, Ballmer B, Li S, Hutter G, Schwarz P, Moos R, Julius C, Miele G, Aguzzi A. J Exp Med. 2010 Sep 27;207(10):2271-81.

Intrigued by reports showing that infectious prions might infect neighboring cells through the uptake of EVs, such as exosomes or apoptotic bodies that are shed either from intact infected or apoptotic infected cells, respectively, we investigated whether MFG-E8 is involved in this process (Fevrier et al., 2004). As EVs expose PS, MFG-E8 might attach to potentially prion-containing EVs and promote their uptake by phagocytic cells, like microglia in the brain, which would then become infected themselves.

To test this, we inoculated wild type and *Mfge8*^{-/-} mice on a mixed background with prions intraperitoneally and intracerebrally. In both cases prion disease was drastically accelerated in the absence of MFG-E8. This acceleration correlated with increased accumulation of prions in the brain and also elevated levels of terminal deoxynucleotidyl transferase dUTP nick end labelling-(TUNEL) positive apoptotic cells in the cerebellum. This indicated that clearance of apoptotic cells and apoptotic bodies was severely impaired in *Mfge8*^{-/-} mice.

We next investigated the cellular source of MFG-E8 in the brain and identified astrocytes as the main producer of MFG-E8 in the brain. In contrast, microglia, the main phagocytic cell type in the brain do not express *Mfge8*, however, these cells strongly express the MFG-E8 ligands integrin $\alpha_v\beta_3$ and $\alpha_v\beta_5$, which both bind MFG-E8's RGD-motif (Hanayama et al., 2002).

We also observed that the acceleration in prion pathogenesis in mice lacking MFG-E8 was dependent on the genetic background of the mouse strains used. The acceleration was only observed on a mixed B6.129 background, but not on a B6 or BALB/c background. We then performed an analysis of short tandem-repeats (STRs)

in the different genetic backgrounds and quantified the number of 129-specific alleles in each background strain. This revealed that the disease incubation time strongly correlated with the number of the 129-specific alleles. The more 129-specific alleles were present in the mice analyzed, the shorter the incubation time of the prion disease was.

When we assessed expression of the *Itgb3* gene, which encodes one chain of the integrins binding to MFG-E8's RGD motif, we found that some mice harbored strain-specific single nucleotide polymorphisms that were associated with accelerated incubation times. These polymorphisms did not result in codon changes, but still could affect splicing or mRNA stability or posttranscriptional control of the *Itgb3* gene and therefor could have an impact on MFG-E8-dependent uptake of apoptotic cells or EVs.

4.3 Using fluorescent MFG-E8 fusion proteins to stain PS⁺ cells *in vivo*

In vivo identification of apoptotic and extracellular vesicle-bound live cells using image-based deep learning. **Kranich J***, **, Chlis NK*, Rausch L, Latha A, Schifferer M, Kurz T, Foltyn-Arfa Kia A, Simons M, Theis FJ**, Brocker T**. *J Extracell Vesicles*. 2020 Jul 16;9(1):1792683. *equally contributed first author, ** corresponding author.

The initial aim of this study was to develop a method to visualize, quantify and characterize apoptotic cells in different organs. Apoptotic cells in intact tissues or organs are very rare and difficult to detect as they are rapidly removed by phagocytes. (Elliott and Ravichandran, 2010). A lot of dying cells are produced during organ isolation and preparation, hence our aim was to label dying cells *in situ* in the living mouse before organ removal by injecting PS-binding reagents.

The most widely used PS-binding reagent Annexin V requires high levels of Ca²⁺ and a special buffer for PS-binding and was therefore not suitable for our approach, as we couldn't be sure that sufficient concentrations of Ca²⁺ are present in every tissue. Thus, we developed novel PS-binding proteins based on the PS-binding protein MFG-E8, which binds to PS independently of Ca²⁺. We fused a fluorescent reporter (such as enhanced green fluorescent protein, EGFP) to the C-terminus of MFG-E8, expressed it recombinantly in a mammalian cell line and purified it by affinity chromatography.

After having confirmed that MFG-E8-EGFP stains the same cells as Annexin V, but in the absence of Ca²⁺, we applied it intravenously to mice that underwent irradiation to induce cell death.

We used imaging flow cytometry (IFC) to analyze the MFG-E8-EGFP stained cells, which has the advantage over conventional flow cytometry that this technique produces brightfield and fluorescent images of every cell and thus provides morphological information of the stained proteins.

MFG-E8-EGFP reliably labeled apoptotic cells in irradiated mice and in non-irradiated controls. As expected, the frequency of apoptotic cells was greatly increased in bone marrow and spleen after irradiation.

To our surprise, we not only detected apoptotic cells, which were fully stained, and had intensely stained apoptotic bodies attached, but also cells that had unstained cell bodies and had only one or a few strongly stained spots attached to their surface (Figure 8). This observation was only possible using IFC. As these spots looked like cellular attachments, we suspected that these were EVs. This we could confirm by transmission electron microscopy (TEM) on sorted PS⁺ cells, as these cells had multiple EVs attached on their surface.

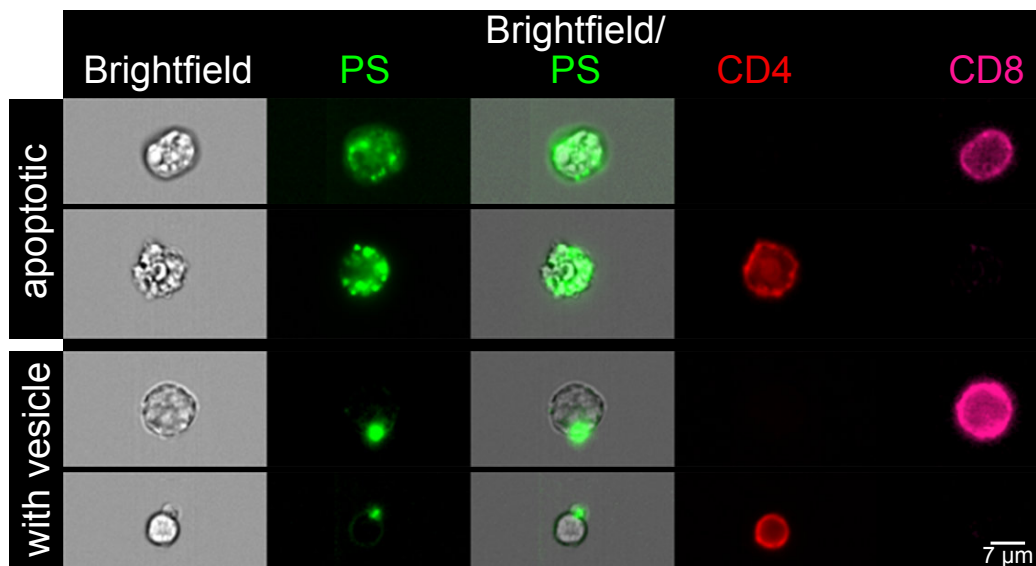


Figure 8. Apoptotic vs. EV⁺ cells.

T cells were stained with MFG-E8-EGFP to visualize PS. Upper panel shows PS⁺ apoptotic and the lower panel PS⁺ live EV-decorated cells.

One challenge was to discriminate true apoptotic cells from live EV-decorated cells in an IFC experiment. For this, we developed a deep learning algorithm that decided based on the brightfield and fluorescent image of the MFG-E8-EGFP staining if a cell was apoptotic or EV-decorated. With this algorithm we were then able to quantify apoptotic and EV-decorated in mice infected with an acute virus (lymphocytic choriomeningitis virus, LCMV). Our analysis revealed that apoptotic cells were very rare in all mice analyzed but did increase upon infection. What was striking was the number of EV-decorated cells in both uninfected and infected mice. Approx. 90% of all PS⁺ cells stained with MFG-E8-EGFP were EV⁺ and only approx. 10% were apoptotic. This was unexpected, as PS-staining was always used to detect apoptotic

cells. Our results now show that most of the cells detected using PS-staining are EV⁺ and not apoptotic. Furthermore, this study was the first report describing EV-decorated cells in tissues.

We then showed that especially activated T cells extensively bind EVs in infected mice. Using co-stainings with exosome markers like CD9 and CD63 and markers of antigen-presenting cells (MHC-II) we identified the source of the EVs being antigen-presenting cells.

Identification and characterization of PS⁺ cells in COVID-19 patients

Rausch L, Lutz K, Schifferer M, Winheim E, Gruber R, Oesterhaus EF, Rinke L, Hellmuth JC, Scherer C, Muenchhoff M, Mandel C, Bergwelt-Baildon M, Simons M, Straub T, Krug AB, **Kranich J***, Brocker T*. Binding of phosphatidylserine-positive microparticles by PBMCs classifies disease severity in COVID-19 patients. *J Extracell Vesicles*. 2021 Dec;10(14):e12173. * equally contributed last author.

COVID-19 is associated with severe thromboinflammation, which is regarded as a key driver of the pathology seen in SARS-CoV-2 patients (Gu et al., 2021). As PS is a marker for activated platelets and platelet-derived microparticles (PMPs), key players of the coagulation cascade (Zhao et al., 2016), we decided to investigate the distribution of PS⁺ cells in the blood of SARS-CoV-2 patients using our in-house developed Ca²⁺-independent PS-binding reagent MFG-E8-EGFP.

With this reagent we stained peripheral blood mononucleated cells (PBMCs) and analyzed them using IFC. We found a positive correlation between the number of PS⁺ PBMCs and disease severity. The higher the disease severity, the higher was the number of PBMCs with exposed PS on their surface. Not only correlated this number with the WHO clinical score, but also with patient survival and the requirement for ventilation.

When we then analyzed PS⁺ PBMCs in more detail using our previously developed deep learning tool that digitally sorts PS⁺ cells into apoptotic and EV-decorated cells (see [chapter 4.3](#); Kranich et al., 2020) we separately analyzed apoptotic and EV⁺ PBMCs.

While apoptotic PBMCs were significantly elevated in all patients, there was no correlation with disease severity. In contrast, the number of EV⁺ PBMCs showed a very strong correlation with disease severity and was more predictive for the severity score than established markers for inflammation and coagulation.

Next, we assessed the cellular subsets that preferentially bound EVs. We found strong EV-binding by B cells, dendritic cells, and monocytes in all patients regardless

of disease severity. T cells, however showed differential EV binding depending on the clinical score. Patients with mild disease showed no EV-binding by CD4⁺ T cells and low EV-binding by CD8⁺ T cells. Patients with a moderate disease score showed a significant increase in EV-binding by CD4⁺ T cells. EV-binding by CD8⁺ T cells was higher in these patients than in patients with mild disease. Patients with severe disease showed the highest EV binding by both CD4⁺ and CD8⁺ T cells.

We then investigated the origin of the EVs that attached to the PBMCs by TEM and IFC. TEM images of sorted PS⁺ PBMCs showed very irregular EVs with variable morphology typical for PMPs (Arraud et al., 2014). To confirm our notion that these EVs originated from platelets, we co-stained EV⁺ PBMCs with platelet markers, like CD41 and analyzed the cells by IFC. The result clearly showed that T cell-associated PS⁺ EVs were of platelet origin.

We then tried to identify transcriptomic differences between PS⁻ and PS⁺ CD8⁺ T cells by RNAseq and found that PS⁺ EVs had a higher proliferative capacity than their PS⁻ counterparts and an upregulation of effector-associated genes, while memory associated genes were rather repressed.

More work is needed to identify the precise role of the EVs that bind to T cells and to determine if this hampers T-cell responses despite driving T-cell proliferation and effector gene expression. As programmed death-ligand 1 (PD-L1) was also found on some of the T cell-associated EVs, prolonged EV-binding might contribute to T-cell exhaustion.

4.4 How EVs modulate T-cell responses

Rausch L, Flaskamp L, Ashokkumar A, Trefzer A, Ried C, Buchholz VR, Obst R, Straub T, Brocker T*, **Kranich J***. Phosphatidylserine-positive extracellular vesicles boost effector CD8⁺ T cell responses during viral infection. *Proc Natl Acad Sci U S A*. 2023 Apr 18;120(16):e2210047120. * equally contributed last author.

After having shown that EVs bind to activated T cells during LCMV (see [chapter 4.3](#); Kranich et al., 2020) and COVID infections (see [chapter 4.4](#); Rausch et al., 2021) we wanted to further investigate how EV influence T-cell responses.

Similar to previous studies we i.v. administered MFG-E8-EGFP to LCMV-infected mice to stain EV-decorated cells *in vivo* and monitored EV-decoration of CD8⁺ T cells at different timepoints. We found strong EV-binding by CD8⁺ T cells but observed that this was a transient phenomenon, peaking at day five after infection. 15 days after the infection EV-binding by T cells was almost completely absent and even lower than in uninfected controls.

Another interesting observation was that while EV-binding by T cells was increased in the spleen, free EVs in the blood were reduced in infected mice. This indicates that EV-binding cells in the spleen act as a sink for EVs in the blood.

Next, we investigated if EV-binding was antigen dependent. For this, we adoptively transferred *in vitro* activated TCR-transgenic LCMV-specific P14 cells (Pircher et al., 1989) and non-specific OT-I T cells recognizing an ovalbumin peptide (Hogquist et al., 1994) into previously LCMV-infected mice. On day five we quantified EV-binding on both transferred T-cell subsets by injecting MFG-E8-EGFP and analysis using IFC. We found that both, antigen-specific and non-specific T cells were able to bind EVs, although significantly more antigen-specific T cells had bound EVs, indicating a role of the TCR in EV-binding. In this experimental setup we also assessed whether the transcription factor nuclear factor of activated T-cell (NFAT) was differentially activated in EV⁺ and EV⁻ cells. In non-activated T cells NFAT is present in the cytoplasm in its inactive form. Upon TCR stimulation, NFAT is dephosphorylated and

rapidly translocates to the nucleus where it switches on expression of effector genes (Feske et al., 2001). We monitored whether NFAT is in the cytoplasm or in the nucleus using IFC. By quantifying the pixel overlap between the NFAT and the nuclear staining we could determine the degree of active nuclear versus inactive cytoplasmic NFAT. This analysis clearly showed that only antigen-specific EV⁺ T cells, but not EV⁻ antigen-specific or EV⁺ non-specific T cells had a strong accumulation of NFAT in the nucleus. This was the first indication that EVs might stimulate T cells in an antigen-dependent manner. This warranted further investigation.

We then decided to analyze EV⁺ T cells by stochastic optical reconstruction microscopy (STORM). With this method a resolution of up to 20nm is possible. This is achieved using blinking fluorochromes that switch between an on and off state. By collecting multiple frames, the signals of individual fluorochromes are used to reconstruct an image (Rust et al., 2006). As this technique requires special fluorochromes that cycle between an on and off state in a special buffer, we could not use MFG-E8-EGFP to stain EVs. However, we had already developed novel PS-binding reagents, which consist only of the C1 domain of MFG-E8 (Figure 6). After biotinylation of this domain we construct C1-tetramers by adding Streptavidin. These molecules bind PS with exquisite specificity and sensitivity. We used Streptavidin coupled to AlexaFluor647 to generate C1-tetramers that can be used for STORM superresolution microscopy.

EV⁺ T cells in LCMV-infected mice were stained by injecting these C1-tetramers. Then PS⁺ and PS⁻ CD8⁺ T cells were sorted, stained with anti-CD9 as an additional exosome marker and imaged by STORM superresolution microscopy. The results were striking and revealed that PS⁺CD9⁺ exosomes strongly co-localized with CD8, which is part of the TCR complex. The results also showed that PS⁻ T cells showed a much lower degree of TCR clustering. As clustering is needed for TCR signaling (Yokosuka et al., 2005), PS⁻ cells show lower signaling than PS⁺ cells, which confirmed out previous NFAT translocation results.

Transcriptomic analysis of PS⁺ and PS⁻ effector CD8⁺ T cells from infected mice showed an enrichment of gene clusters involved in cell cycle and cell division and

also an increase in effector gene expression, while gene clusters associated with memory formation were repressed in PS⁺ cells. Cell-cycle analysis using nuclear stainings confirmed that significantly more PS⁺ cells were in the G₂/M phase than PS⁻ cells.

At this stage we did not have definite proof that EVs were responsible for these effects. It was still possible that recently activated T cells were merely better at binding EVs. To answer the question, if it was really EVs that stimulated T cells and caused NFAT translocation we used antigen-pulsed *in vitro* generated EVs that were injected into H2-K^{bm1} mice that are unable to present the peptide to T cells present on the *in vitro* generated EVs. To generate EVs loaded with peptides from ovalbumin, we pulsed bone marrow-derived dendritic cells with antigen and harvested EVs from these cells. To be able to track the EVs after injection, we stained them with the membrane dye PKH26. Before we injected these EVs into H2-K^{bm1} mice, which are unable to present the ovalbumin peptide to T cells due to a mutation in the H2-K locus (Clarke et al., 2000), we adoptively transferred *in vitro* activated antigen-specific OT-I or non-specific P14 T cells. In this setup the only source of antigen that can be seen by the transferred OT-I T cells are the injected EVs. We then analyzed nuclear translocation of NFAT in EV⁺ and EV⁻ antigen-specific OT-I or non-specific P14 cells. Strikingly, EV⁺ antigen-specific OT-I cells had the highest degree of nuclear NFAT. No nuclear NFAT translocation was observed on OT-I cells that did not bind EVs or in P14 cells, even when they had bound EVs.

These results clearly show that EVs are able to stimulate previously activated T cells in an antigen dependent manner. This leads to increased proliferation and expression of effector genes. As EV-binding by T cells quickly subsides after virus clearance, EVs might act as a danger signal while virus is still present boosting the effector response as long as it is required.

5. Outlook

The studies discussed in the previous chapters show that EVs modulate immune responses by boosting effector functions and proliferation of CD8⁺ T cells during viral infections by antigen that is present on EVs. As EVs can be a source of antigen, it is plausible that they could also contribute to exhaustion of T cells in chronic viral infections or in cancer. The next step would be to analyze whether this is the case. During acute LCMV-infections, the presence of EV-decorated T cells is transient and 15 days after the infection EV-decorated T cells are not present anymore. It would be interesting to investigate if this is also the case during chronic infections or if instead EVs are a continuous source of antigen for T cells driving their exhaustion.

As EVs have the potential to boost effector CD8⁺ T cells, EV-binding by T cells could be an interesting target for therapeutic interventions in viral infections or cancer. Under certain conditions, e.g., if EVs contribute to T-cell exhaustion, it might also be beneficial to reduce EV-binding by T cells. Therefore, we are currently developing strategies to increase or diminish EV-binding by T cells with the aim to improve or inhibit T-cell effector functions.

6. Literature

1. Al-Nedawi, K., B. Meehan, R.S. Kerbel, A.C. Allison, and J. Rak. 2009. Endothelial expression of autocrine VEGF upon the uptake of tumor-derived microvesicles containing oncogenic EGFR. *Proc Natl Acad Sci U S A* 106:3794-3799.
2. Al-Nedawi, K., B. Meehan, J. Micallef, V. Lhotak, L. May, A. Guha, and J. Rak. 2008. Intercellular transfer of the oncogenic receptor EGFRvIII by microvesicles derived from tumour cells. *Nat Cell Biol* 10:619-624.
3. Anand, S., M. Samuel, and S. Mathivanan. 2021. Exomeres: A New Member of Extracellular Vesicles Family. *Subcell Biochem* 97:89-97.
4. Arraud, N., R. Linares, S. Tan, C. Gounou, J.M. Pasquet, S. Mornet, and A.R. Brisson. 2014. Extracellular vesicles from blood plasma: determination of their morphology, size, phenotype and concentration. *J Thromb Haemost* 12:614-627.
5. Atabai, K., R. Fernandez, X. Huang, I. Ueki, A. Kline, Y. Li, S. Sadatmansoori, C. Smith-Steinhart, W. Zhu, R. Pytela, Z. Werb, and D. Sheppard. 2005. Mfge8 is critical for mammary gland remodeling during involution. *Mol Biol Cell* 16:5528-5537.
6. Ayala-Mar, S., J. Donoso-Quezada, and J. González-Valdez. 2021. Clinical Implications of Exosomal PD-L1 in Cancer Immunotherapy. *Journal of Immunology Research* 2021:8839978.
7. Bassé, F., J.G. Stout, P.J. Sims, and T. Wiedmer. 1996. Isolation of an erythrocyte membrane protein that mediates Ca²⁺-dependent transbilayer movement of phospholipid. *The Journal of biological chemistry* 271:17205-17210.
8. Becker, A., B.K. Thakur, J.M. Weiss, H.S. Kim, H. Peinado, and D. Lyden. 2016. Extracellular Vesicles in Cancer: Cell-to-Cell Mediators of Metastasis. *Cancer Cell* 30:836-848.
9. Bricogne, C., M. Fine, P.M. Pereira, J. Sung, M. Tijani, Y. Wang, R. Henriques, M.K. Collins, and D.W. Hilgemann. 2019. TMEM16F activation by Ca(2+) triggers plasma membrane expansion and directs PD-1 trafficking. *Sci Rep* 9:619.
10. Bruce Alberts, A.J., Julian Lewis, Martin Raff, Keith Roberts, and Peter Walter. 2002. *Molecular Biology of the Cell*. Garland Science, New York.
11. Chen, G., A.C. Huang, W. Zhang, G. Zhang, M. Wu, W. Xu, Z. Yu, J. Yang, B. Wang, H. Sun, H. Xia, Q. Man, W. Zhong, L.F. Antelo, B. Wu, X. Xiong, X. Liu, L. Guan, T. Li, S. Liu, R. Yang, Y. Lu, L. Dong, S. McGettigan, R. Somasundaram, R. Radhakrishnan, G. Mills, Y. Lu, J. Kim, Y.H. Chen, H. Dong, Y. Zhao, G.C. Karakousis, T.C. Mitchell, L.M. Schuchter, M. Herlyn, E.J. Wherry, X. Xu, and W. Guo. 2018. Exosomal PD-L1 contributes to immunosuppression and is associated with anti-PD-1 response. *Nature* 560:382-386.
12. Chen, J., J. Yang, W. Wang, D. Guo, C. Zhang, S. Wang, X. Lu, X. Huang, P. Wang, G. Zhang, J. Zhang, J. Wang, and Z. Cai. 2022. Tumor extracellular vesicles mediate anti-PD-L1 therapy resistance by decoying anti-PD-L1. *Cellular & molecular immunology* 19:1290-1301.
13. Clarke, S.R., M. Barnden, C. Kurts, F.R. Carbone, J.F. Miller, and W.R. Heath. 2000. Characterization of the ovalbumin-specific TCR transgenic line OT-I: MHC elements for positive and negative selection. *Immunology and cell biology* 78:110-117.
14. de Vasconcelos, N.M., N. Van Opdenbosch, H. Van Gorp, E. Parthoens, and M. Lamkanfi. 2019. Single-cell analysis of pyroptosis dynamics reveals conserved

- GSDMD-mediated subcellular events that precede plasma membrane rupture. *Cell Death Differ* 26:146-161.
15. Ehlen, H.W., M. Chinenkova, M. Moser, H.M. Munter, Y. Krause, S. Gross, B. Brachvogel, M. Wuelling, U. Kornak, and A. Vortkamp. 2013. Inactivation of anoctamin-6/Tmem16f, a regulator of phosphatidylserine scrambling in osteoblasts, leads to decreased mineral deposition in skeletal tissues. *J Bone Miner Res* 28:246-259.
 16. Elliott, M.R., and K.S. Ravichandran. 2010. Clearance of apoptotic cells: implications in health and disease. *The Journal of cell biology* 189:1059-1070.
 17. Feske, S., J. Giltmane, R. Dolmetsch, L.M. Staudt, and A. Rao. 2001. Gene regulation mediated by calcium signals in T lymphocytes. *Nat Immunol* 2:316-324.
 18. Fevrier, B., D. Vilette, F. Archer, D. Loew, W. Faigle, M. Vidal, H. Laude, and G. Raposo. 2004. Cells release prions in association with exosomes. *Proc Natl Acad Sci U S A* 101:9683-9688.
 19. Fujii, T., A. Sakata, S. Nishimura, K. Eto, and S. Nagata. 2015. TMEM16F is required for phosphatidylserine exposure and microparticle release in activated mouse platelets. *Proc Natl Acad Sci U S A* 112:12800-12805.
 20. Furuta, Y., O. Pena-Ramos, Z. Li, L. Chiao, and Z. Zhou. 2021. Calcium ions trigger the exposure of phosphatidylserine on the surface of necrotic cells. *PLoS Genet* 17:e1009066.
 21. Garcia-Diaz, A., D.S. Shin, B.H. Moreno, J. Saco, H. Escuin-Ordinas, G.A. Rodriguez, J.M. Zaretsky, L. Sun, W. Hugo, X. Wang, G. Parisi, C.P. Saus, D.Y. Torrejon, T.G. Graeber, B. Comin-Anduix, S. Hu-Lieskovan, R. Damoiseaux, R.S. Lo, and A. Ribas. 2017. Interferon Receptor Signaling Pathways Regulating PD-L1 and PD-L2 Expression. *Cell Rep* 19:1189-1201.
 22. Gu, S.X., T. Tyagi, K. Jain, V.W. Gu, S.H. Lee, J.M. Hwa, J.M. Kwan, D.S. Krause, A.I. Lee, S. Halene, K.A. Martin, H.J. Chun, and J. Hwa. 2021. Thrombocytopeny and endotheliopathy: crucial contributors to COVID-19 thromboinflammation. *Nat Rev Cardiol* 18:194-209.
 23. György, B., T.G. Szabó, M. Pásztói, Z. Pál, P. Misják, B. Aradi, V. László, E. Pállinger, E. Pap, A. Kittel, G. Nagy, A. Falus, and E.I. Buzás. 2011. Membrane vesicles, current state-of-the-art: emerging role of extracellular vesicles. *Cellular and molecular life sciences : CMLS* 68:2667-2688.
 24. Hanayama, R., M. Tanaka, K. Miwa, A. Shinohara, A. Iwamatsu, and S. Nagata. 2002. Identification of a factor that links apoptotic cells to phagocytes. *Nature* 417:182-187.
 25. Hanayama, R., M. Tanaka, K. Miyasaka, K. Aozasa, M. Koike, Y. Uchiyama, and S. Nagata. 2004. Autoimmune disease and impaired uptake of apoptotic cells in MFG-E8-deficient mice. *Science* 304:1147-1150.
 26. Hao, S., O. Bai, F. Li, J. Yuan, S. Laferte, and J. Xiang. 2007. Mature dendritic cells pulsed with exosomes stimulate efficient cytotoxic T-lymphocyte responses and antitumour immunity. *Immunology* 120:90-102.
 27. Hogquist, K.A., S.C. Jameson, W.R. Heath, J.L. Howard, M.J. Bevan, and F.R. Carbone. 1994. T cell receptor antagonist peptides induce positive selection. *Cell* 76:17-27.
 28. Huber, C., C. Thielen, H. Seeger, P. Schwarz, F. Montrasio, M.R. Wilson, E. Heinen, Y.X. Fu, G. Miele, and A. Aguzzi. 2005. Lymphotoxin-beta receptor-dependent genes in lymph node and follicular dendritic cell transcriptomes. *J Immunol* 174:5526-5536.

29. Kay, J.G., and G.D. Fairn. 2019. Distribution, dynamics and functional roles of phosphatidylserine within the cell. *Cell Commun Signal* 17:126.
30. Kovar, M., O. Boyman, X. Shen, I. Hwang, R. Kohler, and J. Sprent. 2006. Direct stimulation of T cells by membrane vesicles from antigen-presenting cells. *Proc Natl Acad Sci U S A* 103:11671-11676.
31. Kranich, J., N.K. Chlis, L. Rausch, A. Latha, M. Schifferer, T. Kurz, A. Foltyn-Arfa Kia, M. Simons, F.J. Theis, and T. Brocker. 2020. In vivo identification of apoptotic and extracellular vesicle-bound live cells using image-based deep learning. *J Extracell Vesicles* 9:1792683.
32. Kranich, J., N.J. Krautler, E. Heinen, M. Polymenidou, C. Bridel, A. Schildknecht, C. Huber, M.H. Kosco-Vilbois, R. Zinkernagel, G. Miele, and A. Aguzzi. 2008. Follicular dendritic cells control engulfment of apoptotic bodies by secreting Mfge8. *J Exp Med* 205:1293-1302.
33. Krautler, N.J., V. Kana, J. Kranich, Y. Tian, D. Perera, D. Lemm, P. Schwarz, A. Armulik, J.L. Browning, M. Tallquist, T. Buch, J.B. Oliveira-Martins, C. Zhu, M. Hermann, U. Wagner, R. Brink, M. Heikenwalder, and A. Aguzzi. 2012. Follicular dendritic cells emerge from ubiquitous perivascular precursors. *Cell* 150:194-206.
34. Lanna, A., B. Vaz, C. D'Ambra, S. Valvo, C. Vuotto, V. Chiurchiù, O. Devine, M. Sanchez, G. Borsellino, A.N. Akbar, M. De Bardi, D.W. Gilroy, M.L. Dustin, B. Blumer, and M. Karin. 2022. An intercellular transfer of telomeres rescues T cells from senescence and promotes long-term immunological memory. *Nat Cell Biol* 24:1461-1474.
35. Matsumoto, A., Y. Takahashi, K. Ogata, S. Kitamura, N. Nakagawa, A. Yamamoto, Y. Ishihama, and Y. Takakura. 2021. Phosphatidylserine-deficient small extracellular vesicle is a major somatic cell-derived sEV subpopulation in blood. *iScience* 24:102839.
36. Miyanishi, M., K. Tada, M. Koike, Y. Uchiyama, T. Kitamura, and S. Nagata. 2007. Identification of Tim4 as a phosphatidylserine receptor. *Nature* 450:435-439.
37. Miyasaka, K., R. Hanayama, M. Tanaka, and S. Nagata. 2004. Expression of milk fat globule epidermal growth factor 8 in immature dendritic cells for engulfment of apoptotic cells. *European journal of immunology* 34:1414-1422.
38. Nakano, T., Y. Ishimoto, J. Kishino, M. Umeda, K. Inoue, K. Nagata, K. Ohashi, K. Mizuno, and H. Arita. 1997. Cell adhesion to phosphatidylserine mediated by a product of growth arrest-specific gene 6. *The Journal of biological chemistry* 272:29411-29414.
39. Neven, K.Y., T.S. Nawrot, and V. Bollati. 2017. Extracellular Vesicles: How the External and Internal Environment Can Shape Cell-To-Cell Communication. *Curr Environ Health Rep* 4:30-37.
40. Nishi, C., S. Toda, K. Segawa, and S. Nagata. 2014. Tim4- and MerTK-mediated engulfment of apoptotic cells by mouse resident peritoneal macrophages. *Mol Cell Biol* 34:1512-1520.
41. Nolte-'t Hoen, E.N., S.I. Buschow, S.M. Anderton, W. Stoorvogel, and M.H. Wauben. 2009. Activated T cells recruit exosomes secreted by dendritic cells via LFA-1. *Blood* 113:1977-1981.
42. Obydenny, S.I., A.N. Sveshnikova, F.I. Ataulakhanov, and M.A. Pantelev. 2016. Dynamics of calcium spiking, mitochondrial collapse and phosphatidylserine exposure in platelet subpopulations during activation. *J Thromb Haemost* 14:1867-1881.

43. Palmgren, M.G., and P. Nissen. 2011. P-type ATPases. *Annu Rev Biophys* 40:243-266.
44. Pircher, H., K. Bürki, R. Lang, H. Hengartner, and R.M. Zinkernagel. 1989. Tolerance induction in double specific T-cell receptor transgenic mice varies with antigen. *Nature* 342:559-561.
45. Raposo, G., H.W. Nijman, W. Stoorvogel, R. Liejendekker, C.V. Harding, C.J. Melief, and H.J. Geuze. 1996. B lymphocytes secrete antigen-presenting vesicles. *J Exp Med* 183:1161-1172.
46. Rausch, L., L. Flaskamp, A. Ashokkumar, A. Trefzer, C. Ried, V.R. Buchholz, R. Obst, T. Straub, T. Brocker, and J. Kranich. 2023. Phosphatidylserine-positive extracellular vesicles boost effector CD8(+) T cell responses during viral infection. *Proc Natl Acad Sci U S A* 120:e2210047120.
47. Rausch, L., K. Lutz, M. Schifferer, E. Winheim, R. Gruber, E.F. Oesterhaus, L. Rinke, J.C. Hellmuth, C. Scherer, M. Muenchhoff, C. Mandel, M. Bergwelt-Baildon, M. Simons, T. Straub, A.B. Krug, J. Kranich, and T. Brocker. 2021. Binding of phosphatidylserine-positive microparticles by PBMCs classifies disease severity in COVID-19 patients. *Journal of Extracellular Vesicles* 10:e12173.
48. Raymond, A., M.A. Ensslin, and B.D. Shur. 2009. SED1/MFG-E8: a bi-motif protein that orchestrates diverse cellular interactions. *Journal of cellular biochemistry* 106:957-966.
49. Rust, M.J., M. Bates, and X. Zhuang. 2006. Sub-diffraction-limit imaging by stochastic optical reconstruction microscopy (STORM). *Nat Methods* 3:793-795.
50. Sang, Y., M. Roest, B. de Laat, P.G. de Groot, and D. Huskens. 2021. Interplay between platelets and coagulation. *Blood Rev* 46:100733.
51. Santavanond, J.P., S.F. Rutter, G.K. Atkin-Smith, and I.K.H. Poon. 2021. Apoptotic Bodies: Mechanism of Formation, Isolation and Functional Relevance. *Subcell Biochem* 97:61-88.
52. Sapor, M.L., H. Ji, B. Wang, A.R. Poe, K. Dubey, X. Ren, J.Q. Ni, and C. Han. 2018. Phosphatidylserine Externalization Results from and Causes Neurite Degeneration in Drosophila. *Cell Rep* 24:2273-2286.
53. Segawa, K., S. Kurata, Y. Yanagihashi, T.R. Brummelkamp, F. Matsuda, and S. Nagata. 2014. Caspase-mediated cleavage of phospholipid flippase for apoptotic phosphatidylserine exposure. *Science* 344:1164-1168.
54. Segawa, K., and S. Nagata. 2015. An Apoptotic 'Eat Me' Signal: Phosphatidylserine Exposure. *Trends Cell Biol* 25:639-650.
55. Shlomovitz, I., M. Speir, and M. Gerlic. 2019. Flipping the dogma - phosphatidylserine in non-apoptotic cell death. *Cell Commun Signal* 17:139.
56. Sidhom, K., P.O. Obi, and A. Saleem. 2020. A Review of Exosomal Isolation Methods: Is Size Exclusion Chromatography the Best Option? *Int J Mol Sci* 21:
57. Sung, B.H., T. Ketova, D. Hoshino, A. Zijlstra, and A.M. Weaver. 2015. Directional cell movement through tissues is controlled by exosome secretion. *Nat Commun* 6:7164.
58. Suzuki, J., D.P. Denning, E. Imanishi, H.R. Horvitz, and S. Nagata. 2013. Xk-related protein 8 and CED-8 promote phosphatidylserine exposure in apoptotic cells. *Science* 341:403-406.
59. Suzuki, J., M. Umeda, P.J. Sims, and S. Nagata. 2010. Calcium-dependent phospholipid scrambling by TMEM16F. *Nature* 468:834-838.
60. Théry, C., K.W. Witwer, E. Aikawa, et al. 2018. Minimal information for studies of extracellular vesicles 2018 (MISEV2018): a position statement of the

- International Society for Extracellular Vesicles and update of the MISEV2014 guidelines. *J Extracell Vesicles* 7:1535750.
61. Urabe, F., N. Kosaka, K. Ito, T. Kimura, S. Egawa, and T. Ochiya. 2020. Extracellular vesicles as biomarkers and therapeutic targets for cancer. *Am J Physiol Cell Physiol* 318:C29-c39.
 62. Vermes, I., C. Haanen, H. Steffens-Nakken, and C. Reutelingsperger. 1995. A novel assay for apoptosis. Flow cytometric detection of phosphatidylserine expression on early apoptotic cells using fluorescein labelled Annexin V. *Journal of immunological methods* 184:39-51.
 63. Yabas, M., C.E. Teh, S. Frankenreiter, D. Lal, C.M. Roots, B. Whittle, D.T. Andrews, Y. Zhang, N.C. Teoh, J. Sprent, L.E. Tze, E.M. Kucharska, J. Kofler, G.C. Farrell, S. Bröer, C.C. Goodnow, and A. Enders. 2011. ATP11C is critical for the internalization of phosphatidylserine and differentiation of B lymphocytes. *Nat Immunol* 12:441-449.
 64. Yates, A.G., R.C. Pink, U. Erdbrügger, P.R. Siljander, E.R. Dellar, P. Pantazi, N. Akbar, W.R. Cooke, M. Vatish, E. Dias-Neto, D.C. Anthony, and Y. Couch. 2022. In sickness and in health: The functional role of extracellular vesicles in physiology and pathology in vivo: Part I: Health and Normal Physiology: Part I: Health and Normal Physiology. *J Extracell Vesicles* 11:e12151.
 65. Yokosuka, T., K. Sakata-Sogawa, W. Kobayashi, M. Hiroshima, A. Hashimoto-Tane, M. Tokunaga, M.L. Dustin, and T. Saito. 2005. Newly generated T cell receptor microclusters initiate and sustain T cell activation by recruitment of Zap70 and SLP-76. *Nat Immunol* 6:1253-1262.
 66. Yoshida, T., and R. Hanayama. 2022. TIM4-Affinity Methods Targeting Phosphatidylserine for Isolation or Detection of Extracellular Vesicles. *Methods in molecular biology* 2466:23-36.
 67. Zachowski, A. 1993. Phospholipids in animal eukaryotic membranes: transverse asymmetry and movement. *The Biochemical journal* 294 (Pt 1):1-14.
 68. Zhao, L., Y. Bi, J. Kou, J. Shi, and D. Piao. 2016. Phosphatidylserine exposing-platelets and microparticles promote procoagulant activity in colon cancer patients. *J Exp Clin Cancer Res* 35:54.
 69. Zhou, W., M.Y. Fong, Y. Min, G. Somlo, L. Liu, M.R. Palomares, Y. Yu, A. Chow, S.T. O'Connor, A.R. Chin, Y. Yen, Y. Wang, E.G. Marcusson, P. Chu, J. Wu, X. Wu, A.X. Li, Z. Li, H. Gao, X. Ren, M.P. Boldin, P.C. Lin, and S.E. Wang. 2014. Cancer-secreted miR-105 destroys vascular endothelial barriers to promote metastasis. *Cancer Cell* 25:501-515.
 70. Zitvogel, L., A. Regnault, A. Lozier, J. Wolfers, C. Flament, D. Tenza, P. Ricciardi-Castagnoli, G. Raposo, and S. Amigorena. 1998. Eradication of established murine tumors using a novel cell-free vaccine: dendritic cell-derived exosomes. *Nat Med* 4:594-600.
 71. Zullig, S., and M.O. Hengartner. 2004. Cell biology. Tickling macrophages, a serious business. *Science* 304:1123-1124.
 72. Zwaal, R.F., P. Comfurius, and E.M. Bevers. 1998. Lipid-protein interactions in blood coagulation. *Biochim Biophys Acta* 1376:433-453.

7. Publication Record

7.1 Publications as first or last author

- 1.) Follicular dendritic cells control engulfment of apoptotic bodies by secreting Mfge8. Kranich J, Krautler NJ, Heinen E, Polymenidou M, Bridel C, Schildknecht A, Huber C, Kosco-Vilbois MH, Zinkernagel R, Miele G, Aguzzi A.; *J Exp Med*. 2008 Jun 9;205(6):1293-302. IF (2008): 15.463.
- 2.) Engulfment of cerebral apoptotic bodies controls the course of prion disease in a mouse strain-dependent manner. Kranich J, Krautler NJ, Falsig J, Ballmer B, Li S, Hutter G, Schwarz P, Moos R, Julius C, Miele G, Aguzzi A. *J Exp Med*. 2010 Sep 27;207(10):2271-81. IF (2010): 14.776.
- 3.) In vivo identification of apoptotic and extracellular vesicle-bound live cells using image-based deep learning. Kranich J*, **, Chlis NK*, Rausch L, Latha A, Schifferer M, Kurz T, Foltyn-Arfa Kia A, Simons M, Theis FJ**, Brocker T**. *J Extracell Vesicles*. 2020 Jul 16;9(1):1792683. IF (2019): 14.976. * equally contributed, ** corresponding author.
- 4.) Predicting single-cell gene expression profiles of imaging flow cytometry data with machine learning. Chlis NK, Rausch L, Brocker T, **Kranich J***, Theis FJ* . *Nucleic Acids Res*. Oct. 2020, gkaa926. *IF (2019): 11.501*. * equally contributed.
- 5.) Binding of phosphatidylserine-positive microparticles by PBMCs classifies disease severity in COVID-19 patients. Rausch L, Lutz K, Schifferer M, Winheim E, Gruber R, Oesterhaus EF, Rinke L, Hellmuth JC, Scherer C, Muenchhoff M, Mandel C, Bergwelt-Baildon M, Simons M, Straub T, Krug AB, Kranich J*, Brocker T*. *J Extracell Vesicles*. 2021 Dec;10(14). *Shared senior authorship.
- 6.) Phosphatidylserine-positive extracellular vesicles boost effector CD8⁺ T cell responses during viral infection. Rausch L, Flaskamp L, Ashokkumar A, Trefzer A, Ried C, Buchholz VR, Obst R, Straub T, Brocker T*, Kranich J*. *Proc Natl Acad Sci U S A*. 2023 Apr 18;120(16). *Shared senior authorship.

7.2 Publications as co-author

- 1.) Coincident scrapie infection and nephritis lead to urinary prion excretion. Seeger H, Heikenwalder M, Zeller N, **Kranich J**, Schwarz P, Gaspert A, Seifert B, Miele G, Aguzzi A.; *Science*, 2005 Oct 14;310(5746):324-6.
- 2.) Stromal complement receptor CD21/35 facilitates lymphoid prion colonization and pathogenesis. Zabel MD, Heikenwalder M, Prinz M, Arrighi I, Schwarz P, **Kranich J**, von Teichman A, Haas KM, Zeller N, Tedder TF, Weis JH, Aguzzi A.; *J Immunol*. 2007 Nov 1;179(9):6144-52. *IF (2007): 6.068*.
- 3.) Transcriptional Stability of Cultured Cells upon Prion Infection. Julius C, Hutter G, Wagner U, Seeger H, Kana V, **Kranich J**, Klöhn P, Weissmann C, Miele G, Aguzzi A.; *J Mol Biol*. 2008 Feb 1;375(5):1222-33.
- 4.) Lymphotoxin-dependent prion replication in inflammatory stromal cells of granulomas. Heikenwalder M, Kurrer MO, Margalith I, **Kranich J**, Zeller N, Haybaeck J, Polymenidou M, Matter M, Bremer J, Jackson WS, Lindquist S, Sigurdson CJ, Aguzzi A. *Immunity*. 2008 Dec;29(6):998-1008.
- 5.) Regulation of inflammatory responses by gut microbiota and chemoattractant receptor GPR43. Maslowski KM, Vieira AT, Ng A, **Kranich J**, Sierro F, Yu D, Schilter HC, Rolph MS, Mackay F, Artis D, Xavier RJ, Teixeira MM, Mackay CR. *Nature*. 2009 Oct 29;461(7268):1282-6.
- 6.) Liposome-siRNA-peptide complexes cross the blood-brain barrier and significantly decrease PrP on neuronal cells and PrP in infected cell cultures. Pulford B, Reim N, Bell A, Veatch J, Forster G, Bender H, Meyerett C, Hafeman S, Michel B, Johnson T, Wyckoff AC, Miele G, Julius C, **Kranich J**, Schenkel A, Dow S, Zabel MD. *PLoS One*. 2010 Jun 14;5(6):e11085.
- 7.) Programming of marginal zone B cell fate by basic kuppel-like factor (BKLF/KLF3). Turchinovich G, Vu TT, Frommer F, **Kranich J**, Schmid S, Alles M, Loubert J-B, Goulet J-P, Zimmer-Strobl U, Schneider P, Bachl J, Pearson R, Crossley M, Agenès F and Kirberg J. *Blood*. 2011 Feb 4.
- 8.) Follicular dendritic cells emerge from ubiquitous perivascular precursors. Krautler NJ, Kana V, **Kranich J**, Tian Y, Perera D, Lemm D, Schwarz P, Armulik A, Browning JL, Tallquist M, Buch T, Oliveira-Martins JB, Zhu C, Hermann M, Wagner U, Brink R, Heikenwalder M, Aguzzi A. *Cell*. 2012 Jul 6;150(1):194-206.
- 9.) Alternative splicing of MALT1 controls signalling and activation of CD4(+) T cells. Meininger I, Griesbach RA, Hu D, Gehring T, Seeholzer T, Bertossi A, **Kranich J**, Oeckinghaus A, Eitelhuber AC, Greczmiel U, Gewies A, Schmidt-Supprian M, Ruland J, Brocker T, Heissmeyer V, Heyd F, Krappmann D. *Nat Commun*. 2016 Apr 12;7:11292.
- 10.) Gut microbial metabolites limit the frequency of autoimmune T cells and protect against type 1 diabetes. Mariño E, Richards JL, McLeod KH, Stanley D, Yap YA, Knight J, McKenzie C, **Kranich J**, Oliveira AC, Rossello FJ, Krishnamurthy B, Nefzger CM, Macia

L, Thorburn A, Baxter AG, Morahan G, Wong LH, Polo JM, Moore RJ, Lockett TJ, Clarke JM, Topping DL, Harrison LC, Mackay CR. *Nat Immunol*. 2017 May;18(5):552-562.

- 11.) The host-cell restriction factor SERINC5 restricts HIV-1 infectivity without altering the lipid composition and organization of viral particles. Trautz B, Wiedemann H, Lüchtenborg C, Pierini V, **Kranich J**, Glass B, Kräusslich HG, Brocker T, Pizzato M, Ruggieri A, Brügger B, Fackler OT. *J Biol Chem*. 2017 Aug 18;292(33):13702-13713.
- 12.) Roquin Suppresses the PI3K-mTOR Signaling Pathway to Inhibit T Helper Cell Differentiation and Conversion of Treg to Tfr Cells. Essig K, Hu D, Guimaraes JC, Alterauge D, Edelmann S, Raj T, **Kranich J**, Behrens G, Heiseke A, Floess S, Klein J, Maiser A, Marschall S, Hrabé de Angelis M, Leonhardt H, Calkhoven CF, Noessner E, Brocker T, Huehn J, Krug AB, Zavolan M, Baumjohann D, Heissmeyer V. *Immunity*. 2017 Dec 19;47(6):1067-1082.
- 13.) Dynamic adoption of anergy by antigen-exhausted CD4+ T cells. Trefzer A, Kadam P, Wang SH, Pennavaria S, Lober B, Akçaboza B, **Kranich J**, Brocker T, Nakano N, Irmeler M, Beckers J, Straub T, Obst R. *Cell Rep*. 2021 Feb 9;34(6):108748.
- 14.) Impaired function and delayed regeneration of dendritic cells in COVID-19. Winheim E, Rinke L, Lutz K, Reischer A, Leutbecher A, Wolfram L, Rausch L, **Kranich J**, Wratil PR, Huber JE, Baumjohann D, Rothenfusser S, Schubert B, Hilgendorff A, Hellmuth JC, Scherer C, Muenchhoff M, von Bergwelt-Baildon M, Stark K, Straub T, Brocker T, Keppler OT, Subklewe M, Krug AB. *PLoS Pathog*. 2021 Oct 6;17(10):e1009742.
- 15.) Procoagulant platelet sentinels prevent inflammatory bleeding through GPIIBIIIA and GPVI. Kaiser R, Escaig R, **Kranich J**, Hoffknecht ML, Anjum A, Polewka V, Mader M, Hu W, Belz L, Gold C, Titova A, Lorenz M, Pekayvaz K, Kääb S, Gaertner F, Stark K, Brocker T, Massberg S, Nicolai L. *Blood*. 2022 Jul 14;140(2):121-139. doi: 10.1182/blood.2021014914.
- 16.) Mechanosensing via a GpIIb/Src/14-3-3ζ axis critically regulates platelet migration in vascular inflammation. Kaiser R, Anjum A, Kammerer L, Loew Q, Akhalkatsi A, Rossaro D, Escaig R, Droste Zu Senden A, Raude B, Lorenz M, Gold C, Pekayvaz K, Brocker T, **Kranich J**, Holch JW, Spiekermann K, Massberg S, Gaertner F, Nicolai L. *Blood*. 2023 Jun 15;141(24):2973-2992.
- 17.) The small molecule inhibitor BX-795 uncouples IL-2 production from inhibition of Th2 inflammation and induces CD4+ T cells resembling iTreg. Tauber PA, Kratzer B, Schatzlmaier P, Smole U, Köhler C, Rausch L, **Kranich J**, Trapin D, Neunkirchner A, Zabel M, Jutz S, Steinberger P, Gadermaier G, Brocker T, Stockinger H, Derdak S, Pickl WF. *Front Immunol*. 2023 Apr 6;14:1094694.

7.3 Reviews

- 1.) Commensal flora and the regulation of inflammatory and autoimmune responses. **Kranich J**, Maslowski KM and Mackay CR. *Semin Immunol*. 2011 Feb 1.
- 2.) Microbial influences on epithelial integrity and immune function as a basis for inflammatory diseases. Macia L, Thorburn AN, Binge LC, Marino E, Rogers KE, Maslowski KM, Vieira AT, **Kranich J**, Mackay CR. *Immunol Rev*. 2012 Jan;245(1):164-76.
- 3.) Follicular dendritic cells: origin, phenotype, and function in health and disease. Aguzzi A, **Kranich J**, Krautler NJ. *Trends Immunol*. 2014 Mar;35(3):105-13.
- 4.) How Follicular Dendritic Cells Shape the B-Cell Antigenome. **Kranich J**, Krautler NJ. *Front Immunol*. 2016 Jun 21;7:225.

8. Acknowledgements

I would like to express my gratitude to Professor Thomas Brocker for his enormous support, invaluable assistance, and wise counsel throughout my research endeavors. Working alongside him has been an absolute privilege, and our collaboration has been and still is great fun.

I extend my gratitude to Professor Adriano Aguzzi for his great support, exceptional mentorship. His guidance has been instrumental in shaping my academic journey, and I am very thankful for the knowledge and inspiration he shared with me.

I am also thankful to Jörg Kirberg for his exceptional supervision during my diploma thesis, which laid the foundation for my research pursuits. I thank Charles Mackay for providing me with the incredible opportunity to work in his lab in Sydney as a Postdoc.

A special thank you goes to Tatyana Chtanova for her help, valuable advice, and continuous support during my time in Sydney.

I am very grateful to all my colleagues and collaborators, whose contributions are of enormous value. While it is impossible to mention everyone, I want to specifically acknowledge my colleagues and collaborators at the BMC Anne Krug, Vigo Heissmeyer, Ludger Klein, and Reinhard Obst.

I would also like to express my gratitude to the practical students, bachelor, master, and PhD students who contributed to the studies, too numerous to mention individually. However, I want to highlight the exceptional contributions of Nike Kräutler, Lisa Rausch, Ashretha Latha, Tilman Kurz, and Lavinia Flaskamp.

Special thanks go to Petra Schwarz, Christine Ried, and Aga Foltyn-Arfa Kia for their outstanding technical support, without which this research would not have been possible.

I am grateful to Reinhard Obst for his stimulating scientific discussions over lunch and for his valuable advice on teaching.

I extend my appreciation to the Fachmentorat, Thomas Brocker, Vigo Heissmeyer, and Veit Hornung for their time, support, and efforts in evaluating this thesis.

Lastly, I would like to thank my family for their endless support and encouragement throughout this, often challenging journey.

9. Appendix

9.1 Follicular dendritic cells control engulfment of apoptotic bodies by secreting Mfge8.

Kranich J, Krautler NJ, Heinen E, Polymenidou M, Bridel C, Schildknecht A, Huber C, Kosco-Vilbois MH, Zinkernagel R, Miele G, Aguzzi A.; J Exp Med. 2008 Jun 9;205(6):1293-302.

Follicular dendritic cells control engulfment of apoptotic bodies by secreting Mfge8

Jan Kranich,¹ Nike Julia Krautler,¹ Ernst Heinen,³ Magdalini Polymenidou,¹ Claire Bridel,¹ Anita Schildknecht,² Christoph Huber,⁴ Marie H. Kosco-Vilbois,⁵ Rolf Zinkernagel,² Gino Miele,⁶ and Adriano Aguzzi¹

¹Institute of Neuropathology and ²Institute of Experimental Immunology, University Hospital of Zurich, 8091 Zurich, Switzerland

³Institute of Human Histology, University of Liège, 4000 Liège, Belgium

⁴Department of Immunology, The Scripps Research Institute, La Jolla, CA 92037

⁵NovImmune SA, 1211 Geneva, Switzerland

⁶Translational Medicine Research Collaboration, Sir James Black Centre, University of Dundee, Dundee DD1 5EH, Scotland, UK

The secreted phosphatidylserine-binding protein milk fat globule epidermal growth factor 8 (Mfge8) mediates engulfment of apoptotic germinal center B cells by tingible-body macrophages (TBMφs). Impairment of this process can contribute to autoimmunity. We show that Mfge8 is identical to the mouse follicular dendritic cell (FDC) marker FDC-M1. In bone-marrow chimeras between wild-type and *Mfge8*^{-/-} mice, all splenic Mfge8 was derived from FDCs rather than TBMφs. However, *Mfge8*^{-/-} TBMφs acquired and displayed Mfge8 only when embedded in *Mfge8*^{+/+} stroma, or when situated in lymph nodes draining exogenous recombinant Mfge8. These findings indicate a licensing role for FDCs in TBMφ-mediated removal of excess B cells. Lymphotoxin-deficient mice lacked FDCs and splenic Mfge8, and suffer from autoimmunity similar to *Mfge8*^{-/-} mice. Hence, FDCs facilitate TBMφ-mediated corpse removal, and their malfunction may be involved in autoimmunity.

CORRESPONDENCE

Adriano Aguzzi:
Adriano.Aguzzi@usz.ch

Follicular DCs (FDCs) reside in primary B cell follicles and germinal centers (GCs) (1). FDCs retain native immune complexes with complement and Fcγ receptors (2), and display them to B cells, which they embrace with intricate dendritic networks. This is thought to facilitate the GC reactions, and the selection of B cells that gives rise to high-affinity antibodies (3) and long-term memory B cells (4). But others (5) have questioned the importance of FDCs because primary immune responses, affinity maturation, and memory B cells arise in mice engineered to lack the retention of immune complexes by FDCs (6), and even in *Lta*^{-/-} mice that are deficient in lymphotoxin (LT) signaling and lack FDCs completely (7). Hence, the functional contribution of FDCs to affinity maturation remains unclear.

Some biomarkers, including the complement receptors CD21/35 and the complement factor C4 (8), allow for FDC immunodetection in vivo, yet none of them are exclusively

restricted to FDCs. A more specific marker is hybridoma clone 4C11, whose reactivity is confined to FDCs and tingible-body macrophages (TBMφs) (9). The antigen recognized by 4C11 was provisionally termed FDC-M1, but its identity has remained unknown.

Phagocytosis of apoptotic GC B cells, the remnants of which are recognizable as tingible bodies inside TBMφs, is thought to be a crucial function of TBMφs. Apoptotic cells are engulfed upon opsonization by milk fat globule epidermal growth factor (EGF) 8 (Mfge8) (10), which binds bifunctionally to phosphatidylserine on apoptotic cells and to integrins expressed by phagocytes (11). Originally identified as a membrane component of milk-fat globules (12), *Mfge8* was reported to be expressed by various phagocytes, including TBMφs, activated peritoneal macrophages (PMφs), and immature DCs (10, 11).

Mfge8^{-/-} mice suffer from impaired engulfment of GC B cell corpses by TBMφs. Consequently, their TBMφs carry supernumerary nonengulfed apoptotic B cells, which cause

The online version of this article contains supplemental material.

them to appear enlarged. This defect is associated with systemic lupus erythematosus (SLE) and autoimmune glomerulonephritis (10). In this report, we provide conclusive evidence that the FDC-M1 antigen identified by clone 4C11 is identical to Mfge8, that FDCs are the only source of splenic Mfge8, and that TBMφs only acquire surface Mfge8 if situated in the proximity of *Mfge8*-expressing FDCs or in lymph nodes that drain exogenous Mfge8. The absence of FDCs in mice lacking LTs or their receptors correlated with the profound depletion of splenic Mfge8 in LT-deficient mice, suggesting that impairment of FDC homeostasis contributes to their autoimmune pathologies.

RESULTS AND DISCUSSION

FDC-M1 and Mfge8 are identical

The present report originated from our serendipitous observation that FDC-M1⁺ networks were completely absent from splenic cryosections of *Mfge8*^{-/-} mice stained with anti-FDC-M1 antibody 4C11 (Fig. S1, available at <http://www.jem.org/cgi/content/full/jem.20071019/DC1>). This was unexpected, because no FDC abnormalities had been reported in *Mfge8*^{-/-} mice despite progressive splenomegaly, enlarged splenic TBMφs, and hyperplastic follicles with increased numbers of peanut agglutinin-positive (PNA⁺) GCs (10). The absence of 4C11 immunoreactivity in *Mfge8*^{-/-} spleens did not result from an absence of mature FDCs, because FDC networks were easily identifiable by CD21/35 immunostains (Fig. S1).

The anti-Mfge8 antibodies 18A2-G10 and 2422 (11) identified FDC networks and colocalized with 4C11 immunostains (Fig. 1 A). We therefore considered the possibility that FDC-M1 and Mfge8 are the same antigen. Indeed, preincubation with excess rMfge8, but not with rEGF or recombinant prion protein (rPrP), inhibited the binding of both 18A2-G10 and 4C11 to FDC networks. The presence of FDCs in these sections was independently confirmed by PrP^C-specific immunolabeling, which is abundantly expressed by FDCs (13) (Fig. 1 B).

We then assessed whether anti-FDC-M1 antibody 4C11 immunoprecipitates Mfge8. Paramagnetic beads were conjugated to immunoaffinity-purified antibodies 4C11, anti-Mfge8 antibody 2422, or rat IgG2c isotype control antibody. Beads were incubated with protein extracts from WT or *Mfge8*^{-/-} spleens, and precipitated proteins were analyzed by Western blotting with anti-Mfge8 antibody 18A2-G10. After immunoprecipitation with anti-Mfge8 antibodies, two bands with molecular masses of ~45 and 55 kD were detected (Fig. 1 C). After immunoprecipitation with anti-FDC-M1 beads, two signals were obtained with molecular masses matching those of the 2422 immunoprecipitation (Fig. 1 C). Both signals were absent in spleens from *Mfge8*^{-/-} mice, confirming their identity as genuine Mfge8.

We next verified the interaction of rMfge8 with anti-FDC-M1 antibody 4C11 by surface plasmon resonance (SPR). 4C11 was injected onto Biacore sensor chip surfaces covalently coated with rMfge8 or, for control, rPrP. Inter-

action of 4C11 with immobilized rMfge8 was observed over several serial injections until binding had reached saturation (Fig. 1 D, I). When anti-Mfge8 antibody 2422 was subsequently injected, its binding was minimal (Fig. 1 D, I, arrow, 2422), suggesting that 4C11 interfered with the binding of 2422 to rMfge8. Binding of anti-Mfge8 antibody 18A2-G10, in contrast, was not affected (Fig. 1 D, I, arrow, 18A2-G10). Rat IgG2c did not interact with immobilized rMfge8 (not depicted).

Antibodies were then reinjected in a different order. First, 2422 was added until saturation was reached (Fig. 1 D, II). 4C11 was injected, yet it did not bind to rMfge8 (Fig. 1 D, II, arrow, 4C11). In contrast, 18A2-G10 always bound to rMfge8, even in the presence of previously bound 2422 or 4C11 (Fig. 1 D, I and II). Hence, the 18A2-G10 epitope is distinct from those of the other two antibodies. These results indicate that 4C11 and 2422 abrogate each other's binding to Mfge8, either because they share a common or overlapping epitope, or because they sterically hinder each other. This was confirmed by the next experiment: immobilized 18A2-G10 was used to capture rMfge8. Then, the antibodies 18A2-G10, 2422, and 4C11 were added in a sandwich design. Under these conditions, injected 18A2-G10 did not bind to surfaces decorated with 18A2-G10-captured rMfge8, confirming that 18A2-G10 binds to a single epitope on Mfge8 (Fig. 1 D, III). Subsequent injection of 4C11 resulted in a strong interaction with captured rMfge8. When 2422 was applied, no binding occurred. We then reversed the order of injections: 2422 was added before 4C11. In this case, the first antibody, 2422, interacted with 18A2-G10-captured rMfge8, whereas 4C11 did not (Fig. 1 D, IV).

These data show that the FDC-M1 antigen identified by antibody 4C11 is Mfge8. The molecular identification of FDC-M1 expands the arsenal of tools for functional and morphological studies of FDCs in many ways. Because Mfge8 is secreted, its histological assignment by RNA in situ hybridization (ISH) is more informative of its cellular origin than immunohistology and will help define the precise histogenesis of FDCs. Also, we found that anti-Mfge8 antibody 18A2-G10 labels FDCs on formalin-fixed, paraffin-embedded tissue (unpublished data), thereby enabling the recognition of FDCs in archived tissue.

FDCs are the major source of Mfge8 in the spleen

The finding that Mfge8 is detected in TBMφs within splenic follicles (10) may be compatible with the above results if Mfge8 were secreted by FDCs and trapped by TBMφs. We tested this proposition in reciprocal BM chimeras between *Mfge8*^{-/-} and WT mice. FDCs are stromal and radioresistant, whereas TBMφs are mononuclear phagocytes of hematopoietic origin and are thought to be radiosensitive (14). To provide an independent histogenetic marker, lethally irradiated *Mfge8*^{-/-} mice expressing the CD45.2 allelic variant were reconstituted with BM from CD45.1 congenic WT mice, and vice versa.

The mean reconstitution efficiency determined by FACS analysis of peripheral blood was $93.8 \pm 3.6\%$ (unpublished

data). The donor origin of TBM ϕ s was confirmed by multi-color immunofluorescence with antibodies against CD45.1, CD45.2, and CD68 in >50 follicles of five mice per group. The results ruled out the possibility that host-derived TBM ϕ s may have survived irradiation (Fig. S2, available at <http://www.jem.org/cgi/content/full/jem.20071019/DC1>). Immuno-

stains of *Mfge8*^{-/-}→*Mfge8*^{-/-} (all CD45.2⁺) and WT→WT (all CD45.1⁺) spleens confirmed the absence of cross-reactivity (Fig. S2). Two-color immunolabeling of *Mfge8*^{-/-}→WT spleens with antibodies against CD68 (cyan) and CD45.1 (red) confirmed that TBM ϕ s were not host derived, whereas TBM ϕ s of WT→*Mfge8*^{-/-} spleens did not express CD45.2 (Fig. S2).

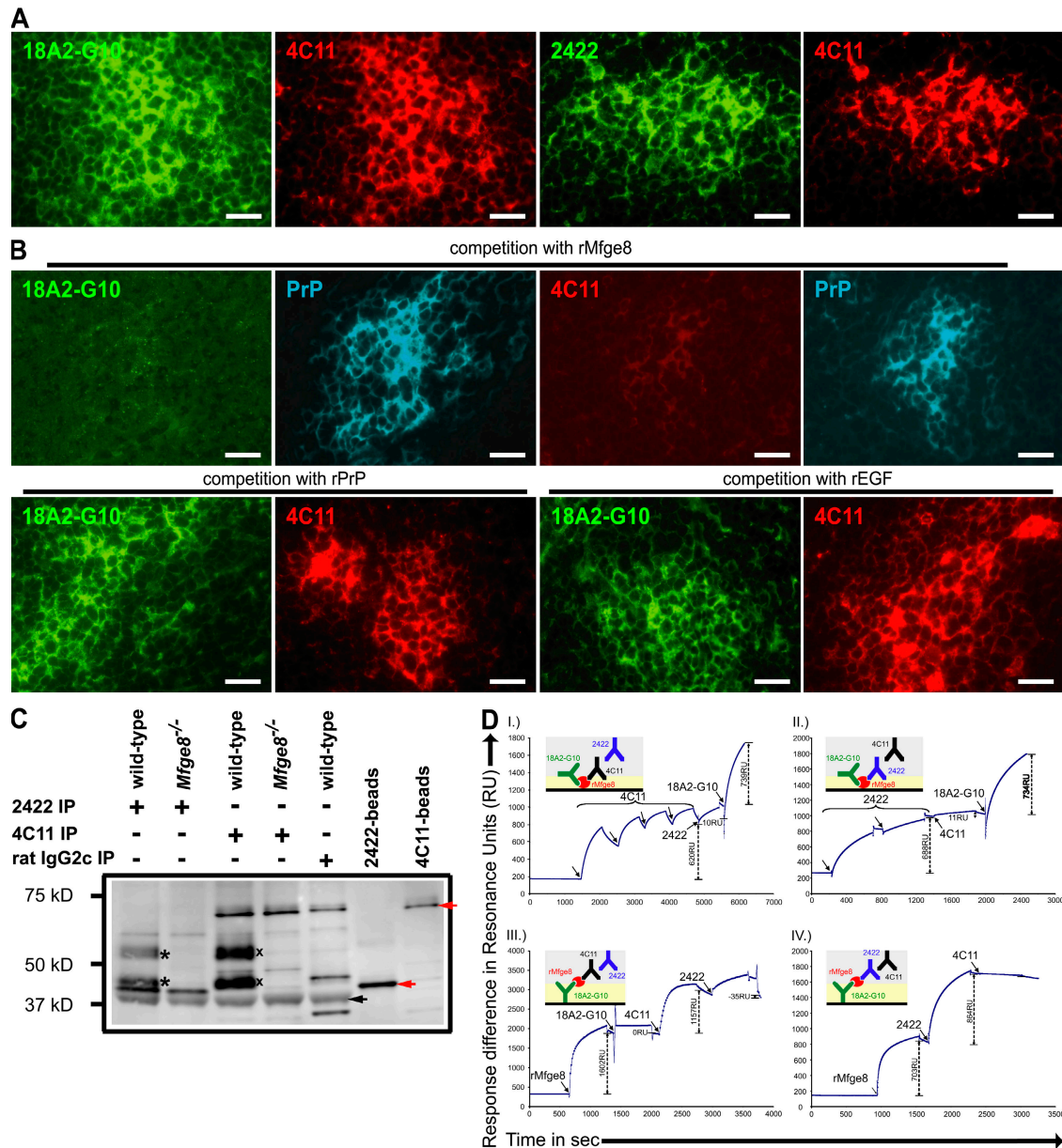


Figure 1. FDC-M1 and Mfge8 are identical. (A) Two-color immunolabeling of a WT spleen stained with anti-Mfge8 antibody 18A2-G10 (green) and anti-FDC-M1 antibody 4C11 (red), or anti-Mfge8 antibody 2422 (green) and 4C11 (red). Both anti-Mfge8 antibodies showed colocalization with 4C11. (B) Preincubation with 25 μ g/ml rMfge8 blocked the labeling of FDCs with 18A2-G10 or 4C11. To visualize FDCs, sections were stained with anti-PrP antibody POM2. For control, sections were preincubated with rEGF or rPrP. Bars, 100 μ m. (C) Splenic protein extracts (WT and *Mfge8*^{-/-}) were immunoprecipitated with 2422 or 4C11, or to a rat IgG2c isotype control antibody. Control beads were coupled with 2422 or 4C11 but were not exposed to splenic extracts. Western blots were probed with 18A2-G10. Mfge8-specific bands are indicated (* and x). Arrows indicate nonspecific bands. (D) Sensograms indicating binding of each protein after subtraction of their binding to a control protein-coupled surface. Black arrows indicate antibody injections. (insets) Schematic representations of binding and competition events. For control, injections of all proteins were made on two flow cells, with one cell coated with the protein of interest.

Therefore, in all chimeras the overwhelming majority of TBM ϕ s always originated from donor BM.

Early analyses of BM chimeras suggested a hematopoietic derivation of FDCs (15), but most current evidence favors

a stromal origin (14, 16). Indeed, *Ptprc*, which encodes CD45, was markedly reduced in MACS-enriched FDC clusters (17), whereas *Mfge8* and *Cxcl13* (a B cell-attracting chemokine expressed by FDCs; reference 18) were increased

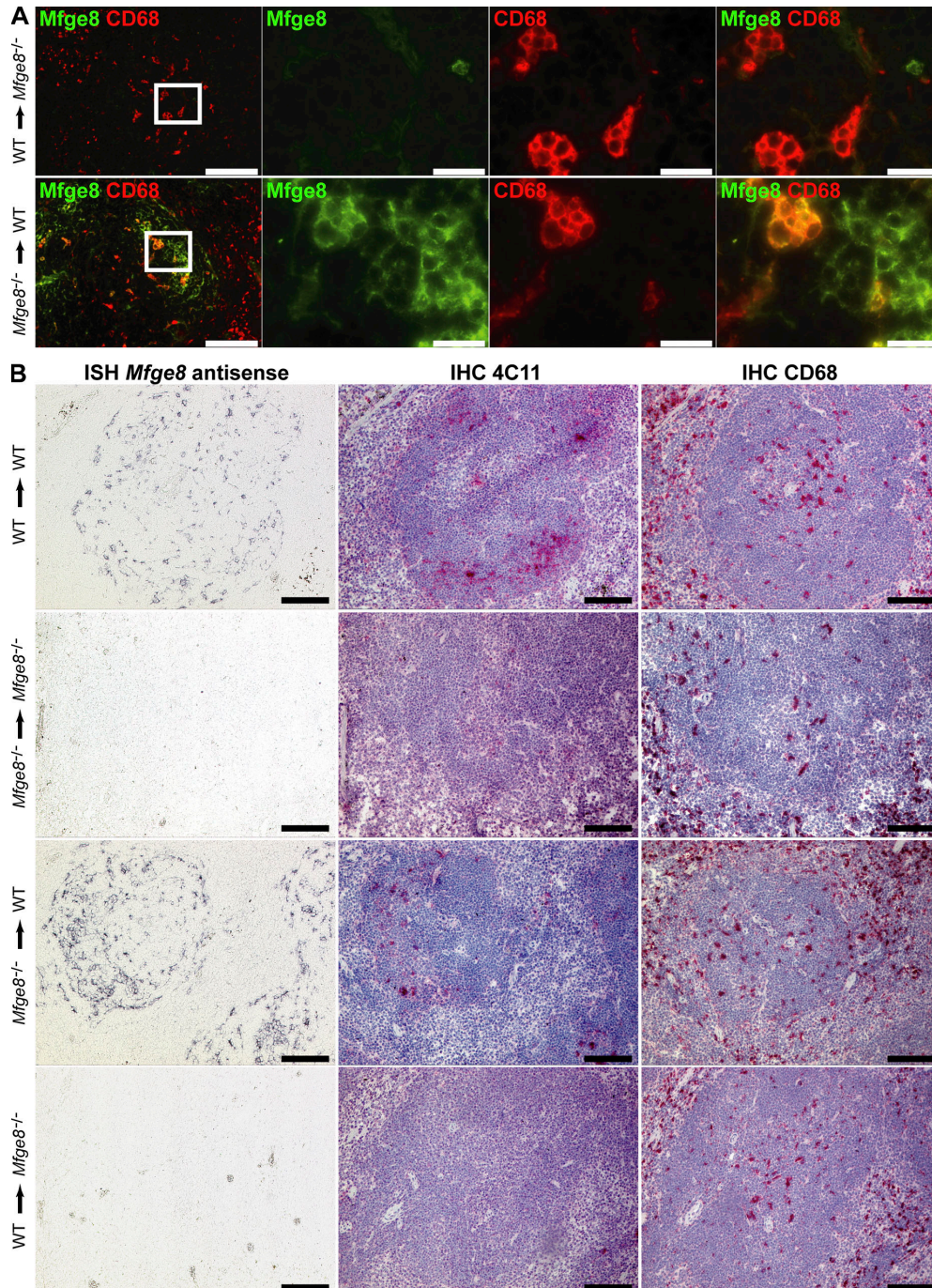


Figure 2. Analysis of splenic *Mfge8* expression by immunofluorescence and ISH. (A) BM chimeras were stained with anti-*Mfge8* antibody (clone 2422; green) and anti-CD68 antibody (red). *Mfge8* immunoreactivity of FDCs and CD68⁺ TBM ϕ s was only observed when FDCs were of WT origin. Figures show areas inside follicles. White squares mark the areas shown at a higher magnification. Bars, 20 μ m. (B) Splenic *Mfge8* expression was assessed by ISH. Consecutive sections were immunolabeled with 4C11 and anti-CD68. *Mfge8* expression and 4C11 immunostaining was only found in WT mice irrespective of the BM genotype (top and second from bottom). *Mfge8*^{-/-} mice receiving BM from either *Mfge8*^{-/-} or WT mice showed no *Mfge8*-specific signal after ISH and no 4C11 immunostaining. Bars, 100 μ m.

(Fig. S3, available at <http://www.jem.org/cgi/content/full/jem.20071019/DC1>). We conclude that FDCs do not express CD45, and were therefore not identifiable as host derived in CD45.1/CD45.2 immunostains.

BM-chimeric mice were immunized and boosted with OVA/alum to induce GCs before analysis. 9 wk after reconstitution, splenic *Mfge8* and CD68 expression were analyzed immunohistochemically. Surprisingly, *Mfge8*^{-/-} mice that had received WT BM (WT→*Mfge8*^{-/-}) completely lacked splenic *Mfge8* immunoreactivity. Not only radioresistant FDCs but also BM-derived CD68⁺ TBMφs were phenotypically *Mfge8* negative (Fig. 2 A, top) although they had clearly originated from *Mfge8*^{+/+} donors (Fig. S2). In contrast, spleens of WT mice reconstituted with *Mfge8*^{-/-} BM (*Mfge8*^{-/-}→WT) contained not only *Mfge8*⁺ FDCs but also phenotypically *Mfge8*-positive TBMφs originating from *Mfge8*^{-/-} donors (Fig. 2 A). Irrespective of their genotype, therefore, TBMφs were always *Mfge8*⁺ whenever FDCs expressed *Mfge8*, yet they were always *Mfge8*⁻ whenever FDCs lacked *Mfge8*.

We then determined the transcriptional patterns of splenic *Mfge8* by RNA ISH. In WT→WT mice, *Mfge8* transcription was restricted to follicles (Fig. 2 B) and was strongest in GCs, where FDCs reside. Some *Mfge8*⁺ cells were found in the periphery of follicles. These cells were radioresistant and may represent immature FDC precursor cells (19). Overall, the ISH visualized more *Mfge8*⁺ cells than 4C11 immunohistochemistry, probably owing to the higher sensitivity of the former.

Consecutive sections were immunostained with 4C11 and anti-CD68 antibodies. In this case, both *Mfge8* immunostains and *Mfge8* ISH visualized characteristic FDC networks, confirming that *Mfge8* is indeed produced by FDCs rather than being secreted by other cell types and taken up by FDCs (Fig. 2 B). No ISH signal was detected on *Mfge8*^{-/-}→*Mfge8*^{-/-} chimeric spleens, confirming the specificity of the *Mfge8* in situ riboprobe (Fig. 2 B).

The *Mfge8* expression pattern in *Mfge8*^{-/-}→WT chimeras was identical to that of WT mice, whereas *Mfge8* expression was completely absent from WT→*Mfge8*^{-/-} chimeras (Fig. 2 B). Therefore, radioresistant cells including FDCs, rather than radiosensitive cells including TBMφs, are the source of *Mfge8* in the spleen. *Mfge8* expression in WT→*Mfge8*^{-/-} chimeric spleens was below detectability by quantitative RT-PCR (<0.25% WT splenocyte RNA spiked into *Mfge8*^{-/-} splenocyte RNA; not depicted), whereas *Mfge8*^{-/-}→WT spleens showed expression levels similar to WT→WT spleens (Fig. S4 A, available at <http://www.jem.org/cgi/content/full/jem.20071019/DC1>).

We then searched for *Mfge8* transcripts within CD68⁺ macrophages by combining fluorescent ISH (green) with CD68 immunofluorescence stains on individual cryosections (Fig. S4 B). In immunized WT spleens, none of the CD68⁺ TBMφs (white arrows) colocalized with the green *Mfge8* ISH signal, which was absent in the *Mfge8*^{-/-} spleens. Conversely, all cells showing *Mfge8* transcripts were negative in the CD68

immunostaining (Fig. S4 B, yellow arrows). Hence, FDCs but not TBMφs transcribe *Mfge8*.

PMφs express *Mfge8* only upon stimulation

PMφs were previously found to express *Mfge8* upon stimulation with thioglycollate (11). We analyzed *Mfge8* expression in stimulated PMφs isolated from BM chimeras. *Mfge8* expression was only detectable in PMφs from WT→WT and WT→*Mfge8*^{-/-} chimeras but not in those of *Mfge8*^{-/-}→WT and *Mfge8*^{-/-}→*Mfge8*^{-/-} chimeras, and was only detectable in stimulated but not in unstimulated cells (Fig. S5, available at <http://www.jem.org/cgi/content/full/jem.20071019/DC1>). These results confirm that extralymphatic PMφs do not express *Mfge8* under normal conditions but only after stimulation (11).

Naive, nonimmunized mice displayed *Mfge8*-expressing FDC networks, implying that FDCs express *Mfge8* constitutively. In contrast, *Mfge8* transcription by PMφ appears to be dependent on inflammatory stimuli and was never detectable in vivo in TBMφs, not even after immunization, when most TBMφs are highly immunoreactive for secondarily acquired *Mfge8* protein.

TBMφs can acquire *Mfge8* from extracellular sources

The above indicates that TBMφs appear immunohistochemically *Mfge8*⁺ because they take up FDC-derived *Mfge8*, either before or during the ingestion of apoptotic B cells. To further challenge this hypothesis, 10 μg r*Mfge8* or rPrP was injected into the footpads of *Mfge8*^{-/-} or *Prnp*^{0/0} mice, respectively. 20 h later, the draining popliteal lymph nodes were collected and immunostained for *Mfge8*. Although no *Mfge8* immunolabeling was observed in the contralateral lymph node after PBS injection (Fig. 3, middle), *Mfge8* was readily detectable in draining lymph nodes after *Mfge8* injection. FDC networks, visualized by immunofluorescence for the complement receptors CD21/35, were only weakly *Mfge8*⁺ (Fig. 3, left), indicating that they trapped only small amounts of *Mfge8*. In contrast, CD68⁺ TBMφs were strongly immunoreactive for *Mfge8*. No PrP immunoreactivity was observed in the draining lymph nodes of *Prnp*^{0/0} mice 20h after injection (Fig. 3, right), indicating that TBMφs do not generically incorporate all soluble recombinant proteins. We conclude that *Mfge8* is synthesized by FDCs, secreted, and eventually acquired by macrophages exposing appropriate receptors.

Lack of *Mfge8* expression by FDCs impairs corpse engulfment

Mfge8^{-/-} mice suffer from splenomegaly and a phagocytosis defect of TBMφs (10). We used BM chimeras to determine whether these phenotypes are caused by stromal or hematopoietic *Mfge8* deficiency. Only *Mfge8*^{-/-}→*Mfge8*^{-/-} and WT→*Mfge8*^{-/-} mice developed splenomegaly, with spleen weights approximately twice as high as those of WT→WT and *Mfge8*^{-/-}→WT mice (Fig. S6, available at <http://www.jem.org/cgi/content/full/jem.20071019/DC1>). Therefore, the splenomegaly of aged *Mfge8*^{-/-} mice could be unambiguously ascribed to the lack of *Mfge8* expression by stromal cells,

and could not be corrected by any putative hematopoietic *Mfge8* expression.

Mfge8^{-/-} spleens were found to host enlarged TBMφs, whose surfaces were loaded with nonengulfed apoptotic bodies (10). In light of the above results, this phenotype may be attributed to the absence of FDC-produced *Mfge8*. We tested this possibility by quantifying the number of TdT-mediated dUTP-biotin nick-end labeling (TUNEL)-positive apoptotic cells associated with each TBMφ. We first determined the mean number of TUNEL⁺ cells associated with all macrophages within splenic white pulp follicles. *Mfge8*^{-/-}→*Mfge8*^{-/-} and WT→*Mfge8*^{-/-} chimeras displayed marginally increased numbers of macrophage-bound apoptotic cells over WT→WT and *Mfge8*^{-/-}→WT chimeras (unpublished data), but statistical significance was not attained. We then performed the same analysis but counted only those macrophages that resided within PNA⁺ GCs. The mean number of TUNEL⁺ apoptotic

cells per CD68⁺ TBMφ was determined in at least 13 PNA⁺ GCs in each group of mice. TBMφs of *Mfge8*^{-/-}→*Mfge8*^{-/-} and WT→WT mice were found to be associated with 6 ± 1.8 and 2.4 ± 0.5 TUNEL⁺ cells, respectively. TBMφs of WT→*Mfge8*^{-/-} mice were associated with significantly more TUNEL⁺ cells (5.8 ± 1.6) than TBMφs of *Mfge8*^{-/-}→WT mice (2.5 ± 0.9; P < 0.0001; Fig. 4 A). We conclude that the apoptotic load of macrophages was increased whenever *Mfge8* was absent from radioresistant stromal cells, supporting the contention that FDC-derived *Mfge8* regulates the engulfment of apoptotic cells.

We found apoptotic lymphocytes in various degradation stages within TBMφs of all chimeric mice, including *Mfge8*^{-/-}→*Mfge8*^{-/-} mice (Fig. 4 B). This points to the existence of hitherto unexplored, *Mfge8*-independent mechanisms of corpse removal and may explain why *Mfge8*^{-/-} mice only suffer from mild SLE. Complement factors may also be

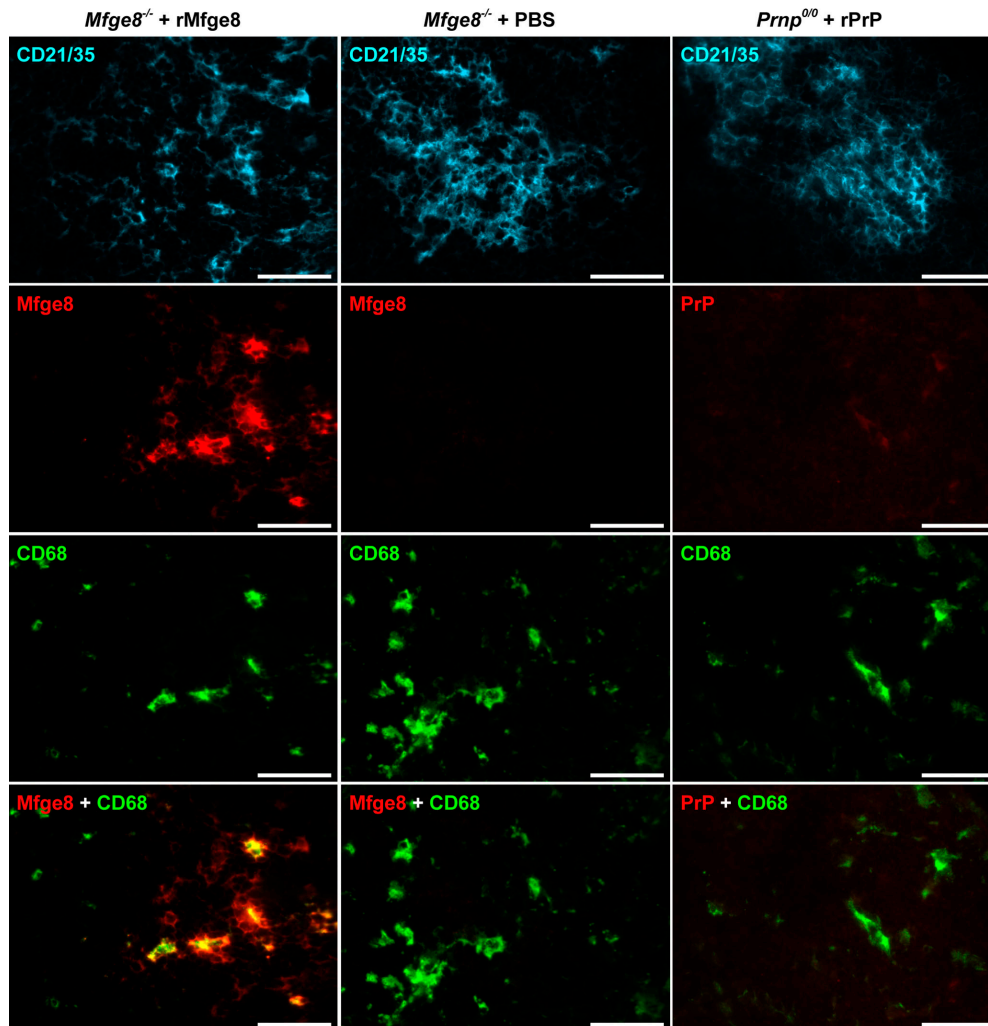


Figure 3. TBMφs bind extracellular *Mfge8*. Footpads of *Mfge8*^{-/-} mice were injected with 10 μg r*Mfge8*. For control, PBS or rPrP was injected into the contralateral footpad of *Prnp*^{0/0} mice. 20 h later, popliteal lymph nodes were collected and analyzed by immunofluorescence with anti-*Mfge8* and anti-PrP antibodies. TBMφs and FDCs showed strong and weak *Mfge8* staining, respectively. rPrP was undetectable in the lymph nodes of *Prnp*^{0/0} mice. Bars, 50 μm.

involved, because FDCs are a source of splenic C1q (20) and *C1q*-ablated mice develop SLE (21).

Efficient degradation of apoptotic cells in splenic follicles depends on LT signaling

Because FDC development and maintenance require LT signaling, LTs may control *Mfge8* availability and, consequently, removal of apoptotic cells from GCs. We tested

this prediction in *Ltbr*^{-/-}, *Lta*^{-/-}, and *Ltb*^{-/-} mice, whose splenic follicles contain PNA⁺ clusters and few IgM^{low}IgD⁺ B cells (22) but are disorganized and contain no FDCs (23). We found splenic *Mfge8* to be decreased almost 200-fold in *Ltbr*^{-/-} mice and ~70–90-fold in *Lta*^{-/-} and *Ltb*^{-/-} mice (Fig. S7, available at <http://www.jem.org/cgi/content/full/jem.20071019/DC1>). We then compared the prevalence of TBM ϕ -associated apoptotic cells in the spleens of *Ltbr*^{-/-},

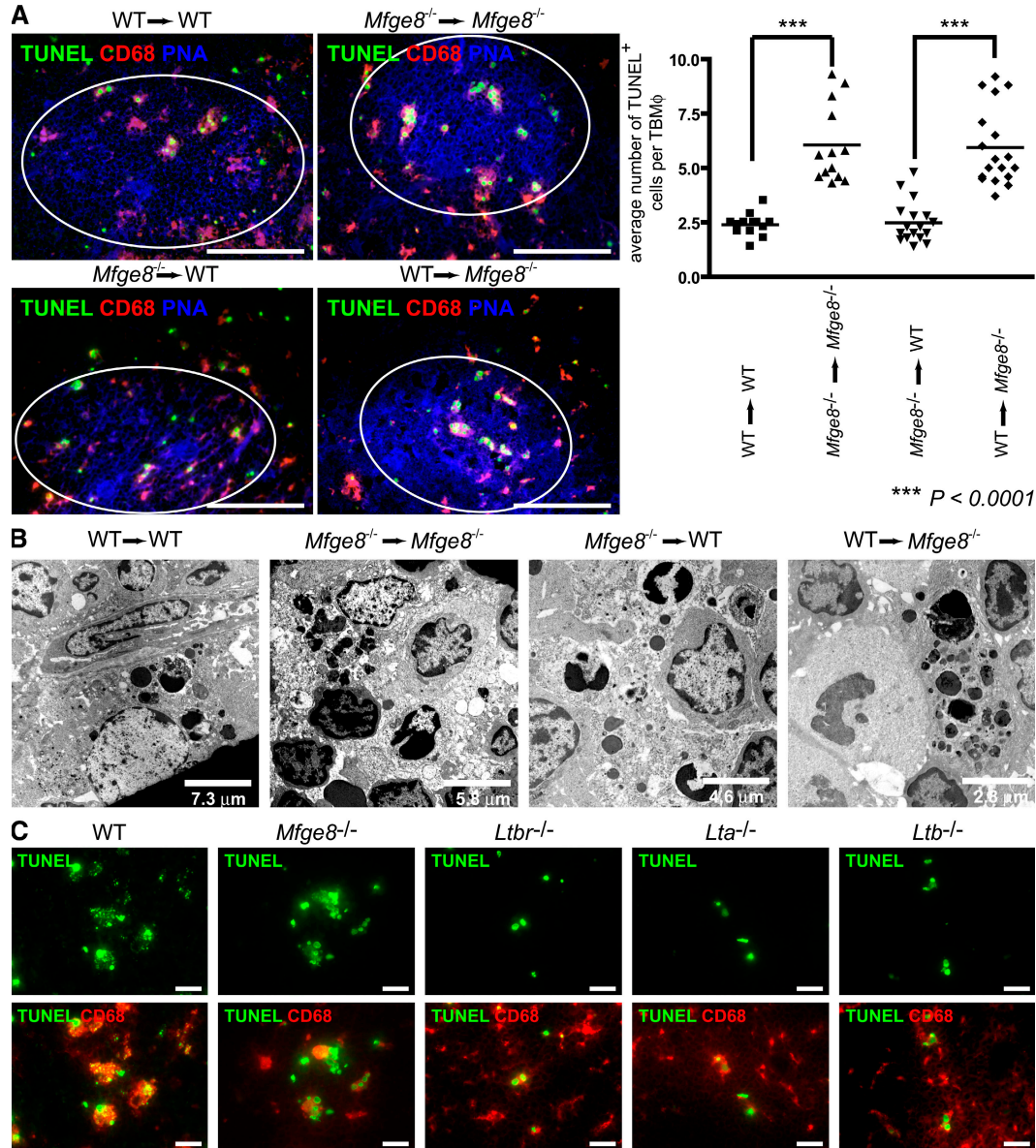


Figure 4. Impaired engulfment of apoptotic bodies in the absence of stromal *Mfge8*. (A) Apoptotic cells, TBM ϕ s, and GCs were visualized by TUNEL, anti-CD68, and PNA, respectively, on splenic cryosections 9 wk after BM reconstitution and after immunization. (right) Each datapoint represents the mean number of TUNEL⁺ cells per TBM ϕ in one individual GC. *Mfge8*^{-/-}→*Mfge8*^{-/-} and WT→*Mfge8*^{-/-} mice showed increased numbers of TUNEL⁺ cells per TBM ϕ . Horizontal bars represent means. White circles (left) indicate GCs. Bars, 100 μ m. (B) Ultrastructural features of TBM ϕ s of aged BM-chimeric mice 41 wk after reconstitution. Apoptotic cells in various degradation stages were observed inside TBM ϕ s of all chimeric mice. (C) Engulfment of apoptotic cells by TBM ϕ s in WT, *Mfge8*^{-/-}, *Ltbr*^{-/-}, *Lta*^{-/-}, and *Ltb*^{-/-} mice was analyzed by TUNEL (green) and CD68 (red) staining. WT TBM ϕ s contained copious TUNEL⁺ material. The latter was also observed in *Mfge8*^{-/-} mice, but most TUNEL⁺ cells were large and intact. *Ltbr*^{-/-}, *Lta*^{-/-}, and *Ltb*^{-/-} macrophages were small and only contained intact TUNEL⁺ cells. At least three mice per genotype and ≥ 10 follicles per mouse were analyzed. Bars, 20 μ m.

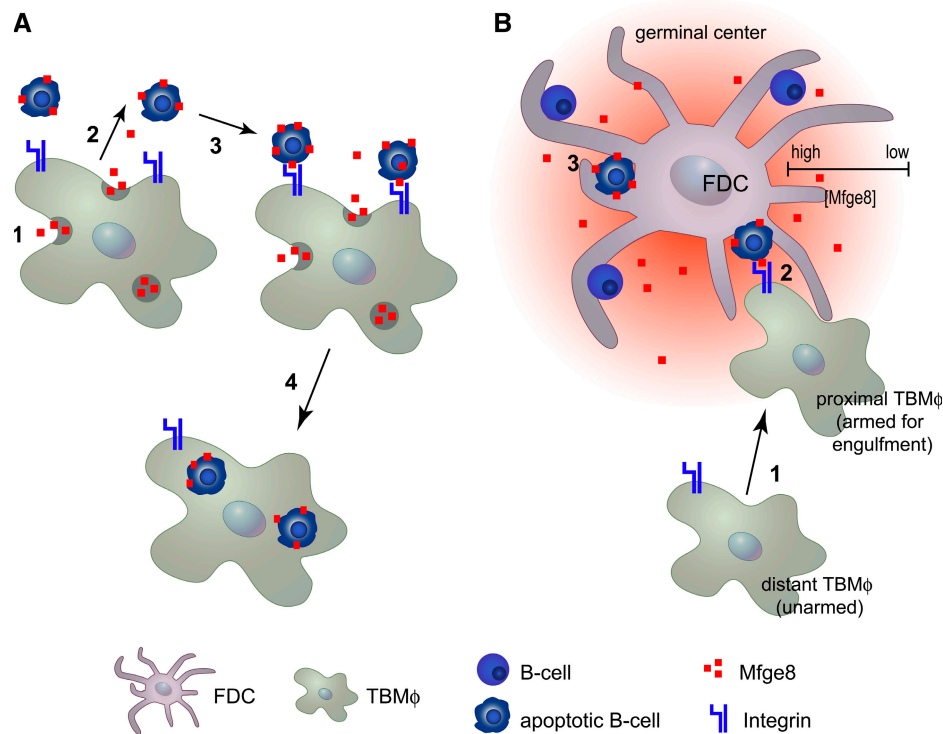


Figure 5. Mfge8-dependent removal of apoptotic cells from the GC. (A) In acute inflammatory conditions, macrophages secrete *Mfge8* (step 1; reference 30), which targets apoptotic bodies (step 2) and allows macrophages to bind them via integrins (step 3). The Mfge8–integrin interaction results in engulfment (step 4). (B) Revised model of splenic Mfge8-dependent engulfment. In this case, Mfge8 is not produced by macrophages but by FDCs. These establish a local Mfge8 gradient within GCs (step 1). TBMφs are therefore licensed for selective engulfment at the sites of apoptosis (step 2). Apoptotic cells are presumably decorated by Mfge8 while in contact with FDCs (step 3).

Lta^{-/-}, and *Ltb*^{-/-} mice immunized with OVA (Fig. 4 C). TBMφs of WT mice contained tingible bodies identifiable as small TUNEL⁺ particles inside TBMφs (Fig. 4 C, far left). Small degraded TUNEL⁺ bodies were also observed in *Mfge8*^{-/-} mice (Fig. 4 C, second from the left). In contrast, although *Ltbr*^{-/-} follicles contained some CD68⁺ cells binding TUNEL⁺ cells, the latter appeared largely intact, and the accumulation of small characteristic TUNEL⁺ tingible bodies within TBMφs was absent (Fig. 4 C). Similar results were observed in mice devoid of LTα or LTβ (Fig. 4 C), confirming a severe impairment of macrophage-mediated degradation of apoptotic cells in the GCs of all mice defective in LT signaling.

The realization that FDCs are the major source of Mfge8 in GCs points to a previously unrecognized role for these cells in GC homeostasis. In addition to modulating the survival of GC B cells, FDCs appear to regulate their removal once these cells have undergone apoptosis. These results indicate that FDCs provide Mfge8 to GCs, which then binds to phosphatidylserine on apoptotic B cells and targets them for removal by TBMφs. This would explain why TBMφs register as Mfge8⁺ upon ingestion of apoptotic B cells, and indeed, we were able to show that TBMφs take up extracellular Mfge8 after subcutaneous injection of rMfge8 (Fig. 3).

This model predicates a functional interaction of two distinct cell types, FDCs and TBMφs, in the removal of apoptotic cells from GCs. This is plausible for physiological and anatomical reasons. Apoptosis of GC B cells is very frequent, and their rapid and efficient removal seems important to avoid autoimmunity. But the paucity of scavenging cells, TBMφs, may limit the removal process. However, it would be wasteful for TBMφs to produce both Mfge8 and its receptors, α_vβ₃ and α_vβ₅ integrins. Conversely, these data suggest a tunable mechanism, with FDCs establishing a gradient of Mfge8 availability within GCs. Through their strategic microanatomical positioning within follicles, FDCs arm TBMφs for engulfment only in the vicinity of apoptotic B cells. Accordingly, the apoptotic body load was dramatically increased in macrophages residing within GCs. Because of their intimacy with GC B cells, FDCs may directly decorate negatively selected B cells with Mfge8 (Fig. 5). This two-tiered mechanism may help ensure that numerous dying cells are recognized and degraded by far fewer TBMφs.

Lack of LT signaling, which results in the absence of FDCs, suppressed splenic *Mfge8* expression, and combined TUNEL assays and CD68 immunostains indicated that the efficient removal of apoptotic cells was also impaired. These findings hint to a signaling hierarchy that is driven by LTs, enrolls LTβR-dependent signaling within FDCs, and enables topographically controlled apoptotic cell removal within GCs.

Ltbr^{-/-}, *Lta*^{-/-}, and *Ltb*^{-/-} mice develop severe systemic autoimmunity with lymphocytic infiltrates in multiple organs. Although this disease is more severe than that of *Mfge8*^{-/-} mice, the similarities are evident and include elevated levels of autoimmune antibodies and renal pathology (10, 24). In LT-deficient mice, this phenotype was originally attributed to decreased *Aire* expression in medullary thymic epithelial cells (24). This view, however, was challenged by reports of unaltered frequencies of *Aire*⁺ medullary thymic epithelial cells in *Lta*^{-/-} mice (25) and unaltered *Aire* expression in *Ltbr*^{-/-} mice (26, 27). Our findings suggest an alternative explanation for the autoimmunity in the latter mice. By depleting follicular *Mfge8*, LT signaling defects suppress the licensing activity that FDCs exert on TBMφs and, in turn, impair corpse removal from GCs. Hence, FDCs may control housekeeping functions required for the operation of lymphoid organs and for avoiding autoimmune phenomena.

MATERIALS AND METHODS

Mice. *Mfge8*^{-/-} mice were generated in the laboratory of S. Nagata (Kyoto University, Kyoto, Japan) and were bred on a (C57BL/6 × 129)F₁ mixed background (10). *Pmp*^{o/o} mice and *Ltbr*^{-/-}, *Lta*^{-/-}, and *Ltb*^{-/-} mice were described previously (22, 28, 29). C57BL/6-CD45.1 mice were obtained from Harlan Laboratories. All experiments were in accordance with Swiss federal legislation and were approved by local authorities.

Immunohistochemical analysis. Acetone-fixed cryosections were blocked (0.5% BSA, 1% goat serum in PBS) and primary antibodies were added. Primary antibodies were 4C11 (NovImmune SA or BD Biosciences), 18A2-G10 (MBL International), 2422 (Qbiogene), anti-CD21/35, anti-CD45.2-FITC, anti-CD45.1-biotin (all from BD Biosciences), anti-CD68 (AbD Serotec), and anti-PrP antibody POM2-Cy5 (developed in our laboratory). For competition experiments, 18A2-G10 or 4C11 were preincubated with 25 μg/ml rMfge8, rEGF (both from R&D Systems), or rPrP (produced in our laboratory). Sections were analyzed by fluorescence microscopy (BX61; Olympus). TUNEL assays were performed with the ApopTaq Plus Fluorescein In Situ Apoptosis Detection Kit (Millipore) according to the manufacturer's instructions. Before TUNEL stainings, unfixed sections were blocked and stained with biotinylated PNA (Vector Laboratories) and anti-CD68 antibodies, and then fixed with paraformaldehyde. Quantitation of TUNEL⁺ cells per macrophage was performed in a stringently blinded fashion. One scientist recorded micrographs of GCs, and a second scientist (blinded with respect to the genotypes of the mice) counted the number of apoptotic bodies per macrophage.

Immunoprecipitation and Western blotting. Paramagnetic beads (Dyna-beads M280 Tosylactivated; Invitrogen) were conjugated with 4C11, 2422, or rat IgG2c isotype control antibody according to the manufacturer's manual and incubated with spleen homogenates. Immunoprecipitates were analyzed by Western blotting using anti-Mfge8 antibody 18A2-G10. For detection, goat anti-Armenian hamster IgG-horseradish peroxidase was used.

SPR. SPR was performed on a Biacore 3000 instrument (GE Healthcare). Antibodies or recombinant proteins were immobilized on flow cells of an activated CM5 chip (Biacore) to 10,000 and 15,000 response units, respectively. All recombinant proteins or antibodies were injected at a concentration of 50 μg/ml diluted in HBS-EP buffer. The flow rate was 5 μl/min. For control, all protein injections were made on two flow cells, where the first flow cell was coated with control protein/antibody and the second was coated with the protein/antibody of interest.

BM chimeras. BM recipients were lethally irradiated (950 rad). Donor BM was isolated by flushing tibias and femurs. Recipient mice received 10⁷

donor BM cells i.v. Reconstitution efficiency was assed after 5 wk by FACS analysis of blood leukocytes. 6 wk after engraftment, mice were immunized i.p. with 100 μg OVA (Sigma-Aldrich) in alum (Imject Alum; Thermo Fisher Scientific). 2 wk later, mice were boosted with the same dose of OVA.

RNA ISH. Digoxigenin (DIG)-labeled *Mfge8* riboprobe was obtained by transcription of pBluescript II KS+ (Stratagene) containing the open reading frame of *Mfge8*. ISH was performed on spleen cryosections. For fluorescent ISH, sections were prestained with biotinylated anti-CD68 antibody and postfixed in 4% paraformaldehyde, followed by acetylation. After prehybridization, 200 ng/ml of DIG-labeled RNA probe was added to the hybridization buffer and incubated at 72°C overnight. For detection, either anti-DIG-alkaline phosphatase or anti-DIG-fluorescein antibody with a fluorescent enhancer kit (Roche) was used.

FDC cluster isolation and quantitative real-time PCR analysis. FDCs from lymph nodes were isolated as described previously (17). FDC-enriched and flow-through fractions were lysed in TRIzol. RNA was isolated and cDNA was synthesized. Quantitative real-time PCR was performed using the SYBR Green PCR Master Mix (Qiagen) on a 7900HT Fast Real-Time PCR System (Applied Biosystems) using the default cycling conditions. Expression levels were normalized using *Gapdh*. The following primers were used: *Gapdh* forward primer, 5'-CCACCCAGCAAGGAGACT-3'; *Gapdh* reverse primer, 5'-GAAATTGTGAGGGAGATGCT-3'; *Mfge8* forward primer, 5'-ATATGGGTTTCATGGGC-TTG-3'; *Mfge8* reverse primer, 5'-GAGGCTGTAAGCCACCTTGA-3'; *Cxcl13* forward primer, 5'-TCGTGCCAAATGGTTACAAA-3'; *Cxcl13* reverse primer, 5'-ACAAGGATGTGGGTTGGGTA-3'; *Ptprc* forward primer, 5'-AAACGATCGGTGACTTTTGG-3'; and *Ptprc* reverse primer, 5'-AGCTCTTCCCCTTTCATGT-3'.

Electron microscopy. Samples were fixed in 2% glutaraldehyde in 0.1 M cacodylate buffer (pH 7.4), washed and postfixed in a mixture of 1% OsO₄ and 1.5% K₄Fe(CN)₆ in 0.1 M cacodylate buffer (pH 7.4), dehydrated, and embedded in Epon 812 (Fluka). The resin specimens were trimmed, and 70–90-nm sections were cut. Ultrathin sections were collected on copper 6200 grids and contrasted with uranyl acetate and lead acetate before examination with a transmission electron microscope (CX 100 II; JEOL Ltd.).

Online supplemental material. Fig. S1 shows that *Mfge8*^{-/-} mice lack FDC-M1⁺ networks. Fig. S2 reveals that TBMφs are donor derived. Fig. S3 depicts *Ptprc* expression as down-regulated in FDC-enriched clusters. Fig. S4 shows that *Mfge8* expression is absent in spleens with stromal *Mfge8* deficiency and that CD68⁺ TBMφs do not contain *Mfge8* RNA. An analysis of *Mfge8* expression in PMφs is depicted in Fig. S5. Fig. S6 shows that stromal *Mfge8* deficiency causes splenomegaly. Fig. S7 demonstrates that splenic *Mfge8* expression depends on LT signaling. Online supplemental material is available at <http://www.jem.org/cgi/content/full/jem.20071019/DC1>.

We thank Shigekazu Nagata for providing us with *Mfge8*^{-/-} mice; Dr. Ariana Gaspert for expert analysis of kidney pathologies; Sophorn Chip for recombinant PrP; Petra Schwarz, Joëlle Piret, Rita Moos, Norbert Wey, Silvia Behnke, and André Fische for excellent technical assistance; and Mike Scott for help with SPR experiments.

The authors have no conflicting financial interests.

Submitted: 22 May 2007

Accepted: 25 April 2008

REFERENCES

- Chen, L.L., J.C. Adams, and R.M. Steinman. 1978. Anatomy of germinal centers in mouse spleen, with special reference to "follicular dendritic cells". *J. Cell Biol.* 77:148–164.
- Tew, J.G., G.J. Thorbecke, and R.M. Steinman. 1982. Dendritic cells in the immune response: characteristics and recommended nomenclature

- (A report from the Reticuloendothelial Society Committee on Nomenclature). *J. Reticuloendothel. Soc.* 31:371–380.
3. Tew, J.G., J. Wu, M. Fagher, A.K. Szakal, and D. Qin. 2001. Follicular dendritic cells: beyond the necessity of T-cell help. *Trends Immunol.* 22:361–367.
 4. Klaus, G.G., J.H. Humphrey, A. Kunkl, and D.W. Dongworth. 1980. The follicular dendritic cell: its role in antigen presentation in the generation of immunological memory. *Immunol. Rev.* 53:3–28.
 5. Kosco-Vilbois, M.H. 2003. Are follicular dendritic cells really good for nothing? *Nat. Rev. Immunol.* 3:764–769.
 6. Hannum, L.G., A.M. Haberman, S.M. Anderson, and M.J. Shlomchik. 2000. Germinal center initiation, variable gene region hypermutation, and mutant B cell selection without detectable immune complexes on follicular dendritic cells. *J. Exp. Med.* 192:931–942.
 7. Matsumoto, M., S.F. Lo, C.J. Carruthers, J. Min, S. Mariathasan, G. Huang, D.R. Plas, S.M. Martin, R.S. Geha, M.H. Nahm, and D.D. Chaplin. 1996. Affinity maturation without germinal centres in lymphotoxin-alpha-deficient mice. *Nature.* 382:462–466.
 8. Taylor, P.R., M.C. Pickering, M.H. Kosco-Vilbois, M.J. Walport, M. Botto, S. Gordon, and L. Martinez-Pomares. 2002. The follicular dendritic cell restricted epitope, FDC-M2, is complement C4; localization of immune complexes in mouse tissues. *Eur. J. Immunol.* 32:1888–1896.
 9. Kosco, M.H., E. Pflugfelder, and D. Gray. 1992. Follicular dendritic cell-dependent adhesion and proliferation of B cells in vitro. *J. Immunol.* 148:2331–2339.
 10. Hanayama, R., M. Tanaka, K. Miyasaka, K. Aozasa, M. Koike, Y. Uchiyama, and S. Nagata. 2004. Autoimmune disease and impaired uptake of apoptotic cells in MFG-E8-deficient mice. *Science.* 304:1147–1150.
 11. Hanayama, R., M. Tanaka, K. Miwa, A. Shinohara, A. Iwamatsu, and S. Nagata. 2002. Identification of a factor that links apoptotic cells to phagocytes. *Nature.* 417:182–187.
 12. Stubbs, J.D., C. Lekutis, K.L. Singer, A. Bui, D. Yuzuki, U. Srinivasan, and G. Parry. 1990. cDNA cloning of a mouse mammary epithelial cell surface protein reveals the existence of epidermal growth factor-like domains linked to factor VIII-like sequences. *Proc. Natl. Acad. Sci. USA.* 87:8417–8421.
 13. Thielen, C., N. Antoine, F. Melot, J.Y. Cesbron, E. Heinen, and R. Tsunoda. 2001. Human FDC express PrPc in vivo and in vitro. *Dev. Immunol.* 8:259–266.
 14. Humphrey, J.H., D. Grennan, and V. Sundaram. 1984. The origin of follicular dendritic cells in the mouse and the mechanism of trapping of immune complexes on them. *Eur. J. Immunol.* 14:859–864.
 15. Kapasi, Z.F., D. Qin, W.G. Kerr, M.H. Kosco-Vilbois, L.D. Shultz, J.G. Tew, and A.K. Szakal. 1998. Follicular dendritic cell (FDC) precursors in primary lymphoid tissues. *J. Immunol.* 160:1078–1084.
 16. Yoshida, K., M. Kaji, T. Takahashi, T.K. van den Berg, and C.D. Dijkstra. 1995. Host origin of follicular dendritic cells induced in the spleen of SCID mice after transfer of allogeneic lymphocytes. *Immunology.* 84: 117–126.
 17. Sukumar, S., A.K. Szakal, and J.G. Tew. 2006. Isolation of functionally active murine follicular dendritic cells. *J. Immunol. Methods.* 313:81–95.
 18. Shi, K., K. Hayashida, M. Kaneko, J. Hashimoto, T. Tomita, P.E. Lipsky, H. Yoshikawa, and T. Ochi. 2001. Lymphoid chemokine B cell-attracting chemokine-1 (CXCL13) is expressed in germinal center of ectopic lymphoid follicles within the synovium of chronic arthritis patients. *J. Immunol.* 166:650–655.
 19. Pasparakis, M., S. Kousteni, J. Peschon, and G. Kollias. 2000. Tumor necrosis factor and the p55TNF receptor are required for optimal development of the marginal sinus and for migration of follicular dendritic cell precursors into splenic follicles. *Cell. Immunol.* 201:33–41.
 20. Schwaeble, W., M.K. Schafer, F. Petry, T. Fink, D. Knebel, E. Weihe, and M. Loos. 1995. Follicular dendritic cells, interdigitating cells, and cells of the monocyte-macrophage lineage are the C1q-producing sources in the spleen. Identification of specific cell types by in situ hybridization and immunohistochemical analysis. *J. Immunol.* 155:4971–4978.
 21. Walport, M.J., K.A. Davies, and M. Botto. 1998. C1q and systemic lupus erythematosus. *Immunobiology.* 199:265–285.
 22. Futterer, A., K. Mink, A. Luz, M.H. Kosco-Vilbois, and K. Pfeffer. 1998. The lymphotoxin beta receptor controls organogenesis and affinity maturation in peripheral lymphoid tissues. *Immunity.* 9:59–70.
 23. Fu, Y.X., and D.D. Chaplin. 1999. Development and maturation of secondary lymphoid tissues. *Annu. Rev. Immunol.* 17:399–433.
 24. Chin, R.K., J.C. Lo, O. Kim, S.E. Blink, P.A. Christiansen, P. Peterson, Y. Wang, C. Ware, and Y.X. Fu. 2003. Lymphotoxin pathway directs thymic Aire expression. *Nat. Immunol.* 4:1121–1127.
 25. Rossi, S.W., M.Y. Kim, A. Leibbrandt, S.M. Parnell, W.E. Jenkinson, S.H. Glanville, F.M. McConnell, H.S. Scott, J.M. Penninger, E.J. Jenkinson, et al. 2007. RANK signals from CD4⁺3⁻ inducer cells regulate development of Aire-expressing epithelial cells in the thymic medulla. *J. Exp. Med.* 204:1267–1272.
 26. Boehm, T., S. Scheu, K. Pfeffer, and C.C. Bleul. 2003. Thymic medullary epithelial cell differentiation, thymocyte emigration, and the control of autoimmunity require lympho-epithelial cross talk via LTβR. *J. Exp. Med.* 198:757–769.
 27. Venanzi, E.S., D.H. Gray, C. Benoist, and D. Mathis. 2007. Lymphotoxin pathway and Aire influences on thymic medullary epithelial cells are unconnected. *J. Immunol.* 179:5693–5700.
 28. Bueler, H., M. Fischer, Y. Lang, H. Bluethmann, H.P. Lipp, S.J. DeArmond, S.B. Prusiner, M. Aguet, and C. Weissmann. 1992. Normal development and behaviour of mice lacking the neuronal cell-surface PrP protein. *Nature.* 356:577–582.
 29. Koni, P.A., R. Sacca, P. Lawton, J.L. Browning, N.H. Ruddle, and R.A. Flavell. 1997. Distinct roles in lymphoid organogenesis for lymphotoxins alpha and beta revealed in lymphotoxin beta-deficient mice. *Immunity.* 6:491–500.
 30. Zullig, S., and M.O. Hengartner. 2004. Cell biology. Ticking macrophages, a serious business. *Science.* 304:1123–1124.

9.2 Engulfment of cerebral apoptotic bodies controls the course of prion disease in a mouse strain-dependent manner.

Kranich J, Krautler NJ, Falsig J, Ballmer B, Li S, Hutter G, Schwarz P, Moos R, Julius C, Miele G, Aguzzi A. *J Exp Med.* 2010 Sep 27;207(10):2271-81.

Engulfment of cerebral apoptotic bodies controls the course of prion disease in a mouse strain–dependent manner

Jan Kranich, Nike Julia Krautler, Jeppe Falsig, Boris Ballmer, Shulei Li, Gregor Hutter, Petra Schwarz, Rita Moos, Christian Julius, Gino Miele, and Adriano Aguzzi

Institute of Neuropathology, University Hospital of Zurich, 8091 Zurich, Switzerland

Progressive accumulation of PrP^{Sc}, a hallmark of prion diseases, occurs when conversion of PrP^C into PrP^{Sc} is faster than PrP^{Sc} clearance. Engulfment of apoptotic bodies by phagocytes is mediated by Mfge8 (milk fat globule epidermal growth factor 8). In this study, we show that brain Mfge8 is primarily produced by astrocytes. Mfge8 ablation induced accelerated prion disease and reduced clearance of cerebellar apoptotic bodies in vivo, as well as excessive PrP^{Sc} accumulation and increased prion titers in prion-infected C57BL/6 × 129Sv mice and organotypic cerebellar slices derived therefrom. These phenotypes correlated with the presence of 129Sv genomic markers in hybrid mice and were not observed in inbred C57BL/6 *Mfge8*^{-/-} mice, suggesting the existence of additional strain-specific genetic modifiers. Because Mfge8 receptors are expressed by microglia and depletion of microglia increases PrP^{Sc} accumulation in organotypic cerebellar slices, we conclude that engulfment of apoptotic bodies by microglia may be an important pathway of prion clearance controlled by astrocyte-borne Mfge8.

Transmissible spongiform encephalopathies (TSEs) are fatal neurodegenerative disorders afflicting many mammals (Aguzzi, 2006). Prions, the infectious particles that cause TSEs, consist mostly of PrP^{Sc}, a β -sheet-rich higher-order aggregate of the membrane protein PrP^C (Prusiner, 1982). TSE-affected brains display neuronal vacuolation and loss, microglial activation, astrogliosis, and deposition of PrP^{Sc} (Prusiner et al., 1983; Weissmann, 2004).

The molecular mechanisms underlying brain damage in prion diseases are not well understood. Grafting experiments of wild-type brain tissue into PrP^C-deficient brains showed that the neuropathological changes only occurred in tissue expressing PrP^C, even if proteinase K (PK)-resistant PrP^{Sc} was also detected in the surrounding *Pmp*^{0/0} tissue (Brandner et al., 1996).

These results indicate that neurotoxicity depends on PrP^C expression by the target cells, whereas PrP^{Sc} does not appear to be intrinsically toxic. This notion was confirmed by neuron-specific ablation of *Pmp* (Mallucci et al., 2003) and in mice expressing anchorless PrP, which is converted into a protease-resistant isoform and forms amyloid plaques yet causes minimal neuronal damage (Chesebro et al., 2005).

Prion diseases exhibit frequent neuronal apoptosis (Liberski et al., 2004). Although inhibition of apoptosis by overexpressing Bcl-2 or ablating Bax did not affect the life expectancy of prion-inoculated mice (Steele et al., 2007), prion-infected brain cells may release membrane fragments even when undergoing nonapoptotic death. Furthermore, exosomes may be released by perfectly healthy cells (Théry et al., 2009) and may conceivably carry prion infectivity.

A trait common to each of these extracellular vesicles is the surface exposure of phosphatidyl

CORRESPONDENCE

Adriano Aguzzi:
adriano.aguzzi@usz.ch

Abbreviations used: CNS, central nervous system; dpi, day postinoculation; FDC, follicular DC; GCV, ganciclovir; ISH, in situ RNA hybridization; MPA, misfolded protein assay; mRNA, messenger RNA; PK, proteinase K; PS, phosphatidyl serine; SCA, scrapie cell assay; STR, short tandem repeat; TSE, transmissible spongiform encephalopathy; TUNEL, terminal transferase dUTP nick end labeling.

J. Kranich and N.J. Krautler contributed equally to this paper. J. Kranich's present address is Garvan Institute of Medical Research, Darlinghurst, New South Wales 2010, Australia.

G. Miele's present address is Translational Medicine Research Collaboration, University of Dundee, Dundee DD1 5EH, Scotland, UK.

G. Hutter's present address is Dept. of Neurosurgery, University Hospital of Basel, 4031 Basel, Switzerland.

© 2010 Kranich et al. This article is distributed under the terms of an Attribution-Noncommercial-Share Alike-No Mirror Sites license for the first six months after the publication date (see <http://www.rupress.org/terms>). After six months it is available under a Creative Commons License (Attribution-Noncommercial-Share Alike 3.0 Unported license, as described at <http://creativecommons.org/licenses/by-nc-sa/3.0/>).

serine (PS), which can be recognized by the secreted ligand, Mfge8 (milk fat globule epidermal growth factor 8; Patton and Keenan, 1975). By virtue of its affinity to PS, Mfge8 helps mediating the removal of apoptotic bodies (Hanayama et al., 2002). Phagocytic cells then bind Mfge8-opsonized apoptotic cells through $\alpha_v\beta_3$ and $\alpha_v\beta_5$ integrins. Mfge8 is secreted by some phagocytic cells, including immature DCs and thioglycolate-activated peritoneal macrophages, as well as nonhematopoietic cells, including mammary epithelial cells (Hanayama and Nagata, 2005) and follicular DCs (FDCs; Kranich et al., 2008). A recent study described a potential involvement of Mfge8 expressed by human astrocytes, microglia, and smooth muscle cells in the removal of A β plaques (Boddaert et al., 2007). A microarray screen also identified Mfge8 expression in mouse astrocytes (Cahoy et al., 2008). Another study claimed Mfge8 expression in vitro by the microglial cell line BV-2 (Fuller and Van Eldik, 2008).

In this study, we show by in situ RNA hybridization (ISH) and quantitative RT-PCR that *Mfge8* is primarily expressed by subsets of astrocytes in the central nervous system (CNS). Furthermore, Mfge8 deficiency resulted in accelerated prion pathogenesis and enhanced PrP^{Sc} accumulation in the CNS and was accompanied by elevated numbers of apoptotic cerebellar granule cells. These results suggest that Mfge8 is required for the efficient removal of apoptotic cells in the CNS and possibly also for degradation of prions.

RESULTS

Mfge8-deficient mice show accelerated prion pathogenesis

We inoculated *Mfge8*^{-/-} mice (bred as intercrosses of the C57BL/6 and 129Sv mouse strains) i.c. (intracerebrally) or i.p. with RML6 (Rocky Mountain Laboratory strain, passage 6) prions (1,000 LD₅₀ units). We monitored the mice for clinical signs of scrapie and defined the incubation period as the time until mice reached the terminal stage of disease. *Mfge8*^{-/-} mice succumbed to scrapie much earlier than *Mfge8*^{+/+} mice. This acceleration was more pronounced after i.c. inoculation (~40 d; Fig. 1 A, left) than after i.p. inoculation (~20 d, Fig. 1 A, right), suggesting that it was caused by the absence of Mfge8 within the CNS rather than in extraneural compartments.

Because Mfge8 is highly expressed by FDCs (Kranich et al., 2008), which are important sites of extraneural prion replication (Aguzzi and Heikenwalder, 2005), we probed the splenic PrP^{Sc} content on PK-treated histoblots. Follicular PrP^{Sc} accumulation was similar in *Mfge8*^{+/+} and *Mfge8*^{-/-} spleens (Fig. S1 A). Along with the accelerated pathogenesis of i.c. inoculated mice, this finding makes it unlikely that extraneural prion-modulating events caused the acceleration in *Mfge8*^{-/-} mice. Therefore, we focused all further analyses on the interplay between Mfge8 and prions within the CNS.

Mfge8-deficient mice exhibit elevated levels of PrP^{Sc}

We reasoned that accelerated disease progression may result from enhanced accumulation of PrP^{Sc}, be it through increased

production or through reduced degradation. This possibility was studied with four methodologies: qualitative assessment of PrP immunoreactivity in histological sections of terminally diseased brains (Fig. 1 B), quantitation of PrP^{Sc} chemiluminescence in Western blots of brain homogenates (Fig. 1 C), quantitation of aggregated PrP (PrP^{MPA}) by the misfolded protein assay (MPA; Fig. 1 D; Lau et al., 2007), and infectivity titer determinations with the scrapie cell assay (SCA; Fig. S1 C). The MPA captures misfolded and aggregated proteins by precipitation with peptoid-coated magnetic beads; captured proteins are then disaggregated and quantitated by sandwich ELISA with anti-PrP antibodies (Polymenidou et al., 2008).

PrP immunoreactivity was much more intense in prion-infected *Mfge8*^{-/-} brains than in *Mfge8*^{+/+} control brains (Fig. 1 B). Also, brains of terminally scrapie-sick *Mfge8*^{-/-} mice displayed increased PK-resistant PrP^{Sc} and PrP^{MPA} ($P < 0.03$ and $P < 0.034$, respectively; Fig. 1, C and D). This is noteworthy because *Mfge8*^{-/-} mice attained terminal scrapie already at ~160 d postinoculation (dpi), i.e., 40 d earlier than *Mfge8*^{+/+} mice. Because brain PrP^{Sc} accumulates exponentially over time, shorter incubation times typically go along with reduced PrP^{Sc} deposition and vice versa (Büeler et al., 1994). Therefore, we analyzed brain homogenates of pre-clinical *Mfge8*^{+/+} and *Mfge8*^{-/-} mice sacrificed at 120 dpi by MPA. Already at this early time point, a tendency toward higher PrP^{Sc} levels was detected in *Mfge8*^{-/-} brains, supporting the idea of accelerated PrP^{Sc} deposition (Fig. 1 D). PrP^C concentrations, as measured by ELISA, did not differ between noninfected *Mfge8*^{+/+} and *Mfge8*^{-/-} brain homogenates (Fig. S1 B), confirming that the increase in PrP^{Sc} was not caused by altered PrP^C expression in *Mfge8*^{-/-} mice.

Next, we asked whether the increased PrP^{Sc} deposition would lead to increased infectivity titers in *Mfge8*^{-/-} brains. We compared brain homogenates from *Mfge8*^{+/+} and *Mfge8*^{-/-} mice at terminal disease stage by SCA using the prion-susceptible neuroblastoma cell line PK1 (Klöhn et al., 2003). We observed a slight trend toward increased infectivity in *Mfge8*^{-/-} brains (7.48 ± 0.07 TCI [infectious tissue culture] units and 7.30 ± 0.12 TCI units in *Mfge8*^{+/+} and *Mfge8*^{-/-} brains, respectively), which, however, did not attain statistical significance (Fig. S1 C).

We also assessed PrP^{Sc} accumulation ex vivo using the prion organotypic slice culture assay (Falsig et al., 2008). Cerebellar *Mfge8*^{+/+} and *Mfge8*^{-/-} slices were infected with 3,000 LD₅₀ units of RML6 prions and harvested after 5 wk. Western blot analysis showed significantly higher ($P < 0.024$) PrP^{Sc} levels in *Mfge8*^{-/-} brain slices (Fig. 1 E), confirming that increased prion accumulation in *Mfge8*^{-/-} mice was entirely independent of any indirect effects caused by Mfge8 deficiency in extraneural compartments.

Next, we analyzed whether accelerated disease progression occurred concomitantly with additional pathological changes. The severity of astrogliosis, microgliosis (Fig. 2, A and B), and spongiosis (Fig. S1 D) at terminal disease was analyzed immunohistochemically. All of these parameters were similar in *Mfge8*^{+/+} and *Mfge8*^{-/-} brains. Thus, the brain

pathology of terminally scrapie-sick *Mfge8*^{-/-} mice was as strong as in *Mfge8*^{+/+} mice, although terminal disease was reached 40 d earlier. We conclude that the processes leading to brain damage were also accelerated.

Increased prevalence of apoptotic cells in the cerebellum of *Mfge8*^{-/-} mice

Beyond accelerated prion disease, *Mfge8*^{-/-} mice have no obvious CNS defects. However, prion infections lead to significant

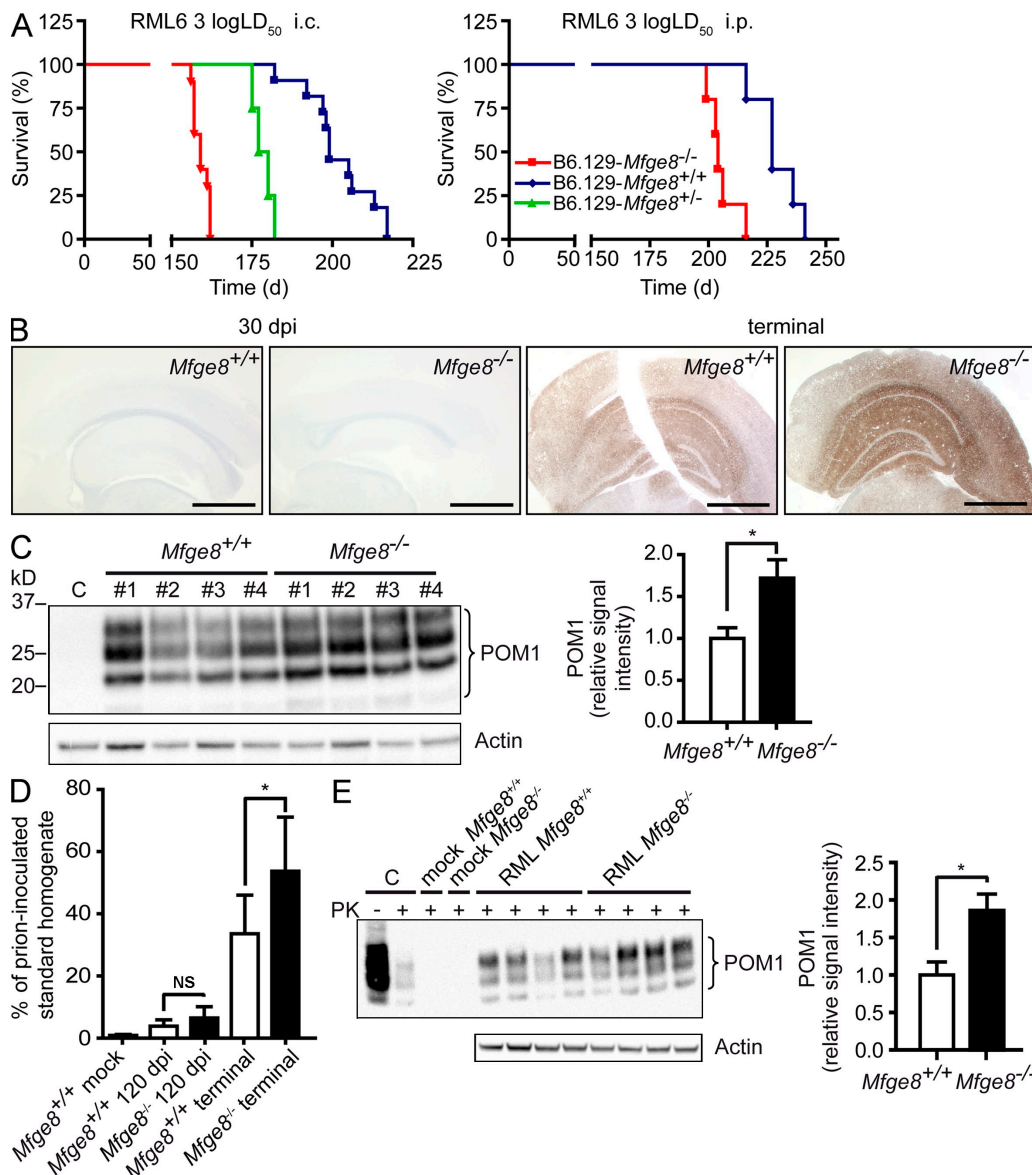


Figure 1. *Mfge8*^{-/-} mice show accelerated disease progression. (A) B6.129-*Mfge8*^{-/-}, B6.129-*Mfge8*^{+/-}, and B6.129-*Mfge8*^{+/+} were inoculated i.c. with 3 log LD₅₀ (n = 10 for *Mfge8*^{-/-}, n = 4 for *Mfge8*^{+/-}, and n = 11 for *Mfge8*^{+/+}) and i.p. with 3 log LD₅₀ per group of RML6 prions. The mean incubation time after i.c. inoculation was significantly accelerated in *Mfge8*^{-/-} mice (159 ± 2 d in *Mfge8*^{-/-}, 179 ± 3 d in *Mfge8*^{+/-}, and 202 ± 3.9 d in *Mfge8*^{+/+} mice; P < 0.0001, logrank). Differences in incubation time after i.p. inoculation were less pronounced (206 ± 6 d in *Mfge8*^{-/-} and 229 ± 10 d in *Mfge8*^{+/+} mice) but still significant (P = 0.004, logrank test). (B) Stainings of brain sections after 30 dpi (left) or at terminal stage (right) using anti-PrP antibody SAF84. Bars, 1 mm. (C) Western blot of PK-digested brain homogenates from i.c. inoculated *Mfge8*^{+/+} and *Mfge8*^{-/-} mice using anti-PrP antibody POM1 (C, uninoculated brain homogenate). Western blot for actin on non-PK-digested sample is shown below. Densitometric quantitation of POM1 signal normalized over actin expression. Bar graph shows mean relative signal intensity (n = 4; *, P = 0.03; Student's *t* test). (D) MPA of brain homogenates from *Mfge8*^{+/+} and *Mfge8*^{-/-} mice at 120 dpi or at terminal disease (n = 6-7 mice per group; *, P = 0.034; Student's *t* test) indicated in percentages of RML6 prion-inoculated brain homogenate. *Mfge8*^{-/-} mice sacrificed at 120 dpi showed a slight increase over *Mfge8*^{+/+} mice. (E) *Mfge8*^{+/+} and *Mfge8*^{-/-} cerebellar slices were inoculated with 3 × 3 log LD₅₀ RML6 prions or with noninfectious brain homogenate (mock), harvested after 5 wk, homogenized, and PK digested (C, brain homogenate from a terminal RML inoculated mouse used as positive control). PrP^{Sc} levels were analyzed by Western blotting using POM1 and normalized against actin (without PK digestion) by densitometry (bar graph; n = 4; *, P = 0.024; Student's *t* test). Error bars represent SD. Histology, Western blot, and MPA results represent at least four independent experiments.

apoptosis in the CNS, and the role of Mfge8 in the removal of apoptotic cells is well established (Hanayama et al., 2002, 2004; Kranich et al., 2008). If the absence of Mfge8 were to impair the removal of prion-infected apoptotic neurons, this might contribute to the rise in PrP^{Sc} in *Mfge8*^{-/-} mice and could explain their shortened incubation time.

Therefore, we determined the prevalence of apoptotic cells by terminal transferase dUTP nick end labeling (TUNEL) in at least three cerebellar regions of five to seven *Mfge8*^{+/+} and *Mfge8*^{-/-} mice. The mean frequency of TUNEL⁺ cells per region was normalized against the total number of DAPI⁺ nuclei in each region of interest. We detected an approximately twofold increase of TUNEL⁺ cells in cerebelli of terminally sick *Mfge8*^{-/-} mice ($P = 0.023$; Fig. 2 C). In other brain areas, TUNEL⁺ cells were rare, and no difference was detected between *Mfge8*^{-/-} and *Mfge8*^{+/+} mice (unpublished data). This finding suggests that Mfge8 is involved in the removal of prion-damaged cells in the cerebellum. The paucity of apoptotic cells in other areas implies that factors other than Mfge8 ensure rapid removal of dead cells there.

Astrocytes express Mfge8

The cellular source of Mfge8 in the CNS is not well characterized. Human and mouse astrocytes, microglia, and smooth muscle cells (Boddaert et al., 2007; Fuller and Van Eldik,

2008) were reported to produce Mfge8, suggesting that microglia in vivo may also be a source of Mfge8. As we did not detect Mfge8 in the CNS by immunohistochemistry using anti-Mfge8 antibodies (unpublished data), we focused on RNA expression analysis as a more reliable tool for detecting the source of secreted proteins such as Mfge8. We performed ISHs using an *Mfge8* RNA probe and found *Mfge8* transcription in the cerebellum at the watershed between internal granular and molecular layers. *Mfge8*-expressing cells lacked the characteristic morphology of Purkinje neurons. In view of their localization and morphology, Bergman glia (a specialized type of astrocytes) were deemed the most likely source of Mfge8 (Fig. 3 A, top). We also found cortical *Mfge8*-expressing cells with a stellate appearance indicative of astrocytes (Fig. 3 A, bottom). To validate the presumption that Mfge8 is expressed by astrocytes, we quantified *Mfge8* messenger RNA (mRNA) expression by quantitative RT-PCR on cultured CNS cells enriched for distinct subpopulations. We found sustained *Mfge8* expression in cultures enriched for astrocytes (purity of the astrocyte population, >95%; unpublished data) but little *Mfge8* mRNA in cultures enriched for oligodendrocytes (purity, ~85%) or for cerebellar granule neurons (purity, ~95%). Conversely, we detected only minute amounts of *Mfge8* RNA in cultured microglia (purity, >95%), although this is the main phagocytic cell type in the CNS

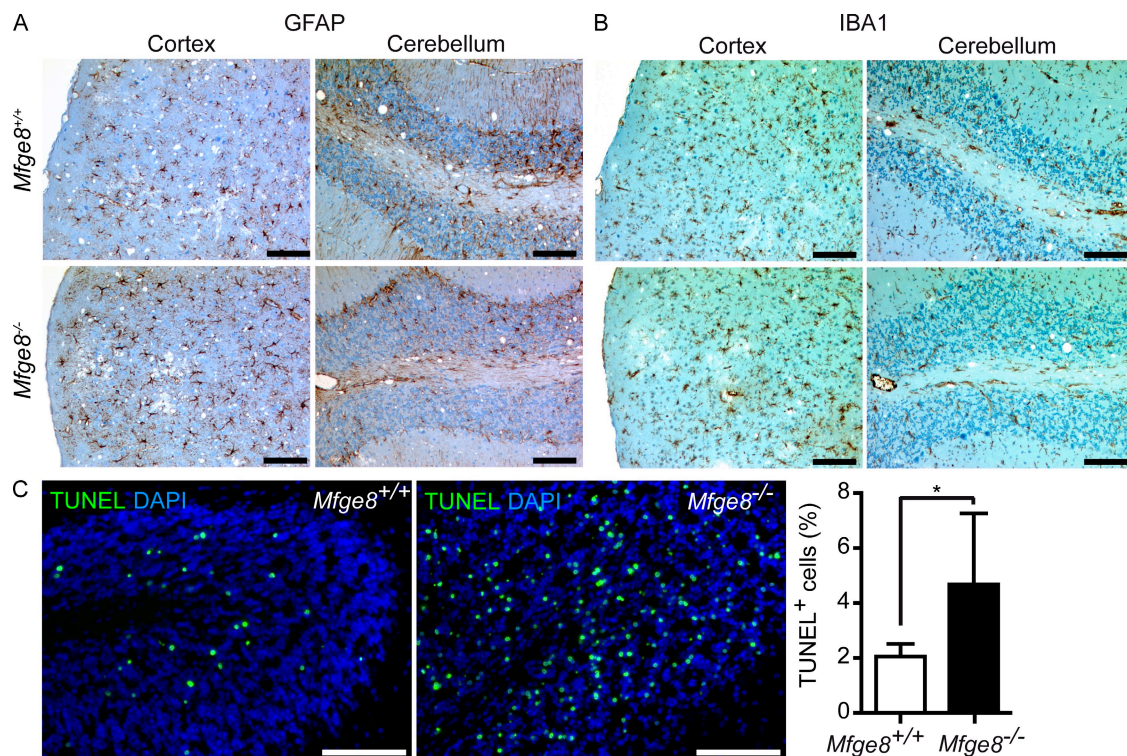


Figure 2. Histopathological analysis of terminal *Mfge8*^{-/-} brains. (A) Astroglia proliferation was analyzed by GFAP staining. (B) Microglial activation was visualized by IBA1 staining. (C) TUNEL staining on cerebellar cryosection of i.c. inoculated B6.129-*Mfge8*^{-/-} ($n = 5$) and B6.129-*Mfge8*^{+/+} mice ($n = 7$). Sections were counterstained with DAPI. Bar graph shows quantitation of TUNEL⁺ cells from at least three cerebellar areas per mouse. Number of TUNEL⁺ cells was normalized against the number of DAPI⁺ nuclei. Graph shows percentage of TUNEL⁺ cells per area \pm SD (*, $P = 0.023$; Student's t test). Results summarize at least five independent experiments. Bars: (A and C) 100 μ m; (B) 200 μ m.

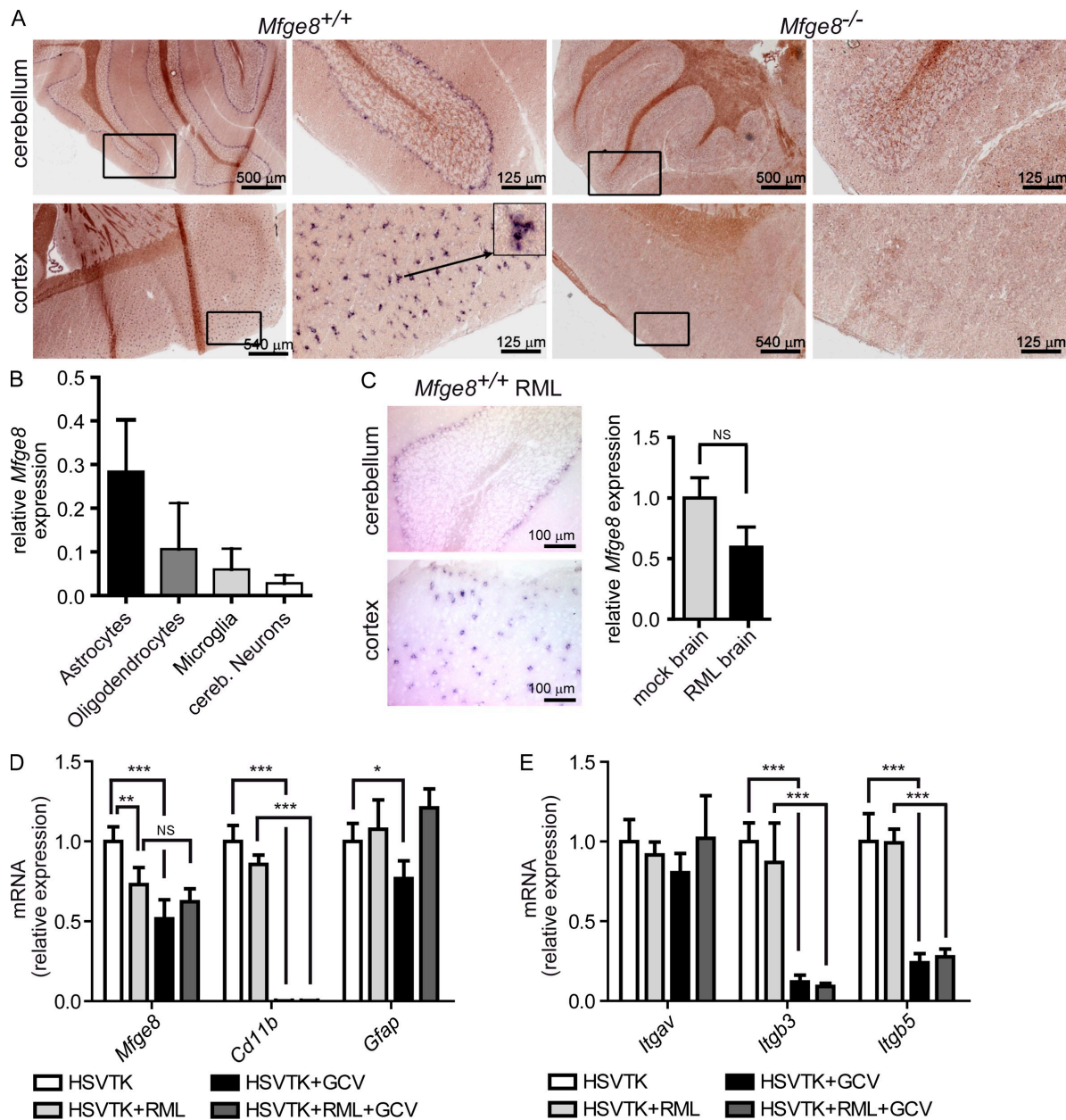
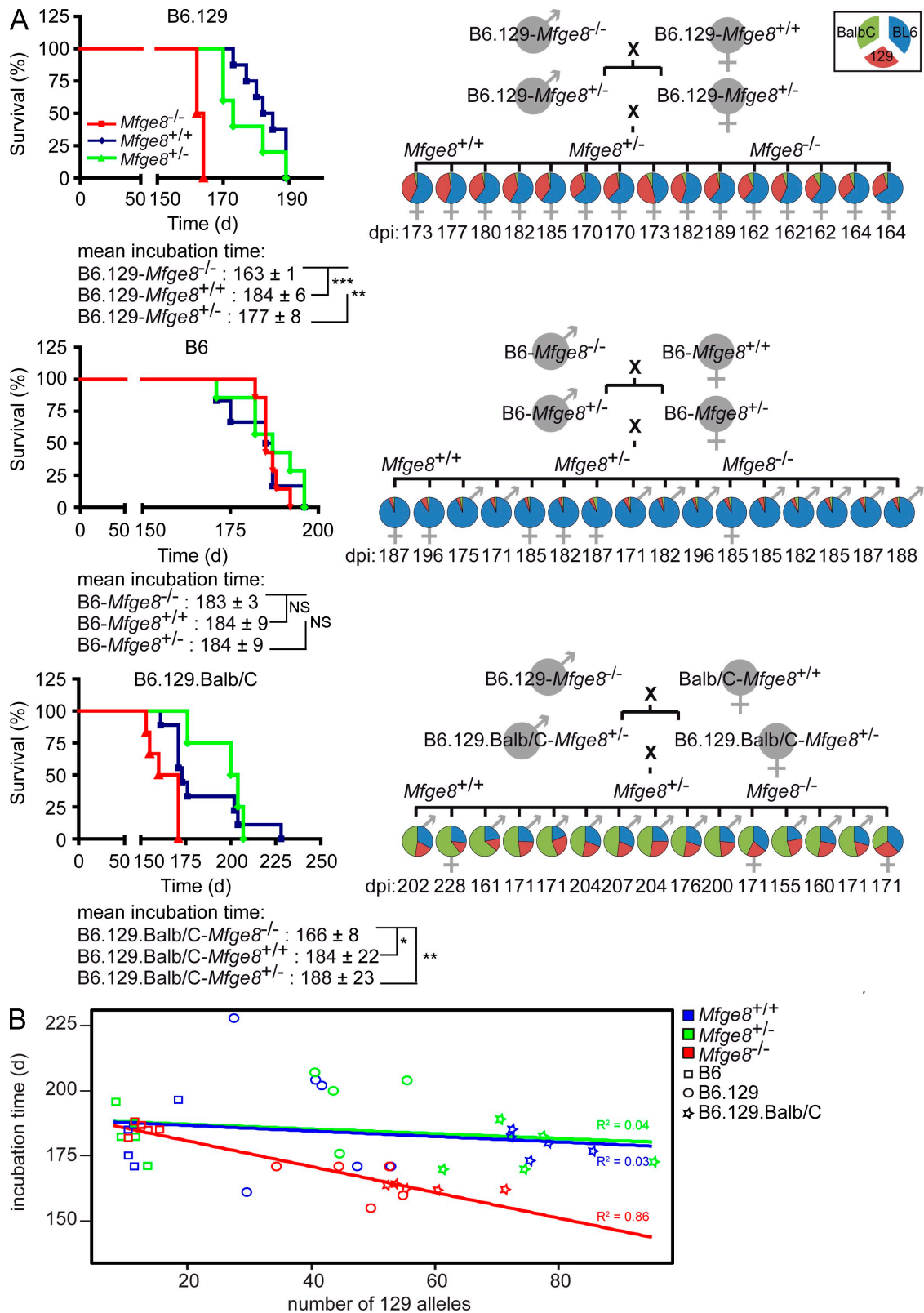


Figure 3. Analysis of the cellular source of *Mfge8*. (A) ISH for *Mfge8* on brain cryosections. *Mfge8*⁺ cells (dark purple) were found in cerebellar (top) and cortical areas (bottom). Low and high magnification photographs of the same cerebellar (top) and cortical (bottom) areas are shown. Boxes indicate areas shown in higher magnifications. The arrow indicates the cell shown in high magnification. (B) Expression of *Mfge8* in cultured astrocytes, microglia, oligodendrocytes, and neurons was quantified by quantitative RT-PCR. *Mfge8* expression in each subset relative to total brain is shown ($n = 3$). (C) ISH for *Mfge8* in prion-inoculated *Mfge8*^{+/+} mice at terminal stage (left). Right panel shows relative *Mfge8* mRNA expression in mock- and RML-inoculated brains as assessed by quantitative RT-PCR ($n = 3$). (D) Quantitative RT-PCR quantitation of *Mfge8*, *Cd11b*, and *Gfap* expression in cerebellar slice cultures from untreated *CD11b*-HSVTK mice (HSVTK), prion-inoculated untreated *CD11b*-HSVTK mice (HSVTK + RML), GCV-treated *CD11b*-HSVTK mice (HSVTK + GCV), and prion-inoculated GCV-treated *CD11b*-HSVTK mice (HSVTK + RML + GCV; Student's t test; $n = 4$). Uninfected HSVTK + GCV slices compared with HSVTK slices have a slight but significant reduction of *Mfge8* (**, $P = 0.0082$). Uninfected HSVTK + GCV slices compared with HSVTK + RML + GCV slices have no difference in expression (NS, $P = 0.1566$). HSVTK + RML + GCV slices compared with HSVTK + RML slices show significant down-regulation (**, $P = 0.0082$). *CD11b* expression is down-regulated by almost 3 logs in GCV -treated slices, confirming efficient depletion of microglia (HSVTK + GCV: ***, $P < 0.0001$; HSVTK + RML + GCV: ***, $P < 0.0001$). *Gfap* expression is slightly reduced after GC treatment (HSVTK + GCV: *, $P = 0.0255$). (E) Analysis of integrin α , (*Itgav*), β_3 (*Itgb3*), and β_5 (*Itgb5*) expression by quantitative RT-PCR (Student's t test; $n = 4$). No significant changes in *Itgav* expression were found. *Itgb3* and *Itgb5* were down-regulated in GCV-treated compared with nontreated slices (*Itgb3* HSVTK + GCV: ***, $P < 0.0001$; *Itgb3* HSVTK + RML + GCV: ***, $P = 0.0007$; *Itgb5* HSVTK + GCV: ***, $P = 0.0002$; *Itgb5* HSVTK + RML + GCV: ***, $P < 0.0001$). Error bars represent SD. ISH and quantitative RT-PCR results are shown representative of 3 and 12 independent experiments, respectively.



(Fig. 3 B), and the microglial cell line BV-2 was reported to express *Mfge8* (Fuller and Van Eldik, 2008). Because explanted microglia tend to dedifferentiate and to become activated, we wondered whether microglia up-regulate *Mfge8* expression upon activation. Therefore, we performed quantitative RT-PCR and ISH on brains of terminally prion-sick mice, which displayed an extremely high density of activated microglia. Even here, the *Mfge8* expression pattern was similar to that of healthy mice (Fig. 3 C, left). In fact, the overall amount of *Mfge8* RNA was slightly reduced in RML-inoculated mice as compared with mice inoculated with noninfected brain homogenate (Fig. 3 C, right). Combination of immunofluorescence to visualize microglia using IB4 (isolectin B4) and ISH for *Mfge8* failed to show colocalization (Fig. S2) of IB4 and *Mfge8*. These results negate a major contribution of microglia to the availability of *Mfge8* within the CNS, be it in health or in disease.

To further address whether microglia might constitute a source of *Mfge8*, cerebellar slice cultures were prepared from *CD11b-HSVTK* mice (Heppner et al., 2005), from which microglia can be depleted by administering ganciclovir (GCV; Falsig et al., 2008). The efficiency of depletion was assessed by quantitative RT-PCR for *CD11b*, which is exclusively expressed in the brain by microglia. *CD11b* expression was reduced by almost 3 logs (Fig. 3 D), confirming that microglia were virtually absent after the addition of GCV. *Mfge8* expression was slightly reduced after microglia depletion (Fig. 3 D, HSVTK + GCV). This suggests that in organotypic slices, which show prodigious levels of microglial activation, some *Mfge8* may be microglia borne (Falsig et al., 2008). Conversely, GCV-treated slices displayed a slight reduction in *Gfap* (*Glial fibrillary acidic protein*) expression, suggesting that astrocytes were also affected by GCV to some degree. Thus, the decrease in *Mfge8* expression might represent a consequence of marginal astrocyte depletion. Alternatively, the depletion of microglia may quench astrocytic transcription of *Mfge8* indirectly, e.g., through the depletion of microglia-borne cytokines. Expression of neuron-specific *Nefn* (*neurofilament heavy chain*) and oligodendrocyte-specific *Mbp* (*myelin basic protein*) was not affected by GCV treatment (unpublished data). Consistent with the *in vivo* results (Fig. 3 C, right), we also observed a slight reduction of *Mfge8* expression in prion-infected slice cultures (Fig. 3 D, HSVTK + RML). The aforementioned findings support the notion that most or all *Mfge8* present in the CNS is not produced by microglia but rather by subsets of astrocytes encompassing cerebellar Bergman glia.

We next analyzed the expression of $\alpha_v\beta_3$ and $\alpha_v\beta_5$ integrins in *CD11b-HSVTK* slices, receptors that were shown to be required for *Mfge8*-dependent engulfment of apoptotic cells (Hanayama et al., 2002). Although quantitative RT-PCR analysis of the α_v subunit (*Itgav*) was unchanged in microglia-

depleted slices, expression of the β_3 (*Itgb3*) and β_5 (*Itgb5*) subunit was decreased by $\sim 90\%$ and 75% , respectively (Fig. 3 E). Although microglia are not the major source of *Mfge8*, they are the major cell type expressing the *Mfge8* receptors $\alpha_v\beta_3$ and $\alpha_v\beta_5$. Thus, our findings strongly suggest that microglia are required for removal of apoptotic prion-infected cells.

The influence of *Mfge8* on prion pathogenesis is modulated by quantitative trait loci

We then tested the reproducibility of the aforementioned findings using RML5 prions (derived from a different passage of the same inoculum as RML6) and also repeated the inoculations using *Mfge8*^{-/-} mice on a different genetic background. Our initial inoculation experiments with RML6 were conducted using the originally published *Mfge8*^{-/-} strain (Hanayama et al., 2004) bred on a mixed C57BL/6 \times 129Sv background (B6.129-*Mfge8*^{-/-}). This resulted in a 40-d acceleration of the disease. Inoculations of B6.129-*Mfge8*^{-/-} with 3 log LD₅₀ of RML5 resulted again in a strongly accelerated incubation time. In the latter experiment, the mean difference was 20 d (Fig. 4 A, top left) and was, again, highly statistically significant ($P = 0.0002$). The variation of the latency between B6.129-*Mfge8*^{-/-} inoculated with RML5 and RML6 (Fig. 1 A) is likely to reflect differences between the infectivity titers of the two inocula.

When we inoculated *Mfge8*^{-/-} mice that had been backcrossed to the C57BL/6 background for 10 generations (B6-*Mfge8*^{-/-}) with 3 log LD₅₀ RML5, we did not observe any acceleration of pathogenesis. B6-*Mfge8*^{-/-}, B6-*Mfge8*^{+/-}, and B6-*Mfge8*^{+/+} mice all succumbed to disease after a time period of ~ 180 d (Fig. 4 A, middle left). Accordingly, the PrP^{Sc} levels and the density of apoptotic granule cells were not altered in B6-*Mfge8*^{-/-} mice (Fig. S3, A and B). These results suggest that the effect of *Mfge8* on the course of prion infections can be overridden by unidentified genetic modifiers that are polymorphic between the B6 and 129Sv strains. To gain more insights into the distribution of these modifiers, we crossed B6.129-*Mfge8*^{-/-} mice to a third genetic background (Balb/C). Inoculation of the resulting F₂ generation littermates (B6.129.Balb/C-*Mfge8*^{-/-}, -*Mfge8*^{+/-}, and -*Mfge8*^{+/+}) showed that pathogenesis was again accelerated by the removal of *Mfge8* (Fig. 4 A, bottom left). The variability of incubation times was increased, most likely because of the increased genetic heterogeneity of the mouse collectives.

To investigate whether differential expression of *Mfge8* or its receptors $\alpha_v\beta_3$ and $\alpha_v\beta_5$ integrins might contribute to the observed background effect, we analyzed their mRNA levels by quantitative RT-PCR on whole brain cDNA from B6 and B6.129 *Mfge8*^{+/-} mice (Fig. S4 A). Expression levels of *Mfge8*, *Itgb3*, and *Itgb5* were similar in all mice analyzed, yet one specific primer pair annealing to the 3' end of the

per mouse. Each chart represents one mouse. Only alleles that could unambiguously be assigned to one of the three different genetic backgrounds are represented in the pie charts. (B) Linear regression analysis comparing incubation time with number of 129Sv alleles. No correlation was seen between incubation time and number of 129Sv alleles in *Mfge8*^{+/+} and *Mfge8*^{+/-} mice. However, there was a strong correlation in *Mfge8*^{-/-} mice. Results represent at least five independent experiments.

Itgb3 open reading frame yielded dramatically different quantitative RT-PCR reads between the two strains (unpublished data). This idiosyncrasy suggested the existence of polymorphisms between the B6 and 129Sv alleles of the *Itgb3* gene leading to differential annealing and artifactual quantitative RT-PCR results. Therefore, we analyzed the microsatellite marker D11Mit128, which is located within 1 cM from the *Itgb3* locus and discriminates between B6 and 129Sv allelotypes, in prion-inoculated mice (Fig. S4 B). We found that only *Mfge8*^{-/-} mice homozygous for the 129Sv allele of D11Mit128 showed accelerated prion pathogenesis (Fig. S4 B, red box plots). Whenever a B6 allele of D11Mit128 was present, the presence or absence of *Mfge8* failed to alter the incubation time (Fig. S4 B, blue and green box plots).

These results suggest that *Mfge8*/α_vβ₃ integrin-dependent phagocytosis is affected by strain-specific *Itgb3* allotypes. Therefore, we sequenced the open reading frame of *Itgb3* of 129Sv, C57BL/6, and Balb/C *Mfge8*^{+/+} mice. We found several strain-specific single nucleotide polymorphisms, yet none of these resulted in codon changes (Fig. S4 C). Thus, the linkage to D11Mit128 may point to noncoding polymorphisms that may affect splicing, mRNA stability, or posttranscriptional control by microRNAs.

We then performed a whole genome linkage analysis of all inoculated mice with 209 short tandem repeats (STRs; mean genetic distance, ~7 cM; 13.5 Mbp) polymorphic between B6, 129Sv, or Balb/C mice (Table S1). Alleles that were shared by two different mouse strains were counted separately (B6 + 129Sv, B6 + Balb/C, or 129Sv + Balb/C), and all remaining alleles were regarded as noninformative (Table I). The percentages of B6 (blue), Balb/C (green), and 129Sv (red) alleles were summarized in pie charts (Fig. 4 A, right). Analysis of covariance was performed to analyze the independent effects of *Mfge8* deficiency and genetic background on incubation time. In crossbred mice, the *Mfge8* genotype significantly correlated with the incubation time of prion disease, even after elimination of possible genetic confounders by adjusting the contribution of each genetic background. The number of 129Sv alleles also influenced the incubation time (Table I). Linear regression analysis revealed a correlation of the incubation time and the amount of 129Sv alleles only in *Mfge8*^{-/-} mice ($R^2 = 0.86$; Fig. 4 B). Therefore, *Mfge8* deficiency accelerates the prion pathogenesis, but only in the genetic context of the 129Sv strain.

DISCUSSION

Many factors control incubation times of prion diseases after i.p. inoculation, including components of the immune system (Mabbott et al., 1998; Aguzzi, 2003), depletion of FDCs (Montrasio et al., 2000), and manipulations of the complement system (Klein et al., 2001; Mabbott et al., 2001). However, interference with prion replication in the CNS is more difficult, and there are only few interventions known to alter the incubation time of prion diseases after i.c. inoculation. Even fewer factors have been found to accelerate pathogenesis after i.c. administration of prions (LaCasse et al., 2008; Spinner

et al., 2008). Mice expressing a mutant TLR4 (Toll-like receptor 4) defective in intracellular signaling were reported to experience accelerated disease after prion inoculation, implying that absence of TLR4 might impair microglia activation and consequently prion clearance. However, there was no difference in PrP^{Sc} levels at terminal disease stage in this model (Spinner et al., 2008). Even in mice engineered to overexpress PrP^C, which have drastically shortened incubation times, the accelerated prion replication does not lead to elevated PrP^{Sc} levels (Fischer et al., 1996). In contrast, *Mfge8*^{-/-} mice displayed enhanced PrP^{Sc} deposition despite accelerated disease progression. These findings strongly suggest that these mice suffer from decreased prion clearance.

Why does the absence of *Mfge8* result in elevated levels of PrP^{Sc}? Upon prion infection, neurons may experience progressive damage and ultimately undergo apoptosis; during this process, they may secrete apoptotic PS-coated bodies containing prions (Ashok and Hegde, 2006; Leblanc et al., 2006). We suggest that astrocyte-derived *Mfge8* opsonizes these prion-laden apoptotic bodies by binding to PS exposed on their surface. Microglia, the main phagocytic cell type of the CNS, express the *Mfge8* receptors, α_vβ₃ and α_vβ₅ integrin heterodimers. Because microglia antagonize prion replication (Falsig et al., 2008), it appears plausible that *Mfge8*-opsonized, prion-laden apoptotic bodies are taken up and degraded

Table I. Statistical analysis of STR results

Source	F	P-value
Number of B6 alleles and <i>Mfge8</i> genotype		
Number of B6 alleles	0.4	0.53
<i>Mfge8</i> genotype	4.2	0.021
Number of 129Sv alleles and <i>Mfge8</i> genotype		
Number of 129Sv alleles	6.3	0.016
<i>Mfge8</i> genotype	5.6	0.007
Number of Balb/C alleles and <i>Mfge8</i> genotype		
Number Balb/C alleles	0.6	0.44
<i>Mfge8</i> genotype	4.1	0.023
Number of B6/129Sv alleles and <i>Mfge8</i> genotype		
Number of B6/129Sv alleles	5.7	0.022
<i>Mfge8</i> genotype	5.3	0.009
Number of B6/Balb/C alleles and <i>Mfge8</i> genotype		
Number of B6/Balb/C alleles	0.3	0.61
<i>Mfge8</i> deficiency	4.2	0.022
Number of 129Sv/Balb/C alleles and <i>Mfge8</i> genotype		
Number of 129Sv/Balb/C alleles	0.1	0.81
<i>Mfge8</i> deficiency	4.2	0.022
Number of unknown alleles and <i>Mfge8</i> genotype		
Number of unknown alleles	0.9	0.34
<i>Mfge8</i> deficiency	3.5	0.039

Summary of results from analysis of covariance for incubation time with *Mfge8* genotype as factor and number of alleles corresponding to the various genetic backgrounds as covariates. The between-subjects factors are *Mfge8*^{+/+} ($n = 16$), *Mfge8*^{+/-} ($n = 14$), and *Mfge8*^{-/-} ($n = 16$). The dependent variable is incubation time. F-values correspond to (1,42) and (2,42) degrees of freedom for the covariates and the genotype, respectively.

by microglia. Because clearance of apoptotic bodies is inefficient in the absence of Mfge8, prions may persist in the brain and exacerbate PrP^{Sc} accumulation, thereby accelerating the disease.

Whereas the brain concentration of PrP^{Sc} was dramatically increased in the absence of Mfge8, prion infectivity titers were altered to a much smaller extent. Because prion titers are likely to reflect the number of individual PrP aggregates capable of nucleating further PrP, these findings suggest that the defective clearance caused by the absence of Mfge8 allows primarily for the elongation of PrP^{Sc} seeds rather than for their numerical expansion.

The aforementioned model implies a multitiered control of phagocytosis in the brain, whereby astrocytes are the source of Mfge8 and microglia are the executioners of phagocytosis. In this model, microglia would operate at highest efficiency only when armed by astrocyte-borne Mfge8. In the absence of the latter, removal of apoptotic cells, and of any prions that might be contained therein, would be impaired. We have discovered an analogous collaboration in germinal centers of lymphoid organs between FDCs and tingible body macrophages. There, FDCs produce Mfge8 and thereby license tingible body macrophages to engulf apoptotic cells (Kranich et al., 2008). In the CNS, an additional level of complexity may be added by the finding that astrocytes express markers of phagocytic pathways, including the Mfge8 receptor $\alpha_v\beta_5$ (Barres, 2008; Cahoy et al., 2008), and may have phagocytic potential of their own.

The regulation of phagocytosis is complex, and several independent, redundant pathways of phagocytosis are known. Mfge8 may not be the only mediator of engulfment, and some hitherto unidentified factors may, in certain situations, compensate for its absence. Strong evidence for the latter scenario comes from our observation that the acceleration of prion pathogenesis seen in *Mfge8*^{-/-} mice is crucially dependent on the genetic background of mice. Although the Mfge8 genotype was the major determinant of incubation time, one or more additional loci (potentially including the Mfge8 receptors) act as important modifiers. Because these loci appear to be polymorphic between the 129Sv and the C57BL/6 strains of mice, it may be possible to identify them through larger-scale analyses of prion pathogenesis in F₂ crosses between said mouse strains.

MATERIALS AND METHODS

Mice. *Mfge8*^{-/-} mice were donated by S. Nagata (Graduate School of Medicine, Kyoto University, Sakyo-ku, Kyoto, Japan) and were on a mixed (C57BL/6 × 129Sv)F₁ (Hanayama et al., 2004) or C57BL/6 background. B6.129.Balb/C-*Mfge8*^{-/-} mice were generated in our facility by intercrossing B6.129-*Mfge8*^{-/-} mice with Balb/C mice (Harlan Laboratories). As controls, C57BL/6 (Harlan Laboratories) or F₁ offspring of crossings between C57BL/6 and 129Sv mice (Charles River) were used. For microglia depletion experiments, *CD11b-HSVTK* mice were used (Heppner et al., 2005). All experiments were performed in accordance with Swiss federal legislation and were approved by the Veterinäramt des Kantons Zurich (Veterinary office of the Canton Zurich).

Inoculations. Mice were inoculated i.p. with 100 μ l of brain homogenate diluted in PBS with 5% BSA and containing 3 log LD₅₀ units of the Rocky Mountain Laboratories scrapie strain (passage 5 and 6, thus called RML5 and

RML6). For i.c. inoculations, 30 μ l of inoculum with 3 log LD₅₀ units was administered. Scrapie was diagnosed according to clinical criteria (ataxia, kyphosis, priapism, and hind leg paresis). Mice were sacrificed on the day of onset of terminal clinical signs of scrapie.

Histoblot, Western blot, ELISA, histology, TUNEL assay, and ISH.

Detection of splenic PrP^{Sc} accumulation by histoblot (Taraboulos et al., 1992), detection of PrP^C and PrP^{Sc} by Western blot (Lau et al., 2007), and quantitation of PrP^C by sandwich ELISA (Polymenidou et al., 2008) were performed as described previously.

Immunohistochemistry for SAF84 (1:200), GFAP (1:1,000), and IBA1 (1:1,000) was performed on paraffin sections and detected with diaminobenzidine (Sigma-Aldrich). Tissue was treated with formic acid to inactivate prion infectivity. Sections were incubated in Ventana buffer, and stains were performed on an immunohistochemistry robot (NEXEX; Ventana Instruments) using an IVIEW DAB Detection kit (Ventana Instruments).

TUNEL stainings were performed on cryosections with the ApopTaq Plus Fluorescein In Situ Apoptosis Detection kit (Millipore) according to the manufacturer's instructions. ISH using an *Mfge8* riboprobe was performed as described previously (Kranich et al., 2008). In selected experiments, slides were subsequently stained with IB4-Alexa Fluor 647 (Invitrogen) and DAPI (Sigma-Aldrich).

MPA. Brain homogenate was diluted in TBS with 0.1% Triton X-100 and subjected to immunoprecipitation using magnetic beads coupled to the peptoid PSR1 (Lau et al., 2007). Samples were incubated 1 h at 37°C under permanent agitation and then washed and denatured with 0.1 N NaOH. After neutralization (0.3 M Na₂H₂PO₄), samples were placed on a magnet, and supernatant was transferred to POM19 (Polymenidou et al., 2005)-coated ELISA plates. After incubation (1 h at 37°C), plates were washed, and POM2-AP (Polymenidou et al., 2005) was added. After incubation with substrate (enhance chemiluminescence; GE Healthcare), plates were read in a luminometry reader (Lumiscan Ascent; Thermo Fisher Scientific).

SCA. SCA was performed as described previously (Klöhn et al., 2003) with minor adaptations. Prion-susceptible neuroblastoma N2aPK1 cells were inoculated with *Mfge8*^{+/+} and *Mfge8*^{-/-} brain homogenate in 96-well plates for 3 d. Prion infectivity titers were determined after cells were split three times 1:3 and three times 1:10. For this, 25,000 cells from each well were filtered onto the membrane of an ELISPOT plate, treated with PK, and denatured. Individual infected (PrP^{Sc} positive) cells were detected by ELISA using the anti-PrP antibody POM1 (Polymenidou et al., 2005). The number of TCI units per aliquot was calculated from the proportion of negative to total wells using the Poisson equation.

Cell-enriched primary cultures. Mixed glia cultures were prepared from cerebra of pups (1–2 d postpartum) as previously described (Giulian and Baker, 1986). Purity of microglia was determined by staining with IB4 and was typically >95%. Purity of oligodendrocyte precursors and astrocytes was determined by NG2 and GFAP staining and was found to typically exceed 85% and 95%, respectively. Cerebellar granule neurons were cultured from 7-d-old mice as previously published (Leist et al., 1997). Cultures consisted of ~95% cerebellar granule neurons and <5% astrocytes, as determined by staining for β_{III} -tubulin and GFAP.

Quantitative RT-PCR. Total RNA from brain or cultured cells was isolated using TRIZOL (Invitrogen) and subjected to cDNA synthesis using QuantiTect Reverse Transcription kit (QIAGEN) according to the manufacturer's instruction. Quantitative real-time PCR was performed on a 7900HT Fast Real-Time PCR system (Applied Biosystems). Expression levels were normalized using *Gapdh* (glyceraldehyde-3-phosphate dehydrogenase).

Gapdh forward (5'-CCACCCAGCAAGGAGACT-3'), *Gapdh* reverse (5'-GAAATGTGAGGGAGATGCT-3'), *Mfge8* forward (5'-ATATGGGTTTCATGGGCTTG-3'), *Mfge8* reverse (5'-GAGGCTGTAAGCCACC-TTGA-3'), *Integrin* α_v forward (5'-CACCCAGAGTCAGAGATGGA-3'),

Integrin α_v reverse (5'-TGCCTTGCTGAATGAACTTG-3'), *Integrin β_3* forward (5'-TGACATCCGAGCAGGTGAAAG-3'), *Integrin β_3* reverse (5'-GAGTAGCAAGGCCAATGAGC-3'), *Integrin β_5* forward (5'-GGTTTCGGGTCTTTTGTGA-3'), *Integrin β_5* reverse (5'-CCGATCTTC-TCCTTGCAGAC-3'), *CD11b* forward (5'-CGGAAAGTAGTGAGAGAACTGTTTC-3'), *CD11b* reverse (5'-CTTATAATCCAAGGGATCACCGAATT-3'), *Gfap* forward (5'-CACGAACGAGTCCCTAGAGC-3'), *Gfap* reverse (5'-GAATGGTGATCGGGTTTCT-3'), and *Mbp* (available from GenBank/EMBL/DBJ under accession no. NM_010777) expression was detected using the commercially available QuantiTect primer assay (QIAGEN).

Organotypic slice cultures and microglia depletion. Organotypic cerebellar brain slices were prepared from 10–11-d-old pups, prion infected with 10^{-4} dilution of RML6 prions, and maintained according to previously published protocols (Falsig et al., 2008). 5 wk postinoculation, slices were harvested, and the PrP^{Sc} content of PK-treated samples was analyzed by Western blotting with anti-PrP antibody POM1. Microglia were depleted from organotypic brain slice cultures as previously described (Falsig et al., 2008).

STR analysis. Whole genome STR analysis was performed using fluorescently labeled primers (FAM, VIC, NED; all from Applied Biosystems; Table S1). Genomic DNA was amplified by PCR, denatured, and sequenced on a 3130xl sequencer (Applied Biosystems). Analysis, allele calling, binning, and calibration of various mouse strains were performed manually and in combination with an in-house-developed software.

Statistical analysis. Continuous data are presented as mean \pm SD and were compared between groups using the unpaired Student's *t* test. Incubation times were analyzed using the Kaplan-Meier method and compared between groups using the logrank test. The relation between incubation time and genetic background was analyzed using linear regression. The combined effect of *Mfge8* genotype and genetic background on incubation time was analyzed using analysis of covariance with *Mfge8* genotype as factor and the number of alleles corresponding to different genetic backgrounds as covariates. *P*-values <0.05 were considered statistically significant. SPSS 13 software (SPSS Inc.) was used for statistical analyses.

Online supplemental material. Fig. S1 shows PrP^{Sc} accumulation in spleen, PrP^C quantitation, and analysis of spongiosis. Fig. S2 shows that IB4⁺ microglia do not express *Mfge8*. Fig. S3 demonstrates that PrP^{Sc} levels and the amount of TUNEL⁺ apoptotic cells in the cerebellum of terminally sick mice are not changed between B6-*Mfge8*^{-/-} and B6-*Mfge8*^{+/+} mice. Fig. S4 depicts *Mfge8* and integrin expression levels in the brain, the correlation between the D11Mit128 allotype, and incubation time and *Igfb3* single nucleotide polymorphisms in mice of different genetic backgrounds. Table S1, included as a separate PDF file, shows an overview of primers used for STR analysis. Online supplemental material is available at <http://www.jem.org/cgi/content/full/jem.20092401/DC1>.

We thank Shigekazu Nagata for providing *Mfge8*^{-/-} mice, Burkhard Seifert for statistical analyses, and Mario Nuvolone, Caihong Zhu, Bei Li, Cristóbal Tostado, Mirzet Delic, Winfried Förderer, Marianne König, André Wethmar, and Norbert Wey for technical assistance.

The Aguzzi laboratory is supported by grants of the Ernst Jung Foundation, the Stammbach Foundation, the European Union (LUPAS, PRIORITY), the Swiss National Science Foundation, a Sinergia grant from the Swiss National Science Foundation, and the National Center of Competence in Research on Neural Plasticity and Repair. A. Aguzzi is a recipient of an Advanced Grant of the European Research Council.

The authors have no conflicting financial interests.

Submitted: 9 November 2009

Accepted: 11 August 2010

REFERENCES

- Aguzzi, A. 2003. Prions and the immune system: a journey through gut, spleen, and nerves. *Adv. Immunol.* 81:123–171. doi:10.1016/S0065-2776(03)81004-0
- Aguzzi, A. 2006. Prion diseases of humans and farm animals: epidemiology, genetics, and pathogenesis. *J. Neurochem.* 97:1726–1739. doi:10.1111/j.1471-4159.2006.03909.x
- Aguzzi, A., and M. Heikenwalder. 2005. Prions, cytokines, and chemokines: a meeting in lymphoid organs. *Immunity.* 22:145–154. doi:10.1016/j.immuni.2004.12.007
- Ashok, A., and R.S. Hegde. 2006. Prions and retroviruses: an endosomal rendezvous? *EMBO Rep.* 7:685–687. doi:10.1038/sj.embor.7400749
- Barres, B.A. 2008. The mystery and magic of glia: a perspective on their roles in health and disease. *Neuron.* 60:430–440. doi:10.1016/j.neuron.2008.10.013
- Boddaert, J., K. Kinugawa, J.C. Lambert, F. Boukhtouche, J. Zoll, R. Merval, O. Blanc-Brude, D. Mann, C. Berr, J. Vilar, et al. 2007. Evidence of a role for lactadherin in Alzheimer's disease. *Am. J. Pathol.* 170:921–929. doi:10.2353/ajpath.2007.060664
- Brandner, S., S. Isenmann, A. Raeber, M. Fischer, A. Sailer, Y. Kobayashi, S. Marino, C. Weissmann, and A. Aguzzi. 1996. Normal host prion protein necessary for scrapie-induced neurotoxicity. *Nature.* 379:339–343. doi:10.1038/379339a0
- Büeler, H., A. Raeber, A. Sailer, M. Fischer, A. Aguzzi, and C. Weissmann. 1994. High prion and PrP^{Sc} levels but delayed onset of disease in scrapie-inoculated mice heterozygous for a disrupted PrP gene. *Mol. Med.* 1:19–30.
- Cahoy, J.D., B. Emery, A. Kaushal, L.C. Foo, J.L. Zamanian, K.S. Christopherson, Y. Xing, J.L. Lubischer, P.A. Krieg, S.A. Krupenko, et al. 2008. A transcriptome database for astrocytes, neurons, and oligodendrocytes: a new resource for understanding brain development and function. *J. Neurosci.* 28:264–278. doi:10.1523/JNEUROSCI.4178-07.2008
- Chesebro, B., M. Trifilo, R. Race, K. Meade-White, C. Teng, R. LaCasse, L. Raymond, C. Favara, G. Baron, S. Priola, et al. 2005. Anchorless prion protein results in infectious amyloid disease without clinical scrapie. *Science.* 308:1435–1439. doi:10.1126/science.1110837
- Falsig, J., C. Julius, I. Margalith, P. Schwarz, F.L. Heppner, and A. Aguzzi. 2008. A versatile prion replication assay in organotypic brain slices. *Nat. Neurosci.* 11:109–117. doi:10.1038/nn2028
- Fischer, M., T. Rüllicke, A. Raeber, A. Sailer, M. Moser, B. Oesch, S. Brandner, A. Aguzzi, and C. Weissmann. 1996. Prion protein (PrP) with amino-proximal deletions restoring susceptibility of PrP knockout mice to scrapie. *EMBO J.* 15:1255–1264.
- Fuller, A.D., and L.J. Van Eldik. 2008. MFG-E8 regulates microglial phagocytosis of apoptotic neurons. *J. Neuroimmune Pharmacol.* 3:246–256. doi:10.1007/s11481-008-9118-2
- Giulian, D., and T.J. Baker. 1986. Characterization of ameboid microglia isolated from developing mammalian brain. *J. Neurosci.* 6:2163–2178.
- Hanayama, R., and S. Nagata. 2005. Impaired involution of mammary glands in the absence of milk fat globule EGF factor 8. *Proc. Natl. Acad. Sci. USA.* 102:16886–16891. doi:10.1073/pnas.0508599102
- Hanayama, R., M. Tanaka, K. Miwa, A. Shinohara, A. Iwamatsu, and S. Nagata. 2002. Identification of a factor that links apoptotic cells to phagocytes. *Nature.* 417:182–187. doi:10.1038/417182a
- Hanayama, R., M. Tanaka, K. Miyasaka, K. Aozasa, M. Koike, Y. Uchiyama, and S. Nagata. 2004. Autoimmune disease and impaired uptake of apoptotic cells in MFG-E8-deficient mice. *Science.* 304:1147–1150. doi:10.1126/science.1094359
- Heppner, F.L., M. Greter, D. Marino, J. Falsig, G. Raivich, N. Hövelmeyer, A. Waisman, T. Rüllicke, M. Prinz, J. Priller, et al. 2005. Experimental autoimmune encephalomyelitis repressed by microglial paralysis. *Nat. Med.* 11:146–152. doi:10.1038/nm1177
- Klein, M.A., P.S. Kaeser, P. Schwarz, H. Weyd, I. Xenarios, R.M. Zinkernagel, M.C. Carroll, J.S. Verbeek, M. Botto, M.J. Walport, et al. 2001. Complement facilitates early prion pathogenesis. *Nat. Med.* 7:488–492. doi:10.1038/86567
- Klöhn, P.C., L. Stoltze, E. Flechsig, M. Enari, and C. Weissmann. 2003. A quantitative, highly sensitive cell-based infectivity assay for mouse

- scrapie prions. *Proc. Natl. Acad. Sci. USA*. 100:11666–11671. doi:10.1073/pnas.1834432100
- Kranich, J., N.J. Krautler, E. Heinen, M. Polymenidou, C. Bridel, A. Schildknecht, C. Huber, M.H. Kosco-Vilbois, R. Zinkernagel, G. Miele, and A. Aguzzi. 2008. Follicular dendritic cells control engulfment of apoptotic bodies by secreting Mfge8. *J. Exp. Med.* 205:1293–1302. doi:10.1084/jem.20071019
- LaCasse, R.A., J.F. Striebel, C. Favara, L. Kercher, and B. Chesebro. 2008. Role of Erk1/2 activation in prion disease pathogenesis: absence of CCR1 leads to increased Erk1/2 activation and accelerated disease progression. *J. Neuroimmunol.* 196:16–26. doi:10.1016/j.jneuroim.2008.02.009
- Lau, A.L., A.Y. Yam, M.M. Michelitsch, X. Wang, C. Gao, R.J. Goodson, R. Shimizu, G. Timoteo, J. Hall, A. Medina-Selby, et al. 2007. Characterization of prion protein (PrP)-derived peptides that discriminate full-length PrPSc from PrPC. *Proc. Natl. Acad. Sci. USA*. 104:11551–11556. doi:10.1073/pnas.0704260104
- Leblanc, P., S. Alais, I. Porto-Carreiro, S. Lehmann, J. Grassi, G. Raposo, and J.L. Darlix. 2006. Retrovirus infection strongly enhances scrapie infectivity release in cell culture. *EMBO J.* 25:2674–2685. doi:10.1038/sj.emboj.7601162
- Leist, M., C. Volbracht, S. Kühnle, E. Fava, E. Ferrando-May, and P. Nicotera. 1997. Caspase-mediated apoptosis in neuronal excitotoxicity triggered by nitric oxide. *Mol. Med.* 3:750–764.
- Liberski, P.P., B. Sikorska, J. Bratosiewicz-Wasik, D.C. Gajdusek, and P. Brown. 2004. Neuronal cell death in transmissible spongiform encephalopathies (prion diseases) revisited: from apoptosis to autophagy. *Int. J. Biochem. Cell Biol.* 36:2473–2490. doi:10.1016/j.biocel.2004.04.016
- Mabbott, N.A., C.F. Farquhar, K.L. Brown, and M.E. Bruce. 1998. Involvement of the immune system in TSE pathogenesis. *Immunol. Today*. 19:201–203. doi:10.1016/S0167-5699(98)01253-5
- Mabbott, N.A., M.E. Bruce, M. Botto, M.J. Walport, and M.B. Pepys. 2001. Temporary depletion of complement component C3 or genetic deficiency of C1q significantly delays onset of scrapie. *Nat. Med.* 7:485–487. doi:10.1038/86562
- Mallucci, G., A. Dickinson, J. Linehan, P.C. Klöhn, S. Brandner, and J. Collinge. 2003. Depleting neuronal PrP in prion infection prevents disease and reverses spongiosis. *Science*. 302:871–874. doi:10.1126/science.1090187
- Montrasio, F., R. Frigg, M. Glatzel, M.A. Klein, F. Mackay, A. Aguzzi, and C. Weissmann. 2000. Impaired prion replication in spleens of mice lacking functional follicular dendritic cells. *Science*. 288:1257–1259. doi:10.1126/science.288.5469.1257
- Patton, S., and T.W. Keenan. 1975. The milk fat globule membrane. *Biochim. Biophys. Acta*. 415:273–309.
- Polymenidou, M., K. Stoeck, M. Glatzel, M. Vey, A. Bellon, and A. Aguzzi. 2005. Coexistence of multiple PrPSc types in individuals with Creutzfeldt-Jakob disease. *Lancet Neurol.* 4:805–814. doi:10.1016/S1474-4422(05)70225-8
- Polymenidou, M., R. Moos, M. Scott, C. Sigurdson, Y.Z. Shi, B. Yajima, I. Hafner-Bratkovic, R. Jerala, S. Hornemann, K. Wuthrich, et al. 2008. The POM monoclonals: a comprehensive set of antibodies to non-overlapping prion protein epitopes. *PLoS One*. 3:e3872. doi:10.1371/journal.pone.0003872
- Prusiner, S.B. 1982. Novel proteinaceous infectious particles cause scrapie. *Science*. 216:136–144. doi:10.1126/science.6801762
- Prusiner, S.B., M.P. McKinley, K.A. Bowman, D.C. Bolton, P.E. Bendheim, D.F. Groth, and G.G. Glenner. 1983. Scrapie prions aggregate to form amyloid-like birefringent rods. *Cell*. 35:349–358. doi:10.1016/0092-8674(83)90168-X
- Spinner, D.S., I.S. Cho, S.Y. Park, J.I. Kim, H.C. Meeker, X. Ye, G. Lafauci, D.J. Kerr, M.J. Flory, B.S. Kim, et al. 2008. Accelerated prion disease pathogenesis in Toll-like receptor 4 signaling-mutant mice. *J. Virol.* 82:10701–10708. doi:10.1128/JVI.00522-08
- Steele, A.D., O.D. King, W.S. Jackson, C.A. Hetz, A.W. Borkowski, P. Thielen, R. Wollmann, and S. Lindquist. 2007. Diminishing apoptosis by deletion of Bax or overexpression of Bcl-2 does not protect against infectious prion toxicity in vivo. *J. Neurosci.* 27:13022–13027. doi:10.1523/JNEUROSCI.3290-07.2007
- Taraboulos, A., K. Jendroska, D. Serban, S.L. Yang, S.J. DeArmond, and S.B. Prusiner. 1992. Regional mapping of prion proteins in brain. *Proc. Natl. Acad. Sci. USA*. 89:7620–7624. doi:10.1073/pnas.89.16.7620
- Théry, C., M. Ostrowski, and E. Segura. 2009. Membrane vesicles as conveyors of immune responses. *Nat. Rev. Immunol.* 9:581–593. doi:10.1038/nri2567
- Weissmann, C. 2004. The state of the prion. *Nat. Rev. Microbiol.* 2:861–871. doi:10.1038/nrmicro1025

9.3 *In vivo* identification of apoptotic and extracellular vesicle-bound live cells using image-based deep learning.

Kranich J*, **, Chlis NK*, Rausch L, Latha A, Schifferer M, Kurz T, Foltyn-Arfa Kia A, Simons M, Theis FJ**, Brocker T**. J Extracell Vesicles. 2020 Jul 16;9(1):1792683. * equally contributed first author, ** corresponding author.

Binding of phosphatidylserine-positive microparticles by PBMCs classifies disease severity in COVID-19 patients

Lisa Rausch¹ | Konstantin Lutz¹ | Martina Schifferer^{2,3} | Elena Winheim¹ |
 Rudi Gruber⁴ | Elina F. Oesterhaus^{5,6} | Linus Rinke¹ | Johannes C. Hellmuth^{5,7} |
 Clemens Scherer^{5,8} | Maximilian Muenchhoff^{5,6,9} | Christopher Mandel^{5,10} |
 Michael Bergwelt-Baildon^{5,7} | Mikael Simons^{2,3,11} | Tobias Straub¹² | Anne B. Krug¹ |
 Jan Kranich¹  | Thomas Brocker¹ 

¹ Institute for Immunology, Biomedical Center (BMC), Faculty of Medicine, LMU Munich, Munich, Germany

² German Center for Neurodegenerative Diseases (DZNE), Munich, Germany

³ Munich Cluster of Systems Neurology (Synergy), Munich, Germany

⁴ bene pharmaChem GmbH & Co.KG., Geretsried, Germany

⁵ COVID-19 Registry of the LMU Munich (CORKUM), University Hospital, LMU Munich, Munich, Germany

⁶ Max von Pettenkofer Institute & Gene Center, Virology, National Reference Center for Retroviruses, LMU München, Munich, Germany

⁷ Department of Medicine III, University Hospital, LMU Munich, Munich, Germany

⁸ Department of Medicine I, University Hospital, LMU Munich, Munich, Germany

⁹ German Center for Infection Research (DZIF), partner site Munich, Germany

¹⁰ Department of Medicine IV, University Hospital, LMU Munich, Munich, Germany

¹¹ Institute of Neuronal Cell Biology, Technical University of Munich, Munich, Germany

¹² Core facility Bioinformatics, Biomedical Center (BMC), Faculty of Medicine, LMU Munich, Munich, Germany

Correspondence

Prof. Dr. Thomas Brocker, Institute for Immunology, Biomedical Center (BMC), Faculty of Medicine, LMU Munich, Großhaderner Str. 9, D-82152 Planegg-Martinsried, Germany.
 Email: brocker@lmu.de

Jan Kranich and Thomas Brocker shared senior authorship.

Funding information

Deutsche Forschungsgemeinschaft (DFG, German Research Foundation), Grant/Award Numbers: Project-ID 210592381 - SFB 1054: TP B03, A06, Project-ID 369799452 - SFB/TR237: TP B14, Project-ID 391217598 - KR2199/10-1; Bavarian State Ministry of Science and the Arts

Abstract

Infection with SARS-CoV-2 is associated with thromboinflammation, involving thrombotic and inflammatory responses, in many COVID-19 patients. In addition, immune dysfunction occurs in patients characterised by T cell exhaustion and severe lymphopenia. We investigated the distribution of phosphatidylserine (PS), a marker of dying cells, activated platelets and platelet-derived microparticles (PMP), during the clinical course of COVID-19. We found an unexpectedly high amount of blood cells loaded with PS⁺ PMPs for weeks after the initial COVID-19 diagnosis. Elevated frequencies of PS⁺ PMP⁺ PBMCs correlated strongly with increasing disease severity. As a marker, PS outperformed established laboratory markers for inflammation, leucocyte composition and coagulation, currently used for COVID-19 clinical scoring. PS⁺ PMPs preferentially bound to CD8⁺ T cells with gene expression signatures of proliferating effector rather than memory T cells. As PS⁺ PMPs carried programmed death-ligand 1 (PD-L1), they may affect T cell expansion or function. Our data provide a novel marker for disease severity and show that PS, which can trigger the blood coagulation cascade, the complement system, and inflammation, resides

This is an open access article under the terms of the [Creative Commons Attribution-NonCommercial-NoDerivs License](https://creativecommons.org/licenses/by-nc-nd/4.0/), which permits use and distribution in any medium, provided the original work is properly cited, the use is non-commercial and no modifications or adaptations are made.

© 2021 The Authors. *Journal of Extracellular Vesicles* published by Wiley Periodicals, LLC on behalf of the International Society for Extracellular Vesicles

on activated immune cells. Therefore, PS may serve as a beacon to attract thromboinflammatory processes towards lymphocytes and cause immune dysfunction in COVID-19.

KEYWORDS

apoptosis, CD8⁺ T cells, COVID-19, lymphopenia, phosphatidylserine, platelet-derived microparticle, SARS-CoV-2, thromboinflammation

1 | INTRODUCTION

The recently emerged human pathogenic severe acute respiratory syndrome coronavirus 2 (SARS-CoV-2) causes various clinical syndromes, summarised under coronavirus disease-2019 (COVID-19). The excessive inflammatory response associated with COVID-19 can cause severe complications such as acute respiratory distress syndrome, septic shock and multi-organ failure (Guan et al., 2020; MacLaren et al., 2020; Wölfel et al., 2020). A significant cause of morbidity and mortality in COVID-19 patients is 'thromboinflammation'. Although not fully understood, inflammation through complement activation and cytokine release, platelet overactivity and apoptosis (thrombocytopenia), as well as coagulation abnormalities (coagulopathy) play critical roles in this complex clinical picture (reviewed in Gu et al. (2021)).

Similar vascular complications occur in the antiphospholipid syndrome, where autoantibodies target phosphatidylserine (PS)/prothrombin complexes (Corban et al., 2017). This syndrome may manifest itself in COVID-19 patients (Zhang et al., 2020), linking PS to thromboinflammation. PS is a plasma membrane component actively retained by an ATP-requiring process at the inner membrane surface in living cells. PS retention stops, for example, during cell death or when cells release PS-containing microparticles or enveloped viruses. Then PS relocates to the outer layer of the cell membrane, where it can interact with extracellular proteins, including coagulation and complement systems. PS activates the alternative and the classical complement pathways (Mevorach et al., 1998; Tan et al., 2010; Wang et al., 1993) by binding to complement C3 (Huong et al., 2001), C3bi (Mevorach et al., 1998) and C1q (Païdassi et al., 2008). Activated platelets release platelet-derived microparticles (PMPs), which cause thrombin formation, coagulation, activation of the complement system, and inflammation in a PS-dependent manner (Melki et al., 2017; Owens & Mackman, 2011; Ridger et al., 2017).

Patients with severe COVID-19 also show striking immune dysregulation, the reasons for which are not entirely understood. A direct correlation between blood clotting components and the immune response exists (Su et al., 2020). Various immune abnormalities such as increased inflammatory cytokines (Del Valle et al., 2020), immune cell exhaustion (Zheng et al., 2020) and general lymphopenia (Cao, 2020; Chen et al., 2020; Huang et al., 2020; Liu et al., 2020; Yang et al., 2020,) correlate with disease severity (Mathew et al., 2020). T cell lymphopenia (Laing et al., 2020), probably caused by excessive apoptotic T cell death similar to sepsis (Hotchkiss & Nicholson, 2006), is of particular relevance as SARS-CoV-2-specific T cell responses control and resolve the primary infection (Liao et al., 2020; Rydzynski Moderbacher et al., 2020; Sekine et al., 2020; Zhou et al., 2020). In fatal COVID-19, the adaptive immune response starts too late (reviewed in Sette and Crotty (2021)), while its rapid onset would be highly beneficial (Braun et al., 2020; Rydzynski Moderbacher et al., 2020; Tan et al., 2020). However, the reasons and precise mechanisms for adaptive immune disturbance, lymphopenia and thromboinflammation in COVID-19 remain poorly defined.

To investigate these aspects of COVID-19 in more detail, we interrogated PBMC of 54 patients from the COVID-19 Registry of the LMU Munich (CORKUM) and 35 healthy and 12 recovered donors between April 2020 and February 2021. We performed image flow cytometry (IFC) and image analysis by deep learning algorithms (Kranich et al., 2020) using highly sensitive reagents specific for PS (Kranich et al., 2020; Trautz et al., 2017). COVID-19 blood samples contained abnormally high numbers of PS⁺ peripheral blood mononuclear cells (PBMC). Although PS is a marker for dying cells, nearly all PS⁺ cells were living cells associated with PS⁺CD41⁺ PMPs or larger PS⁺CD41⁺ platelet fragments. The grade of PS⁺ PMP-associated PBMC correlated with lymphopenia and disease severity, showing a higher correlation than commonly used laboratory diagnostic markers such as IL-6, D-Dimer (Mathew et al., 2020) and C-reactive protein (CRP) (Li et al., 2020). PS⁺ PMPs were strongly associated with dividing effector CD8⁺ T cells with upregulated expression of cell-cycle genes. Fractions of T cell-associated PS⁺ PMPs carried CD274 (PD-L1), which could impact the survival of T cells and potentially contribute to functional inhibition and lymphopenia. As PS⁺ PMPs remained associated with PBMC several weeks after the initial SARS-CoV2-diagnosis, they might sustain the adverse inflammatory and prothrombotic effects over a long time and contribute to the complex clinical picture of thromboinflammation (reviewed in (Gu et al., 2021; Lind, 2021)). Together, our findings reveal an extensive association of PS⁺ PMPs with lymphocytes as a novel marker to classify COVID-19 disease severity and a potentially relevant contributor to thromboinflammation and lymphocyte dysfunction.

2 | RESULTS

2.1 | PBMC from COVID-19 patients show substantial PS surface exposure

To test if immune cell death rates were elevated during COVID-19, we analysed peripheral blood mononuclear cells (PBMC) of COVID-19 patients and compared them to those from healthy and recovered donors. Table S1 show clinical metadata for our cohort of COVID-19 patients and control groups. One hallmark of apoptotic cell death is the PS exposure on the outer membrane surface of cells. To reveal PS on PBMC, we utilised recombinant Milk fat globule-EGF factor 8 protein (MFG-E8) derived recombinant proteins, which bind PS under physiological conditions with high sensitivity on apoptotic cells and subcellular PS⁺ extracellular vesicles (EVs) (Kranich et al., 2020; Trautz et al., 2017). Flow cytometry results showed that the frequencies of PS⁺ cells in blood from all COVID-19 patients were significantly higher than in PBMC from healthy or recovered donors (Figure 1a). To analyse if this data can classify patients according to disease severity, we employed the World Health Organization's (WHO) eight-point ordinal scale for COVID-19 trial endpoints (WorldHealthOrganization, 2020) (Figure 1b). In our patient cohort, the scores WHO 2 and WHO 7 were absent. We combined WHO scores into 'mild' (WHO 1–3), 'moderate' (WHO 4) and 'severe' (WHO 5–8) groups for the subsequent analyses. Additionally, we also included a group of healthy donors (HD, $n = 30$) and recovered patients ($n = 12$, >69 days post 1st SARS-CoV-2⁺ diagnosis by PCR, either never hospitalised or released from the hospital with WHO score 1–2). The frequencies of PS⁺ PBMC increased with severity of COVID-19 disease in the following order: healthy controls (WHO 0) < recovered patients < WHO 1–3 (mild) < WHO 4 (moderate) < WHO 5–8 (severe) (Figure 1c). In severely diseased patients, 30%–90% of all PBMC were PS⁺ (Figure 1c). Accordingly, the individual WHO scores positively correlated with high significance with the frequencies of PS⁺ PBMC of COVID-19 patients. Importantly, the correlation of PS⁺ PBMC against WHO_{max} was much stronger than against the WHO score at sampling time (Figure S1A and 1d).

In order to assess whether the frequency of PS⁺ PBMCs is an independent predictor for a severe disease outcome such as ventilation requirement (Figure 1e) or death (Figure 1f) within our cohort, we performed an area under the receiver operating characteristic curve (AUROC) analysis. Frequency of PS⁺ PBMC was better for predicting ventilation requirement (AUC 0.760, threshold 41.15, specificity 0.53, sensitivity 0.91; Figure 1e) and death (AUC 0.907, threshold 43.525, specificity 0.90, sensitivity 0.83; Figure 1f) than C-reactive protein (CRP), D-Dimer, Ferritin, Fibrinogen, international normalised ratio (INR), partial thromboplastin time (PTT) or number of platelets (Figure S1B and C). Only IL-6 had better prediction scores for ventilation requirement (AUC 0.841, threshold 19.975, specificity 0.71, sensitivity 0.87; Figure 1b) and death (AUC 0.949, threshold 45.05, specificity 0.80, sensitivity 1; Figure S1C). Kaplan-Meier curves show that patients with a frequency of PS⁺ PBMCs higher than 41.15% or 43.53% had a higher incidence of requiring ventilation or succumbing to disease, respectively (Figure 1e). However, our study was an exploratory study with a limited number of patients. Therefore, the predictive capacity of the frequency of PS⁺ PBMCs needs to be validated in a larger cohort.

The blood sampling time points differed within our patient cohort due to organisational reasons. We investigated whether the sampling time point would affect the results and performed PS measurements at several time points for selected patients. These data show that although the frequencies of PS⁺ PBMCs show some variability, we detected strongly elevated levels for up to 30 days (Figure 2A). In contrast, in recovered patients, PS⁺ PBMC returned to the levels of healthy controls. To further assess the influence of sampling time and PS⁺ PBMC frequency, we performed a Spearman correlation test with time since the first diagnosis (FD) or time since symptom onset and found no correlation with PS⁺ PBMC frequencies (Figure S2B). Furthermore, there was also no correlation between the frequency of PS⁺ PBMC and age in healthy donors or recovered patients (Figure S2C).

In summary, the number of PS⁺ PBMC in the blood of COVID-19 patients represents a new parameter that correlates strongly with disease severity.

2.2 | PBMC in COVID-19 patients are associated with PS⁺ EVs, and the amount correlates with the severity of the disease

PS exposure occurs on various cells and cell-derived microparticles, including tumour cells, erythrocytes, neutrophils, monocytes, endothelial cells, activated platelets and PMPs. PS-exposure is a significant regulator of the blood coagulation system (reviewed in Connor et al. (2010)). We have recently shown that most PS⁺ cells in the spleen of virus-infected mice are not dying, but cells carried PS⁺ EVs (Kranich et al., 2020). To determine whether PS⁺ PBMC in COVID-19 patients were apoptotic cells contributing to the described lymphopenia or EV⁺ cells, we analysed the images of PS⁺ PBMC acquired by IFC. Some cells showed almost entirely PS⁺ cell bodies with strongly labeled apoptotic blebs, typical for cell death (Figure 2a). These cells still have an intact cell membrane since they did not stain with the live/dead dye used to exclude necrotic cells from the analysis. However, we also detected many cells with the characteristic round brightfield image morphology of living cells, with only one or a few intensely PS⁺ structures of subcellular size (Figure 2a). These particles resembled cell-associated PS⁺ EVs, which we recently identified in virus-infected mice (Kranich et al., 2020). We next used a machine learning-based convolutional

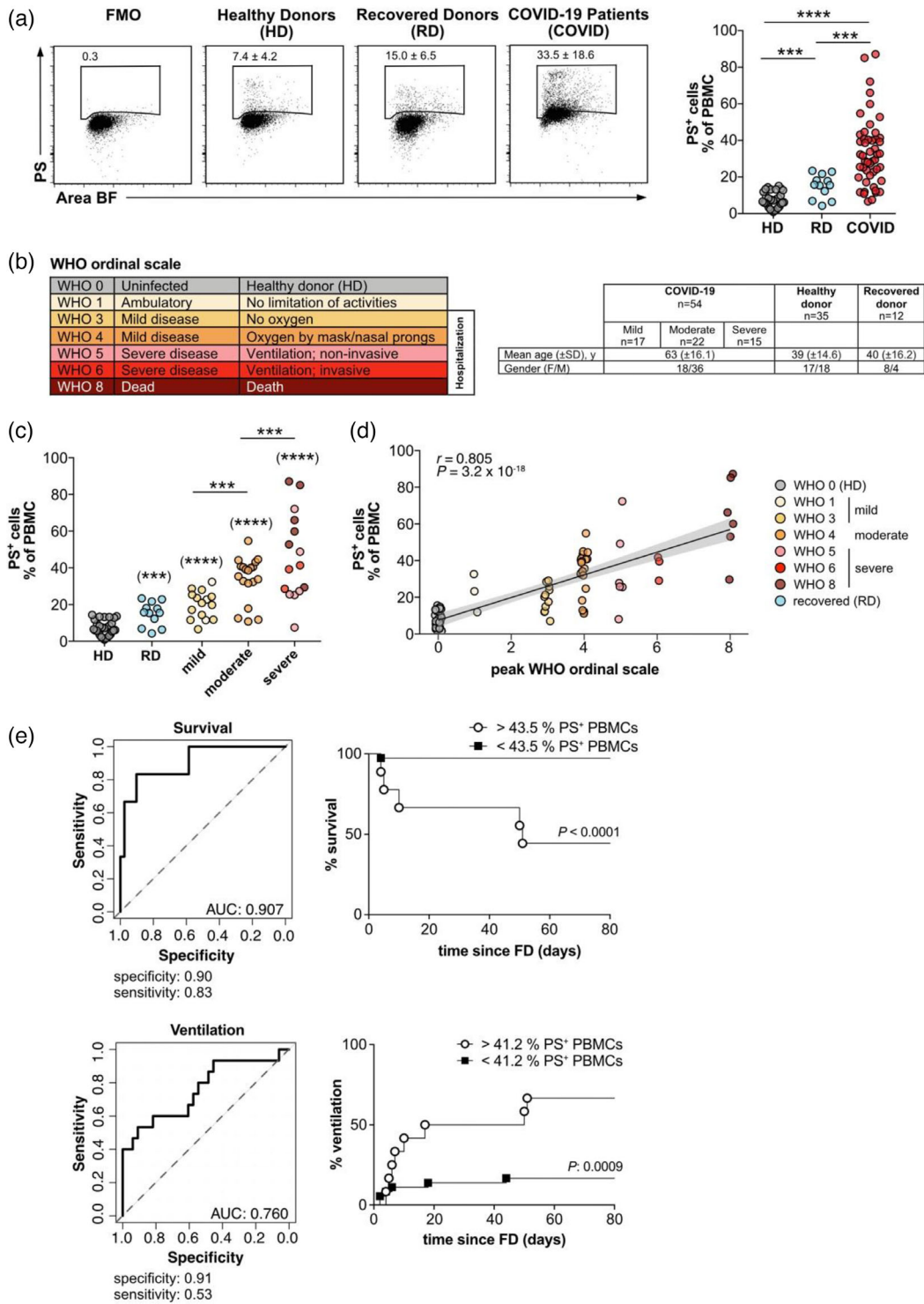


FIGURE 1 The frequencies of PS⁺ PBMC from COVID patients correlates with disease severity. (a) PBMC from COVID-19 patients (COVID), healthy donors (HD) and recovered donors (RD) were stained for PS and analysed by flow cytometry. Numbers in dot plots correspond to the percentage of PS⁺ cells in the gate shown. The right-hand graph shows the summary of all percentages. (b) Overview of WHO ordinal scale and colour code used. Table shows the number, age and gender of the different study groups. (c) Grouped analysis of the data from (a). (d) Same as (c), but plotted against the WHO ordinal scale ($n = 38-79$). PS⁺ PBMCs correlate with the severity of the disease. The plot shows the Spearman correlation test and linear regression line with 95% confidence interval shading (A, C, D: HD, $n = 30$; RD, $n = 12$; COVID, $n = 49$). Significance in (a) and (c) was determined by Mann-Whitney test: * $p < 0.05$, ** $p < 0.01$, *** $p < 0.001$ and **** $p < 0.0001$. Asterisks in brackets show statistically significant differences as compared to HD. FMO: Fluorescence minus one control; Area BF: Area bright field. (e) ROC curve analysis of PS⁺ PBMCs from COVID-19 patients ($n = 49$) for predicting survival (upper plot) and ventilation (lower plot). AUC values (95% CI) (left hand panels) and Kaplan-Meier survival and ventilation curves of patients grouped according to the indicated PS⁺ PBMCs-thresholds (right hand panels) are shown. Time represents the number of days from first diagnosis (FD). Optimal cut-off values for % PS⁺ PBMCs were determined by ROC analysis and used to define the two groups. First measured values of % PS⁺ PBMCs were used for analysis. Significance was determined by Log-rank test

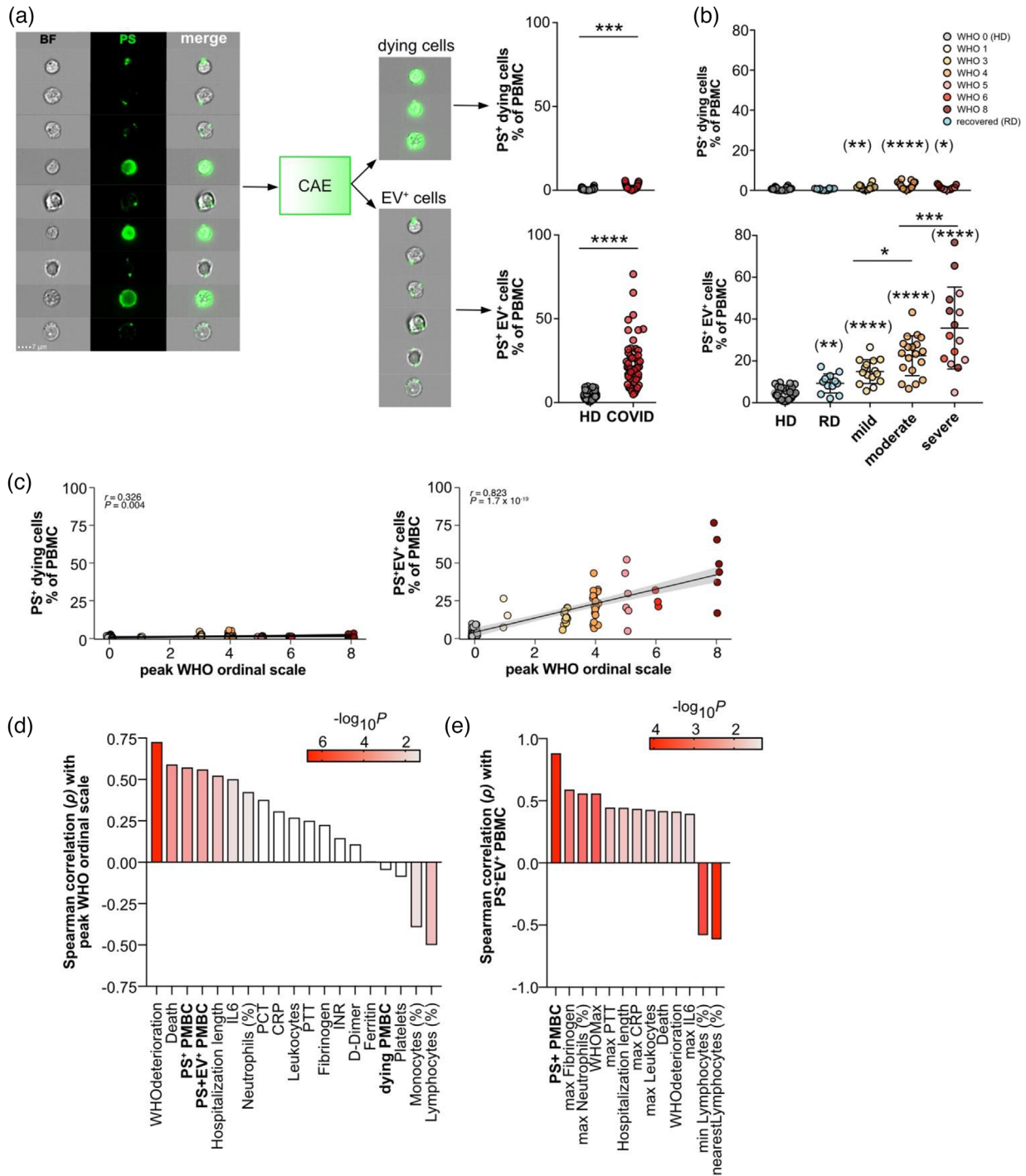


FIGURE 2 EV⁺ cells, but not dying cells from COVID-19 patients correlate with disease severity. (a) PBMC from healthy donors (HD, *n* = 30) and COVID (*n* = 49) were analysed by imaging flow cytometry (IFC). To discriminate dying and EV⁺ cells, PBMC were analysed using IDEAS, CAE and FlowJo. PS⁺ cells were gated, and their TIF images (16-bit, raw) exported using the IDEAS software. CAE results with the classification dying/EV⁺ were re-imported into IDEAS, and separate FCS files containing all cells or only PS⁺/dying cells and PS⁺/EV⁺ cells were generated for further analysis in FlowJo. Dying (a, upper panel) and EV⁺ (a, lower panel) cells are shown as % of PBMC. (b) Results from a) are plotted against groups HD (*n* = 30), RD (*n* = 12), mild (*n* = 15), moderate (*n* = 19) and severe disease (*n* = 15) for dying cells (upper panel) and EV⁺ cells (lower panel). (c) Plotting of the data from (b) against WHO ordinal scale. The plot shows the Spearman correlation test and linear regression line with 95% confidence interval shading (*n* = 38–79). (d) Summary of correlations of selected ‘nearest’ (*n* = 23–49) laboratory and clinical parameters with peak WHO ordinal scale or and selected (e) our measurements of PS⁺, PS⁺EV⁺ and dying cells (bold) (*n* = 23–49). Significance was determined by Mann-Whitney test: **p* < 0.05, ***p* < 0.01, ****p* < 0.001 and *****p* < 0.0001. Asterisks in brackets show statistically significant differences as compared to HD

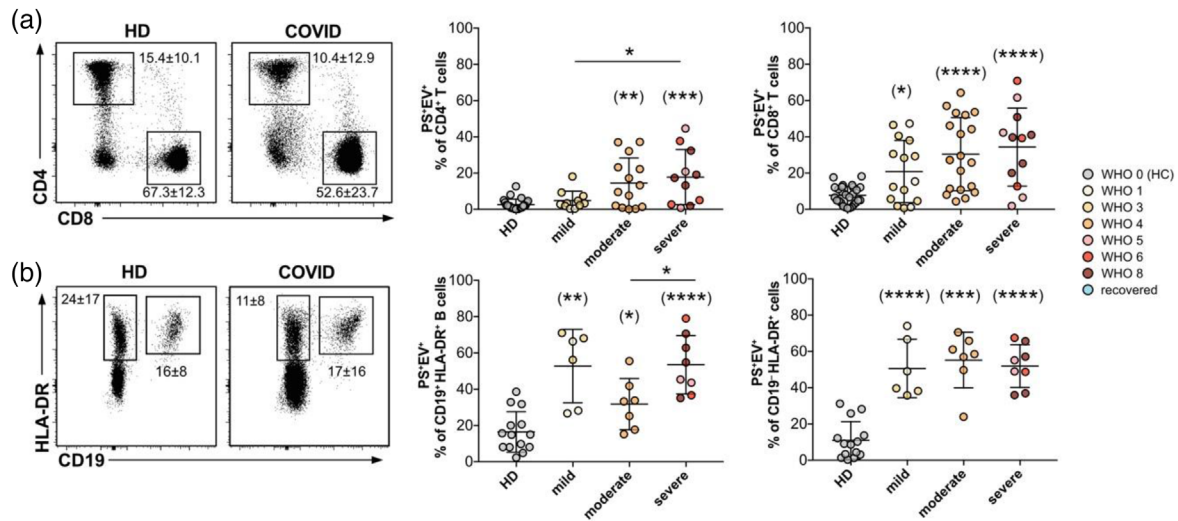


FIGURE 3 Identification of EV⁺ cells in PBMC from COVID-patients and healthy donors. PBMC were analysed by IFC (gating strategy shown in Figure S3A and B). PS⁺ CD4⁺ and CD8⁺ T cells (a) and CD19⁺ HLA-DR⁺ B cells and CD19-HLA-DR⁺ cells (containing mainly dendritic cells, monocytes) (b) were classified as PS⁺EV⁺ using the CAE and their total frequencies were plotted against HD (B, $n = 14$; A, CD4, $n = 24$; a, CD8, $n = 27$), mild (b, $n = 6$; A, CD4, $n = 11$; A, CD8, $n = 15$), moderate (B, $n = 7$; a, CD4, $n = 14$; A, CD8, $n = 19$), severe (b, $n = 8$; a, CD4, $n = 11$; a, CD8, $n = 12$) disease groups. Numbers next to the gates show the mean percentage \pm SD of all cells depicted inside the dot plot that lie within the respective gate, while the graphs show the average frequency \pm SD of EV⁺ cells within the analysed subpopulation. Significance was determined by Mann-Whitney test: * $p < 0.05$, ** $p < 0.01$, *** $p < 0.001$ and **** $p < 0.0001$. Asterisks in brackets show statistically significant differences as compared to HD

autoencoder (CAE) to group PBMC into bona fide PS⁺ dying cells or cells associated with PS⁺ EVs (Figure 2a), as previously validated (Kranich et al., 2020). After training with pre-defined images of PS⁺ dying or PS⁺ EV-associated cells, the CAE algorithm digitally sorts PS⁺ cells into both categories with high precision (Figure 2a). When we analysed the CAE-classified PS⁺ dying cells and PS⁺EV⁺ cells separately (Figure 2a), we found that the majority of PS⁺ PBMC contained live cells associated with PS⁺ EV-like structures rather than PS⁺ dying cells (Figure 2b). Despite the rarity of dying cells, patients with the score WHO 4 showed the highest frequencies (Figure 2b, upper panel). Furthermore, only PS⁺EV⁺ PBMC, not PS⁺ dying cells, classified the patients into disease score groups 'mild' (WHO 1–3), 'moderate' (WHO 4), and 'severe' (WHO 5–8) and separated them clearly from HD and recovered patients (Figure 2b, lower panel). Similarly, PS⁺EV⁺ PBMC, but not PS⁺ dying cells, showed a highly significant correlation with WHO scores (Figure 2c). Several laboratory values that are either increased (leukocytes, IL-6, neutrophils, procalcitonin (PCT), C-reactive protein (CRP), partial thromboplastin time (PTT), D-dimer, etc.) or decreased (lymphocytes) were shown to indicate an unfavorable progression of COVID-19 disease (Lippi & Plebani, 2020).

We confirmed these correlations in our patient cohort (Figure S4A). The frequencies of PS⁺EV⁺ and PS⁺ PBMC ranked in the top groups of measurements among inflammatory and coagulation parameters such as IL-6, PCT, CRP, PTT, D-Dimer and others (Figure S4A). The strongest negative correlations existed with low lymphocyte counts (Figure S4A). For better comparability, we focussed next only on those values determined from the same blood draw or close to our PS-measurements ('nearest values' in Figure S4A, shown in Figure 2d). Here, both PS⁺EV⁺ PBMC and PS⁺ PBMC correlated better than all other blood parameters with peak WHO ordinal scale (Figure 2d). Moreover, PS⁺EV⁺ PBMC frequencies correlated strongly with parameters of coagulation (fibrinogen, PTT), inflammation (IL-6, CRP) and lymphopenia (lymphocyte counts) (Figure 2e and S4B).

As the frequencies of PS⁺ PBMCs in the blood of COVID-patients turned out to be an independent predictor for a severe disease outcome (Figure 1e), we now wondered if PS⁺EV⁺ PBMCs, which constituted the major part of this population, allows such a prediction. Indeed, the AUROC analysis showed comparable prediction values for ventilation requirement (AUC 0.791, threshold 29, specificity 0.91, sensitivity 0.60) and death (AUC 0.866, threshold 31.4, specificity 0.88, sensitivity 0.83) (Figure S1D). Therefore, our new type of PS analysis allows the detection of subcellular particles associated with PBMC of COVID-19 patients. The percentage of PBMC bound to these PS⁺ particles correlated with the maximal (peak) WHO score of COVID-19 patients and allowed to classify patients with higher significance than some of the previously established medical laboratory parameters (Lippi & Plebani, 2020).

2.3 | PS⁺ EVs bind to several PBMC populations

Next, we investigated whether PS⁺ EVs would selectively associate with specific PBMC subpopulations. We examined CD4⁺ and CD8⁺ T cells (Figure 3a), CD19⁺ B cells (Figure 3b) and HLA-DR⁺CD19⁻CD3⁻ PBMC (containing mainly monocytes and

dendritic cells as central blood populations, Figure 3b). In general, CD8⁺ T cells were more strongly associated with PS⁺ EVs than CD4⁺ T cells (Figure 3a). However, both T cell subsets showed a similar tendency of increased PS⁺ EV binding in patients with a higher WHO score (Figure 3a). B cells and blood monocyte-containing populations of patients in the different WHO groups were also associated relatively strongly with PS⁺ EVs (Figure 3b). However, there was no actual grading with the severity of the disease. In summary, most blood cells showed a strong association with PS⁺ EVs in the patients. The frequency of PS⁺ EV⁺ CD8⁺ T cells best reflected the severity of COVID-19 disease.

2.4 | PS⁺ EVs associated with PBMC from COVID-19 patients are PS⁺CD41⁺ platelet-derived microparticles

EVs classify according to their size and origin into exosomes (up to 150 nm), microvesicles or microparticles (MPs; 100–1000 nm) and apoptotic EVs or apoptotic bodies (100–5000nm) (Mathieu et al., 2018). To better characterise the EVs associated with lymphocytes in COVID-19 patients, we isolated PS⁺ lymphocytes (B and T cells, PS⁺CD19⁺CD3ε⁺) from COVID-19 patients by FACS. We used recombinantly expressed, biotinylated MFG-E8-derived PS-binding domain mCl, which was multimerised by streptavidin (SA) (mCl-multimer/SA-APC) for PS-detection by flow cytometry (Figure S3C) and mCl-multimer/SA-gold for PS-detection by subsequent transmission electron microscopy (TEM). TEM pictures show cell-associated particles of a subcellular size bound to lymphocytes, which morphologically resemble T cells (Figure 4a–f). Many (Figure 4b, d, and f, open white arrows), but not all EVs (Figure 4c, arrows), were PS⁺, and most EVs were >100 nm in size (Figure 4b, d and f). The particles were mainly round and had different shapes and contained other smaller components, cell contents or organelles (Figure 4b, d, white star). However, we also found PS⁺ tubular elongated structures (Figure 4d, black star). Relatively large particles with highly diverse shapes, including tubular shapes and content are known features of PMPs, 50% of which are PS positive (Arraud et al., 2014; Ponomareva et al., 2017; Reininger et al., 2006). Hyperactivated platelets in COVID-19 patients (Teuwen et al., 2020) are sources for PMPs and contribute to the hypercoagulability state of the disease (Klok et al., 2020; Middeldorp et al., 2020; Tang et al., 2020). Activated platelets can release two types of EVs, (i) smaller exosomes (40–100 nm in diameter) derived by exocytosis from α-granules and the multivesicular body, and (ii) PS⁺ MP (100–1000 nm in size), formed by budding of the plasma membrane (Aatonen et al., 2014; Heijnen et al., 1999). These similarities let us hypothesise that PMPs attach to PBMC of COVID-19 patients.

To test this hypothesis, we stained PBMC from COVID-19 patients for CD41, a platelet marker, part of a fibrinogen-receptor and present on platelet-derived PMPs (Heijnen et al., 1999) (Figure S5 and 4g). Analysis of flow cytometry data of PBMC confirmed our assumption and showed that many PBMC were positive for the platelet marker CD41 (Figure 4g). However, CD41 could not distinguish PBMC from healthy donors and COVID because CD41⁺ PBMC also existed in healthy donors (Figure 4g, CD41⁺). In contrast, PS-positivity alone distinguished PBMC from healthy donors and COVID-19 patients, as PS⁺ PBMC were highly significantly enriched in patients (Figure 4g, PS⁺).

To analyse PS and CD41 and their possible colocalisation, we performed image analysis of PBMC (Figure S5A, B) and T lymphocytes (Figure 4h and i). In COVID-19 patients, we observed a substantial increase of PS⁺CD41⁺ PBMCs and T cells from 7% to 25% and from 2% to 18%, respectively. The increase in CD41[−]PS⁺ cells was not as pronounced but still significant (Figure 4h and i, Figure S5A and B). This finding shows that most PS⁺ cells acquire PS through the binding of CD41⁺ platelets or their PMPs. To investigate whether the cells preferentially bind whole platelets or smaller PMPs, we quantified CD41^{hi} versus CD41^{low} cells. The CD41^{hi} gate contained mainly cells with large CD41⁺ particles attached, which were also visible in the brightfield (BF) channel – presumably whole platelets. In contrast, the cells in the CD41^{low} gate were associated with small, more dimly stained spots that were too small to be visible in the BF channel – presumably PMPs (Figure 4i). While T cells very clearly had a strong preference for PMP binding (15% of CD3⁺ T cells were CD41^{low} and 2% CD41^{hi}, Figure 4i), PBMCs did not show such a clear preference (approx. 15% were CD41^{low}, 9% were CD41^{hi}, Figure S5C). Our data show that PBMCs from COVID-19 patients associate to a high degree with PS⁺ platelets and PMPs, while T cells rarely bind whole platelets, but rather PMPs.

2.5 | PMPs carry markers of activated platelets

SARS-CoV-2-infection causes platelet activation and alters their functions (Manne et al., 2020; Zaid et al., 2020). The results of our study suggested that the PMPs associated with lymphocytes in COVID-19 patients originate from activated CD41⁺ platelets. In addition to PS and CD41, markers such as CD62P (P-selectin) and the tetraspanin CD63 are present on PMPs derived from activated platelets (van der Zee et al., 2006). Our patient cohort showed increased percentages of PS⁺ and CD62P⁺ platelets, both markers for platelet activation (Figure 6a–c), although the increase in CD62P⁺ platelets did not reach statistical significance. When associated with CD8⁺ T cells, platelet-derived molecules PD-L1 (CD274) (Rolfes et al., 2018) and CD86 (Chapman et al., 2012) on PMPs could be potentially negative or positive costimulatory triggers, respectively. Platelets were strongly positive for CD274 (Figure S6B and C), but this was not different between healthy donors and patients (Figure S6B). The same was true for CD86, which we found in similar amounts and generally only very few platelets that were positive for this molecule in both

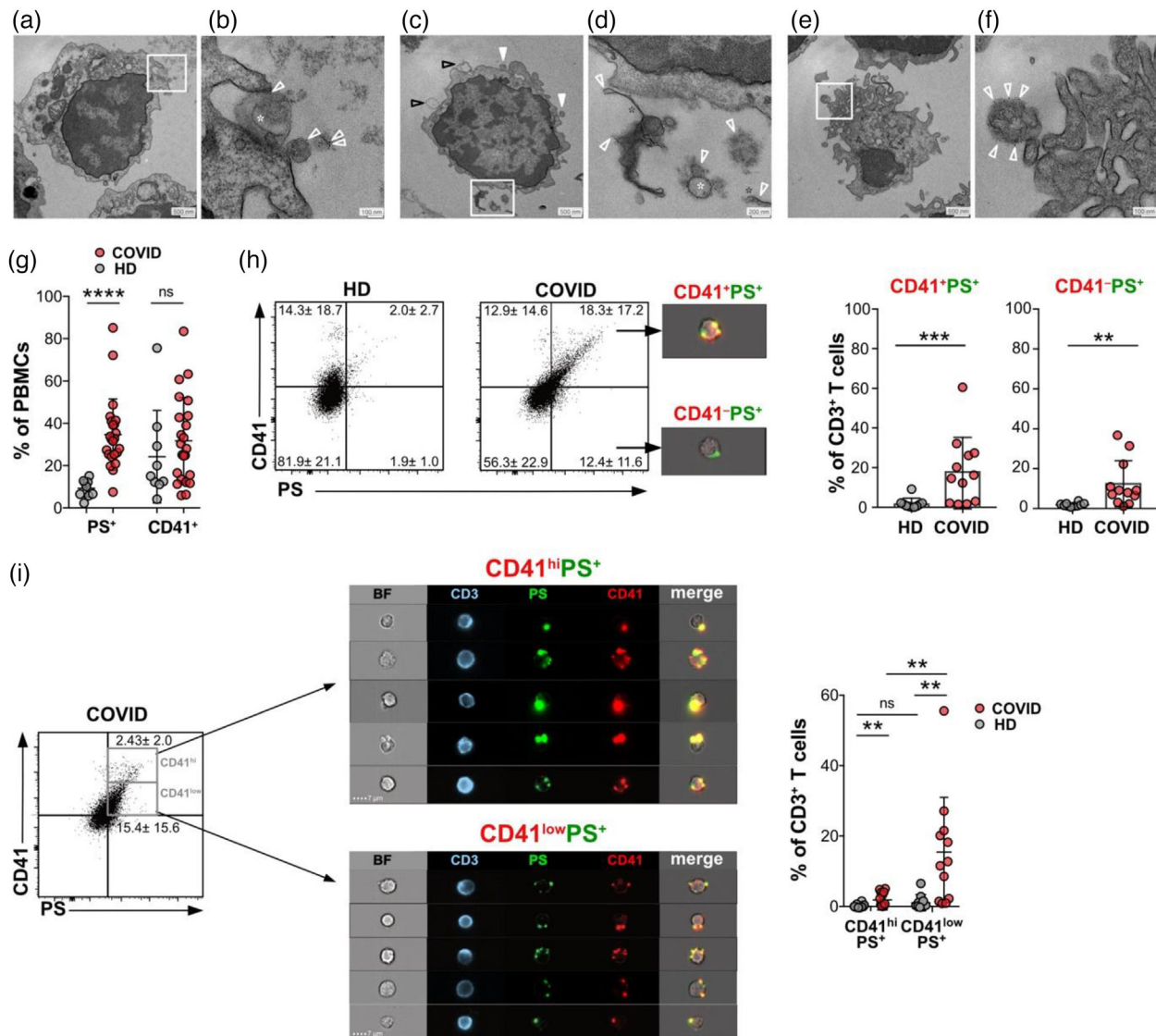


FIGURE 4 Structural and phenotypic characterisation of EVs associated with lymphocytes from COVID patients. Patient parameters for these experiments are depicted in Table S3. PS⁺ CD3^ε⁺ T and CD19⁺ B lymphocytes were isolated from PBMC of COVID patients (WHO_{max} score 3) by FACS-sorting (Figure S3C) and subsequently labeled with mCl-multimer/streptavidin-gold for TEM analysis of PS and analysed structurally by TEM (a-f). (b, d, f) represent the magnified sections (white frame) of (a, c, e), respectively. Open white arrowheads (b, c, f) mark PS labelling by mCl-multimer/streptavidin-gold; arrowheads in C point to PS⁻ EVs; white star (b, d) or black star (d) marks organelle-like structures within EVs, or PS⁺ tubular elongated structures (d), respectively. Analysis of platelet marker CD41 on T cells. (g) PBMC were analysed as shown in Figure S3 (HD, $n = 11$; COVID, $n = 23$) for PS and CD41. (h) CD3^ε⁺ T lymphocytes (gated as in Figure S3D) were stained for CD41 and PS and analysed by IFC (HD, $n = 10$; COVID, $n = 12$). Images represent cells of the respective quadrants. Numbers are the percentage of cells with the respective quadrants and are shown also in the bar graphs. (i) Percentage of T cells in the quadrants of PS⁺ CD41^{hi} and PS⁺ CD41^{low} CD3^ε⁺ T cells. Dot plots show the gating of PS⁺ CD41^{hi} and PS⁺ CD41^{low} CD3^ε⁺ T lymphocytes. IFC images show representative cells of the CD41^{hi} and CD41^{low} gates. The bar graph shows the frequency of PS⁺ CD41^{hi} and PS⁺ CD41^{low} T cells as percent of all CD3^ε⁺ T cells. Statistical significance was determined by paired Wilcoxon test and is indicated by asterisks (ns $p > 0.5$; * $p \leq 0.05$; ** $p \leq 0.01$; *** $p \leq 0.001$; two-tailed unpaired t -test)

groups (Figure S4B and C). We evaluated next if PS⁺EV⁺ CD8⁺ T cells were positive for these platelet markers. PS⁺EV⁺ CD8⁺ T cells showed significantly increased mean fluorescence intensities (MFI) for platelet markers CD41, CD63, CD62P and CD274 compared to their PS⁻ counterparts (Figure 5a and b). The frequency of T cells, which were positive for these markers, was also increased in PS⁺EV⁺ T cells (CD41, CD63, CD62P; Figure 5b). This finding indicated that PMPs carried the surface molecules of their activated 'parent' platelets to the surface of activated CD8⁺ T cells in COVID-19 patients. When we analysed the images of CD41, CD63, CD274 and CD62P stained T cells, we also observed an EV-like staining pattern of these markers, similar to the PS staining (Figure 5c).

To confirm that these markers originate from activated platelets or their PMPs, we quantified PMP-marker colocalisation with PS. We used the bright detail similarity (BDS) feature to quantify the pixel overlap of PS⁺ and PMP-marker⁺ spots identified

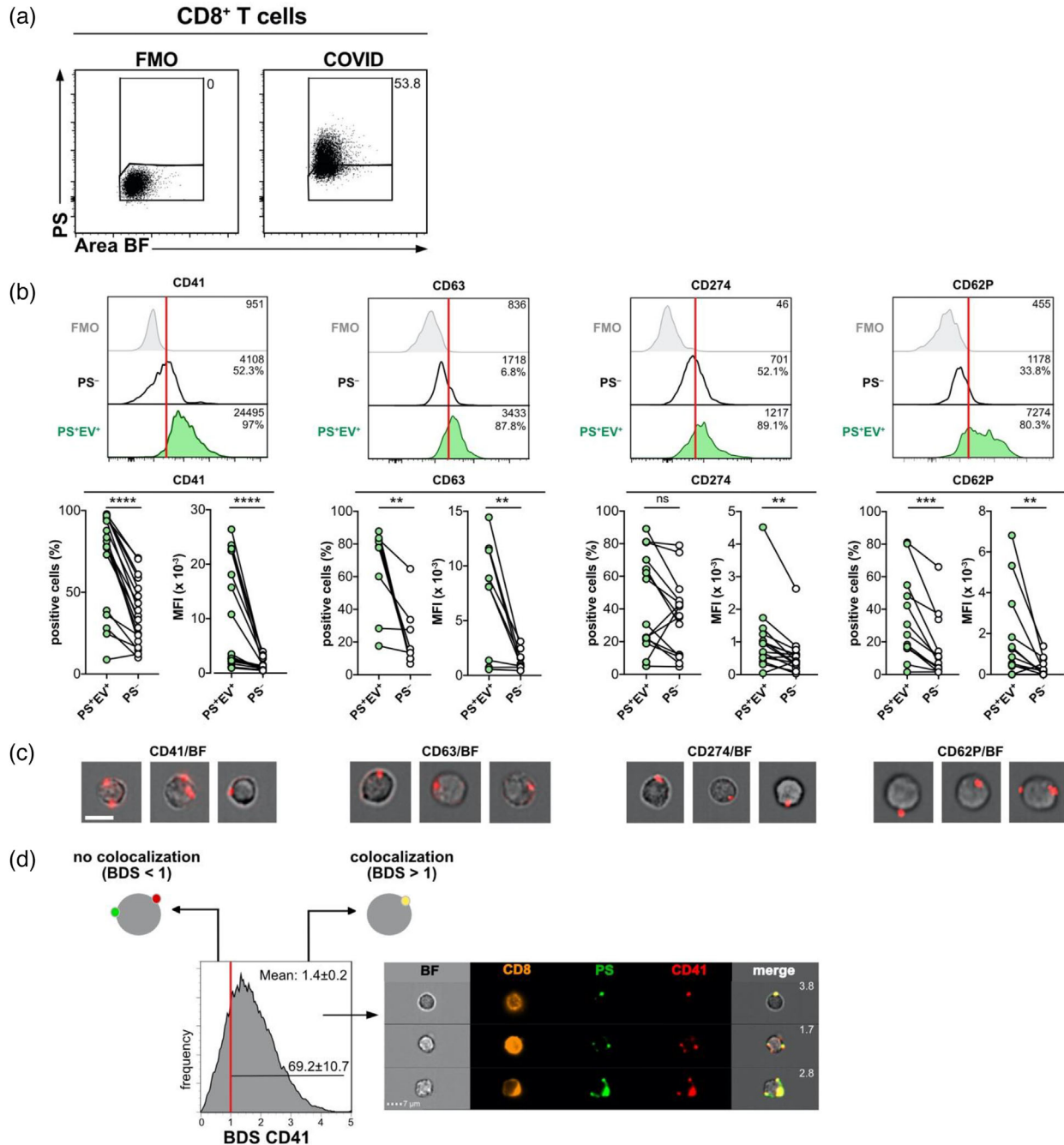


FIGURE 5 EVs bound to CD8⁺ T cells originate from platelets and PMP markers colocalise with PS⁺ EVs. Patient parameters for these experiments are depicted in Table S4. (a) Analysis of CD8⁺ T cells of COVID patients (CD41, *n* = 18; CD63, *n* = 9; CD274, *n* = 15, CD62P, *n* = 13) were gated as shown in Figure S3E and then further separated into PS⁺EV⁺ and PS⁻ T cells. Numbers represent the percentage of cells within the gates. (b) Then cells were analysed separately for expression of platelet-markers CD41, CD63, CD62P and CD274. Median fluorescence intensities (MFI) ± SD of these proteins and % of positive cells are indicated in the histograms. Summaries of all results are shown below histograms. (c) Representative images of CD41⁺, CD63⁺, CD62P⁺ and CD274⁺ CD8⁺ T cells show the EV-like staining pattern of these markers. (d) Colocalisation analysis between PS and PMP-marker staining. To identify PS⁺ spots the Dilate(Peak(M02, PS, Bright, 5),1) and to identify PMP-marker⁺ spots the Dilate(Peak(M_{marker},marker channel, Bright, 1),1) masks were used. To quantify the degree of colocalisation between these masks, bright details similarity scores (BDS) were calculated. Cells with a BDS < 1 did not show any significant colocalisation as determined by visual inspection. Cells with a BDS > 1 showed substantial colocalisation of PS and the respective platelet marker. BDS scores are shown in the representative example images. Histograms show the BDS scores of PS⁺EV⁺ CD8⁺ cells. The mean BDS score and the percentage of cells showing colocalisation (BDS > 1) are indicated within histograms. Statistical significance was determined by paired Wilcoxon test and is indicated by asterisks (ns *p* > 0.5; **p* ≤ 0.05; ***p* ≤ 0.01; ****p* ≤ 0.001)

using a peak mask in the IDEAS software (Figure 5d). As determined by visual inspection, BDS values >1 indicate substantial colocalisation between PS and other markers. This analysis showed that the great majority of all PS⁺EV⁺ CD8⁺ T cells (64%–82%) showed strong colocalisation of PS⁺EVs with CD41 (Figure 5d), CD63, CD62P or CD274 (Figure S8) with average BDS scores ranging from 1.3 to 1.8 (Figure 5 and S8). These results indicate that most of the PMPs attached to CD8⁺ T cells originate from activated platelets and carried platelet markers. Furthermore, since human T cells do not express markers like CD41 and CD62P, it excludes the possibility that the PS⁺EVs attached to T cells originate from T cells themselves or mark eventual focal PS⁺ regions on the T cell surface membrane.

2.6 | PS⁺CD41⁺ PMPs are preferentially bound to proliferating CD8⁺ T cells

Next, we wanted to assess whether there are functional differences between PMP⁺ and PMP⁻ CD8⁺ T cells. For this, we performed RNAseq analysis of FACS-sorted PS⁺ and PS⁻ non-naïve CD8⁺ T cells from peripheral blood of 4 patients (Figure 6a and Figure S3G). Despite heterogeneity between patients, we could identify gene sets that showed clear enrichment in PS⁺ (Figure 6b) and PS⁻ T cells (Figure 6c). Table S5 shows a summary of the gene set enrichment analysis (GSEA) against 4597 datasets in the gene ontology (GO) database.

PS⁺ CD8⁺ T cells had enriched genes controlling cell cycle and division, with normalised enrichment scores (NES) of 2.24 and 2.70 for the gene ontology biological process (GOBP) ‘cell division’ and KEGG ‘cell cycle’ gene sets, respectively. Among the genes upregulated in PS⁺ CD8⁺ T cells of all patients were several cell division control (CDC) genes, such as CDC45, CDCA8, CDC20, CDC6 or transcription factors E2F7 and E2F2, which are involved in cell cycle regulation (DeGregori & Johnson, 2006). Also, Birc5 (survivin) which plays a crucial role in costimulation-driven clonal expansion of T cells (Song et al., 2005), was upregulated in all patients.

Cells in the G2/M phase exhibit a general inhibition of translation (Sachs, 2000). Hence, the reduced expression of genes initiating translation in PS⁺ CD8⁺ T cells is in line with the observed upregulation of proliferation-associated genes (Figure 6c).

Although PS⁻ and PS⁺ CD8⁺ T cells had few apparent differences in gene expression due to the high degree of variability between individual patients, it is striking that binding of PS⁺ PMPs was associated with increased proliferation. To confirm the RNAseq results, we stained CD8⁺ T cells with the proliferation marker Ki-67, which labels dividing and recently dividing cells in G1, S, G2 and M phase, but is absent in resting cells (Scholzen & Gerdes, 2000) and compared the frequency of PS⁻ and PS⁺EV⁺ Ki-67⁺ cells. PS⁺EV⁺ CD8⁺ T cells (Figure 6d and e) and PS⁺EV⁺ CD4⁺ T cells (Figure S8) contained significantly more Ki-67⁺ proliferating cells than their PS⁻ T cell counterparts from the same patient. In both cases, Ki-67 staining localised to the nucleus and PS⁺ PMPs to the periphery of the same cells (Figure 6e and S8B). Our results indicate that PS⁺ PMPs preferentially bind to proliferating T cells and may affect T cells in this cycling stage.

We were also interested to find out, whether CD8⁺ T cells binding PS⁺ PMPs exhibit an effector or memory phenotype. Previous reports showed a high prevalence of SARS-CoV-2-specific T cells mainly among T cells with phenotypes of effector memory (T_{EM}) and terminal effector memory cells reexpressing CD45RA (T_{EMRA}) cells (Kared et al., 2021). We did not observe a clear enrichment of effector or memory genes (Best et al., 2013). However, we found an upregulation of effector-associated genes, such as CXC Motif Chemokine Receptor 3 (Cxcr3), Interferon γ (Ifng), Granzyme A and B (Gzma and Gzmb) and CC-chemokine ligand 5 (Ccl5) in PS⁺ CD8⁺ T cells of all four patients. In contrast, memory-related genes, such as C-X-C Motif Chemokine Receptor 4 (Cxcr4), DNA-binding protein inhibitor ID-3 (Id3) and interleukin-7 receptor (Il7r), showed a subtle downregulation in all patients. These findings indicate that PMP-associated CD8⁺ T cells are proliferating effector cells rather than memory cells. This we also confirmed with flow cytometry using CCR7 and CD45RA as markers (Sallusto et al., 2004). We found PS⁺PMPs preferentially associated with CCR7⁻CD45RA⁻ CD8⁺ T_{EM} cells and terminally differentiated CCR7⁻CD45RA⁺ CD8⁺ T_{EMRA} (Figure S9).

Our novel analysis method allows the detection of dying as well as PS⁺ EV-associated living cells (Figure 2). We next wanted to analyse whether the apoptosis rate of CD8⁺ T cells would be elevated in COVID-19 patients as compared to healthy donors and could contribute to the observed T cell lymphopenia (Laing et al., 2020). To this end, we quantified the number of CD8⁺ T cells classified as apoptotic by the CAE algorithm (Figure S10). The CD8⁺ T cell apoptosis rate was significantly increased in moderate and severe cases compared to healthy donors (Figure S10A and B). This increased rate of apoptosis might ultimately contribute to T cell loss and lymphopenia.

Taken together, we present a robust method, which allows the detection of dying as well as PS⁺EV⁺-associated living cells within PBMCs of COVID-19 patients in a single step. This type of analysis might help understand events that directly affect the immune system and might be caused by EV-immune cell interactions.

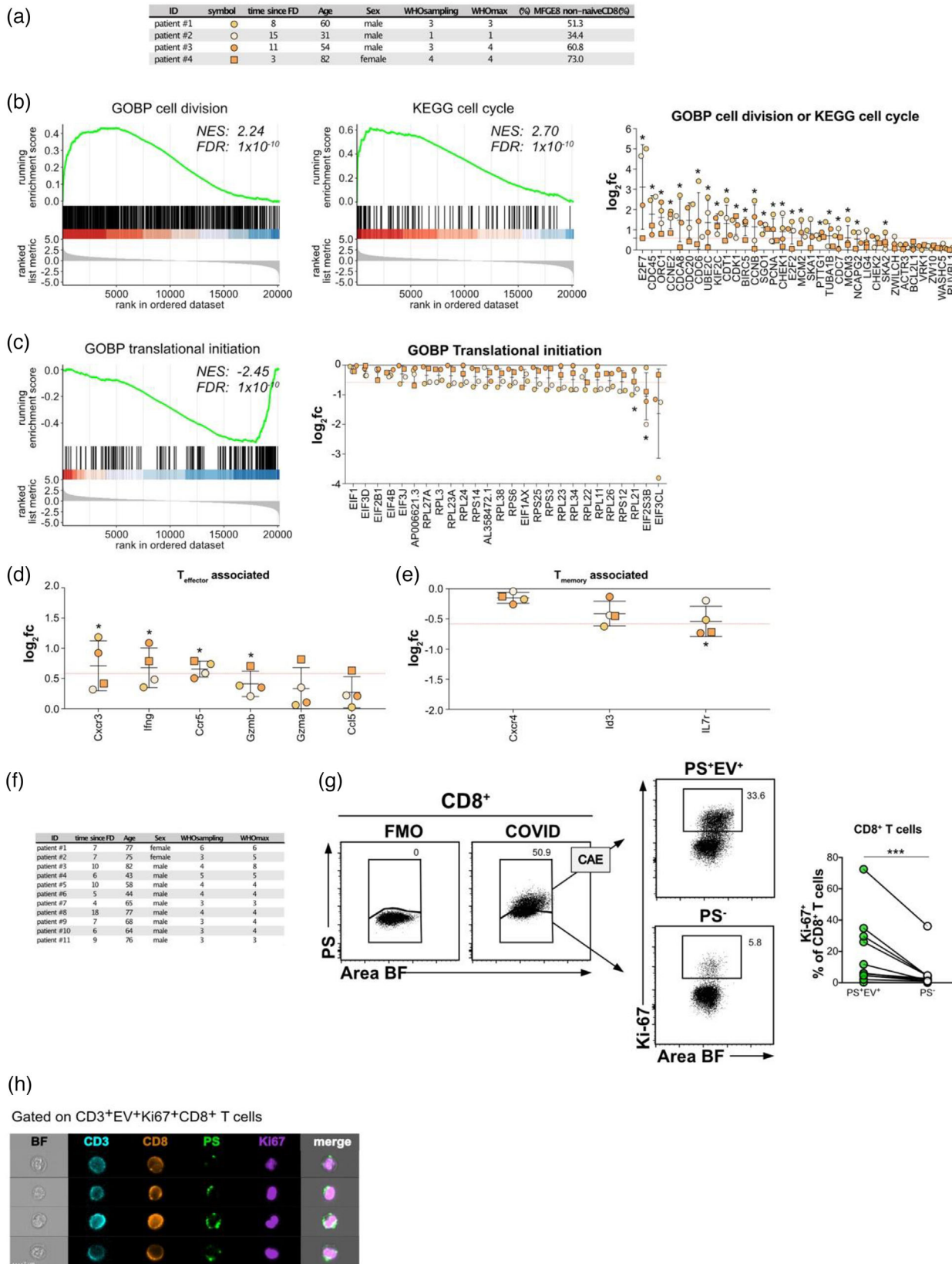


FIGURE 6 PS⁺EV associate with proliferating CD8 T cells. Non-naive PS⁺ and PS⁻ CD8⁺ T cells (gating strategy see Figure S3G) from four patients were sorted and subjected to RNAseq analysis. (a) The table displays patient parameters. (b) GSEA enrichment analysis for the gene sets GOBP cell division and KEGG cell cycle are shown and indicate enrichment in PS⁺ CD8⁺ T cells. Dot plots depict log₂ fold change values of genes in either of these two gene sets and upregulated in all four patients. The red dotted horizontal line indicates a fold change of 1.5 (log₂fc 0.58). *p*-values < 0.05 are indicated with an asterisk. (c) GSEA enrichment analysis for the gene sets GOBP translational initiation and indicates enrichment in PS⁻ CD8⁺ T cells. Dot plots depict log₂ fold change values of genes in this gene set and downregulated in all four patients. The red dotted horizontal line indicates a fold change of -1.5 (log₂fc -0.58).

3 | DISCUSSION

COVID-19 patients have hyperactivated platelets (Zaid et al., 2020), elevated levels of circulating PMPs (Cappellano et al., 2021), and an increased risk of thromboembolic complications contributing to disease severity and mortality. Our results contribute to the complex clinical picture of thromboinflammation (reviewed in Gu et al. (2021) and Lind (2021)). One of our most surprising findings was the high association of PBMC with PS⁺ PMPs and platelets over the disease course, shown with a novel PS-detecting method. The degree of this association correlated more strongly with disease severity than established laboratory indices and might be a promising biomarker for predicting disease severity.

Patients with COVID-19 are mostly lymphopenic (Cao, 2020; Yang et al., 2020), but lymphopenia preferentially affects CD8⁺ T cells (Mathew et al., 2020; Mazzoni et al., 2020). The measurement of dying or apoptotic cells in vivo or fresh ex vivo samples is technically challenging. Phagocytes very efficiently remove dead cells, and sample preparation itself can contribute to cell death. Using novel PS-specific reagents based on lactadherin, we found few but statistically significantly increased amounts of dying PBMCs, but also specifically dying CD8⁺ T cells in the blood of COVID-19 patients.

Antiphospholipid autoantibodies (aPL antibodies), including autoantibodies to the PS/prothrombin complex (antiPS/PT), have been found in COVID-19 patients (Zhang et al., 2020). Hence, it is possible that the association of PS⁺ platelets and PMPs with activated lymphocytes, together with a highly inflammatory environment, may drive the generation of aPL antibodies, further increasing the risk of life-threatening thrombotic events. However, further experiments are necessary to analyse this possibility.

By interacting with the complement cascade activated in COVID-19 patients (Song & FitzGerald, 2020), PS⁺ PMPs could contribute to lymphopenia. Correlation analyses of all blood values with the amounts of PS⁺PMP⁺ PBMCs showed the strongest negative correlation with decreased lymphocyte counts in patients' blood, that is, with established lymphopenia. PS and PS⁺ PMP can activate complement pathways (Mevorach et al., 1998; Tan et al., 2010; Wang et al., 1993), thrombin formation, coagulation and inflammation (Melki et al., 2017; Owens & Mackman, 2011; Ridger et al., 2017). Therefore, one could speculate that PS⁺PMP⁺ T cells might trigger for example the complement cascade on their surface, which might cause cell damage, death and T cell removal by phagocytes.

Moreover, the presence of an activated complement system in COVID-patients (Song & FitzGerald, 2020) could increase the release of PMPs from platelets (Sims et al., 1988) to self-reinforce this spiral. PS⁺ PMPs might facilitate the assembly and dissemination of procoagulant enzyme complexes (Sims et al., 1988). Attracting these reactions to the surface of lymphocytes might cause further functional inhibition or cell death.

'Long Covid' is a phenomenon that occurs in around 10% of COVID-19 patients and seems to be associated with persistent tissue damage in severe cases. However, also patients with mild COVID-19 disease scores might be affected (Mahase, 2020). We identified PS⁺PMP⁺ PBMCs of patients during many weeks post initial diagnosis with only minimal signs of returning to normal levels. Therefore, prolonged adverse effects of PS⁺ PMPs on the immune system could contribute to 'long COVID'. The frequencies of PS⁺ and PS⁺EV⁺ PBMCs in our cohort of recovered patients was only slightly, but statistically significantly elevated when compared to those of healthy donors. As these patients had only mild symptoms (WHO 1–2), it might be interesting to monitor also patients with 'long COVID' or those recovered from severe disease. Eventually PS⁺EV⁺ PBMCs could also be a marker for late COVID-19 symptoms.

Especially CD8⁺ T_{EM} and T_{EMRA} cells, among which most SARS-CoV2-specific clones were identified (Kared et al., 2021) showed enhanced PMP-binding in COVID-19 patients. COVID-19 T cell responses begin too late (Sette & Crotty, 2021), and T cells may be exhausted (Zheng et al., 2020). The association of PS⁺ PMPs with T cells could contribute to these deficiencies and potentially impact the immune and inflammatory antiviral responses. Activated platelets may associate with T cells in the blood of HIV-infected individuals (Green et al., 2015) and link the coagulation and inflammatory cascade with T cells. In vitro, platelets can inhibit proliferation, cytokine production and PD1 expression of T cells (Polasky et al., 2020). Since PMPs derive from platelets, they may also have similar functions as their 'parent'-platelets. We found that between 10% and 80% of CD8⁺ T cells were associated with PD-L1(CD274)⁺ PMP. The fact that we could detect this immunoregulatory molecule on a high frequency of PS⁺ and PS⁻ PMPs raises the possibility that PMPs can suppress CD8⁺ T cells via PD-L1/PD1 interaction. Previous studies suggested that SARS-CoV-2-specific CD8⁺ T cells can have an exhausted phenotype due to their expression of inhibitory receptors such as PD1 (De Biasi et al., 2020; Diao et al., 2020; Song et al., 2020; Zheng et al., 2020). Analogous to PD-L1 on

p-values < 0.05 are indicated with an asterisk. (d and e) Log₂ fold change values of genes associated with T effector (f) and T memory (g) cells that were up- or down-regulated, respectively, in all four patients, are shown. Red dotted horizontal line indicates a fold change of 1.5 (log₂fc 0.58) or -1.5 (log₂fc -0.58).

p-values < 0.05 are indicated with an asterisk. (f) Table shows details of PBMC-origin (patient numbers) for validation experiments shown in (g)-(h). (g) PBMC from COVID patients were examined for proliferation with Ki-67. CD8⁺ T cells (*n* = 11) were analysed as shown in Figure SIF. PS⁺CD3⁺CD8⁺ T cells were stained intranuclear for Ki-67. PS⁺ and PS⁻ fractions were classified by IFC. CAE-analysis identified PS⁺EV⁺ live cells. PS⁺EV⁺ and PS⁻CD8⁺ T cells were then analysed for Ki-67, and data from all patients were plotted on the graph. The numbers in the dot plots represent the fraction of cells in the corresponding gate. Statistical significance was determined by paired Wilcoxon test and is indicated by asterisks (ns *p* > 0.5; **p* ≤ 0.05; ***p* ≤ 0.01; ****p* ≤ 0.001). (h) An image selection of CD8 T cells with the markers used

tumor exosomes, which suppress tumor-specific CD8⁺ T cells (Chen et al., 2018), PD-L1 PMPs could favor T cell suppression in COVID-19. However, recent data have suggested that PD1⁺ SARS-CoV-2-specific CD8⁺ T cells are functional (Rha et al., 2021). Furthermore, our RNAseq results showing subtly increased expression levels of the effector molecules IFN γ , granzyme A, and B and increased proliferation also argue against an exhausted phenotype of PS⁺ CD8⁺ T cells and would instead indicate enhanced effector function or terminal differentiation. Enhanced activation of PS⁺EV⁺ CD8⁺ T cells could theoretically be a reason for the observed higher rate of apoptosis in this population, as activation induced cell death (AICD) is known to contribute to loss of effector T cells (Green et al., 2003).

Two recent studies showed that in COVID-19 patients, hyperactivated platelets could form aggregates with leukocytes and macrophages (Hottz et al., 2020; Manne et al., 2020). As these previous studies relied on conventional flow cytometry, but not IFC, they could not differentiate between CD41⁺ platelets and CD41⁺ PMPs. Also, they did not analyse PS⁺ PMPs on the surface of live lymphocytes. Since PMPs constitute the lion's share of CD41⁺PS⁺ particles on T cells of COVID-19 patients and PS may be responsible for the coagulation and inflammatory effects mentioned above, our findings are an unexpected result with high clinical relevance.

PS is a novel marker to classify COVID-19 patients according to disease severity. Moreover, longitudinal studies could test PS as a predictor of disease development. Due to its ease of use by flow cytometry and the high number of positive PS⁺ PBMC during COVID-19, PS detection could be a valuable analytical tool also in other infectious diseases and sepsis.

4 | MATERIALS AND METHODS

4.1 | Study design and recruitment

Recruited patients ($n = 54$) with PCR confirmed SARS-CoV-2 infection were part of the COVID-19 Registry of the LMU University Hospital Munich (CORKUM, WHO trial id DRKS00021225). The Ethics Committee approved the study of the LMU Munich (No: 20-308; 18-415), and patients included (≥ 18 years, mean age 63, Table S1) consented to serial blood sampling. Additional approval was obtained for the analysis shown here (No. 20-308) and for the use of blood samples from healthy donors (No. 18-415). For this study, patient data were anonymised for analysis, and blood samples were collected between April 2020 and February 2021. Of the 54 patients analysed, 52 patients were hospitalised, and two patients were diagnosed in the hospital and discharged. From 15 patients, blood samples from several timepoints could be obtained, which were taken between days 2 and 76 after a positive SARS-CoV-2 PCR test. Clinical and laboratory data were collected and documented by the CORKUM study group and are summarised in Table S1. We used the World Health Organization's (WHO) eight-point ordinal scale for COVID-19 endpoints (WorldHealthOrganization, 2020) to grade disease severity. WHO scores were combined into 'mild' (WHO 1–3), 'moderate' (WHO 4) and 'severe' (WHO 5–8).

Recovered donors (RD, $n = 12$, mean age 40, Table S1) were adults with a prior SARS-CoV-2 infection (≥ 69 days post positive PCR test), who were either diagnosed in the ambulance or released from the hospital with WHO score 1–2.

Healthy donors (HDs, $n = 35$, mean age 39, Table S1) tested negative for SARS-CoV-2 were used as control cohorts. PBMCs were obtained from leucocyte reduction chambers after thrombocyte donations ($n = 10$) or freshly prepared from whole blood ($n = 25$) of healthy hospital and laboratory workers.

4.2 | Sample processing and cell isolation

Peripheral blood was collected into lithium heparin tubes (Sarstedt) and processed within 6 h after venipuncture. Unfixed samples were handled under Biosafety level 2. PBMCs were isolated by Biocoll density gradient (Merck) centrifugation and then directly stained for imaging flow cytometry.

4.3 | Antibody staining and flow cytometry

Antibodies and staining reagents are listed in Table S2. As PS-staining reagents we used the previously published recombinant MFG-E8-eGFP (Kranich et al., 2020; Trautz et al., 2017) and mCl-biotin multimerised with streptavidin-AF647 for flow cytometry or streptavidin-gold for TEM. mCl-multimers are commercially available through BioLegend as ApotrackerTM Tetra reagents. In flow cytometry. All PS-staining reagents are Ca²⁺ independent, highly stable and PS-specific. Freshly isolated PBMCs were incubated with Fc block before live/dead and cell surface antibody staining. PBMCs surface staining was performed in staining buffer (PBS containing 2% of fetal calf serum) for 25 min on ice. Then cells were washed and fixed with 4% PFA for 30 min at room temperature (RT), washed again, filtered and analysed on an ImageStreamx MKII imaging flow cytometer (Luminex). Samples

were acquired with low flow rate/high sensitivity and 60× magnification. Images were acquired using bright field illumination and the excitation lasers 405, 488, 561 and 642 nm.

For intranuclear Ki-67 staining, cells were fixed and permeabilised using the Transcription Factor Staining Buffer Set (ThermoFisher, cat. #00-5523-00) according to the manufacturers' instructions. Intranuclear staining was performed in permeabilisation buffer for 30 min at RT.

4.4 | Cell sorting for gene expression analysis

PBMCs from four patients (see Figure 6a) were stained with anti-CD3-BV421, anti-CD8-BV785, anti-CCR7-APC, anti-CD45RA-PerCPCy5.5, anti-CD19/CD16/CD56/CD14-APCFire750 and MFG-E8-eGFP (see Table S2) in staining buffer (25 min, 4°C) after cells were incubated with Fixable Viability dye eFluor780 in PBS (10 min, 4°C). PS⁺ and PS⁻ single, live, non-naïve (CCR7⁺CD45RA⁻, CCR7⁻CD45RA⁻ and CCR7⁻CD45RA⁺) CD3⁺CD8⁺ T cells were directly sorted into TRIzol reagent (Thermo Fisher) on a FACS Aria Fusion (BD) using a 100 μm nozzle. Samples were stored at -20°C until analysis. RNA isolation and sequencing were performed by Vertis Biotechnologie AG, Freising. Total RNA was isolated and purified using Monarch columns (NEB). Poly(A)⁺ RNA was isolated from the total RNA sample. First-strand cDNA synthesis was primed with a N6 randomised primer. After fragmentation, the Illumina TruSeq sequencing adapters were ligated in a strand specific manner to the 5' and 3' ends of the cDNA fragments. In this way, a strand specific PCR amplification of the cDNA was achieved using a proof-reading enzyme. For Illumina NextSeq sequencing, the samples were pooled in approximately equimolar amounts. The cDNA pool in the size range of 250–700 bp was eluted from a preparative agarose gel. The primers used for PCR amplification were designed for TruSeq sequencing according to the instructions of Illumina. The cDNA size range was 250–700 bp. The cDNA pool was sequenced on an Illumina NextSeq 500 system using 1 × 75 bp read length.

4.5 | RNAseq analysis

Sequencing reads were aligned to the human reference genome (version GRCH38.100) with STAR (version 2.7.3). Expression values (TPM) were calculated with RSEM (version 1.3.3). Post-processing was performed in R/bioconductor (version 4.0.3) using default parameters if not indicated otherwise. Differential gene expression analysis was performed with 'DEseq2' (version 1.28.1) using a model including patient ID as random factor. An adjusted *p* value (FDR) of less than 0.1 was used to classify significantly changed expression. Gene set enrichment analyses were conducted with 'clusterProfiler' (version 3.18.1) on the statistic reported by DEseq2. Data are available at GEO Submission (GSE174786).

4.6 | Cell sorting for TEM

Isolated PBMCs were stained with anti-CD19- and anti-CD3-PE, PS-staining reagent mC1-multimer (SA-AF647) (commercially available at BioLegend) and mC1-biotin (commercially available at BioLegend) multimerised with SA-gold, (Aurion) (see Table S2) in staining buffer (25 min, 4°C) after incubation with Fixable Viability Dye eFluor780 in PBS (10 min, 4°C). After washing, cells were prefixed with freshly prepared 4% EM-grade PFA (Science Services) for 30 min at RT before sorting. Fixed, single, PS⁺CD19⁺ and CD3⁺ cells were sorted on a FACS Aria III (BDBiosciences) using a 130 μm nozzle into PBS containing 0.5% BSA.

After washing with PBS, cells were fixed with 2.5% glutaraldehyde (EM-grade, Science Services) in 0.1 M cacodylate buffer (pH 7.4) for 15 min (Sigma Aldrich) and washed with 0.1 M sodium cacodylate buffer for 10 min at 400 g before postfixation in reduced osmium (1% osmium tetroxide (Science Services), 0.8% potassium ferricyanide (Sigma Aldrich) in 0.1 M sodium cacodylate buffer). The cell pellet was contrasted in 0.5% uranyl acetate in water (Science Services) and dehydrated in an ascending ethanol series. The pellet was embedded in epon resin and hardened for 48 h at 60°C. Ultra-thin sections (50 nm) were cut and deposited onto formvar-coated grids (Plano) and again contrasted using 1% uranyl acetate in water and Ultrastain (Leica). Images were acquired on a JEM 1400plus (JEOL).

4.7 | Imaging flow cytometry and data analysis

Data analysis was performed using the IDEAS software (Version 6.2, Luminex). Compensation matrices were generated using single stained samples and applied to the raw data, and data analysis files were created. Unfocused events were excluded from the analysis based on gradient max feature values. PS⁺ cells were gating using FMO controls. TIFF-images of PS⁺ cells from each sample were exported (16-bit, raw) and analysed by the CAE algorithm as previously described (Kranich et al., 2020). Two *.pop

files containing the object numbers of apoptotic and EV⁺ cells were generated and re-imported into the IDEAS software. Then FCS files from all cells, only apoptotic or only EV⁺ cells, were exported and analysed using FlowJo Version 10.7.1.

4.8 | Colocalisation analysis

We created a spot mask for PS and the respective marker staining to determine the degree of colocalisation between PS⁺ EVs and PMP-marker⁺ (CD41/CD63/CD274/CD62P) cells. PS⁺ spots were identified by the Dilate (Peak(M02, PS, Bright, 5),1) mask and the Dilate(Peak(M_marker, marker channel, Bright, 1),1) mask was used to identify marker⁺ spots. Both masks were combined, and the colocalisation was assessed using the BDS R3 feature of the IDEAS software.

4.9 | Platelet staining

Platelets were stained in whole blood. Hundred microlitres of blood were slowly added to 100 μ l of antibody mix in staining buffer (PBS with 0.1% sodium azide and 2% of FCS). The mixture was gently swirled and incubated for 30 min at room temperature in the dark. Then cells were fixed in 1% PFA in PBS with 0.1% sodium azide for 2 h, centrifuged for 20 min at 5000 g, resuspended in PBS with 0.1% sodium azide and analysed on the ImageStreamx MKII imaging flow cytometer.

4.10 | Statistical analysis

For statistical analysis, the PRISM software (GraphPad Software, La Jolla, CA, USA) was used. For direct comparison between two groups non-parametric, unpaired Mann-Whitney test was used. Statistical significance of paired data was determined by paired Wilcoxon test. p values of ≤ 0.05 are considered significant and denoted with *, ** $p < 0.01$, *** $p < 0.001$ and **** $p < 0.0001$. R version 4.0.3 was used for correlation analysis. Numeric values in the dataset were correlated (Spearman correlation) using the ggcorrmat function of the ggstatsplot package (v0.7.2) with Benjamini-Hochberg correction for multiple testing.

ROC analysis was performed using library 'pROC' (version 1.17.01). Thresholds were determined using the pROCs coords function with the 'best' method.

ACKNOWLEDGEMENTS

We would like to thank all of the COVID-19 Registry of the LMU Munich (CORKUM) investigators and staff and the patients and their families for participating in the CORKUM registry and all health care workers for their outstanding service. We acknowledge the Core Facility Flow Cytometry at the Biomedical Center, LMU Munich, for providing the ImageStreamX MKII imaging flow cytometer, cell sorters and services. We thank Wenbo Hu for providing reagents. T.B. and A.K. are supported by the Deutsche Forschungsgemeinschaft under CRC 1054 (TP B03, grant no. 210592381; and TP A06, grant no. 210592381). A.K. received funding from Deutsche Forschungsgemeinschaft under CRC/TR237-B14 (369799452) and KR2199/10-1 (391217598), and received funding from the Bavarian State Ministry of Science and the Arts.

CONFLICT OF INTERESTS

T.B. and J.K. declare competing interests due an exclusive licensing agreement with BioLegend, Inc. for the commercialisation of mCI-multimer. The remaining authors declare no competing interests.

AUTHOR CONTRIBUTIONS

Lisa Rausch: Formal analysis; Investigation; writing original draft. Konstantin Lutz: Formal analysis. Martina Schifferer: Formal analysis; Investigation; Writing – review & editing. Elena Winheim: Resources. Rudi Gruber: Investigation Formal analysis; Writing – review & editing. Anne B. Krug: Writing – review & editing, supervision, funding acquisition. Linus Rinke: Investigation. Clemens Scherer: Resources. Johannes C. Hellmuth: Resources. Maximilian Muenchhoff: Resources; Writing – review & editing. Christopher Mandel: Resources. Michael Bergwelt: Resources. Mikael Simons: Formal analysis; Funding acquisition; Writing – review & editing. Tobias Straub: Formal analysis. Jan Kranich: Conceptualization; Investigation; Software; Writing – original draft; Supervision. Thomas Brocker: Conceptualization; Funding acquisition; Supervision; Writing – original draft.

ORCID

Jan Kranich  <https://orcid.org/0000-0002-9928-4132>

Thomas Brocker  <https://orcid.org/0000-0001-7060-5433>

REFERENCES

- Aatonen, M. T., Ohman, T., Nyman, T. A., Laitinen, S., Grönholm, M., & Siljander, P. R. (2014). Isolation and characterization of platelet-derived extracellular vesicles. *Journal of Extracellular Vesicles*, 3(1), 24692, <https://doi.org/10.3402/jev.v3.24692>.
- Arraud, N., Linares, R., Tan, S., Gounou, C., Pasquet, J. M., Mornet, S., & Brisson, A. R. (2014). Extracellular vesicles from blood plasma: Determination of their morphology, size, phenotype and concentration. *Journal of Thrombosis and Haemostasis*, 12, 614–627, <https://doi.org/10.1111/jth.12554>.
- Best, J. A., Blair, D. A., Knell, J., Yang, E., Mayya, V., Doedens, A., Dustin, M. L., Goldrath, A. W., & Immunological Genome Project Consortium (2013). Transcriptional insights into the CD8+ T cell response to infection and memory T cell formation. *Nature Immunology*, 14, 404–412, <https://doi.org/10.1038/ni.2536>.
- Braun, J., Loyal, L., Frentsch, M., Wendisch, D., Georg, P., Kurth, F., Hippenstiel, S., Dingeldey, M., Kruse, B., Fauchere, F., Baysal, E., Mangold, M., Henze, L., Lauster, R., Mall, M. A., Beyer, K., Röhm, J., Voigt, S., Schmitz, J., ... Thiel, A. (2020). SARS-CoV-2-reactive T cells in healthy donors and patients with COVID-19. *Nature*, 587, 270–274, <https://doi.org/10.1038/s41586-020-2598-9>.
- Cao, X. (2020). COVID-19: Immunopathology and its implications for therapy. *Nature Reviews Immunology*, 20, 269–270, <https://doi.org/10.1038/s41577-020-0308-3>.
- Cappellano, G., Raineri, D., Rolla, R., Giordano, M., Puricelli, C., Vilardo, B., Manfredi, M., Cantaluppi, V., Sainaghi, P. P., Castello, L., De Vita, N., Scotti, L., Vaschetto, R., Dianzani, U., & Chiochetti, A. (2021). Circulating platelet-derived extracellular vesicles are a hallmark of Sars-Cov-2 infection. *Cells* 10, 85, <https://doi.org/10.3390/cells10010085>.
- Chapman, L. M., Aggrey, A. A., Field, D. J., Srivastava, K., Ture, S., Yui, K., Topham, D. J., Baldwin, W. M. 3rd, & Morrell, C. N. (2012). Platelets present antigen in the context of MHC class I. *Journal of Immunology*, 189, 916–923, <https://doi.org/10.4049/jimmunol.1200580>.
- Chen, G., Huang, A. C., Zhang, W., Zhang, G., Wu, M., Xu, W., Yu, Z., Yang, J., Wang, B., Sun, H., Xia, H., Man, Q., Zhong, W., Antelo, L. F., Wu, B., Xiong, X., Liu, X., Guan, L., Li, T., ... Guo, W. (2018). Exosomal PD-L1 contributes to immunosuppression and is associated with anti-PD-1 response. *Nature*, 560, 382–386, <https://doi.org/10.1038/s41586-018-0392-8>.
- Chen, R., Sang, L., Jiang, M., Yang, Z., Jia, N., Fu, W., Xie, J., Guan, W., Liang, W., Ni, Z., Hu, Y., Liu, L., Shan, H., Lei, C., Peng, Y., Wei, L., Liu, Y., Hu, Y., Peng, P., ... Medical Treatment Expert Group for COVID-19 (2020). Longitudinal hematologic and immunologic variations associated with the progression of COVID-19 patients in China. *Journal of Allergy and Clinical Immunology*, 146, 89–100, <https://doi.org/10.1016/j.jaci.2020.05.003>.
- Connor, D. E., Exner, T. M., Da, D., & Joseph, J. E. (2010). The majority of circulating platelet-derived microparticles fail to bind annexin V, lack phospholipid-dependent procoagulant activity and demonstrate greater expression of glycoprotein Ib. *Thrombosis and Haemostasis*, 103, 1044–1052, <https://doi.org/10.1160/TH09-09-0644>.
- Corban, M. T., Duarte-Garcia, A., McBane, R. D., Matteson, E. L., Lerman, L. O., & Lerman, A. (2017). Antiphospholipid syndrome: Role of vascular endothelial cells and implications for risk stratification and targeted therapeutics. *Journal of the American College of Cardiology*, 69, 2317–2330, <https://doi.org/10.1016/j.jacc.2017.02.058>.
- De Biasi, S., Meschieri, M., Gibellini, L., Bellinazzi, C., Borella, R., Fidanza, L., Gozzi, L., Iannone, A., Lo Tartaro, D., Mattioli, M., Paolini, A., Menozzi, M., Milić, J., Franceschi, G., Fantini, R., Tonelli, R., Sita, M., Sarti, M., Trenti, T., ... Cossarizza, A. (2020). Marked T cell activation, senescence, exhaustion and skewing towards TH17 in patients with COVID-19 pneumonia. *Nature Communications*, 11, 3434, <https://doi.org/10.1038/s41467-020-17292-4>.
- DeGregori, J., & Johnson, D. G. (2006). Distinct and overlapping roles for E2F family members in transcription, proliferation and apoptosis. *Current Molecular Medicine*, 6, 739–748, <https://doi.org/10.2174/1566524010606070739>.
- Del Valle, D. M., Kim-Schulze, S., Huang, H. H., Beckmann, N. D., Nirenberg, S., Wang, B., Lavin, Y., Swartz, T. H., Madduri, D., Stock, A., Marron, T. U., Xie, H., Patel, M., Tuballes, K., Van Oekelen, O., Rahman, A., Kovatch, P., Aberg, J. A., Schadt, E., ... Gnjatich, S. (2020). An inflammatory cytokine signature predicts COVID-19 severity and survival. *Nature Medicine*, 26, 1636–1643, <https://doi.org/10.1038/s41591-020-1051-9>.
- Diao, B., Wang, C., Tan, Y., Chen, X., Liu, Y., Ning, L., Chen, L., Li, M., Liu, Y., Wang, G., Yuan, Z., Feng, Z., Zhang, Y., Wu, Y., & Chen, Y. (2020). Reduction and functional exhaustion of T cells in patients with coronavirus disease 2019 (COVID-19). *Frontiers in Immunology*, 11, 827, <https://doi.org/10.3389/fimmu.2020.00827>.
- Green, D. R., Droin, N., & Pinkoski, M. (2003). Activation-induced cell death in T cells. *Immunological Reviews*, 193, 70–81, <https://doi.org/10.1034/j.1600-065x.2003.00051.x>.
- Green, S. A., Smith, M., Hasley, R. B., Stephany, D., Harned, A., Nagashima, K., Abdullah, S., Pittaluga, S., Imamichi, T., Qin, J., Rupert, A., Ober, A., Lane, H. C., & Catalfamo, M. (2015). Activated platelet-T-cell conjugates in peripheral blood of patients with HIV infection: coupling coagulation/inflammation and T cells. *Aids*, 29, 1297–1308, <https://doi.org/10.1097/QAD.0000000000000701>.
- Gu, S. X., Tyagi, T., Jain, K., Gu, V. W., Lee, S. H., Hwa, J. M., Kwan, J. M., Krause, D. S., Lee, A. I., Halene, S., Martin, K. A., Chun, H. J., & Hwa, J. (2021). Thrombocytopeny and endotheliopathy: crucial contributors to COVID-19 thromboinflammation. *Nature Reviews Cardiology*, 18, 194–209, <https://doi.org/10.1038/s41569-020-00469-1>.
- Guan, W. J., Ni, Z. Y., Hu, Y., Liang, W. H., Ou, C. Q., He, J. X., Liu, L., Shan, H., Lei, C. L., Hui, D. S. C., Du, B., Li, L. J., Zeng, G., Yuen, K. Y., Chen, R. C., Tang, C. L., Wang, T., Chen, P. Y., Xiang, J., ... China Medical Treatment Expert Group for Covid-19. (2020) Clinical Characteristics of Coronavirus Disease 2019 in China. *New England Journal of Medicine*, 382, 1708–1720, <https://doi.org/10.1056/NEJMoa2002032>.
- Heijnen, H. F., Schiel, A. E., Fijnheer, R., Geuze, H. J., & Sixma, J. J. (1999). Activated platelets release two types of membrane vesicles: microvesicles by surface shedding and exosomes derived from exocytosis of multivesicular bodies and alpha-granules. *Blood*, 94, 3791–3799.
- Hotchkiss, R. S., & Nicholson, D. W. (2006). Apoptosis and caspases regulate death and inflammation in sepsis. *Nature Reviews Immunology*, 6, 813–822, <https://doi.org/10.1038/nri1943>.
- Hottz, E. D., Azevedo-Quintanilha, I. G., Palhinha, L., Teixeira, L., Barreto, E. A., Pão, C. R. R., Righy, C., Franco, S., Souza, T. M. L., Kurtz, P., Bozza, F. A., & Bozza, P. T. (2020). Platelet activation and platelet-monocyte aggregate formation trigger tissue factor expression in patients with severe COVID-19. *Blood*, 136, 1330–1341, <https://doi.org/10.1182/blood.2020007252>.
- Huang, C., Wang, Y., Li, X., Ren, L., Zhao, J., Hu, Y., Zhang, L., Fan, G., Xu, J., Gu, X., Cheng, Z., Yu, T., Xia, J., Wei, Y., Wu, W., Xie, X., Yin, W., Li, H., Liu, M., ... Cao, B. (2020). Clinical features of patients infected with 2019 novel coronavirus in Wuhan, China. *Lancet*, 395, 497–506, [https://doi.org/10.1016/S0140-6736\(20\)30183-5](https://doi.org/10.1016/S0140-6736(20)30183-5).
- Huang, T. M., Ishida, T., Harashima, H., & Kiwada, H. (2001). The complement system enhances the clearance of phosphatidylserine (PS)-liposomes in rat and guinea pig. *International Journal of Pharmaceutics*, 215, 197–205, [https://doi.org/10.1016/s0378-5173\(00\)00691-8](https://doi.org/10.1016/s0378-5173(00)00691-8).
- Kared, H., Redd, A. D., Bloch, E. M., Bonny, T. S., Sumatoh, H., Kairi, F., Carbajo, D., Abel, B., Newell, E. W., Bettinotti, M. P., Benner, S. E., Patel, E. U., Littlefield, K., Laeyendecker, O., Shoham, S., Sullivan, D., Casadevall, A., Pekosz, A., Nardin, A., ... Quinn, T. C. (2021). SARS-CoV-2-specific CD8+ T cell responses in convalescent COVID-19 individuals. *Journal of Clinical Investigation*, 131, e145476, <https://doi.org/10.1172/JCI145476>.

- Klok, F. A., Kruip, M. J. H. A., van der Meer, N. J. M., Arbous, M. S., Gommers, D. A. M. P. J., Kant, K. M., Kaptein, F. H. J., van Paassen, J., Stals, M. A. M., Huisman, M. V., & Endeman, H. (2020). Incidence of thrombotic complications in critically ill ICU patients with COVID-19. *Thrombosis Research*, *191*, 145–147, <https://doi.org/10.1016/j.thromres.2020.04.013>.
- Kranich, J., Chlis, N. K., Rausch, L., Latha, A., Schifferer, M., Kurz, T., Foltyn-Arfa Kia, A., Simons, M., Theis, F. J., & Brocker, T. (2020). In vivo identification of apoptotic and extracellular vesicle-bound live cells using image-based deep learning. *Journal of Extracellular Vesicles*, *9*, 1792683, <https://doi.org/10.1080/20013078.2020.1792683>.
- Laing, A. G., Lorenc, A., Del Molino Del Barrio, I., Das, A., Fish, M., Monin, L., Muñoz-Ruiz, M., McKenzie, D. R., Hayday, T. S., Francos-Quijorna, I., Kamdar, S., Joseph, M., Davies, D., Davis, R., Jennings, A., Zlatareva, I., Vantourout, P., Wu, Y., Sofra, V., ... Hayday, A. C. (2020). A dynamic COVID-19 immune signature includes associations with poor prognosis. *Nature Medicine*, *26*, 1623–1635, <https://doi.org/10.1038/s41591-020-1038-6>.
- Li, Q., Ding, X., Xia, G., Chen, H. G., Chen, F., Geng, Z., Xu, L., Lei, S., Pan, A., Wang, L., & Wang, Z. (2020). Eosinopenia and elevated C-reactive protein facilitate triage of COVID-19 patients in fever clinic: A retrospective case-control study. *EclinicalMedicine*, *23*, 100375, <https://doi.org/10.1016/j.eclinm.2020.100375>.
- Liao, M., Liu, Y., Yuan, J., Wen, Y., Xu, G., Zhao, J., Cheng, L., Li, J., Wang, X., Wang, F., Liu, L., Amit, I., Zhang, S., & Zhang, Z. (2020). Single-cell landscape of bronchoalveolar immune cells in patients with COVID-19. *Nature Medicine*, *26*, 842–844, <https://doi.org/10.1038/s41591-020-0901-9>.
- Lind, S. E. (2021). Phosphatidylserine is an overlooked mediator of COVID-19 thromboinflammation. *Heliyon*, *7*, e06033, <https://doi.org/10.1016/j.heliyon.2021.e06033>.
- Lippi, G., & Plebani, M. (2020). Laboratory abnormalities in patients with COVID-2019 infection. *Clinical Chemistry and Laboratory Medicine*, *58*, 1131–1134, <https://doi.org/10.1515/cclm-2020-0198>.
- Liu, J., Li, S., Liu, J., Liang, B., Wang, X., Wang, H., Li, W., Tong, Q., Yi, J., Zhao, L., Xiong, L., Guo, C., Tian, J., Luo, J., Yao, J., Pang, R., Shen, H., Peng, C., Liu, T., ... Zheng, X. (2020). Longitudinal characteristics of lymphocyte responses and cytokine profiles in the peripheral blood of SARS-CoV-2 infected patients. *EBioMedicine*, *55*, 102763, <https://doi.org/10.1016/j.ebiom.2020.102763>.
- MacLaren, G., Fisher, D., & Brodie, D. (2020). Preparing for the most critically ill patients with COVID-19: The potential role of extracorporeal membrane oxygenation. *Jama*, *323*, 1245–1246, <https://doi.org/10.1001/jama.2020.2342>.
- Mahase, E. (2020). Long covid could be four different syndromes, review suggests. *Bmj (Clinical Research Ed.)*, *371*, m3981, <https://doi.org/10.1136/bmj.m3981>.
- Manne, B. K., Denorme, F., Middleton, E. A., Portier, L., Rowley, J. W., Stubben, C., Petrey, A. C., Tolley, N. D., Guo, L., Cody, M., Weyrich, A. S., Yost, C. C., Rondina, M. T., & Campbell, R. A. (2020). Platelet gene expression and function in patients with COVID-19. *Blood*, *136*, 1317–1329, <https://doi.org/10.1182/blood.2020007214>.
- Mathew, D., Giles, J. R., Baxter, A. E., Oldridge, D. A., Greenplate, A. R., Wu, J. E., Alanio, C., Kuri-Cervantes, L., Pampena, M. B., D'Andrea, K., Manne, S., Chen, Z., Huang, Y. J., Reilly, J. P., Weisman, A. R., Ittner, C. A. G., Kuthuru, O., Dougherty, J., Nzingha, K., ... Wherry, E. J. (2020). Deep immune profiling of COVID-19 patients reveals distinct immunotypes with therapeutic implications. *Science*, *369*, eabc8511, <https://doi.org/10.1126/science.abc8511>.
- Mathieu, M., Martin Jaular, L., Lavieue, G., & Théry, C. (2018). Specificities of secretion and uptake of exosomes and other extracellular vesicles for cell-to-cell communication. *Nature Cell Biology*, *21*, 1–9, <https://doi.org/10.1038/s41556-018-0250-9>.
- Mazzoni, A., Salvati, L., Maggi, L., Capone, M., Vanni, A., Spinicci, M., Mencarini, J., Caporale, R., Peruzzi, B., Antonelli, A., Trotta, M., Zammarchi, L., Ciani, L., Gori, L., Lazzeri, C., Matucci, A., Vultaggio, A., Rossi, O., Almerigogna, F., ... Cosmi, L. (2020). Impaired immune cell cytotoxicity in severe COVID-19 is IL-6 dependent. *Journal of Clinical Investigation*, *130*, 4694–4703, <https://doi.org/10.1172/JCI138554>.
- Melki, I., Tessandier, N., Zufferey, A., & Boilard, E. (2017). Platelet microvesicles in health and disease. *Platelets*, *28*, 214–221, <https://doi.org/10.1080/09537104.2016.1265924>.
- Mevorach, D., Mascarenhas, J. O., Gershov, D., & Elkon, K. B. (1998). Complement-dependent clearance of apoptotic cells by human macrophages. *Journal of Experimental Medicine*, *188*, 2313–2320, <https://doi.org/10.1084/jem.188.12.2313>.
- Middeldorp, S., Coppens, M., van Haaps, T. F., Foppen, M., Vlaar, A. P., Müller, M. C. A., Bouman, C. C. S., Beenen, L. F. M., Kootte, R. S., Heijmans, J., Smits, L. P., Bonta, P. L., & van Es, N. (2020). Incidence of venous thromboembolism in hospitalized patients with COVID-19. *Journal of Thrombosis and Haemostasis*, *18*, 1995–2002, <https://doi.org/10.1111/jth.14888>.
- Owens, A. P. 3rd, & Mackman, N. (2011). Microparticles in hemostasis and thrombosis. *Circulation Research*, *108*, 1284–1297, <https://doi.org/10.1161/CIRCRESAHA.110.233056>.
- Païdassi, H., Tacnet-Delorme, P., Garlatti, V., Darnault, C., Ghebrehiwet, B., Gaboriaud, C., Arlaud, G. J., & Frachet, P. (2008). C1q binds phosphatidylserine and likely acts as a multiligand-bridging molecule in apoptotic cell recognition. *Journal of Immunology*, *180*, 2329–2338.
- Polasky, C., Wendt, F., Pries, R., & Wollenberg, B. (2020). Platelet induced functional alteration of CD4(+) and CD8(+) T cells in HNSCC. *International Journal of Molecular Sciences*, *21*, 7507, <https://doi.org/10.3390/ijms21207507>.
- Ponomareva, A. A., Nevzorova, T. A., Mordakhanova, E. R., Andrianova, I. A., Rauova, L., Litvinov, R. I., & Weisel, J. W. (2017). Intracellular origin and ultrastructure of platelet-derived microparticles. *Journal of Thrombosis and Haemostasis*, *15*, 1655–1667, <https://doi.org/10.1111/jth.13745>.
- Reininger, A. J., Heijnen, H. F., Schumann, H., Specht, H. M., Schramm, W., & Ruggeri, Z. M. (2006). Mechanism of platelet adhesion to von Willebrand factor and microparticle formation under high shear stress. *Blood*, *107*, 3537–3545, <https://doi.org/10.1182/blood-2005-02-0618>.
- Rha, M. S., Jeong, H. W., Ko, J. H., Choi, S. J., Seo, I. H., Lee, J. S., Sa, M., Kim, A. R., Joo, E. J., Ahn, J. Y., Kim, J. H., Song, K. H., Kim, E. S., Oh, D. H., Ahn, M. Y., Choi, H. K., Jeon, J. H., Choi, J. P., Kim, H. B., ... Shin, E. C. (2021). PD-1-Expressing SARS-CoV-2-Specific CD8(+) T Cells Are Not Exhausted, but Functional in Patients with COVID-19. *Immunity*, *54*, 44–52 e43, <https://doi.org/10.1016/j.immuni.2020.12.002>.
- Ridger, V. C., Boulanger, C. M., Angelillo-Scherrer, A., Badimon, L., Blanc-Brude, O., Bochaton-Piallat, M. L., Boilard, E., Buzas, E. I., Caporali, A., Dignat-George, F., Evans, P. C., Lacroix, R., Lutgens, E., Ketelhuth, D. F. J., Nieuwland, R., Toti, F., Tunon, J., Weber, C., & Hofer, I. E. (2017). Microvesicles in vascular homeostasis and diseases. Position Paper of the European Society of Cardiology (ESC) Working Group on Atherosclerosis and Vascular Biology. *Thrombosis and Haemostasis*, *117*, 1296–1316, <https://doi.org/10.1160/TH16-12-0943>.
- Rolfes, V., Idel, C., Pries, R., Plötze-Martin, K., Habermann, J., Gemoll, T., Bohnet, S., Latz, E., Ribbat-Idel, J., Franklin, B. S., & Wollenberg, B. (2018). PD-L1 is expressed on human platelets and is affected by immune checkpoint therapy. *Oncotarget*, *9*, 27460–27470, <https://doi.org/10.18632/oncotarget.25446>.
- Rydzynski Moderbacher, C., Ramirez, S. I., Dan, J. M., Grifoni, A., Hastie, K. M., Weiskopf, D., Belanger, S., Abbott, R. K., Kim, C., Choi, J., Kato, Y., Crotty, E. G., Kim, C., Rawlings, S. A., Mateus, J., Tse, L. P. V., Frazier, A., Baric, R., Peters, B., ... Crotty, S. (2020). Antigen-Specific Adaptive Immunity to SARS-CoV-2 in Acute COVID-19 and Associations with Age and Disease Severity. *Cell*, *183*, 996–1012 e1019, <https://doi.org/10.1016/j.cell.2020.09.038>.
- Sachs, A. B. (2000). Cell cycle-dependent translation initiation: IRES elements prevail. *Cell*, *101*, 243–245, [https://doi.org/10.1016/s0092-8674\(00\)80834-x](https://doi.org/10.1016/s0092-8674(00)80834-x).
- Sallusto, F., Geginat, J., & Lanzavecchia, A. (2004). Central memory and effector memory T cell subsets: Function, generation, and maintenance. *Annual Review of Immunology*, *22*, 745–763, <https://doi.org/10.1146/annurev.immunol.22.012703.104702>.
- Scholzen, T., & Gerdes, J. (2000). The Ki-67 protein: From the known and the unknown. *Journal of Cellular Physiology*, *182*, 311–322, [https://doi.org/10.1002/\(sici\)1097-4652\(200003\)182:3<311::Aid-jcp1>3.0.Co;2-9](https://doi.org/10.1002/(sici)1097-4652(200003)182:3<311::Aid-jcp1>3.0.Co;2-9).

- Sekine, T., Perez-Potti, A., Rivera-Ballesteros, O., Strålin, K., Gorin J. B., Olsson A., Llewellyn-Lacey, S., Kamal, H., Bogdanovic, G., Muschiol S., Wullmann D. J., Kammann, T., Emgård, J., Parrot, T., Folkesson, E., Karolinska COVID-19 Study Group, Rooyackers, O., Eriksson, L. I., Henter, J. I., ... Buggert, M. (2020). Robust T cell immunity in convalescent individuals with asymptomatic or mild COVID-19. *Cell* 183, 158–168 e114, <https://doi.org/10.1016/j.cell.2020.08.017>.
- Sette, A., & Crotty, S. (2021). Adaptive immunity to SARS-CoV-2 and COVID-19. *Cell*, 184, 861–880, <https://doi.org/10.1016/j.cell.2021.01.007>.
- Sims, P. J., Faioni, E. M., Wiedmer, T., & Shattil, S. J. (1988). Complement proteins C5b-9 cause release of membrane vesicles from the platelet surface that are enriched in the membrane receptor for coagulation factor Va and express prothrombinase activity. *Journal of Biological Chemistry*, 263, 18205–18212.
- Song, J. W., Zhang, C., Fan, X., Meng, F. P., Xu, Z., Xia, P., Cao, W. J., Yang, T., Dai, X. P., Wang, S. Y., Xu, R. N., Jiang, T. J., Li, W. G., Zhang, D. W., Zhao, P., Shi, M., Agrati, C., Ippolito, G., Maeurer, M., ... Zhang, J. Y. (2020). Immunological and inflammatory profiles in mild and severe cases of COVID-19. *Nature Communications*, 11, 3410, <https://doi.org/10.1038/s41467-020-17240-2>.
- Song, J., So, T., Cheng, M., Tang, X., & Croft, M. (2005). Sustained survivin expression from OX40 costimulatory signals drives T cell clonal expansion. *Immunity*, 22, 621–631, <https://doi.org/10.1016/j.immuni.2005.03.012>.
- Song, W. C., & FitzGerald, G. A. (2020). COVID-19, microangiopathy, hemostatic activation, and complement. *Journal of Clinical Investigation*, 130, 3950–3953, <https://doi.org/10.1172/JCI140183>.
- Su, Y., Chen, D., Yuan, D., Lausted, C., Choi, J., Dai, C. L., Voillet, V., Duvvuri, V. R., Scherler, K., Troisch, P., Baloni, P., Qin, G., Smith, B., Kornilov, S. A., Rostomily, C., Xu, A., Li, J., Dong, S., Rothchild, A., ... Heath, J. R. (2020). Multi-omics resolves a sharp disease-state shift between mild and moderate COVID-19. *Cell*, 183, 1479–1495 e1420, <https://doi.org/10.1016/j.cell.2020.10.037>.
- Tan, A. T., Linster, M., Tan, C. W., Le Bert, N., Chia, W. N., Kunasegaran, K., Zhuang, Y., Tham, C. Y. L., Chia, A., Smith, G. J. D., Young, B., Kalimuddin, S., Low, J. G. H., Lye, D., Wang, L. F., & Bertoletti, A. (2021). Early induction of functional SARS-CoV-2-specific T cells associates with rapid viral clearance and mild disease in COVID-19 patients. *Cell Reports*, 34(6), 108728, <http://doi.org/10.1016/j.celrep.2021.108728>.
- Tan, L. A., Yu, B., Sim, F. C., Kishore, U., & Sim, R. B. (2010). Complement activation by phospholipids: The interplay of factor H and Clq. *Protein Cell*, 1, 1033–1049, <https://doi.org/10.1007/s13238-010-0125-8>.
- Tang, N., Li, D., Wang, X., & Sun, Z. (2020). Abnormal coagulation parameters are associated with poor prognosis in patients with novel coronavirus pneumonia. *Journal of Thrombosis and Haemostasis*, 18, 844–847, <https://doi.org/10.1111/jth.14768>.
- Teuwen, L. A., Geldhof, V., Pasut, A., & Carmeliet, P. (2020). COVID-19: the vasculature unleashed. *Nature Reviews Immunology*, 20, 389–391, <https://doi.org/10.1038/s41577-020-0343-0>.
- Trautz, B., Wiedemann, H., Lüchtenborg, C., Pierini, V., Kranich, J., Glass, B., Kräusslich, H.-G., Brocker, T., Pizzato, M., Ruggieri, A., Brügger, B., & Fackler, O. T. (2017). The host-cell restriction factor SERINC5 restricts HIV-1 infectivity without altering the lipid composition and organization of viral particles. *Journal of Biological Chemistry*, 292(33), 13702–13713, <http://doi.org/10.1074/jbc.m117.797332>.
- van der Zee, P. M., Biró, E., Ko, Y., de Winter, R. J., Hack, C. E., Sturk, A., & Nieuwland, R. (2006). P-selectin- and CD63-exposing platelet microparticles reflect platelet activation in peripheral arterial disease and myocardial infarction. *Clinical Chemistry*, 52, 657–664, <https://doi.org/10.1373/clinchem.2005.057414>.
- Wang, R. H., Phillips, G. Jr., Medof, M. E., & Mold, C. (1993). Activation of the alternative complement pathway by exposure of phosphatidylethanolamine and phosphatidylserine on erythrocytes from sickle cell disease patients. *Journal of Clinical Investigation*, 92, 1326–1335, <https://doi.org/10.1172/JCI116706>.
- Wölfel, R., Corman, V. M., Guggemos, W., Seilmaier, M., Zange, S., Müller, M. A., Niemeyer, D., Jones, T. C., Vollmar, P., Rothe, C., Hoelscher, M., Bleicker, T., Brünink, S., Schneider, J., Ehmann, R., Zwirgmaier, K., Drosten, C., & Wendtner, C. (2020). Virological assessment of hospitalized patients with COVID-2019. *Nature*, 581, 465–469, <https://doi.org/10.1038/s41586-020-2196-x>.
- WorldHealthOrganization (2020). Novel Coronavirus: COVID-19 Therapeutic Trial Synopsis. *WHO R&D Blueprint*, Draft February 18, 2020. www.who.int/blueprint/priority-diseases/key-action/COVID-19_Treatment_Trial_Design_Master_Protocol_synopsis_Final_18022020.pdf
- Yang, X., Yu, Y., Xu, J., Shu, H., Xia, J., Liu, H., Wu, Y., Zhang, L., Yu, Z., Fang, M., Yu, T., Wang, Y., Pan, S., Zou, X., Yuan, S., & Shang, Y. (2020). Clinical course and outcomes of critically ill patients with SARS-CoV-2 pneumonia in Wuhan, China: A single-centered, retrospective, observational study. *The Lancet Respiratory Medicine*, 8, 475–481, [https://doi.org/10.1016/S2213-2600\(20\)30079-5](https://doi.org/10.1016/S2213-2600(20)30079-5).
- Zaid, Y., Puhm, F., Allaey, I., Naya, A., Oudghiri, M., Khalki, L., Limami, Y., Zaid, N., Sadki, K., Ben El Haj, R., Mahir, W., Belayachi, L., Belefquih, B., Benouda, A., Cheikh, A., Langlois, M. A., Cherrah, Y., Flamand, L., Guessous, F., & Boilard, E. (2020). Platelets can associate with SARS-Cov-2 RNA and are hyperactivated in COVID-19. *Circulation Research*, 127, 1404–18, <https://doi.org/10.1161/CIRCRESAHA.120.317703>.
- Zhang, Y., Xiao, M., Zhang, S., Xia, P., Cao, W., Jiang, W., Chen, H., Ding, X., Zhao, H., Zhang, H., Wang, C., Zhao, J., Sun, X., Tian, R., Wu, W., Wu, D., Ma, J., Chen, Y., Zhang, D., ... Zhang, S. (2020). Coagulopathy and antiphospholipid antibodies in patients with Covid-19. *The New England Journal of Medicine*, 382, e38, <https://doi.org/10.1056/NEJMc2007575>.
- Zheng, H. Y., Zhang, M., Yang, C. X., Zhang, N., Wang, X. C., Yang, X. P., Dong, X. Q., & Zheng, Y. T. (2020). Elevated exhaustion levels and reduced functional diversity of T cells in peripheral blood may predict severe progression in COVID-19 patients. *Cellular & Molecular Immunology*, 17, 541–543, <https://doi.org/10.1038/s41423-020-0401-3>.
- Zheng, M., Gao, Y., Wang, G., Song, G., Liu, S., Sun, D., Xu, Y., & Tian, Z. (2020). Functional exhaustion of antiviral lymphocytes in COVID-19 patients. *Cellular & Molecular Immunology*, 17, 533–535, <https://doi.org/10.1038/s41423-020-0402-2>.
- Zhou, R., To, K. K., Wong, Y. C., Liu, L., Zhou, B., Li, X., Huang, H., Mo, Y., Luk, T. Y., Lau, T. T., Yeung, P., Chan, W. M., Wu, A. K., Lung, K. C., Tsang, O. T., Leung, W. S., Hung, I. F., Yuen, K. Y., & Chen, Z. (2020). Acute SARS-CoV-2 infection impairs dendritic cell and T cell responses. *Immunity*, 53, 864–877 e865, <https://doi.org/10.1016/j.immuni.2020.07.026>.

SUPPORTING INFORMATION

Additional supporting information may be found in the online version of the article at the publisher's website.

How to cite this article: Rausch, L., Lutz, K., Schifferer, M., Winheim, E., Gruber, R., Oesterhaus, E. F., Rinke, L., Hellmuth, J. C., Scherer, C., Muenchhoff, M., Mandel, C., Bergwelt-Baildon, M., Simons, M., Straub, T., Krug, A. B., Kranich, J., & Brocker, T. (2021). Binding of phosphatidylserine-positive microparticles by PBMCs classifies disease severity in COVID-19 patients. *Journal of Extracellular Vesicles*, 10, e12173. <https://doi.org/10.1002/jev2.12173>

9.4 Binding of phosphatidylserine-positive microparticles by PBMCs classifies disease severity in COVID-19 patients.

Rausch L, Lutz K, Schifferer M, Winheim E, Gruber R, Oesterhaus EF, Rinke L, Hellmuth JC, Scherer C, Muenchhoff M, Mandel C, Bergwelt-Baildon M, Simons M, Straub T, Krug AB, **Kranich J***, Brocker T*. J Extracell Vesicles. 2021 Dec;10(14):e12173. * equally contributed last author.

RESEARCH ARTICLE

Binding of phosphatidylserine-positive microparticles by PBMCs classifies disease severity in COVID-19 patients

Lisa Rausch¹ | Konstantin Lutz¹ | Martina Schifferer^{2,3} | Elena Winheim¹ |
 Rudi Gruber⁴ | Elina F. Oesterhaus^{5,6} | Linus Rinke¹ | Johannes C. Hellmuth^{5,7} |
 Clemens Scherer^{5,8} | Maximilian Muenchhoff^{5,6,9} | Christopher Mandel^{5,10} |
 Michael Bergwelt-Baildon^{5,7} | Mikael Simons^{2,3,11} | Tobias Straub¹² | Anne B. Krug¹ |
 Jan Kranich¹  | Thomas Brocker¹ 

¹ Institute for Immunology, Biomedical Center (BMC), Faculty of Medicine, LMU Munich, Munich, Germany

² German Center for Neurodegenerative Diseases (DZNE), Munich, Germany

³ Munich Cluster of Systems Neurology (Synergy), Munich, Germany

⁴ bene pharmaChem GmbH & Co.KG., Geretsried, Germany

⁵ COVID-19 Registry of the LMU Munich (CORKUM), University Hospital, LMU Munich, Munich, Germany

⁶ Max von Pettenkofer Institute & Gene Center, Virology, National Reference Center for Retroviruses, LMU München, Munich, Germany

⁷ Department of Medicine III, University Hospital, LMU Munich, Munich, Germany

⁸ Department of Medicine I, University Hospital, LMU Munich, Munich, Germany

⁹ German Center for Infection Research (DZIF), partner site Munich, Germany

¹⁰ Department of Medicine IV, University Hospital, LMU Munich, Munich, Germany

¹¹ Institute of Neuronal Cell Biology, Technical University of Munich, Munich, Germany

¹² Core facility Bioinformatics, Biomedical Center (BMC), Faculty of Medicine, LMU Munich, Munich, Germany

Correspondence

Prof. Dr. Thomas Brocker, Institute for Immunology, Biomedical Center (BMC), Faculty of Medicine, LMU Munich, Großhaderner Str. 9, D-82152 Planegg-Martinsried, Germany.
 Email: brocker@lmu.de

Jan Kranich and Thomas Brocker shared senior authorship.

Funding information

Deutsche Forschungsgemeinschaft (DFG, German Research Foundation), Grant/Award Numbers: Project-ID 210592381 - SFB 1054: TP B03, A06, Project-ID 369799452 - SFB/TR237: TP B14, Project-ID 391217598 - KR2199/10-1; Bavarian State Ministry of Science and the Arts

Abstract

Infection with SARS-CoV-2 is associated with thromboinflammation, involving thrombotic and inflammatory responses, in many COVID-19 patients. In addition, immune dysfunction occurs in patients characterised by T cell exhaustion and severe lymphopenia. We investigated the distribution of phosphatidylserine (PS), a marker of dying cells, activated platelets and platelet-derived microparticles (PMP), during the clinical course of COVID-19. We found an unexpectedly high amount of blood cells loaded with PS⁺ PMPs for weeks after the initial COVID-19 diagnosis. Elevated frequencies of PS⁺ PMP⁺ PBMCs correlated strongly with increasing disease severity. As a marker, PS outperformed established laboratory markers for inflammation, leucocyte composition and coagulation, currently used for COVID-19 clinical scoring. PS⁺ PMPs preferentially bound to CD8⁺ T cells with gene expression signatures of proliferating effector rather than memory T cells. As PS⁺ PMPs carried programmed death-ligand 1 (PD-L1), they may affect T cell expansion or function. Our data provide a novel marker for disease severity and show that PS, which can trigger the blood coagulation cascade, the complement system, and inflammation, resides

This is an open access article under the terms of the [Creative Commons Attribution-NonCommercial-NoDerivs License](https://creativecommons.org/licenses/by-nc-nd/4.0/), which permits use and distribution in any medium, provided the original work is properly cited, the use is non-commercial and no modifications or adaptations are made.

© 2021 The Authors. *Journal of Extracellular Vesicles* published by Wiley Periodicals, LLC on behalf of the International Society for Extracellular Vesicles

on activated immune cells. Therefore, PS may serve as a beacon to attract thromboinflammatory processes towards lymphocytes and cause immune dysfunction in COVID-19.

KEYWORDS

apoptosis, CD8+ T cells, COVID-19, lymphopenia, phosphatidylserine, platelet-derived microparticle, SARS-CoV-2, thromboinflammation

1 | INTRODUCTION

The recently emerged human pathogenic severe acute respiratory syndrome coronavirus 2 (SARS-CoV-2) causes various clinical syndromes, summarised under coronavirus disease-2019 (COVID-19). The excessive inflammatory response associated with COVID-19 can cause severe complications such as acute respiratory distress syndrome, septic shock and multi-organ failure (Guan et al., 2020; MacLaren et al., 2020; Wölfel et al., 2020). A significant cause of morbidity and mortality in COVID-19 patients is 'thromboinflammation'. Although not fully understood, inflammation through complement activation and cytokine release, platelet overactivity and apoptosis (thrombocytopenia), as well as coagulation abnormalities (coagulopathy) play critical roles in this complex clinical picture (reviewed in Gu et al. (2021)).

Similar vascular complications occur in the antiphospholipid syndrome, where autoantibodies target phosphatidylserine (PS)/prothrombin complexes (Corban et al., 2017). This syndrome may manifest itself in COVID-19 patients (Zhang et al., 2020), linking PS to thromboinflammation. PS is a plasma membrane component actively retained by an ATP-requiring process at the inner membrane surface in living cells. PS retention stops, for example, during cell death or when cells release PS-containing microparticles or enveloped viruses. Then PS relocates to the outer layer of the cell membrane, where it can interact with extracellular proteins, including coagulation and complement systems. PS activates the alternative and the classical complement pathways (Mevorach et al., 1998; Tan et al., 2010; Wang et al., 1993) by binding to complement C3 (Huong et al., 2001), C3bi (Mevorach et al., 1998) and C1q (Païdassi et al., 2008). Activated platelets release platelet-derived microparticles (PMPs), which cause thrombin formation, coagulation, activation of the complement system, and inflammation in a PS-dependent manner (Melki et al., 2017; Owens & Mackman, 2011; Ridger et al., 2017).

Patients with severe COVID-19 also show striking immune dysregulation, the reasons for which are not entirely understood. A direct correlation between blood clotting components and the immune response exists (Su et al., 2020). Various immune abnormalities such as increased inflammatory cytokines (Del Valle et al., 2020), immune cell exhaustion (Zheng et al., 2020) and general lymphopenia (Cao, 2020; Chen et al., 2020; Huang et al., 2020; Liu et al., 2020; Yang et al., 2020,) correlate with disease severity (Mathew et al., 2020). T cell lymphopenia (Laing et al., 2020), probably caused by excessive apoptotic T cell death similar to sepsis (Hotchkiss & Nicholson, 2006), is of particular relevance as SARS-CoV-2-specific T cell responses control and resolve the primary infection (Liao et al., 2020; Rydzynski Moderbacher et al., 2020; Sekine et al., 2020; Zhou et al., 2020). In fatal COVID-19, the adaptive immune response starts too late (reviewed in Sette and Crotty (2021)), while its rapid onset would be highly beneficial (Braun et al., 2020; Rydzynski Moderbacher et al., 2020; Tan et al., 2020). However, the reasons and precise mechanisms for adaptive immune disturbance, lymphopenia and thromboinflammation in COVID-19 remain poorly defined.

To investigate these aspects of COVID-19 in more detail, we interrogated PBMC of 54 patients from the COVID-19 Registry of the LMU Munich (CORKUM) and 35 healthy and 12 recovered donors between April 2020 and February 2021. We performed image flow cytometry (IFC) and image analysis by deep learning algorithms (Kranich et al., 2020) using highly sensitive reagents specific for PS (Kranich et al., 2020; Trautz et al., 2017). COVID-19 blood samples contained abnormally high numbers of PS⁺ peripheral blood mononuclear cells (PBMC). Although PS is a marker for dying cells, nearly all PS⁺ cells were living cells associated with PS⁺CD41⁺ PMPs or larger PS⁺CD41⁺ platelet fragments. The grade of PS⁺ PMP-associated PBMC correlated with lymphopenia and disease severity, showing a higher correlation than commonly used laboratory diagnostic markers such as IL-6, D-Dimer (Mathew et al., 2020) and C-reactive protein (CRP) (Li et al., 2020). PS⁺ PMPs were strongly associated with dividing effector CD8⁺ T cells with upregulated expression of cell-cycle genes. Fractions of T cell-associated PS⁺ PMPs carried CD274 (PD-L1), which could impact the survival of T cells and potentially contribute to functional inhibition and lymphopenia. As PS⁺ PMPs remained associated with PBMC several weeks after the initial SARS-CoV2-diagnosis, they might sustain the adverse inflammatory and prothrombotic effects over a long time and contribute to the complex clinical picture of thromboinflammation (reviewed in (Gu et al., 2021; Lind, 2021)). Together, our findings reveal an extensive association of PS⁺ PMPs with lymphocytes as a novel marker to classify COVID-19 disease severity and a potentially relevant contributor to thromboinflammation and lymphocyte dysfunction.

2 | RESULTS

2.1 | PBMC from COVID-19 patients show substantial PS surface exposure

To test if immune cell death rates were elevated during COVID-19, we analysed peripheral blood mononuclear cells (PBMC) of COVID-19 patients and compared them to those from healthy and recovered donors. Table S1 show clinical metadata for our cohort of COVID-19 patients and control groups. One hallmark of apoptotic cell death is the PS exposure on the outer membrane surface of cells. To reveal PS on PBMC, we utilised recombinant Milk fat globule-EGF factor 8 protein (MFG-E8) derived recombinant proteins, which bind PS under physiological conditions with high sensitivity on apoptotic cells and subcellular PS⁺ extracellular vesicles (EVs) (Kranich et al., 2020; Trautz et al., 2017). Flow cytometry results showed that the frequencies of PS⁺ cells in blood from all COVID-19 patients were significantly higher than in PBMC from healthy or recovered donors (Figure 1a). To analyse if this data can classify patients according to disease severity, we employed the World Health Organization's (WHO) eight-point ordinal scale for COVID-19 trial endpoints (WorldHealthOrganization, 2020) (Figure 1b). In our patient cohort, the scores WHO 2 and WHO 7 were absent. We combined WHO scores into 'mild' (WHO 1–3), 'moderate' (WHO 4) and 'severe' (WHO 5–8) groups for the subsequent analyses. Additionally, we also included a group of healthy donors (HD, $n = 30$) and recovered patients ($n = 12$, >69 days post 1st SARS-CoV-2⁺ diagnosis by PCR, either never hospitalised or released from the hospital with WHO score 1–2). The frequencies of PS⁺ PBMC increased with severity of COVID-19 disease in the following order: healthy controls (WHO 0) < recovered patients < WHO 1–3 (mild) < WHO 4 (moderate) < WHO 5–8 (severe) (Figure 1c). In severely diseased patients, 30%–90% of all PBMC were PS⁺ (Figure 1c). Accordingly, the individual WHO scores positively correlated with high significance with the frequencies of PS⁺ PBMC of COVID-19 patients. Importantly, the correlation of PS⁺ PBMC against WHO_{max} was much stronger than against the WHO score at sampling time (Figure S1A and 1d).

In order to assess whether the frequency of PS⁺ PBMCs is an independent predictor for a severe disease outcome such as ventilation requirement (Figure 1e) or death (Figure 1f) within our cohort, we performed an area under the receiver operating characteristic curve (AUROC) analysis. Frequency of PS⁺ PBMC was better for predicting ventilation requirement (AUC 0.760, threshold 41.15, specificity 0.53, sensitivity 0.91; Figure 1e) and death (AUC 0.907, threshold 43.525, specificity 0.90, sensitivity 0.83; Figure 1f) than C-reactive protein (CRP), D-Dimer, Ferritin, Fibrinogen, international normalised ratio (INR), partial thromboplastin time (PTT) or number of platelets (Figure S1B and C). Only IL-6 had better prediction scores for ventilation requirement (AUC 0.841, threshold 19.975, specificity 0.71, sensitivity 0.87; Figure 1b) and death (AUC 0.949, threshold 45.05, specificity 0.80, sensitivity 1; Figure S1C). Kaplan-Meier curves show that patients with a frequency of PS⁺ PBMCs higher than 41.15% or 43.53% had a higher incidence of requiring ventilation or succumbing to disease, respectively (Figure 1e). However, our study was an exploratory study with a limited number of patients. Therefore, the predictive capacity of the frequency of PS⁺ PBMCs needs to be validated in a larger cohort.

The blood sampling time points differed within our patient cohort due to organisational reasons. We investigated whether the sampling time point would affect the results and performed PS measurements at several time points for selected patients. These data show that although the frequencies of PS⁺ PBMCs show some variability, we detected strongly elevated levels for up to 30 days (Figure 2A). In contrast, in recovered patients, PS⁺ PBMC returned to the levels of healthy controls. To further assess the influence of sampling time and PS⁺ PBMC frequency, we performed a Spearman correlation test with time since the first diagnosis (FD) or time since symptom onset and found no correlation with PS⁺ PBMC frequencies (Figure S2B). Furthermore, there was also no correlation between the frequency of PS⁺ PBMC and age in healthy donors or recovered patients (Figure S2C).

In summary, the number of PS⁺ PBMC in the blood of COVID-19 patients represents a new parameter that correlates strongly with disease severity.

2.2 | PBMC in COVID-19 patients are associated with PS⁺ EVs, and the amount correlates with the severity of the disease

PS exposure occurs on various cells and cell-derived microparticles, including tumour cells, erythrocytes, neutrophils, monocytes, endothelial cells, activated platelets and PMPs. PS-exposure is a significant regulator of the blood coagulation system (reviewed in Connor et al. (2010)). We have recently shown that most PS⁺ cells in the spleen of virus-infected mice are not dying, but cells carried PS⁺ EVs (Kranich et al., 2020). To determine whether PS⁺ PBMC in COVID-19 patients were apoptotic cells contributing to the described lymphopenia or EV⁺ cells, we analysed the images of PS⁺ PBMC acquired by IFC. Some cells showed almost entirely PS⁺ cell bodies with strongly labeled apoptotic blebs, typical for cell death (Figure 2a). These cells still have an intact cell membrane since they did not stain with the live/dead dye used to exclude necrotic cells from the analysis. However, we also detected many cells with the characteristic round brightfield image morphology of living cells, with only one or a few intensely PS⁺ structures of subcellular size (Figure 2a). These particles resembled cell-associated PS⁺ EVs, which we recently identified in virus-infected mice (Kranich et al., 2020). We next used a machine learning-based convolutional

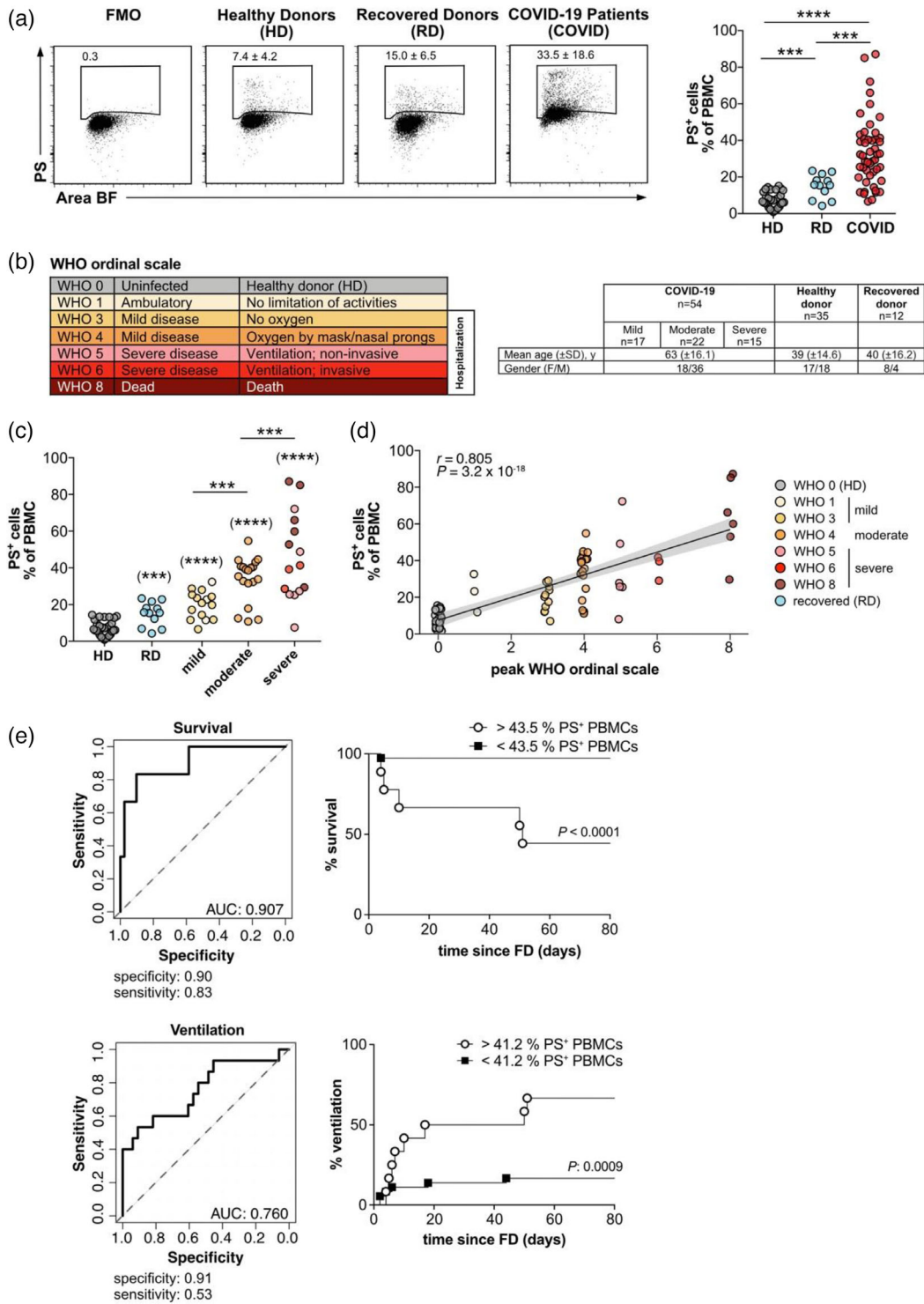


FIGURE 1 The frequencies of PS⁺ PBMC from COVID patients correlates with disease severity. (a) PBMC from COVID-19 patients (COVID), healthy donors (HD) and recovered donors (RD) were stained for PS and analysed by flow cytometry. Numbers in dot plots correspond to the percentage of PS⁺ cells in the gate shown. The right-hand graph shows the summary of all percentages. (b) Overview of WHO ordinal scale and colour code used. Table shows the number, age and gender of the different study groups. (c) Grouped analysis of the data from (a). (d) Same as (c), but plotted against the WHO ordinal scale ($n = 38-79$). PS⁺ PBMCs correlate with the severity of the disease. The plot shows the Spearman correlation test and linear regression line with 95% confidence interval shading (A, C, D: HD, $n = 30$; RD, $n = 12$; COVID, $n = 49$). Significance in (a) and (c) was determined by Mann-Whitney test: * $p < 0.05$, ** $p < 0.01$, *** $p < 0.001$ and **** $p < 0.0001$. Asterisks in brackets show statistically significant differences as compared to HD. FMO: Fluorescence minus one control; Area BF: Area bright field. (e) ROC curve analysis of PS⁺ PBMCs from COVID-19 patients ($n = 49$) for predicting survival (upper plot) and ventilation (lower plot). AUC values (95% CI) (left hand panels) and Kaplan-Meier survival and ventilation curves of patients grouped according to the indicated PS⁺ PBMCs-thresholds (right hand panels) are shown. Time represents the number of days from first diagnosis (FD). Optimal cut-off values for % PS⁺ PBMCs were determined by ROC analysis and used to define the two groups. First measured values of % PS⁺ PBMCs were used for analysis. Significance was determined by Log-rank test

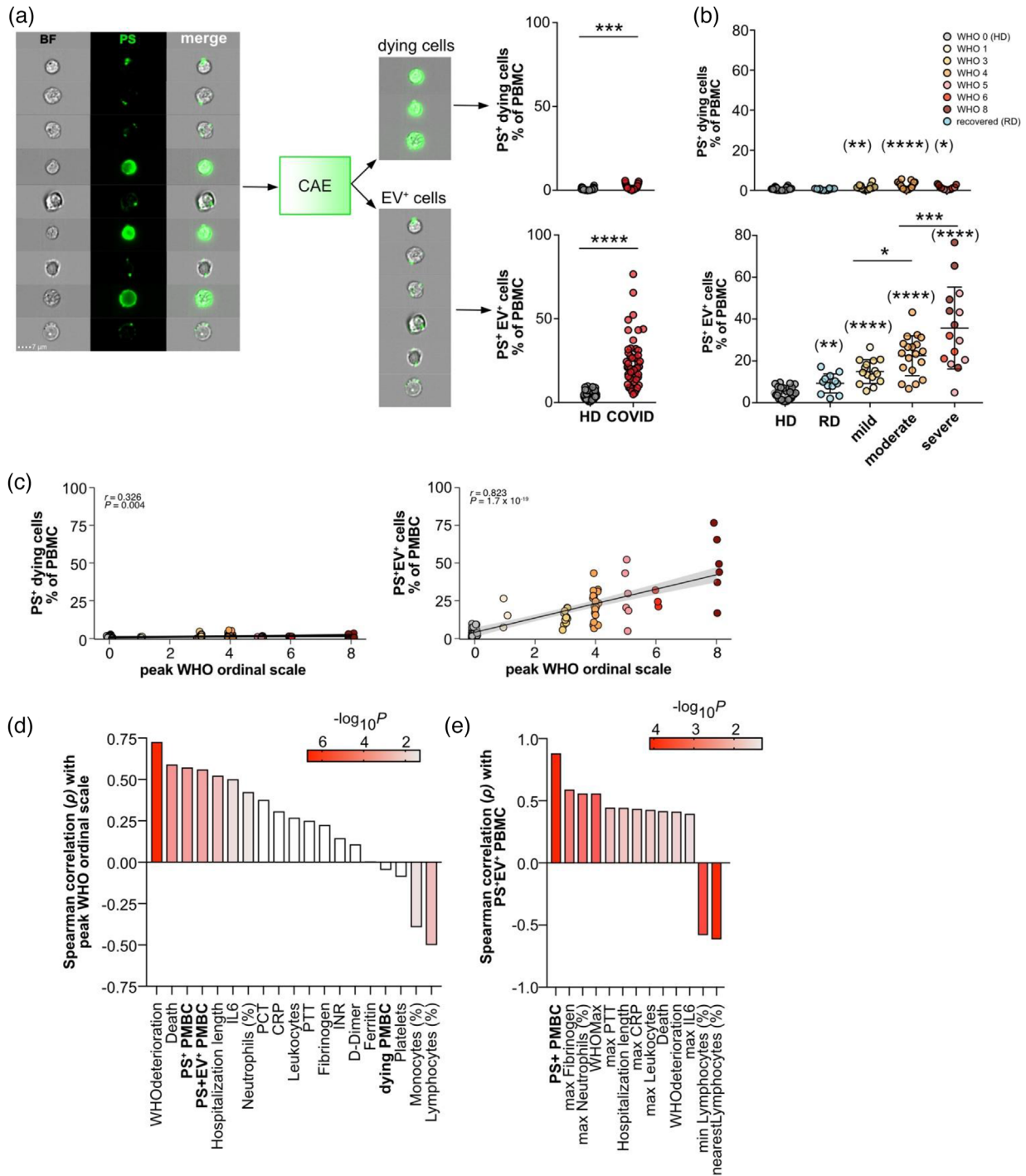


FIGURE 2 EV⁺ cells, but not dying cells from COVID-19 patients correlate with disease severity. (a) PBMC from healthy donors (HD, *n* = 30) and COVID (*n* = 49) were analysed by imaging flow cytometry (IFC). To discriminate dying and EV⁺ cells, PBMC were analysed using IDEAS, CAE and FlowJo. PS⁺ cells were gated, and their TIF images (16-bit, raw) exported using the IDEAS software. CAE results with the classification dying/EV⁺ were re-imported into IDEAS, and separate FCS files containing all cells or only PS⁺/dying cells and PS⁺/EV⁺ cells were generated for further analysis in FlowJo. Dying (a, upper panel) and EV⁺ (a, lower panel) cells are shown as % of PBMC. (b) Results from a) are plotted against groups HD (*n* = 30), RD (*n* = 12), mild (*n* = 15), moderate (*n* = 19) and severe disease (*n* = 15) for dying cells (upper panel) and EV⁺ cells (lower panel). (c) Plotting of the data from (b) against WHO ordinal scale. The plot shows the Spearman correlation test and linear regression line with 95% confidence interval shading (*n* = 38–79). (d) Summary of correlations of selected ‘nearest’ (*n* = 23–49) laboratory and clinical parameters with peak WHO ordinal scale or and selected (e) our measurements of PS⁺, PS⁺EV⁺ and dying cells (bold) (*n* = 23–49). Significance was determined by Mann-Whitney test: **p* < 0.05, ***p* < 0.01, ****p* < 0.001 and *****p* < 0.0001. Asterisks in brackets show statistically significant differences as compared to HD

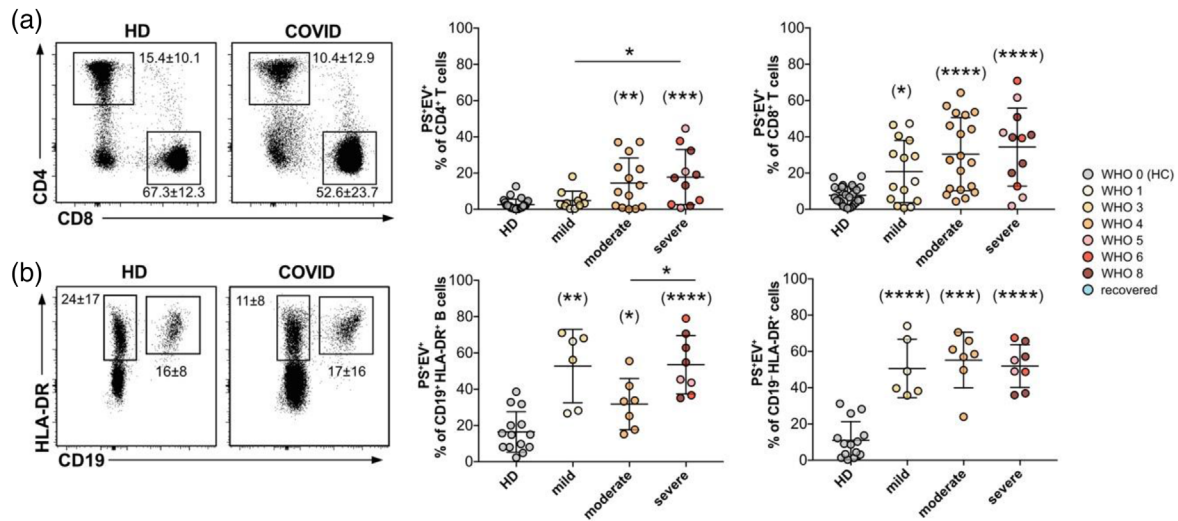


FIGURE 3 Identification of EV⁺ cells in PBMC from COVID-patients and healthy donors. PBMC were analysed by IFC (gating strategy shown in Figure S3A and B). PS⁺ CD4⁺ and CD8⁺ T cells (a) and CD19⁺ HLA-DR⁺ B cells and CD19⁺ HLA-DR⁺ cells (containing mainly dendritic cells, monocytes) (b) were classified as PS⁺EV⁺ using the CAE and their total frequencies were plotted against HD (B, $n = 14$; A, CD4, $n = 24$; a, CD8, $n = 27$), mild (b, $n = 6$; A, CD4, $n = 11$; A, CD8, $n = 15$), moderate (B, $n = 7$; a, CD4, $n = 14$; A, CD8, $n = 19$), severe (b, $n = 8$; a, CD4, $n = 11$; a, CD8, $n = 12$) disease groups. Numbers next to the gates show the mean percentage \pm SD of all cells depicted inside the dot plot that lie within the respective gate, while the graphs show the average frequency \pm SD of EV⁺ cells within the analysed subpopulation. Significance was determined by Mann-Whitney test: * $p < 0.05$, ** $p < 0.01$, *** $p < 0.001$ and **** $p < 0.0001$. Asterisks in brackets show statistically significant differences as compared to HD

autoencoder (CAE) to group PBMC into bona fide PS⁺ dying cells or cells associated with PS⁺ EVs (Figure 2a), as previously validated (Kranich et al., 2020). After training with pre-defined images of PS⁺ dying or PS⁺ EV-associated cells, the CAE algorithm digitally sorts PS⁺ cells into both categories with high precision (Figure 2a). When we analysed the CAE-classified PS⁺ dying cells and PS⁺EV⁺ cells separately (Figure 2a), we found that the majority of PS⁺ PBMC contained live cells associated with PS⁺ EV-like structures rather than PS⁺ dying cells (Figure 2b). Despite the rarity of dying cells, patients with the score WHO 4 showed the highest frequencies (Figure 2b, upper panel). Furthermore, only PS⁺EV⁺ PBMC, not PS⁺ dying cells, classified the patients into disease score groups 'mild' (WHO 1–3), 'moderate' (WHO 4), and 'severe' (WHO 5–8) and separated them clearly from HD and recovered patients (Figure 2b, lower panel). Similarly, PS⁺EV⁺ PBMC, but not PS⁺ dying cells, showed a highly significant correlation with WHO scores (Figure 2c). Several laboratory values that are either increased (leukocytes, IL-6, neutrophils, procalcitonin (PCT), C-reactive protein (CRP), partial thromboplastin time (PTT), D-dimer, etc.) or decreased (lymphocytes) were shown to indicate an unfavorable progression of COVID-19 disease (Lippi & Plebani, 2020).

We confirmed these correlations in our patient cohort (Figure S4A). The frequencies of PS⁺EV⁺ and PS⁺ PBMC ranked in the top groups of measurements among inflammatory and coagulation parameters such as IL-6, PCT, CRP, PTT, D-Dimer and others (Figure S4A). The strongest negative correlations existed with low lymphocyte counts (Figure S4A). For better comparability, we focussed next only on those values determined from the same blood draw or close to our PS-measurements ('nearest values' in Figure S4A, shown in Figure 2d). Here, both PS⁺EV⁺ PBMC and PS⁺ PBMC correlated better than all other blood parameters with peak WHO ordinal scale (Figure 2d). Moreover, PS⁺EV⁺ PBMC frequencies correlated strongly with parameters of coagulation (fibrinogen, PTT), inflammation (IL-6, CRP) and lymphopenia (lymphocyte counts) (Figure 2e and S4B).

As the frequencies of PS⁺ PBMCs in the blood of COVID-patients turned out to be an independent predictor for a severe disease outcome (Figure 1e), we now wondered if PS⁺EV⁺ PBMCs, which constituted the major part of this population, allows such a prediction. Indeed, the AUROC analysis showed comparable prediction values for ventilation requirement (AUC 0.791, threshold 29, specificity 0.91, sensitivity 0.60) and death (AUC 0.866, threshold 31.4, specificity 0.88, sensitivity 0.83) (Figure S1D). Therefore, our new type of PS analysis allows the detection of subcellular particles associated with PBMC of COVID-19 patients. The percentage of PBMC bound to these PS⁺ particles correlated with the maximal (peak) WHO score of COVID-19 patients and allowed to classify patients with higher significance than some of the previously established medical laboratory parameters (Lippi & Plebani, 2020).

2.3 | PS⁺ EVs bind to several PBMC populations

Next, we investigated whether PS⁺ EVs would selectively associate with specific PBMC subpopulations. We examined CD4⁺ and CD8⁺ T cells (Figure 3a), CD19⁺ B cells (Figure 3b) and HLA-DR⁺CD19⁻CD3⁻ PBMC (containing mainly monocytes and

dendritic cells as central blood populations, Figure 3b). In general, CD8⁺ T cells were more strongly associated with PS⁺ EVs than CD4⁺ T cells (Figure 3a). However, both T cell subsets showed a similar tendency of increased PS⁺ EV binding in patients with a higher WHO score (Figure 3a). B cells and blood monocyte-containing populations of patients in the different WHO groups were also associated relatively strongly with PS⁺ EVs (Figure 3b). However, there was no actual grading with the severity of the disease. In summary, most blood cells showed a strong association with PS⁺ EVs in the patients. The frequency of PS⁺ EV⁺ CD8⁺ T cells best reflected the severity of COVID-19 disease.

2.4 | PS⁺ EVs associated with PBMC from COVID-19 patients are PS⁺CD41⁺ platelet-derived microparticles

EVs classify according to their size and origin into exosomes (up to 150 nm), microvesicles or microparticles (MPs; 100–1000 nm) and apoptotic EVs or apoptotic bodies (100–5000nm) (Mathieu et al., 2018). To better characterise the EVs associated with lymphocytes in COVID-19 patients, we isolated PS⁺ lymphocytes (B and T cells, PS⁺CD19⁺CD3ε⁺) from COVID-19 patients by FACS. We used recombinantly expressed, biotinylated MFG-E8-derived PS-binding domain mCl, which was multimerised by streptavidin (SA) (mCl-multimer/SA-APC) for PS-detection by flow cytometry (Figure S3C) and mCl-multimer/SA-gold for PS-detection by subsequent transmission electron microscopy (TEM). TEM pictures show cell-associated particles of a subcellular size bound to lymphocytes, which morphologically resemble T cells (Figure 4a–f). Many (Figure 4b, d, and f, open white arrows), but not all EVs (Figure 4c, arrows), were PS⁺, and most EVs were >100 nm in size (Figure 4b, d and f). The particles were mainly round and had different shapes and contained other smaller components, cell contents or organelles (Figure 4b, d, white star). However, we also found PS⁺ tubular elongated structures (Figure 4d, black star). Relatively large particles with highly diverse shapes, including tubular shapes and content are known features of PMPs, 50% of which are PS positive (Arraud et al., 2014; Ponomareva et al., 2017; Reininger et al., 2006). Hyperactivated platelets in COVID-19 patients (Teuwen et al., 2020) are sources for PMPs and contribute to the hypercoagulability state of the disease (Klok et al., 2020; Middeldorp et al., 2020; Tang et al., 2020). Activated platelets can release two types of EVs, (i) smaller exosomes (40–100 nm in diameter) derived by exocytosis from α-granules and the multivesicular body, and (ii) PS⁺ MP (100–1000 nm in size), formed by budding of the plasma membrane (Aatonen et al., 2014; Heijnen et al., 1999). These similarities let us hypothesise that PMPs attach to PBMC of COVID-19 patients.

To test this hypothesis, we stained PBMC from COVID-19 patients for CD41, a platelet marker, part of a fibrinogen-receptor and present on platelet-derived PMPs (Heijnen et al., 1999) (Figure S5 and 4g). Analysis of flow cytometry data of PBMC confirmed our assumption and showed that many PBMC were positive for the platelet marker CD41 (Figure 4g). However, CD41 could not distinguish PBMC from healthy donors and COVID because CD41⁺ PBMC also existed in healthy donors (Figure 4g, CD41⁺). In contrast, PS-positivity alone distinguished PBMC from healthy donors and COVID-19 patients, as PS⁺ PBMC were highly significantly enriched in patients (Figure 4g, PS⁺).

To analyse PS and CD41 and their possible colocalisation, we performed image analysis of PBMC (Figure S5A, B) and T lymphocytes (Figure 4h and i). In COVID-19 patients, we observed a substantial increase of PS⁺CD41⁺ PBMCs and T cells from 7% to 25% and from 2% to 18%, respectively. The increase in CD41[−]PS⁺ cells was not as pronounced but still significant (Figure 4h and i, Figure S5A and B). This finding shows that most PS⁺ cells acquire PS through the binding of CD41⁺ platelets or their PMPs. To investigate whether the cells preferentially bind whole platelets or smaller PMPs, we quantified CD41^{hi} versus CD41^{low} cells. The CD41^{hi} gate contained mainly cells with large CD41⁺ particles attached, which were also visible in the brightfield (BF) channel – presumably whole platelets. In contrast, the cells in the CD41^{low} gate were associated with small, more dimly stained spots that were too small to be visible in the BF channel – presumably PMPs (Figure 4i). While T cells very clearly had a strong preference for PMP binding (15% of CD3⁺ T cells were CD41^{low} and 2% CD41^{hi}, Figure 4i), PBMCs did not show such a clear preference (approx. 15% were CD41^{low}, 9% were CD41^{hi}, Figure S5C). Our data show that PBMCs from COVID-19 patients associate to a high degree with PS⁺ platelets and PMPs, while T cells rarely bind whole platelets, but rather PMPs.

2.5 | PMPs carry markers of activated platelets

SARS-CoV-2-infection causes platelet activation and alters their functions (Manne et al., 2020; Zaid et al., 2020). The results of our study suggested that the PMPs associated with lymphocytes in COVID-19 patients originate from activated CD41⁺ platelets. In addition to PS and CD41, markers such as CD62P (P-selectin) and the tetraspanin CD63 are present on PMPs derived from activated platelets (van der Zee et al., 2006). Our patient cohort showed increased percentages of PS⁺ and CD62P⁺ platelets, both markers for platelet activation (Figure 6a–c), although the increase in CD62P⁺ platelets did not reach statistical significance. When associated with CD8⁺ T cells, platelet-derived molecules PD-L1 (CD274) (Rolfes et al., 2018) and CD86 (Chapman et al., 2012) on PMPs could be potentially negative or positive costimulatory triggers, respectively. Platelets were strongly positive for CD274 (Figure S6B and C), but this was not different between healthy donors and patients (Figure S6B). The same was true for CD86, which we found in similar amounts and generally only very few platelets that were positive for this molecule in both

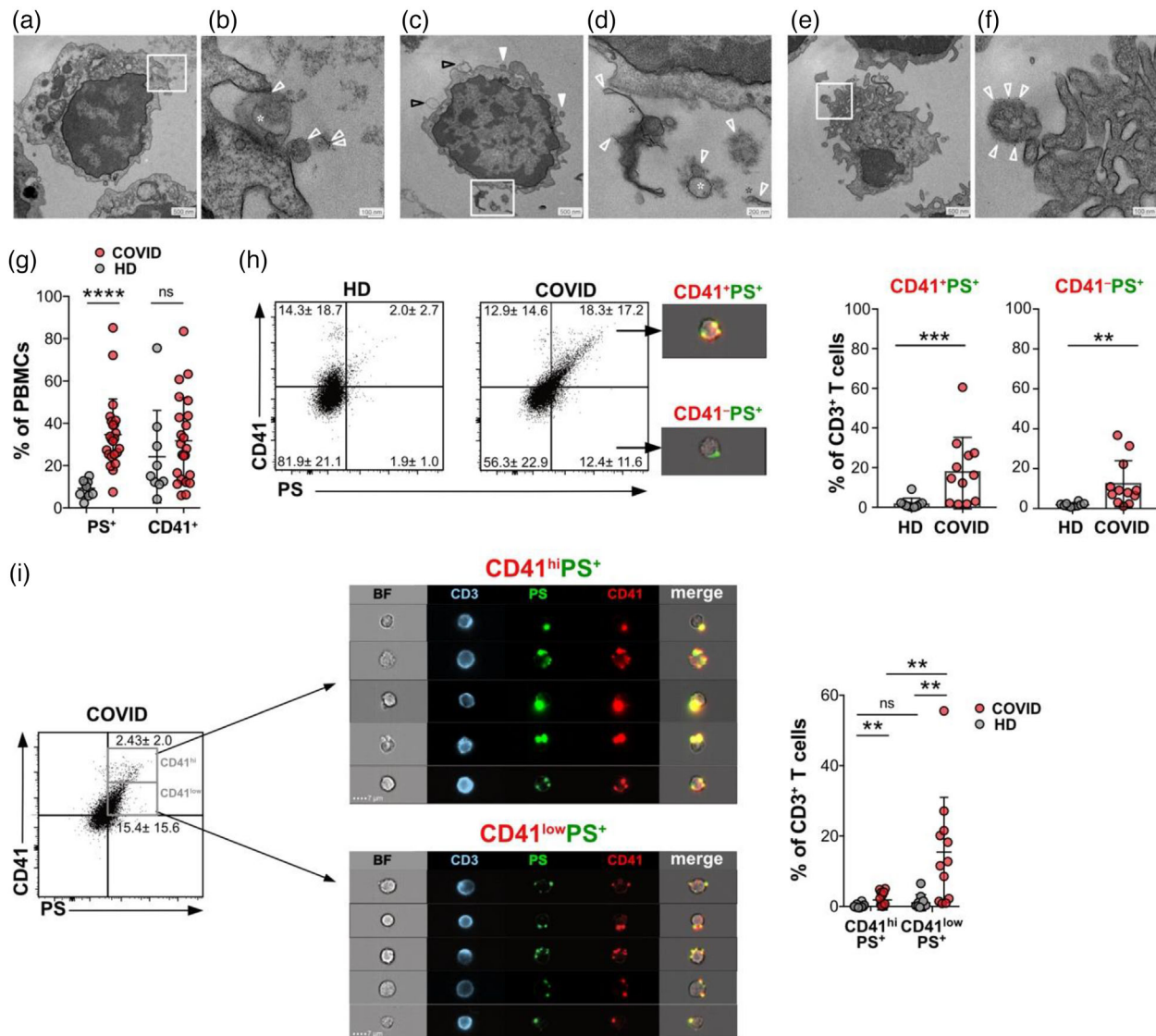


FIGURE 4 Structural and phenotypic characterisation of EVs associated with lymphocytes from COVID patients. Patient parameters for these experiments are depicted in Table S3. PS⁺ CD3^ε⁺ T and CD19⁺ B lymphocytes were isolated from PBMC of COVID patients (WHO_{max} score 3) by FACS-sorting (Figure S3C) and subsequently labeled with mCl-multimer/streptavidin-gold for TEM analysis of PS and analysed structurally by TEM (a-f). (b, d, f) represent the magnified sections (white frame) of (a, c, e), respectively. Open white arrowheads (b, c, f) mark PS labelling by mCl-multimer/streptavidin-gold; arrowheads in C point to PS⁻ EVs; white star (b, d) or black star (d) marks organelle-like structures within EVs, or PS⁺ tubular elongated structures (d), respectively. Analysis of platelet marker CD41 on T cells. (g) PBMC were analysed as shown in Figure S3 (HD, $n = 11$; COVID, $n = 23$) for PS and CD41. (h) CD3^ε⁺ T lymphocytes (gated as in Figure S3D) were stained for CD41 and PS and analysed by IFC (HD, $n = 10$; COVID, $n = 12$). Images represent cells of the respective quadrants. Numbers are the percentage of cells with the respective quadrants and are shown also in the bar graphs. (i) Percentage of T cells in the quadrants of PS⁺ CD41^{hi} and PS⁺ CD41^{low} CD3^ε⁺ T cells. Dot plots show the gating of PS⁺ CD41^{hi} and PS⁺ CD41^{low} CD3^ε⁺ T lymphocytes. IFC images show representative cells of the CD41^{hi} and CD41^{low} gates. The bar graph shows the frequency of PS⁺ CD41^{hi} and PS⁺ CD41^{low} T cells as percent of all CD3^ε⁺ T cells. Statistical significance was determined by paired Wilcoxon test and is indicated by asterisks (ns $p > 0.5$; * $p \leq 0.05$; ** $p \leq 0.01$; *** $p \leq 0.001$; two-tailed unpaired t -test)

groups (Figure S4B and C). We evaluated next if PS⁺EV⁺ CD8⁺ T cells were positive for these platelet markers. PS⁺EV⁺ CD8⁺ T cells showed significantly increased mean fluorescence intensities (MFI) for platelet markers CD41, CD63, CD62P and CD274 compared to their PS⁻ counterparts (Figure 5a and b). The frequency of T cells, which were positive for these markers, was also increased in PS⁺EV⁺ T cells (CD41, CD63, CD62P; Figure 5b). This finding indicated that PMPs carried the surface molecules of their activated 'parent' platelets to the surface of activated CD8⁺ T cells in COVID-19 patients. When we analysed the images of CD41, CD63, CD274 and CD62P stained T cells, we also observed an EV-like staining pattern of these markers, similar to the PS staining (Figure 5c).

To confirm that these markers originate from activated platelets or their PMPs, we quantified PMP-marker colocalisation with PS. We used the bright detail similarity (BDS) feature to quantify the pixel overlap of PS⁺ and PMP-marker⁺ spots identified

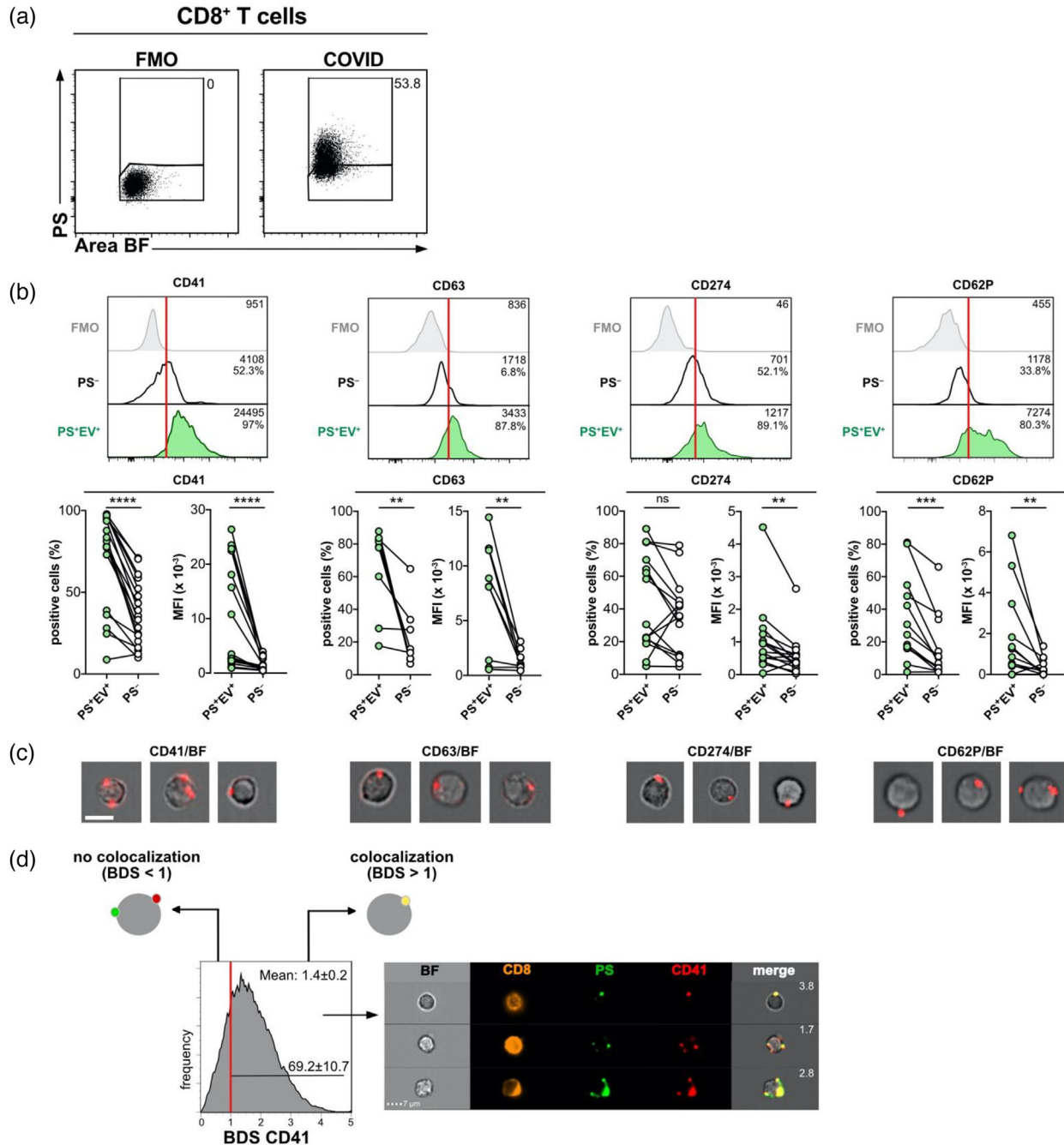


FIGURE 5 EVs bound to CD8⁺ T cells originate from platelets and PMP markers colocalise with PS⁺ EVs. Patient parameters for these experiments are depicted in Table S4. (a) Analysis of CD8⁺ T cells of COVID patients (CD41, *n* = 18; CD63, *n* = 9; CD274, *n* = 15, CD62P, *n* = 13) were gated as shown in Figure S3E and then further separated into PS⁺EV⁺ and PS⁻ T cells. Numbers represent the percentage of cells within the gates. (b) Then cells were analysed separately for expression of platelet-markers CD41, CD63, CD62P and CD274. Median fluorescence intensities (MFI) ± SD of these proteins and % of positive cells are indicated in the histograms. Summaries of all results are shown below histograms. (c) Representative images of CD41⁺, CD63⁺, CD62P⁺ and CD274⁺ CD8⁺ T cells show the EV-like staining pattern of these markers. (d) Colocalisation analysis between PS and PMP-marker staining. To identify PS⁺ spots the Dilate(Peak(M02, PS, Bright, 5),1) and to identify PMP-marker⁺ spots the Dilate(Peak(M_{marker},marker channel, Bright, 1),1) masks were used. To quantify the degree of colocalisation between these masks, bright details similarity scores (BDS) were calculated. Cells with a BDS < 1 did not show any significant colocalisation as determined by visual inspection. Cells with a BDS > 1 showed substantial colocalisation of PS and the respective platelet marker. BDS scores are shown in the representative example images. Histograms show the BDS scores of PS⁺EV⁺ CD8⁺ cells. The mean BDS score and the percentage of cells showing colocalisation (BDS > 1) are indicated within histograms. Statistical significance was determined by paired Wilcoxon test and is indicated by asterisks (ns *p* > 0.5; **p* ≤ 0.05; ***p* ≤ 0.01; ****p* ≤ 0.001)

using a peak mask in the IDEAS software (Figure 5d). As determined by visual inspection, BDS values >1 indicate substantial colocalisation between PS and other markers. This analysis showed that the great majority of all PS⁺EV⁺ CD8⁺ T cells (64%–82%) showed strong colocalisation of PS⁺EVs with CD41 (Figure 5d), CD63, CD62P or CD274 (Figure S8) with average BDS scores ranging from 1.3 to 1.8 (Figure 5 and S8). These results indicate that most of the PMPs attached to CD8⁺ T cells originate from activated platelets and carried platelet markers. Furthermore, since human T cells do not express markers like CD41 and CD62P, it excludes the possibility that the PS⁺EVs attached to T cells originate from T cells themselves or mark eventual focal PS⁺ regions on the T cell surface membrane.

2.6 | PS⁺CD41⁺ PMPs are preferentially bound to proliferating CD8⁺ T cells

Next, we wanted to assess whether there are functional differences between PMP⁺ and PMP⁻ CD8⁺ T cells. For this, we performed RNAseq analysis of FACS-sorted PS⁺ and PS⁻ non-naïve CD8⁺ T cells from peripheral blood of 4 patients (Figure 6a and Figure S3G). Despite heterogeneity between patients, we could identify gene sets that showed clear enrichment in PS⁺ (Figure 6b) and PS⁻ T cells (Figure 6c). Table S5 shows a summary of the gene set enrichment analysis (GSEA) against 4597 datasets in the gene ontology (GO) database.

PS⁺ CD8⁺ T cells had enriched genes controlling cell cycle and division, with normalised enrichment scores (NES) of 2.24 and 2.70 for the gene ontology biological process (GOBP) ‘cell division’ and KEGG ‘cell cycle’ gene sets, respectively. Among the genes upregulated in PS⁺ CD8⁺ T cells of all patients were several cell division control (CDC) genes, such as CDC45, CDCA8, CDC20, CDC6 or transcription factors E2F7 and E2F2, which are involved in cell cycle regulation (DeGregori & Johnson, 2006). Also, Birc5 (survivin) which plays a crucial role in costimulation-driven clonal expansion of T cells (Song et al., 2005), was upregulated in all patients.

Cells in the G2/M phase exhibit a general inhibition of translation (Sachs, 2000). Hence, the reduced expression of genes initiating translation in PS⁺ CD8⁺ T cells is in line with the observed upregulation of proliferation-associated genes (Figure 6c).

Although PS⁻ and PS⁺ CD8⁺ T cells had few apparent differences in gene expression due to the high degree of variability between individual patients, it is striking that binding of PS⁺ PMPs was associated with increased proliferation. To confirm the RNAseq results, we stained CD8⁺ T cells with the proliferation marker Ki-67, which labels dividing and recently dividing cells in G1, S, G2 and M phase, but is absent in resting cells (Scholzen & Gerdes, 2000) and compared the frequency of PS⁻ and PS⁺EV⁺ Ki-67⁺ cells. PS⁺EV⁺ CD8⁺ T cells (Figure 6d and e) and PS⁺EV⁺ CD4⁺ T cells (Figure S8) contained significantly more Ki-67⁺ proliferating cells than their PS⁻ T cell counterparts from the same patient. In both cases, Ki-67 staining localised to the nucleus and PS⁺ PMPs to the periphery of the same cells (Figure 6e and S8B). Our results indicate that PS⁺ PMPs preferentially bind to proliferating T cells and may affect T cells in this cycling stage.

We were also interested to find out, whether CD8⁺ T cells binding PS⁺ PMPs exhibit an effector or memory phenotype. Previous reports showed a high prevalence of SARS-CoV-2-specific T cells mainly among T cells with phenotypes of effector memory (T_{EM}) and terminal effector memory cells reexpressing CD45RA (T_{EMRA}) cells (Kared et al., 2021). We did not observe a clear enrichment of effector or memory genes (Best et al., 2013). However, we found an upregulation of effector-associated genes, such as CXC Motif Chemokine Receptor 3 (Cxcr3), Interferon γ (Ifng), Granzyme A and B (Gzma and Gzmb) and CC-chemokine ligand 5 (Ccl5) in PS⁺ CD8⁺ T cells of all four patients. In contrast, memory-related genes, such as C-X-C Motif Chemokine Receptor 4 (Cxcr4), DNA-binding protein inhibitor ID-3 (Id3) and interleukin-7 receptor (Il7r), showed a subtle downregulation in all patients. These findings indicate that PMP-associated CD8⁺ T cells are proliferating effector cells rather than memory cells. This we also confirmed with flow cytometry using CCR7 and CD45RA as markers (Sallusto et al., 2004). We found PS⁺PMPs preferentially associated with CCR7⁻CD45RA⁻ CD8⁺ T_{EM} cells and terminally differentiated CCR7⁻CD45RA⁺ CD8⁺ T_{EMRA} (Figure S9).

Our novel analysis method allows the detection of dying as well as PS⁺ EV-associated living cells (Figure 2). We next wanted to analyse whether the apoptosis rate of CD8⁺ T cells would be elevated in COVID-19 patients as compared to healthy donors and could contribute to the observed T cell lymphopenia (Laing et al., 2020). To this end, we quantified the number of CD8⁺ T cells classified as apoptotic by the CAE algorithm (Figure S10). The CD8⁺ T cell apoptosis rate was significantly increased in moderate and severe cases compared to healthy donors (Figure S10A and B). This increased rate of apoptosis might ultimately contribute to T cell loss and lymphopenia.

Taken together, we present a robust method, which allows the detection of dying as well as PS⁺EV⁺-associated living cells within PBMCs of COVID-19 patients in a single step. This type of analysis might help understand events that directly affect the immune system and might be caused by EV-immune cell interactions.

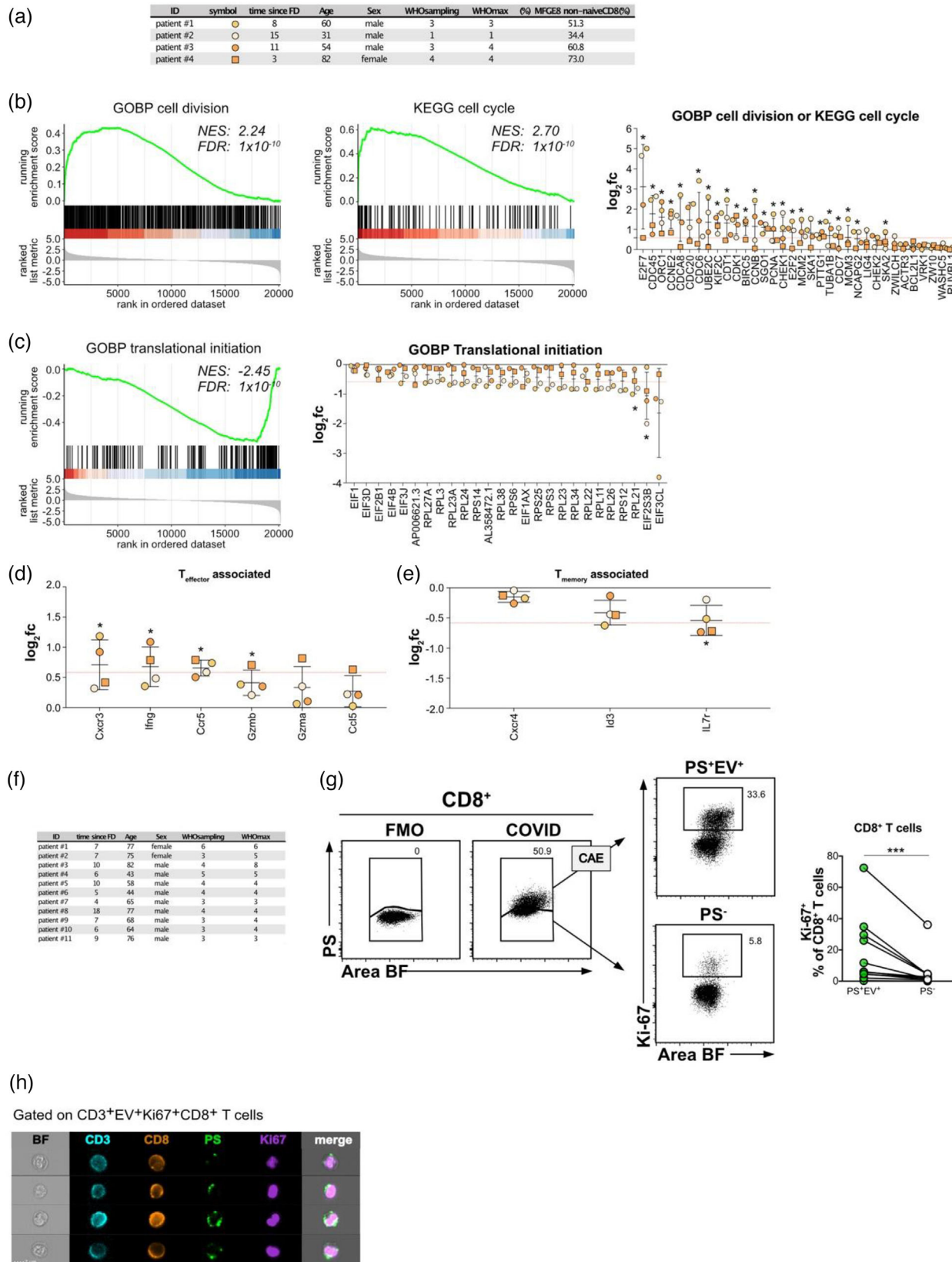


FIGURE 6 PS⁺EV associate with proliferating CD8 T cells. Non-naive PS⁺ and PS⁻ CD8⁺ T cells (gating strategy see Figure S3G) from four patients were sorted and subjected to RNAseq analysis. (a) The table displays patient parameters. (b) GSEA enrichment analysis for the gene sets GOBP cell division and KEGG cell cycle are shown and indicate enrichment in PS⁺ CD8⁺ T cells. Dot plots depict log₂ fold change values of genes in either of these two gene sets and upregulated in all four patients. The red dotted horizontal line indicates a fold change of 1.5 (log₂fc 0.58). *p*-values < 0.05 are indicated with an asterisk. (c) GSEA enrichment analysis for the gene sets GOBP translational initiation and indicates enrichment in PS⁻ CD8⁺ T cells. Dot plots depict log₂ fold change values of genes in this gene set and downregulated in all four patients. The red dotted horizontal line indicates a fold change of -1.5 (log₂fc -0.58).

3 | DISCUSSION

COVID-19 patients have hyperactivated platelets (Zaid et al., 2020), elevated levels of circulating PMPs (Cappellano et al., 2021), and an increased risk of thromboembolic complications contributing to disease severity and mortality. Our results contribute to the complex clinical picture of thromboinflammation (reviewed in Gu et al. (2021) and Lind (2021)). One of our most surprising findings was the high association of PBMC with PS⁺ PMPs and platelets over the disease course, shown with a novel PS-detecting method. The degree of this association correlated more strongly with disease severity than established laboratory indices and might be a promising biomarker for predicting disease severity.

Patients with COVID-19 are mostly lymphopenic (Cao, 2020; Yang et al., 2020), but lymphopenia preferentially affects CD8⁺ T cells (Mathew et al., 2020; Mazzoni et al., 2020). The measurement of dying or apoptotic cells in vivo or fresh ex vivo samples is technically challenging. Phagocytes very efficiently remove dead cells, and sample preparation itself can contribute to cell death. Using novel PS-specific reagents based on lactadherin, we found few but statistically significantly increased amounts of dying PBMCs, but also specifically dying CD8⁺ T cells in the blood of COVID-19 patients.

Antiphospholipid autoantibodies (aPL antibodies), including autoantibodies to the PS/prothrombin complex (antiPS/PT), have been found in COVID-19 patients (Zhang et al., 2020). Hence, it is possible that the association of PS⁺ platelets and PMPs with activated lymphocytes, together with a highly inflammatory environment, may drive the generation of aPL antibodies, further increasing the risk of life-threatening thrombotic events. However, further experiments are necessary to analyse this possibility.

By interacting with the complement cascade activated in COVID-19 patients (Song & FitzGerald, 2020), PS⁺ PMPs could contribute to lymphopenia. Correlation analyses of all blood values with the amounts of PS⁺ PMP⁺ PBMCs showed the strongest negative correlation with decreased lymphocyte counts in patients' blood, that is, with established lymphopenia. PS and PS⁺ PMP can activate complement pathways (Mevorach et al., 1998; Tan et al., 2010; Wang et al., 1993), thrombin formation, coagulation and inflammation (Melki et al., 2017; Owens & Mackman, 2011; Ridger et al., 2017). Therefore, one could speculate that PS⁺ PMP⁺ T cells might trigger for example the complement cascade on their surface, which might cause cell damage, death and T cell removal by phagocytes.

Moreover, the presence of an activated complement system in COVID-patients (Song & FitzGerald, 2020) could increase the release of PMPs from platelets (Sims et al., 1988) to self-reinforce this spiral. PS⁺ PMPs might facilitate the assembly and dissemination of procoagulant enzyme complexes (Sims et al., 1988). Attracting these reactions to the surface of lymphocytes might cause further functional inhibition or cell death.

'Long Covid' is a phenomenon that occurs in around 10% of COVID-19 patients and seems to be associated with persistent tissue damage in severe cases. However, also patients with mild COVID-19 disease scores might be affected (Mahase, 2020). We identified PS⁺ PMP⁺ PBMCs of patients during many weeks post initial diagnosis with only minimal signs of returning to normal levels. Therefore, prolonged adverse effects of PS⁺ PMPs on the immune system could contribute to 'long COVID'. The frequencies of PS⁺ and PS⁺EV⁺ PBMCs in our cohort of recovered patients was only slightly, but statistically significantly elevated when compared to those of healthy donors. As these patients had only mild symptoms (WHO 1–2), it might be interesting to monitor also patients with 'long COVID' or those recovered from severe disease. Eventually PS⁺EV⁺ PBMCs could also be a marker for late COVID-19 symptoms.

Especially CD8⁺ T_{EM} and T_{EMRA} cells, among which most SARS-CoV2-specific clones were identified (Kared et al., 2021) showed enhanced PMP-binding in COVID-19 patients. COVID-19 T cell responses begin too late (Sette & Crotty, 2021), and T cells may be exhausted (Zheng et al., 2020). The association of PS⁺ PMPs with T cells could contribute to these deficiencies and potentially impact the immune and inflammatory antiviral responses. Activated platelets may associate with T cells in the blood of HIV-infected individuals (Green et al., 2015) and link the coagulation and inflammatory cascade with T cells. In vitro, platelets can inhibit proliferation, cytokine production and PD1 expression of T cells (Polasky et al., 2020). Since PMPs derive from platelets, they may also have similar functions as their 'parent'-platelets. We found that between 10% and 80% of CD8⁺ T cells were associated with PD-L1(CD274)⁺ PMP. The fact that we could detect this immunoregulatory molecule on a high frequency of PS⁺ and PS⁻ PMPs raises the possibility that PMPs can suppress CD8⁺ T cells via PD-L1/PD1 interaction. Previous studies suggested that SARS-CoV-2-specific CD8⁺ T cells can have an exhausted phenotype due to their expression of inhibitory receptors such as PD1 (De Biasi et al., 2020; Diao et al., 2020; Song et al., 2020; Zheng et al., 2020). Analogous to PD-L1 on

p-values < 0.05 are indicated with an asterisk. (d and e) Log₂ fold change values of genes associated with T effector (f) and T memory (g) cells that were up- or down-regulated, respectively, in all four patients, are shown. Red dotted horizontal line indicates a fold change of 1.5 (log₂fc 0.58) or -1.5 (log₂fc -0.58).

p-values < 0.05 are indicated with an asterisk. (f) Table shows details of PBMC-origin (patient numbers) for validation experiments shown in (g)-(h). (g) PBMC from COVID patients were examined for proliferation with Ki-67. CD8⁺ T cells (*n* = 11) were analysed as shown in Figure SIF. PS⁺CD3⁺CD8⁺ T cells were stained intranuclear for Ki-67. PS⁺ and PS⁻ fractions were classified by IFC. CAE-analysis identified PS⁺EV⁺ live cells. PS⁺EV⁺ and PS⁻CD8⁺ T cells were then analysed for Ki-67, and data from all patients were plotted on the graph. The numbers in the dot plots represent the fraction of cells in the corresponding gate. Statistical significance was determined by paired Wilcoxon test and is indicated by asterisks (ns *p* > 0.5; **p* ≤ 0.05; ***p* ≤ 0.01; ****p* ≤ 0.001). (h) An image selection of CD8 T cells with the markers used

tumor exosomes, which suppress tumor-specific CD8⁺ T cells (Chen et al., 2018), PD-L1 PMPs could favor T cell suppression in COVID-19. However, recent data have suggested that PD1⁺ SARS-CoV-2-specific CD8⁺ T cells are functional (Rha et al., 2021). Furthermore, our RNAseq results showing subtly increased expression levels of the effector molecules IFN γ , granzyme A, and B and increased proliferation also argue against an exhausted phenotype of PS⁺ CD8⁺ T cells and would instead indicate enhanced effector function or terminal differentiation. Enhanced activation of PS⁺EV⁺ CD8⁺ T cells could theoretically be a reason for the observed higher rate of apoptosis in this population, as activation induced cell death (AICD) is known to contribute to loss of effector T cells (Green et al., 2003).

Two recent studies showed that in COVID-19 patients, hyperactivated platelets could form aggregates with leukocytes and macrophages (Hottz et al., 2020; Manne et al., 2020). As these previous studies relied on conventional flow cytometry, but not IFC, they could not differentiate between CD41⁺ platelets and CD41⁺ PMPs. Also, they did not analyse PS⁺ PMPs on the surface of live lymphocytes. Since PMPs constitute the lion's share of CD41⁺PS⁺ particles on T cells of COVID-19 patients and PS may be responsible for the coagulation and inflammatory effects mentioned above, our findings are an unexpected result with high clinical relevance.

PS is a novel marker to classify COVID-19 patients according to disease severity. Moreover, longitudinal studies could test PS as a predictor of disease development. Due to its ease of use by flow cytometry and the high number of positive PS⁺ PBMC during COVID-19, PS detection could be a valuable analytical tool also in other infectious diseases and sepsis.

4 | MATERIALS AND METHODS

4.1 | Study design and recruitment

Recruited patients ($n = 54$) with PCR confirmed SARS-CoV-2 infection were part of the COVID-19 Registry of the LMU University Hospital Munich (CORKUM, WHO trial id DRKS00021225). The Ethics Committee approved the study of the LMU Munich (No: 20-308; 18-415), and patients included (≥ 18 years, mean age 63, Table S1) consented to serial blood sampling. Additional approval was obtained for the analysis shown here (No. 20-308) and for the use of blood samples from healthy donors (No. 18-415). For this study, patient data were anonymised for analysis, and blood samples were collected between April 2020 and February 2021. Of the 54 patients analysed, 52 patients were hospitalised, and two patients were diagnosed in the hospital and discharged. From 15 patients, blood samples from several timepoints could be obtained, which were taken between days 2 and 76 after a positive SARS-CoV-2 PCR test. Clinical and laboratory data were collected and documented by the CORKUM study group and are summarised in Table S1. We used the World Health Organization's (WHO) eight-point ordinal scale for COVID-19 endpoints (WorldHealthOrganization, 2020) to grade disease severity. WHO scores were combined into 'mild' (WHO 1–3), 'moderate' (WHO 4) and 'severe' (WHO 5–8).

Recovered donors (RD, $n = 12$, mean age 40, Table S1) were adults with a prior SARS-CoV-2 infection (≥ 69 days post positive PCR test), who were either diagnosed in the ambulance or released from the hospital with WHO score 1–2.

Healthy donors (HDs, $n = 35$, mean age 39, Table S1) tested negative for SARS-CoV-2 were used as control cohorts. PBMCs were obtained from leucocyte reduction chambers after thrombocyte donations ($n = 10$) or freshly prepared from whole blood ($n = 25$) of healthy hospital and laboratory workers.

4.2 | Sample processing and cell isolation

Peripheral blood was collected into lithium heparin tubes (Sarstedt) and processed within 6 h after venipuncture. Unfixed samples were handled under Biosafety level 2. PBMCs were isolated by Biocoll density gradient (Merck) centrifugation and then directly stained for imaging flow cytometry.

4.3 | Antibody staining and flow cytometry

Antibodies and staining reagents are listed in Table S2. As PS-staining reagents we used the previously published recombinant MFG-E8-eGFP (Kranich et al., 2020; Trautz et al., 2017) and mCl-biotin multimerised with streptavidin-AF647 for flow cytometry or streptavidin-gold for TEM. mCl-multimers are commercially available through BioLegend as ApotrackerTM Tetra reagents. In flow cytometry. All PS-staining reagents are Ca²⁺ independent, highly stable and PS-specific. Freshly isolated PBMCs were incubated with Fc block before live/dead and cell surface antibody staining. PBMCs surface staining was performed in staining buffer (PBS containing 2% of fetal calf serum) for 25 min on ice. Then cells were washed and fixed with 4% PFA for 30 min at room temperature (RT), washed again, filtered and analysed on an ImageStreamx MKII imaging flow cytometer (Luminex). Samples

were acquired with low flow rate/high sensitivity and 60× magnification. Images were acquired using bright field illumination and the excitation lasers 405, 488, 561 and 642 nm.

For intranuclear Ki-67 staining, cells were fixed and permeabilised using the Transcription Factor Staining Buffer Set (ThermoFisher, cat. #00-5523-00) according to the manufacturers' instructions. Intranuclear staining was performed in permeabilisation buffer for 30 min at RT.

4.4 | Cell sorting for gene expression analysis

PBMCs from four patients (see Figure 6a) were stained with anti-CD3-BV421, anti-CD8-BV785, anti-CCR7-APC, anti-CD45RA-PerCPCy5.5, anti-CD19/CD16/CD56/CD14-APCFire750 and MFG-E8-eGFP (see Table S2) in staining buffer (25 min, 4°C) after cells were incubated with Fixable Viability dye eFluor780 in PBS (10 min, 4°C). PS⁺ and PS⁻ single, live, non-naïve (CCR7⁺CD45RA⁻, CCR7⁻CD45RA⁻ and CCR7⁻CD45RA⁺) CD3⁺CD8⁺ T cells were directly sorted into TRIzol reagent (Thermo Fisher) on a FACS Aria Fusion (BD) using a 100 μm nozzle. Samples were stored at -20°C until analysis. RNA isolation and sequencing were performed by Vertis Biotechnologie AG, Freising. Total RNA was isolated and purified using Monarch columns (NEB). Poly(A)⁺ RNA was isolated from the total RNA sample. First-strand cDNA synthesis was primed with a N6 randomised primer. After fragmentation, the Illumina TruSeq sequencing adapters were ligated in a strand specific manner to the 5' and 3' ends of the cDNA fragments. In this way, a strand specific PCR amplification of the cDNA was achieved using a proof-reading enzyme. For Illumina NextSeq sequencing, the samples were pooled in approximately equimolar amounts. The cDNA pool in the size range of 250–700 bp was eluted from a preparative agarose gel. The primers used for PCR amplification were designed for TruSeq sequencing according to the instructions of Illumina. The cDNA size range was 250–700 bp. The cDNA pool was sequenced on an Illumina NextSeq 500 system using 1 × 75 bp read length.

4.5 | RNAseq analysis

Sequencing reads were aligned to the human reference genome (version GRCH38.100) with STAR (version 2.7.3). Expression values (TPM) were calculated with RSEM (version 1.3.3). Post-processing was performed in R/bioconductor (version 4.0.3) using default parameters if not indicated otherwise. Differential gene expression analysis was performed with 'DEseq2' (version 1.28.1) using a model including patient ID as random factor. An adjusted *p* value (FDR) of less than 0.1 was used to classify significantly changed expression. Gene set enrichment analyses were conducted with 'clusterProfiler' (version 3.18.1) on the statistic reported by DEseq2. Data are available at GEO Submission (GSE174786).

4.6 | Cell sorting for TEM

Isolated PBMCs were stained with anti-CD19- and anti-CD3-PE, PS-staining reagent mC1-multimer (SA-AF647) (commercially available at BioLegend) and mC1-biotin (commercially available at BioLegend) multimerised with SA-gold, (Aurion) (see Table S2) in staining buffer (25 min, 4°C) after incubation with Fixable Viability Dye eFluor780 in PBS (10 min, 4°C). After washing, cells were prefixed with freshly prepared 4% EM-grade PFA (Science Services) for 30 min at RT before sorting. Fixed, single, PS⁺CD19⁺ and CD3⁺ cells were sorted on a FACS Aria III (BDBiosciences) using a 130 μm nozzle into PBS containing 0.5% BSA.

After washing with PBS, cells were fixed with 2.5% glutaraldehyde (EM-grade, Science Services) in 0.1 M cacodylate buffer (pH 7.4) for 15 min (Sigma Aldrich) and washed with 0.1 M sodium cacodylate buffer for 10 min at 400 g before postfixation in reduced osmium (1% osmium tetroxide (Science Services), 0.8% potassium ferricyanide (Sigma Aldrich) in 0.1 M sodium cacodylate buffer). The cell pellet was contrasted in 0.5% uranyl acetate in water (Science Services) and dehydrated in an ascending ethanol series. The pellet was embedded in epon resin and hardened for 48 h at 60°C. Ultra-thin sections (50 nm) were cut and deposited onto formvar-coated grids (Plano) and again contrasted using 1% uranyl acetate in water and Ultrastain (Leica). Images were acquired on a JEM 1400plus (JEOL).

4.7 | Imaging flow cytometry and data analysis

Data analysis was performed using the IDEAS software (Version 6.2, Luminex). Compensation matrices were generated using single stained samples and applied to the raw data, and data analysis files were created. Unfocused events were excluded from the analysis based on gradient max feature values. PS⁺ cells were gating using FMO controls. TIFF-images of PS⁺ cells from each sample were exported (16-bit, raw) and analysed by the CAE algorithm as previously described (Kranich et al., 2020). Two *.pop

files containing the object numbers of apoptotic and EV⁺ cells were generated and re-imported into the IDEAS software. Then FCS files from all cells, only apoptotic or only EV⁺ cells, were exported and analysed using FlowJo Version 10.7.1.

4.8 | Colocalisation analysis

We created a spot mask for PS and the respective marker staining to determine the degree of colocalisation between PS⁺ EVs and PMP-marker⁺ (CD41/CD63/CD274/CD62P) cells. PS⁺ spots were identified by the Dilate (Peak(M02, PS, Bright, 5),1) mask and the Dilate(Peak(M_marker, marker channel, Bright, 1),1) mask was used to identify marker⁺ spots. Both masks were combined, and the colocalisation was assessed using the BDS R3 feature of the IDEAS software.

4.9 | Platelet staining

Platelets were stained in whole blood. Hundred microlitres of blood were slowly added to 100 μ l of antibody mix in staining buffer (PBS with 0.1% sodium azide and 2% of FCS). The mixture was gently swirled and incubated for 30 min at room temperature in the dark. Then cells were fixed in 1% PFA in PBS with 0.1% sodium azide for 2 h, centrifuged for 20 min at 5000 g, resuspended in PBS with 0.1% sodium azide and analysed on the ImageStreamx MKII imaging flow cytometer.

4.10 | Statistical analysis

For statistical analysis, the PRISM software (GraphPad Software, La Jolla, CA, USA) was used. For direct comparison between two groups non-parametric, unpaired Mann-Whitney test was used. Statistical significance of paired data was determined by paired Wilcoxon test. p values of ≤ 0.05 are considered significant and denoted with *, ** $p < 0.01$, *** $p < 0.001$ and **** $p < 0.0001$. R version 4.0.3 was used for correlation analysis. Numeric values in the dataset were correlated (Spearman correlation) using the ggcorrmat function of the ggstatsplot package (v0.7.2) with Benjamini-Hochberg correction for multiple testing.

ROC analysis was performed using library 'pROC' (version 1.17.01). Thresholds were determined using the pROCs coords function with the 'best' method.

ACKNOWLEDGEMENTS

We would like to thank all of the COVID-19 Registry of the LMU Munich (CORKUM) investigators and staff and the patients and their families for participating in the CORKUM registry and all health care workers for their outstanding service. We acknowledge the Core Facility Flow Cytometry at the Biomedical Center, LMU Munich, for providing the ImageStreamX MKII imaging flow cytometer, cell sorters and services. We thank Wenbo Hu for providing reagents. T.B. and A.K. are supported by the Deutsche Forschungsgemeinschaft under CRC 1054 (TP B03, grant no. 210592381; and TP A06, grant no. 210592381). A.K. received funding from Deutsche Forschungsgemeinschaft under CRC/TR237-B14 (369799452) and KR2199/10-1 (391217598), and received funding from the Bavarian State Ministry of Science and the Arts.

CONFLICT OF INTERESTS

T.B. and J.K. declare competing interests due an exclusive licensing agreement with BioLegend, Inc. for the commercialisation of mCI-multimer. The remaining authors declare no competing interests.

AUTHOR CONTRIBUTIONS

Lisa Rausch: Formal analysis; Investigation; writing original draft. Konstantin Lutz: Formal analysis. Martina Schifferer: Formal analysis; Investigation; Writing – review & editing. Elena Winheim: Resources. Rudi Gruber: Investigation Formal analysis; Writing – review & editing. Anne B. Krug: Writing – review & editing, supervision, funding acquisition. Linus Rinke: Investigation. Clemens Scherer: Resources. Johannes C. Hellmuth: Resources. Maximilian Muenchhoff: Resources; Writing – review & editing. Christopher Mandel: Resources. Michael Bergwelt: Resources. Mikael Simons: Formal analysis; Funding acquisition; Writing – review & editing. Tobias Straub: Formal analysis. Jan Kranich: Conceptualization; Investigation; Software; Writing – original draft; Supervision. Thomas Brocker: Conceptualization; Funding acquisition; Supervision; Writing – original draft.

ORCID

Jan Kranich  <https://orcid.org/0000-0002-9928-4132>

Thomas Brocker  <https://orcid.org/0000-0001-7060-5433>

REFERENCES

- Aatonen, M. T., Ohman, T., Nyman, T. A., Laitinen, S., Grönholm, M., & Siljander, P. R. (2014). Isolation and characterization of platelet-derived extracellular vesicles. *Journal of Extracellular Vesicles*, 3(1), 24692, <https://doi.org/10.3402/jev.v3.24692>.
- Arraud, N., Linares, R., Tan, S., Gounou, C., Pasquet, J. M., Mornet, S., & Brisson, A. R. (2014). Extracellular vesicles from blood plasma: Determination of their morphology, size, phenotype and concentration. *Journal of Thrombosis and Haemostasis*, 12, 614–627, <https://doi.org/10.1111/jth.12554>.
- Best, J. A., Blair, D. A., Knell, J., Yang, E., Mayya, V., Doedens, A., Dustin, M. L., Goldrath, A. W., & Immunological Genome Project Consortium (2013). Transcriptional insights into the CD8+ T cell response to infection and memory T cell formation. *Nature Immunology*, 14, 404–412, <https://doi.org/10.1038/ni.2536>.
- Braun, J., Loyal, L., Frentsch, M., Wendisch, D., Georg, P., Kurth, F., Hippenstiel, S., Dingeldey, M., Kruse, B., Fauchere, F., Baysal, E., Mangold, M., Henze, L., Lauster, R., Mall, M. A., Beyer, K., Röhm, J., Voigt, S., Schmitz, J., ... Thiel, A. (2020). SARS-CoV-2-reactive T cells in healthy donors and patients with COVID-19. *Nature*, 587, 270–274, <https://doi.org/10.1038/s41586-020-2598-9>.
- Cao, X. (2020). COVID-19: Immunopathology and its implications for therapy. *Nature Reviews Immunology*, 20, 269–270, <https://doi.org/10.1038/s41577-020-0308-3>.
- Cappellano, G., Raineri, D., Rolla, R., Giordano, M., Puricelli, C., Vilardo, B., Manfredi, M., Cantaluppi, V., Sainaghi, P. P., Castello, L., De Vita, N., Scotti, L., Vaschetto, R., Dianzani, U., & Chiochetti, A. (2021). Circulating platelet-derived extracellular vesicles are a hallmark of Sars-Cov-2 infection. *Cells* 10, 85, <https://doi.org/10.3390/cells10010085>.
- Chapman, L. M., Aggrey, A. A., Field, D. J., Srivastava, K., Ture, S., Yui, K., Topham, D. J., Baldwin, W. M. 3rd, & Morrell, C. N. (2012). Platelets present antigen in the context of MHC class I. *Journal of Immunology*, 189, 916–923, <https://doi.org/10.4049/jimmunol.1200580>.
- Chen, G., Huang, A. C., Zhang, W., Zhang, G., Wu, M., Xu, W., Yu, Z., Yang, J., Wang, B., Sun, H., Xia, H., Man, Q., Zhong, W., Antelo, L. F., Wu, B., Xiong, X., Liu, X., Guan, L., Li, T., ... Guo, W. (2018). Exosomal PD-L1 contributes to immunosuppression and is associated with anti-PD-1 response. *Nature*, 560, 382–386, <https://doi.org/10.1038/s41586-018-0392-8>.
- Chen, R., Sang, L., Jiang, M., Yang, Z., Jia, N., Fu, W., Xie, J., Guan, W., Liang, W., Ni, Z., Hu, Y., Liu, L., Shan, H., Lei, C., Peng, Y., Wei, L., Liu, Y., Hu, Y., Peng, P., ... Medical Treatment Expert Group for COVID-19 (2020). Longitudinal hematologic and immunologic variations associated with the progression of COVID-19 patients in China. *Journal of Allergy and Clinical Immunology*, 146, 89–100, <https://doi.org/10.1016/j.jaci.2020.05.003>.
- Connor, D. E., Exner, T. M., Da, D., & Joseph, J. E. (2010). The majority of circulating platelet-derived microparticles fail to bind annexin V, lack phospholipid-dependent procoagulant activity and demonstrate greater expression of glycoprotein Ib. *Thrombosis and Haemostasis*, 103, 1044–1052, <https://doi.org/10.1160/TH09-09-0644>.
- Corban, M. T., Duarte-Garcia, A., McBane, R. D., Matteson, E. L., Lerman, L. O., & Lerman, A. (2017). Antiphospholipid syndrome: Role of vascular endothelial cells and implications for risk stratification and targeted therapeutics. *Journal of the American College of Cardiology*, 69, 2317–2330, <https://doi.org/10.1016/j.jacc.2017.02.058>.
- De Biasi, S., Meschieri, M., Gibellini, L., Bellinazzi, C., Borella, R., Fidanza, L., Gozzi, L., Iannone, A., Lo Tartaro, D., Mattioli, M., Paolini, A., Menozzi, M., Milić, J., Franceschi, G., Fantini, R., Tonelli, R., Sita, M., Sarti, M., Trenti, T., ... Cossarizza, A. (2020). Marked T cell activation, senescence, exhaustion and skewing towards TH17 in patients with COVID-19 pneumonia. *Nature Communications*, 11, 3434, <https://doi.org/10.1038/s41467-020-17292-4>.
- DeGregori, J., & Johnson, D. G. (2006). Distinct and overlapping roles for E2F family members in transcription, proliferation and apoptosis. *Current Molecular Medicine*, 6, 739–748, <https://doi.org/10.2174/1566524010606070739>.
- Del Valle, D. M., Kim-Schulze, S., Huang, H. H., Beckmann, N. D., Nirenberg, S., Wang, B., Lavin, Y., Swartz, T. H., Madduri, D., Stock, A., Marron, T. U., Xie, H., Patel, M., Tuballes, K., Van Oekelen, O., Rahman, A., Kovatch, P., Aberg, J. A., Schadt, E., ... Gnjatovic, S. (2020). An inflammatory cytokine signature predicts COVID-19 severity and survival. *Nature Medicine*, 26, 1636–1643, <https://doi.org/10.1038/s41591-020-1051-9>.
- Diao, B., Wang, C., Tan, Y., Chen, X., Liu, Y., Ning, L., Chen, L., Li, M., Liu, Y., Wang, G., Yuan, Z., Feng, Z., Zhang, Y., Wu, Y., & Chen, Y. (2020). Reduction and functional exhaustion of T cells in patients with coronavirus disease 2019 (COVID-19). *Frontiers in Immunology*, 11, 827, <https://doi.org/10.3389/fimmu.2020.00827>.
- Green, D. R., Droin, N., & Pinkoski, M. (2003). Activation-induced cell death in T cells. *Immunological Reviews*, 193, 70–81, <https://doi.org/10.1034/j.1600-065x.2003.00051.x>.
- Green, S. A., Smith, M., Hasley, R. B., Stephany, D., Harned, A., Nagashima, K., Abdullah, S., Pittaluga, S., Imamichi, T., Qin, J., Rupert, A., Ober, A., Lane, H. C., & Catalfamo, M. (2015). Activated platelet-T-cell conjugates in peripheral blood of patients with HIV infection: coupling coagulation/inflammation and T cells. *Aids*, 29, 1297–1308, <https://doi.org/10.1097/QAD.0000000000000701>.
- Gu, S. X., Tyagi, T., Jain, K., Gu, V. W., Lee, S. H., Hwa, J. M., Kwan, J. M., Krause, D. S., Lee, A. I., Halene, S., Martin, K. A., Chun, H. J., & Hwa, J. (2021). Thrombocytopeny and endotheliopathy: crucial contributors to COVID-19 thromboinflammation. *Nature Reviews Cardiology*, 18, 194–209, <https://doi.org/10.1038/s41569-020-00469-1>.
- Guan, W. J., Ni, Z. Y., Hu, Y., Liang, W. H., Ou, C. Q., He, J. X., Liu, L., Shan, H., Lei, C. L., Hui, D. S. C., Du, B., Li, L. J., Zeng, G., Yuen, K. Y., Chen, R. C., Tang, C. L., Wang, T., Chen, P. Y., Xiang, J., ... China Medical Treatment Expert Group for Covid-19. (2020) Clinical Characteristics of Coronavirus Disease 2019 in China. *New England Journal of Medicine*, 382, 1708–1720, <https://doi.org/10.1056/NEJMoa2002032>.
- Heijnen, H. F., Schiel, A. E., Fijnheer, R., Geuze, H. J., & Sixma, J. J. (1999). Activated platelets release two types of membrane vesicles: microvesicles by surface shedding and exosomes derived from exocytosis of multivesicular bodies and alpha-granules. *Blood*, 94, 3791–3799.
- Hotchkiss, R. S., & Nicholson, D. W. (2006). Apoptosis and caspases regulate death and inflammation in sepsis. *Nature Reviews Immunology*, 6, 813–822, <https://doi.org/10.1038/nri1943>.
- Hottz, E. D., Azevedo-Quintanilha, I. G., Palhinha, L., Teixeira, L., Barreto, E. A., Pão, C. R. R., Righy, C., Franco, S., Souza, T. M. L., Kurtz, P., Bozza, F. A., & Bozza, P. T. (2020). Platelet activation and platelet-monocyte aggregate formation trigger tissue factor expression in patients with severe COVID-19. *Blood*, 136, 1330–1341, <https://doi.org/10.1182/blood.2020007252>.
- Huang, C., Wang, Y., Li, X., Ren, L., Zhao, J., Hu, Y., Zhang, L., Fan, G., Xu, J., Gu, X., Cheng, Z., Yu, T., Xia, J., Wei, Y., Wu, W., Xie, X., Yin, W., Li, H., Liu, M., ... Cao, B. (2020). Clinical features of patients infected with 2019 novel coronavirus in Wuhan, China. *Lancet*, 395, 497–506, [https://doi.org/10.1016/S0140-6736\(20\)30183-5](https://doi.org/10.1016/S0140-6736(20)30183-5).
- Huang, T. M., Ishida, T., Harashima, H., & Kiwada, H. (2001). The complement system enhances the clearance of phosphatidylserine (PS)-liposomes in rat and guinea pig. *International Journal of Pharmaceutics*, 215, 197–205, [https://doi.org/10.1016/s0378-5173\(00\)00691-8](https://doi.org/10.1016/s0378-5173(00)00691-8).
- Kared, H., Redd, A. D., Bloch, E. M., Bonny, T. S., Sumatoh, H., Kairi, F., Carbajo, D., Abel, B., Newell, E. W., Bettinotti, M. P., Benner, S. E., Patel, E. U., Littlefield, K., Laeyendecker, O., Shoham, S., Sullivan, D., Casadevall, A., Pekosz, A., Nardin, A., ... Quinn, T. C. (2021). SARS-CoV-2-specific CD8+ T cell responses in convalescent COVID-19 individuals. *Journal of Clinical Investigation*, 131, e145476, <https://doi.org/10.1172/JCI145476>.

- Klok, F. A., Kruip, M. J. H. A., van der Meer, N. J. M., Arbous, M. S., Gommers, D. A. M. P. J., Kant, K. M., Kaptein, F. H. J., van Paassen, J., Stals, M. A. M., Huisman, M. V., & Endeman, H. (2020). Incidence of thrombotic complications in critically ill ICU patients with COVID-19. *Thrombosis Research*, *191*, 145–147, <https://doi.org/10.1016/j.thromres.2020.04.013>.
- Kranich, J., Chlis, N. K., Rausch, L., Latha, A., Schifferer, M., Kurz, T., Foltyn-Arfa Kia, A., Simons, M., Theis, F. J., & Brocker, T. (2020). In vivo identification of apoptotic and extracellular vesicle-bound live cells using image-based deep learning. *Journal of Extracellular Vesicles*, *9*, 1792683, <https://doi.org/10.1080/20013078.2020.1792683>.
- Laing, A. G., Lorenc, A., Del Molino Del Barrio, I., Das, A., Fish, M., Monin, L., Muñoz-Ruiz, M., McKenzie, D. R., Hayday, T. S., Francos-Quijorna, I., Kamdar, S., Joseph, M., Davies, D., Davis, R., Jennings, A., Zlatareva, I., Vantourout, P., Wu, Y., Sofra, V., ... Hayday, A. C. (2020). A dynamic COVID-19 immune signature includes associations with poor prognosis. *Nature Medicine*, *26*, 1623–1635, <https://doi.org/10.1038/s41591-020-1038-6>.
- Li, Q., Ding, X., Xia, G., Chen, H. G., Chen, F., Geng, Z., Xu, L., Lei, S., Pan, A., Wang, L., & Wang, Z. (2020). Eosinopenia and elevated C-reactive protein facilitate triage of COVID-19 patients in fever clinic: A retrospective case-control study. *EclinicalMedicine*, *23*, 100375, <https://doi.org/10.1016/j.eclinm.2020.100375>.
- Liao, M., Liu, Y., Yuan, J., Wen, Y., Xu, G., Zhao, J., Cheng, L., Li, J., Wang, X., Wang, F., Liu, L., Amit, I., Zhang, S., & Zhang, Z. (2020). Single-cell landscape of bronchoalveolar immune cells in patients with COVID-19. *Nature Medicine*, *26*, 842–844, <https://doi.org/10.1038/s41591-020-0901-9>.
- Lind, S. E. (2021). Phosphatidylserine is an overlooked mediator of COVID-19 thromboinflammation. *Heliyon*, *7*, e06033, <https://doi.org/10.1016/j.heliyon.2021.e06033>.
- Lippi, G., & Plebani, M. (2020). Laboratory abnormalities in patients with COVID-2019 infection. *Clinical Chemistry and Laboratory Medicine*, *58*, 1131–1134, <https://doi.org/10.1515/cclm-2020-0198>.
- Liu, J., Li, S., Liu, J., Liang, B., Wang, X., Wang, H., Li, W., Tong, Q., Yi, J., Zhao, L., Xiong, L., Guo, C., Tian, J., Luo, J., Yao, J., Pang, R., Shen, H., Peng, C., Liu, T., ... Zheng, X. (2020). Longitudinal characteristics of lymphocyte responses and cytokine profiles in the peripheral blood of SARS-CoV-2 infected patients. *EBioMedicine*, *55*, 102763, <https://doi.org/10.1016/j.ebiom.2020.102763>.
- MacLaren, G., Fisher, D., & Brodie, D. (2020). Preparing for the most critically ill patients with COVID-19: The potential role of extracorporeal membrane oxygenation. *Jama*, *323*, 1245–1246, <https://doi.org/10.1001/jama.2020.2342>.
- Mahase, E. (2020). Long covid could be four different syndromes, review suggests. *Bmj (Clinical Research Ed.)*, *371*, m3981, <https://doi.org/10.1136/bmj.m3981>.
- Manne, B. K., Denorme, F., Middleton, E. A., Portier, I., Rowley, J. W., Stubben, C., Petrey, A. C., Tolley, N. D., Guo, L., Cody, M., Weyrich, A. S., Yost, C. C., Rondina, M. T., & Campbell, R. A. (2020). Platelet gene expression and function in patients with COVID-19. *Blood*, *136*, 1317–1329, <https://doi.org/10.1182/blood.2020007214>.
- Mathew, D., Giles, J. R., Baxter, A. E., Oldridge, D. A., Greenplate, A. R., Wu, J. E., Alanio, C., Kuri-Cervantes, L., Pampena, M. B., D'Andrea, K., Manne, S., Chen, Z., Huang, Y. J., Reilly, J. P., Weisman, A. R., Ittner, C. A. G., Kuthuru, O., Dougherty, J., Nzingha, K., ... Wherry, E. J. (2020). Deep immune profiling of COVID-19 patients reveals distinct immunotypes with therapeutic implications. *Science*, *369*, eabc8511, <https://doi.org/10.1126/science.abc8511>.
- Mathieu, M., Martin Jaular, L., Lavieue, G., & Théry, C. (2018). Specificities of secretion and uptake of exosomes and other extracellular vesicles for cell-to-cell communication. *Nature Cell Biology*, *21*, 1–9, <https://doi.org/10.1038/s41556-018-0250-9>.
- Mazzoni, A., Salvati, L., Maggi, L., Capone, M., Vanni, A., Spinicci, M., Mencarini, J., Caporale, R., Peruzzi, B., Antonelli, A., Trotta, M., Zammarchi, L., Ciani, L., Gori, L., Lazzeri, C., Matucci, A., Vultaggio, A., Rossi, O., Almerigogna, F., ... Cosmi, L. (2020). Impaired immune cell cytotoxicity in severe COVID-19 is IL-6 dependent. *Journal of Clinical Investigation*, *130*, 4694–4703, <https://doi.org/10.1172/JCI138554>.
- Melki, I., Tessandier, N., Zufferey, A., & Boilard, E. (2017). Platelet microvesicles in health and disease. *Platelets*, *28*, 214–221, <https://doi.org/10.1080/09537104.2016.1265924>.
- Mevorach, D., Mascarenhas, J. O., Gershov, D., & Elkon, K. B. (1998). Complement-dependent clearance of apoptotic cells by human macrophages. *Journal of Experimental Medicine*, *188*, 2313–2320, <https://doi.org/10.1084/jem.188.12.2313>.
- Middeldorp, S., Coppens, M., van Haaps, T. F., Foppen, M., Vlaar, A. P., Müller, M. C. A., Bouman, C. C. S., Beenen, L. F. M., Kootte, R. S., Heijmans, J., Smits, L. P., Bonta, P. I., & van Es, N. (2020). Incidence of venous thromboembolism in hospitalized patients with COVID-19. *Journal of Thrombosis and Haemostasis*, *18*, 1995–2002, <https://doi.org/10.1111/jth.14888>.
- Owens, A. P. 3rd, & Mackman, N. (2011). Microparticles in hemostasis and thrombosis. *Circulation Research*, *108*, 1284–1297, <https://doi.org/10.1161/CIRCRESAHA.110.233056>.
- Païdassi, H., Tacnet-Delorme, P., Garlatti, V., Darnault, C., Ghebrehiwet, B., Gaboriaud, C., Arlaud, G. J., & Frachet, P. (2008). C1q binds phosphatidylserine and likely acts as a multiligand-bridging molecule in apoptotic cell recognition. *Journal of Immunology*, *180*, 2329–2338.
- Polasky, C., Wendt, F., Pries, R., & Wollenberg, B. (2020). Platelet induced functional alteration of CD4(+) and CD8(+) T cells in HNSCC. *International Journal of Molecular Sciences*, *21*, 7507, <https://doi.org/10.3390/ijms21207507>.
- Ponomareva, A. A., Nevzorova, T. A., Mordakhanova, E. R., Andrianova, I. A., Rauova, L., Litvinov, R. I., & Weisel, J. W. (2017). Intracellular origin and ultrastructure of platelet-derived microparticles. *Journal of Thrombosis and Haemostasis*, *15*, 1655–1667, <https://doi.org/10.1111/jth.13745>.
- Reininger, A. J., Heijnen, H. F., Schumann, H., Specht, H. M., Schramm, W., & Ruggeri, Z. M. (2006). Mechanism of platelet adhesion to von Willebrand factor and microparticle formation under high shear stress. *Blood*, *107*, 3537–3545, <https://doi.org/10.1182/blood-2005-02-0618>.
- Rha, M. S., Jeong, H. W., Ko, J. H., Choi, S. J., Seo, I. H., Lee, J. S., Sa, M., Kim, A. R., Joo, E. J., Ahn, J. Y., Kim, J. H., Song, K. H., Kim, E. S., Oh, D. H., Ahn, M. Y., Choi, H. K., Jeon, J. H., Choi, J. P., Kim, H. B., ... Shin, E. C. (2021). PD-1-Expressing SARS-CoV-2-Specific CD8(+) T Cells Are Not Exhausted, but Functional in Patients with COVID-19. *Immunity*, *54*, 44–52 e43, <https://doi.org/10.1016/j.immuni.2020.12.002>.
- Ridger, V. C., Boulanger, C. M., Angelillo-Scherrer, A., Badimon, L., Blanc-Brude, O., Bochaton-Piallat, M. L., Boilard, E., Buzas, E. I., Caporali, A., Dignat-George, F., Evans, P. C., Lacroix, R., Lutgens, E., Ketelhuth, D. F. J., Nieuwland, R., Toti, F., Tunon, J., Weber, C., & Hofer, I. E. (2017). Microvesicles in vascular homeostasis and diseases. Position Paper of the European Society of Cardiology (ESC) Working Group on Atherosclerosis and Vascular Biology. *Thrombosis and Haemostasis*, *117*, 1296–1316, <https://doi.org/10.1160/TH16-12-0943>.
- Rolfes, V., Idel, C., Pries, R., Plötze-Martin, K., Habermann, J., Gemoll, T., Bohnet, S., Latz, E., Ribbat-Idel, J., Franklin, B. S., & Wollenberg, B. (2018). PD-L1 is expressed on human platelets and is affected by immune checkpoint therapy. *Oncotarget*, *9*, 27460–27470, <https://doi.org/10.18632/oncotarget.25446>.
- Rydzynski Moderbacher, C., Ramirez, S. I., Dan, J. M., Grifoni, A., Hastie, K. M., Weiskopf, D., Belanger, S., Abbott, R. K., Kim, C., Choi, J., Kato, Y., Crotty, E. G., Kim, C., Rawlings, S. A., Mateus, J., Tse, L. P. V., Frazier, A., Baric, R., Peters, B., ... Crotty, S. (2020). Antigen-Specific Adaptive Immunity to SARS-CoV-2 in Acute COVID-19 and Associations with Age and Disease Severity. *Cell*, *183*, 996–1012 e1019, <https://doi.org/10.1016/j.cell.2020.09.038>.
- Sachs, A. B. (2000). Cell cycle-dependent translation initiation: IRES elements prevail. *Cell*, *101*, 243–245, [https://doi.org/10.1016/s0092-8674\(00\)80834-x](https://doi.org/10.1016/s0092-8674(00)80834-x).
- Sallusto, F., Geginat, J., & Lanzavecchia, A. (2004). Central memory and effector memory T cell subsets: Function, generation, and maintenance. *Annual Review of Immunology*, *22*, 745–763, <https://doi.org/10.1146/annurev.immunol.22.012703.104702>.
- Scholzen, T., & Gerdes, J. (2000). The Ki-67 protein: From the known and the unknown. *Journal of Cellular Physiology*, *182*, 311–322, [https://doi.org/10.1002/\(sici\)1097-4652\(200003\)182:3<311::Aid-jcp1>3.0.Co;2-9](https://doi.org/10.1002/(sici)1097-4652(200003)182:3<311::Aid-jcp1>3.0.Co;2-9).

- Sekine, T., Perez-Potti, A., Rivera-Ballesteros, O., Strålin, K., Gorin J. B., Olsson A., Llewellyn-Lacey, S., Kamal, H., Bogdanovic, G., Muschiol S., Wullmann D. J., Kammann, T., Emgård, J., Parrot, T., Folkesson, E., Karolinska COVID-19 Study Group, Rooyackers, O., Eriksson, L. I., Henter, J. I., ... Buggert, M. (2020). Robust T cell immunity in convalescent individuals with asymptomatic or mild COVID-19. *Cell* 183, 158–168 e114, <https://doi.org/10.1016/j.cell.2020.08.017>.
- Sette, A., & Crotty, S. (2021). Adaptive immunity to SARS-CoV-2 and COVID-19. *Cell*, 184, 861–880, <https://doi.org/10.1016/j.cell.2021.01.007>.
- Sims, P. J., Faioni, E. M., Wiedmer, T., & Shattil, S. J. (1988). Complement proteins C5b-9 cause release of membrane vesicles from the platelet surface that are enriched in the membrane receptor for coagulation factor Va and express prothrombinase activity. *Journal of Biological Chemistry*, 263, 18205–18212.
- Song, J. W., Zhang, C., Fan, X., Meng, F. P., Xu, Z., Xia, P., Cao, W. J., Yang, T., Dai, X. P., Wang, S. Y., Xu, R. N., Jiang, T. J., Li, W. G., Zhang, D. W., Zhao, P., Shi, M., Agrati, C., Ippolito, G., Maeurer, M., ... Zhang, J. Y. (2020). Immunological and inflammatory profiles in mild and severe cases of COVID-19. *Nature Communications*, 11, 3410, <https://doi.org/10.1038/s41467-020-17240-2>.
- Song, J., So, T., Cheng, M., Tang, X., & Croft, M. (2005). Sustained survivin expression from OX40 costimulatory signals drives T cell clonal expansion. *Immunity*, 22, 621–631, <https://doi.org/10.1016/j.immuni.2005.03.012>.
- Song, W. C., & FitzGerald, G. A. (2020). COVID-19, microangiopathy, hemostatic activation, and complement. *Journal of Clinical Investigation*, 130, 3950–3953, <https://doi.org/10.1172/JCI140183>.
- Su, Y., Chen, D., Yuan, D., Lausted, C., Choi, J., Dai, C. L., Voillet, V., Duvvuri, V. R., Scherler, K., Troisch, P., Baloni, P., Qin, G., Smith, B., Kornilov, S. A., Rostomily, C., Xu, A., Li, J., Dong, S., Rothchild, A., ... Heath, J. R. (2020). Multi-omics resolves a sharp disease-state shift between mild and moderate COVID-19. *Cell*, 183, 1479–1495 e1420, <https://doi.org/10.1016/j.cell.2020.10.037>.
- Tan, A. T., Linster, M., Tan, C. W., Le Bert, N., Chia, W. N., Kunasegaran, K., Zhuang, Y., Tham, C. Y. L., Chia, A., Smith, G. J. D., Young, B., Kalimuddin, S., Low, J. G. H., Lye, D., Wang, L. F., & Bertoletti, A. (2021). Early induction of functional SARS-CoV-2-specific T cells associates with rapid viral clearance and mild disease in COVID-19 patients. *Cell Reports*, 34(6), 108728, <http://doi.org/10.1016/j.celrep.2021.108728>.
- Tan, L. A., Yu, B., Sim, F. C., Kishore, U., & Sim, R. B. (2010). Complement activation by phospholipids: The interplay of factor H and Clq. *Protein Cell*, 1, 1033–1049, <https://doi.org/10.1007/s13238-010-0125-8>.
- Tang, N., Li, D., Wang, X., & Sun, Z. (2020). Abnormal coagulation parameters are associated with poor prognosis in patients with novel coronavirus pneumonia. *Journal of Thrombosis and Haemostasis*, 18, 844–847, <https://doi.org/10.1111/jth.14768>.
- Teuwen, L. A., Geldhof, V., Pasut, A., & Carmeliet, P. (2020). COVID-19: the vasculature unleashed. *Nature Reviews Immunology*, 20, 389–391, <https://doi.org/10.1038/s41577-020-0343-0>.
- Trautz, B., Wiedemann, H., Lüchtenborg, C., Pierini, V., Kranich, J., Glass, B., Kräusslich, H.-G., Brocker, T., Pizzato, M., Ruggieri, A., Brügger, B., & Fackler, O. T. (2017). The host-cell restriction factor SERINC5 restricts HIV-1 infectivity without altering the lipid composition and organization of viral particles. *Journal of Biological Chemistry*, 292(33), 13702–13713, <http://doi.org/10.1074/jbc.m117.797332>.
- van der Zee, P. M., Biró, E., Ko, Y., de Winter, R. J., Hack, C. E., Sturk, A., & Nieuwland, R. (2006). P-selectin- and CD63-exposing platelet microparticles reflect platelet activation in peripheral arterial disease and myocardial infarction. *Clinical Chemistry*, 52, 657–664, <https://doi.org/10.1373/clinchem.2005.057414>.
- Wang, R. H., Phillips, G. Jr., Medof, M. E., & Mold, C. (1993). Activation of the alternative complement pathway by exposure of phosphatidylethanolamine and phosphatidylserine on erythrocytes from sickle cell disease patients. *Journal of Clinical Investigation*, 92, 1326–1335, <https://doi.org/10.1172/JCI116706>.
- Wölfel, R., Corman, V. M., Guggemos, W., Seilmaier, M., Zange, S., Müller, M. A., Niemeyer, D., Jones, T. C., Vollmar, P., Rothe, C., Hoelscher, M., Bleicker, T., Brünink, S., Schneider, J., Ehmann, R., Zwirgmaier, K., Drosten, C., & Wendtner, C. (2020). Virological assessment of hospitalized patients with COVID-2019. *Nature*, 581, 465–469, <https://doi.org/10.1038/s41586-020-2196-x>.
- WorldHealthOrganization (2020). Novel Coronavirus: COVID-19 Therapeutic Trial Synopsis. *WHO R&D Blueprint*, Draft February 18, 2020. www.who.int/blueprint/priority-diseases/key-action/COVID-19_Treatment_Trial_Design_Master_Protocol_synopsis_Final_18022020.pdf
- Yang, X., Yu, Y., Xu, J., Shu, H., Xia, J., Liu, H., Wu, Y., Zhang, L., Yu, Z., Fang, M., Yu, T., Wang, Y., Pan, S., Zou, X., Yuan, S., & Shang, Y. (2020). Clinical course and outcomes of critically ill patients with SARS-CoV-2 pneumonia in Wuhan, China: A single-centered, retrospective, observational study. *The Lancet Respiratory Medicine*, 8, 475–481, [https://doi.org/10.1016/S2213-2600\(20\)30079-5](https://doi.org/10.1016/S2213-2600(20)30079-5).
- Zaid, Y., Puhm, F., Allaey, I., Naya, A., Oudghiri, M., Khalki, L., Limami, Y., Zaid, N., Sadki, K., Ben El Haj, R., Mahir, W., Belayachi, L., Belefquih, B., Benouda, A., Cheikh, A., Langlois, M. A., Cherrah, Y., Flamand, L., Guessous, F., & Boilard, E. (2020). Platelets can associate with SARS-Cov-2 RNA and are hyperactivated in COVID-19. *Circulation Research*, 127, 1404–18, <https://doi.org/10.1161/CIRCRESAHA.120.317703>.
- Zhang, Y., Xiao, M., Zhang, S., Xia, P., Cao, W., Jiang, W., Chen, H., Ding, X., Zhao, H., Zhang, H., Wang, C., Zhao, J., Sun, X., Tian, R., Wu, W., Wu, D., Ma, J., Chen, Y., Zhang, D., ... Zhang, S. (2020). Coagulopathy and antiphospholipid antibodies in patients with Covid-19. *The New England Journal of Medicine*, 382, e38, <https://doi.org/10.1056/NEJMc2007575>.
- Zheng, H. Y., Zhang, M., Yang, C. X., Zhang, N., Wang, X. C., Yang, X. P., Dong, X. Q., & Zheng, Y. T. (2020). Elevated exhaustion levels and reduced functional diversity of T cells in peripheral blood may predict severe progression in COVID-19 patients. *Cellular & Molecular Immunology*, 17, 541–543, <https://doi.org/10.1038/s41423-020-0401-3>.
- Zheng, M., Gao, Y., Wang, G., Song, G., Liu, S., Sun, D., Xu, Y., & Tian, Z. (2020). Functional exhaustion of antiviral lymphocytes in COVID-19 patients. *Cellular & Molecular Immunology*, 17, 533–535, <https://doi.org/10.1038/s41423-020-0402-2>.
- Zhou, R., To, K. K., Wong, Y. C., Liu, L., Zhou, B., Li, X., Huang, H., Mo, Y., Luk, T. Y., Lau, T. T., Yeung, P., Chan, W. M., Wu, A. K., Lung, K. C., Tsang, O. T., Leung, W. S., Hung, I. F., Yuen, K. Y., & Chen, Z. (2020). Acute SARS-CoV-2 infection impairs dendritic cell and T cell responses. *Immunity*, 53, 864–877 e865, <https://doi.org/10.1016/j.immuni.2020.07.026>.

SUPPORTING INFORMATION

Additional supporting information may be found in the online version of the article at the publisher's website.

How to cite this article: Rausch, L., Lutz, K., Schifferer, M., Winheim, E., Gruber, R., Oesterhaus, E. F., Rinke, L., Hellmuth, J. C., Scherer, C., Muenchhoff, M., Mandel, C., Bergwelt-Baildon, M., Simons, M., Straub, T., Krug, A. B., Kranich, J., & Brocker, T. (2021). Binding of phosphatidylserine-positive microparticles by PBMCs classifies disease severity in COVID-19 patients. *Journal of Extracellular Vesicles*, 10, e12173. <https://doi.org/10.1002/jev2.12173>

9.5 Phosphatidylserine-positive extracellular vesicles boost effector CD8⁺ T cell responses during viral infection.

Rausch L, Flaskamp L, Ashokkumar A, Trefzer A, Ried C, Buchholz VR, Obst R, Straub T, Brocker T, **Kranich J***. Proc Natl Acad Sci U S A. 2023 Apr 18;120(16):e2210047120. * equally contributed last author*



Phosphatidylserine-positive extracellular vesicles boost effector CD8⁺ T cell responses during viral infection

Lisa Rausch^{a,1} , Lavinia Flaskamp^{a,1} , Ashretha Ashokkumar^a, Anne Trefzer^{a,2}, Christine Ried^a, Veit R. Buchholz^b , Reinhard Obst^a , Tobias Straub^c, Thomas Brocker^{a,3} , and Jan Kranich^{a,3}

Edited by Michael Dustin, University of Oxford, Oxford, United Kingdom; received June 10, 2022; accepted March 14, 2023

CD8⁺ T cells are crucial for the clearance of viral infections. During the acute phase, proinflammatory conditions increase the amount of circulating phosphatidylserine⁺ (PS) extracellular vesicles (EVs). These EVs interact especially with CD8⁺ T cells; however, it remains unclear whether they can actively modulate CD8⁺ T cell responses. In this study, we have developed a method to analyze cell-bound PS⁺ EVs and their target cells *in vivo*. We show that EV⁺ cell abundance increases during viral infection and that EVs preferentially bind to activated, but not naive, CD8⁺ T cells. Superresolution imaging revealed that PS⁺ EVs attach to clusters of CD8 molecules on the T cell surface. Furthermore, EV-binding induces antigen (Ag)-specific TCR signaling and increased nuclear translocation of the transcription factor Nuclear factor of activated T-cells (NFATc1) *in vivo*. EV-decorated but not EV-free CD8⁺ T cells are enriched for gene signatures associated with T-cell receptor signaling, early effector differentiation, and proliferation. Our data thus demonstrate that PS⁺ EVs provide Ag-specific adjuvant effects to activated CD8⁺ T cells *in vivo*.

extracellular vesicles | exosomes | CD8 T cells | LCMV | phosphatidylserine

T cells confer protection against pathogens and tumors. The initiation and maintenance of T cell responses require specific signals delivered by cell-to-cell interactions and secreted soluble cytokines. In addition, extracellular vesicles (EVs) constitute a mechanism of intercellular communication during immune responses (1). However, the precise mechanisms of how EVs can affect T cells *in vivo* remain unclear (2, 3).

EVs are lipid-bilayer enclosed, spherical structures released by virtually all cell types. They carry various bioactive molecules, including proteins, lipids, and nucleic acids, able to exert functional modifications and phenotypic changes upon interaction with recipient cells (4). Due to their high heterogeneity in origin, size, and composition, several subtypes of EVs have been described, including exosomes and microvesicles (5).

Early studies first demonstrated that exosomes from B cell lines bear peptide/major histocompatibility class (MHC) II complexes and could directly activate CD4⁺ T cells *in vitro* (6). The finding that EVs derived from tumor peptide-pulsed dendritic cells (DCs) can elicit strong CD8⁺ T cell responses and tumor suppression *in vivo* further supported the idea that EVs were involved in antigen (Ag) presentation (7). Numerous follow-up studies showed that Ag-presenting cell (APC)-derived EVs, particularly those released by mature DCs, can serve as sources of Ag and induce T cell proliferation, memory development, and antitumor responses *in vitro* and *in vivo* (1, 7–14). DC-derived EVs carry the relevant MHC-I and -II complexes and costimulatory molecules such as CD86 and CD54 for productive interaction with T cells. However, the precise mechanisms of T cell stimulation are still unknown.

While some reports showed that EVs alone can activate T cells *in vitro* (6, 13–15), other studies suggested that an indirect mode of action as DCs was required for the stimulation of T cells by EVs (1, 9, 12, 16–22). Therefore, the capacity of free EVs to regulate T cell function and differentiation as cell-independent biological modifiers *in vivo* remained unclear.

Like apoptotic cells, also EVs display phosphatidylserine (PS) on their outer membrane layer (23–26). Based on this marker, we previously described a sensitive and robust method to analyze EVs in lymphocytic choriomeningitis virus (LCMV)-infected mice (27) and SARS-CoV-2-infected humans (28). During these acute infections, high frequencies of activated CD8⁺ T cells were associated with PS⁺ EVs. Here, we demonstrate that the binding of PS⁺ EVs to Ag-specific CD8⁺ T cells triggers TCR-signaling *in vivo*, as demonstrated by nuclear accumulation of NFATc1. Specifically, EV-associated CD8⁺ T cells showed enhanced proliferation, effector gene expression signatures, including genes like *Ifng* and *Tnf*. Therefore, our findings establish that EVs can boost effector gene expression by directly associating with activated Ag-specific CD8⁺ T cells during acute infection.

Significance

Many *in vitro* studies have shown a role of extracellular vesicles (EVs) in priming of naive T cells. However, if EVs really play a relevant role in T cell responses *in vivo* remained highly controversial. We have recently developed a method, allowing us to identify and characterize cells binding naturally occurring EVs *in vivo*. With this method, we demonstrate here that activated effector cells, but not naive T cells, extensively engage with EVs during viral infections. We provide convincing evidence from *in vivo* studies that this interaction increases the expression of effector genes and proliferation of CD8⁺ T cells in (lymphocytic choriomeningitis virus) LCMV-infected mice. This, in turn, boosts T cell effector functions.

Author contributions: T.B. and J.K. designed research; L.R., L.F., A.A., and C.R. performed research; A.T., V.R.B., and R.O. contributed new reagents/analytic tools; L.R., L.F., T.S., T.B., and J.K. analyzed data; and T.B. and J.K. wrote the paper.

Competing interest statement: T.B. and J.K. have a licensing agreement with BioLegend, Inc. for the commercialization of the C1 tetramer.

This article is a PNAS Direct Submission.

Copyright © 2023 the Author(s). Published by PNAS. This open access article is distributed under Creative Commons Attribution-NonCommercial-NoDerivatives License 4.0 (CC BY-NC-ND).

¹L.R. and L.F. contributed equally to this work.

²Present address: Numab Therapeutics AG, Translational Science Oncology, 8810 Horgen, Switzerland.

³To whom correspondence may be addressed. Email: jan.kranich@med.uni-muenchen.de or tbrocker@med.uni-muenchen.de.

This article contains supporting information online at <https://www.pnas.org/lookup/suppl/doi:10.1073/pnas.2210047120/-/DCSupplemental>.

Published April 11, 2023.

Results

In Vivo Detection of Naturally Occurring EVs Associated with CD8⁺ T cells. Previously, we found that APC-derived PS⁺ exosomes bind to activated CD8⁺ T cells during LCMV infection (27). However, neither the kinetics of EV appearance nor the T cell subset interacting with EVs is known. Furthermore, it is unclear whether T cell/EV interaction would affect the functional differentiation of T cells.

To address these questions, we used intravenously injected PS-binding Milk fat globule-EGF factor 8 protein (MFG-E8)-eGFP (27) or biotinylated murine MFG-E8 C1 domains tetramerized using Streptavidin (C1 tetramers) (29). Both reagents detect naturally occurring PS⁺ EVs in spleens of mice acutely infected with LCMV Armstrong (LCMV_{Arm}) in vivo at different time points after infection (Fig. 1*A*). We examined single-cell suspensions of live cells (*SI Appendix, Fig. S1A*) by imaging flow cytometry (IFC) using an ImageStream cytometer (Fig. 1*B*). PS⁺ dying cells (live/dead dye⁻, with intact cell membrane) and PS⁺EV⁺ living cells were digitally sorted using a convolutional autoencoder (CAE) module (Fig. 1*B, Right*) (27). The percentage of PS⁺ cells increased sharply in virus-infected mice compared to the noninfected control group (Fig. 1*B*). The frequency of EV⁺ live cells and EV⁺CD8⁺ T cells peaked on day five post infection (p.i.) and declined from day 10 to day 15 p.i. (Fig. 1*B* and *C*). Similarly, apoptosis of total live and CD8⁺ T cells reached its maximum on day five (Fig. 1*C*). While the frequency of bona fide apoptotic PS⁺CD8⁺ T cells remained low (1 to 2% of CD8⁺ T cells) even at the peak response, up to 35% of CD8 T cells were associated with PS⁺ EVs at day five p.i. (Fig. 1*C*). Notably, on day 15, p.i. EV-decoration and apoptosis dropped below the levels of noninfected mice (Fig. 1*C*). These data indicate that EV-decoration of CD8⁺ T cells is transient and correlate with the published kinetics of LCMV_{Arm} titers (30, 31). Furthermore, we detected the peak of EV decoration at the maximum expansion of LCMV-specific CD8⁺ T cells in the spleen, which occurs between day five and day eight after infection (32).

Next, we determined if EVs preferentially associate with a specific T cell subset in LCMV-infected mice. On day five, CD8⁺ effector T cells (CD62L⁻CD44⁺, T_E) showed the highest levels of EV-decoration (Fig. 1*D*). While less than 10% of central memory (CD62L⁺CD44⁺, T_{CM}) CD8⁺ T cells were associated with PS⁺ vesicles, EVs were absent on naive (CD62L⁺CD44⁻, T_N) CD8⁺ T cells. These data reveal that EVs bind differently to distinct CD8⁺ T cell subsets, with a preference for activated T_E cells during acute LCMV infection.

The observed enhanced binding of EVs to CD8⁺ T cells could be caused by increased concentration of EVs in infected animals or altered binding properties of activated T cells, or both. To distinguish between these two factors, we next sought to determine whether the concentration of EVs increases in infected animals. Marker-independent particle analysis indicated that the size of EV particles did not change after infection in serum (Fig. 1*D*). Surprisingly, the serum concentration of particles decreased significantly after virus infection (Fig. 1*D*, NTA). To rule out the possibility that by focusing on PS⁺ EVs we would miss a significant proportion of PS⁻ EVs, we analyzed the frequencies of PS⁺ EVs in both situations (Fig. 1*D*, image stream). Yet, in infected and noninfected animals, the largest proportion (over 95%) of all EVs was PS⁺.

These data suggest that in the case of infection, EV binding to lymphocytes may lead to a statistically significant decrease in the concentration of free EVs in serum. Furthermore, PS is an excellent marker for EVs as most EVs are PS⁺.

EV-Associated CD8⁺ T Cells Show Increased Levels of Nuclear NFATc1. With the above-described approach, we are able to stain naturally occurring PS⁺ EVs in vivo. We showed in a previous study that EVs associated with activated CD8⁺ T cells during acute LCMV infection in vivo carry exosome-markers CD9/CD63 as well as MHC-II, CD86, and CD54, demonstrating their APC origin (27). Several studies have also shown that APC-derived EVs carry MHC-I (1). The presence of these molecules allows EVs potentially to stimulate T cells. T cell receptor (TCR)-triggering induces a calcium-dependent, rapid translocation of NFAT from the cytoplasm to the nucleus, a process which is essential for CD8⁺ T cell cytotoxicity during viral infection (33). Therefore, nuclear translocation of NFAT is a sensitive read-out for TCR signaling. The NFAT-family member NFATc1 is an important regulator of CD8⁺ T_E cell activation and cytotoxicity (34). To investigate whether CD8⁺ T cells having bound naturally occurring PS⁺ EVs display different TCR signaling compared to EV⁻ CD8⁺ T cells, we analyzed the nuclear translocation of NFATc1 in EV⁺ and EV⁻ CD8⁺ T cells during LCMV infection in vivo (Fig. 2*A*). We found significantly higher levels of nuclear NFATc1 as demonstrated by a higher median similarity score (ss) and an increased frequency of nuclear NFATc1 in EV⁺ CD8⁺ T cells compared to EV⁻ CD8⁺ T cells (Fig. 2*A*). As NFAT is rapidly exported from the nucleus (after ~15 min), when TCR-mediated signaling stops (35), these results support the idea that EV-T-cell interactions could cause NFAT translocation.

To investigate whether NFAT translocation in EV⁺ CD8⁺ T cells is driven by TCR stimulation and hence Ag-dependent, we adoptively transferred in vitro activated TCR-transgenic LCMV-specific, P14 CD8⁺ T effector cells [specific for the LCMVgp₃₃₋₄₁ peptide/MHC-I D^b, (36)] together with activated LCMV-irrelevant OT-I CD8⁺ T effector cells [specific for ovalbumin (OVA)₂₅₇₋₂₆₄ peptide/MHC-I K^b, (37)] into mice that had been infected with LCMV 2 d before (Fig. 2*B*). In this setting, OT-I cells do not receive Ag-specific TCR stimulation due to the absence of their cognate Ag from the system.

As expected, 3 d after transfer, due to the presence of their cognate LCMV-Ag P14 T cells had accumulated to higher frequencies as compared to “bystander” OT-I T cells (Fig. 2*C, Left*). Additionally, P14 cells also showed a significantly higher degree of EV association as compared to nonspecific OT-I cells (Fig. 2*C, Right*). This finding suggests that Ag specificity of the TCR may significantly contribute to the binding of EVs to T cells. Most importantly, we found a significantly higher ss and higher levels of intranuclear NFATc1 in EV⁺CD8⁺ P14 T cells compared to their EV⁻ CD8⁺ P14 T cell counterparts within the same animals (Fig. 2*D*). Notably, the amount of nuclear NFATc1 of EV⁺ P14 cells exceeded that of P14 cells stimulated in vitro with antibodies to CD3ε and CD28 (Fig. 2*D*, dotted line). The frequency of nonspecific OT-I cells with nuclear NFATc1 was about half of that of P14 T cells (Fig. 2*D*).

Nevertheless, at rather low levels, EV⁺ OT-I T cells had slightly but significantly more intranuclear NFATc1 than EV⁻ OT-I T cells (Fig. 2*D*). Together, these results further support the idea that EVs may promote the continuous Ag-specific TCR stimulation of activated CD8⁺ T cells during acute LCMV infection.

To confirm EV-TCR interaction, we performed direct stochastic optical reconstruction microscopy (dSTORM) on fluorescence-activated cell sorting (FACS)-sorted PS⁺ and PS⁻ CD8⁺ T cells from LCMV-infected mice. As we were limited to three dSTORM compatible fluorochromes, we used PS [stained in vivo with C1 tetramers (C1-SA-AF647)] and CD9-CF568 to identify EVs and

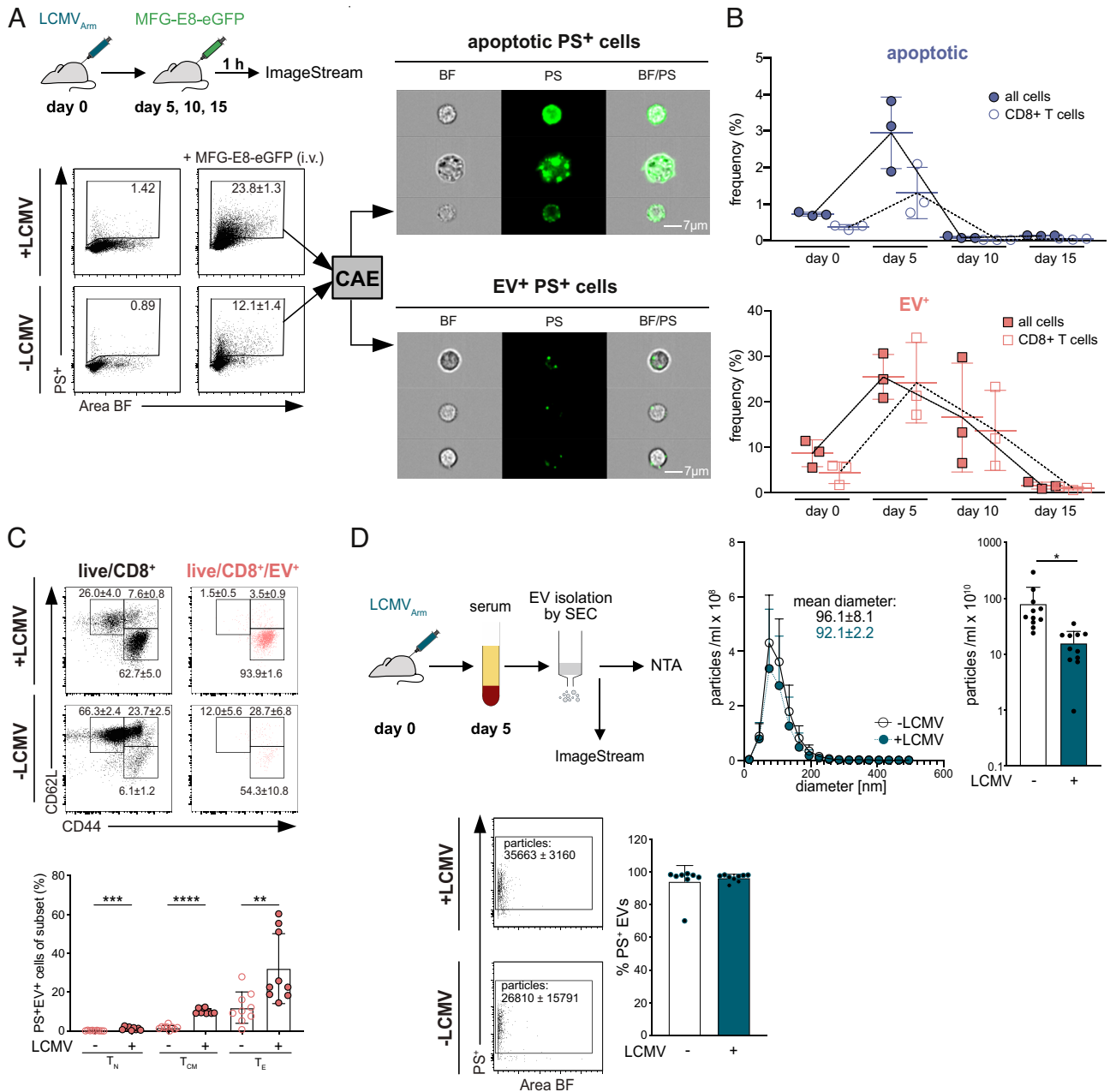


Fig. 1. MFG-E8-eGFP detects PS⁺ apoptotic and PS⁺ EV-decorated cells in vivo. (A) Flow chart shows experimental setup for analysis of PS⁺ cells in mice. Splenocytes were analyzed by IFC using an ImageStream cytometer. Dot plots display the gating strategy of live/dead PS⁺ cells from the spleens of noninfected and LCMV_{Arm}-infected mice. Area and aspect ratio of the bright field (BF) channel were used to identify single cells (SI Appendix, Fig. S1). Numbers in the gate indicate the mean percentages ±SD of PS⁺ cells from MFG-E8-eGFP-injected mice (n = 3) and control (PBS)-injected mice (n = 1). Only live cells were analyzed (SI Appendix, Fig. S1A) with the convolutional autoencoder (CAE) module as described previously (Kranich et al. 27). Representative images of bright field (BF), PS, and BF/PS overlay channels of PS⁺ (SI Appendix, Fig. S1B) and PS⁺ cells are shown. (Scale bar: 7 μm.) Shown are representative results from two independent experiments. (B) Mice were infected with LCMV_{Arm} (n = 3 per timepoint), and frequencies of EV⁺ (red) and apoptotic (blue) total live cells and CD8⁺ T cells were determined on days 5, 10, and day 15 p.i. using the CAE. Gating see SI Appendix, Fig. S1C. Representative results from two independent experiments are shown. (C) Representative dot plots of different T cell subsets binding naturally occurring PS⁺EVs after i.v. administration of MFG-E8-eGFP are shown. Gates show total live CD8⁺ (Left, black) and live/CD8⁺/EV⁺ (Right, red) CD62L⁺CD44⁺ naive (T_N), CD62L⁺CD44⁺ central memory (T_{CM}), and CD62L⁺CD44⁺ effector (T_E) T cells in spleens of LCMV-infected (Upper) and noninfected (Lower) mice. Values next to the gate indicate the frequencies ±SD of cells within the respective gate. Bar graphs visualize frequencies ±SD of T_N, T_{CM}, and T_E CD8⁺ T cells that have bound PS⁺EVs. Bar graphs show the results from nine LCMV-infected and nine noninfected mice pooled from three independent experiments. (D) Analysis of serum EVs isolated from noninfected and LCMV_{Arm}-infected mice (day five p.i.). Upper panel shows nanoparticle tracker (NTA) analysis of EV fractions 2 to 7 isolated by size exclusion chromatography, n = 4, representative results from three independent experiments are shown. Bar graphs show particles/mL in noninfected and infected sera, n = 11, pooled results from three independent experiments are shown. Lower panel shows ImageStream analysis of serum EVs. Gating strategy, unstained, dye only, and detergent controls see SI Appendix, Fig. S1D. Dot plots show PS⁺ EVs present in sera of infected and noninfected mice. Mean number (±SD) of PS⁺ particles are indicated next to the gate. Bar graph shows percentage of PS⁺ EVs (n = 7 and 8 for noninfected and infected, respectively). Pooled results of two independent experiments are shown. Unpaired Student's *t* test was used to determine statistical significance, with **P* < 0.05, ***P* < 0.01, and ****P* < 0.001.

CD8-CF488 to identify the TCR complex (Fig. 2E), as CD8 colocalizes with TCRab in activated T cells (38). Indeed, on PS⁺ CD8 T cells, we could readily identify PS⁺ CD9⁺ double-positive clusters of EV size (approximately 200 nm, Fig. 2F, Upper), which were

nearly absent on PS⁻ CD8 T cells (Fig. 2F, Lower). These PS⁺CD9⁺ EVs colocalized with CD8 (Fig. 2F, I.I, I.II, II.I) and therefore with the TCR complex. Quantification of total CD8⁺ clusters revealed a significant increase of CD8⁺ clusters on PS⁺ CD8 T cells (Fig. 2F,

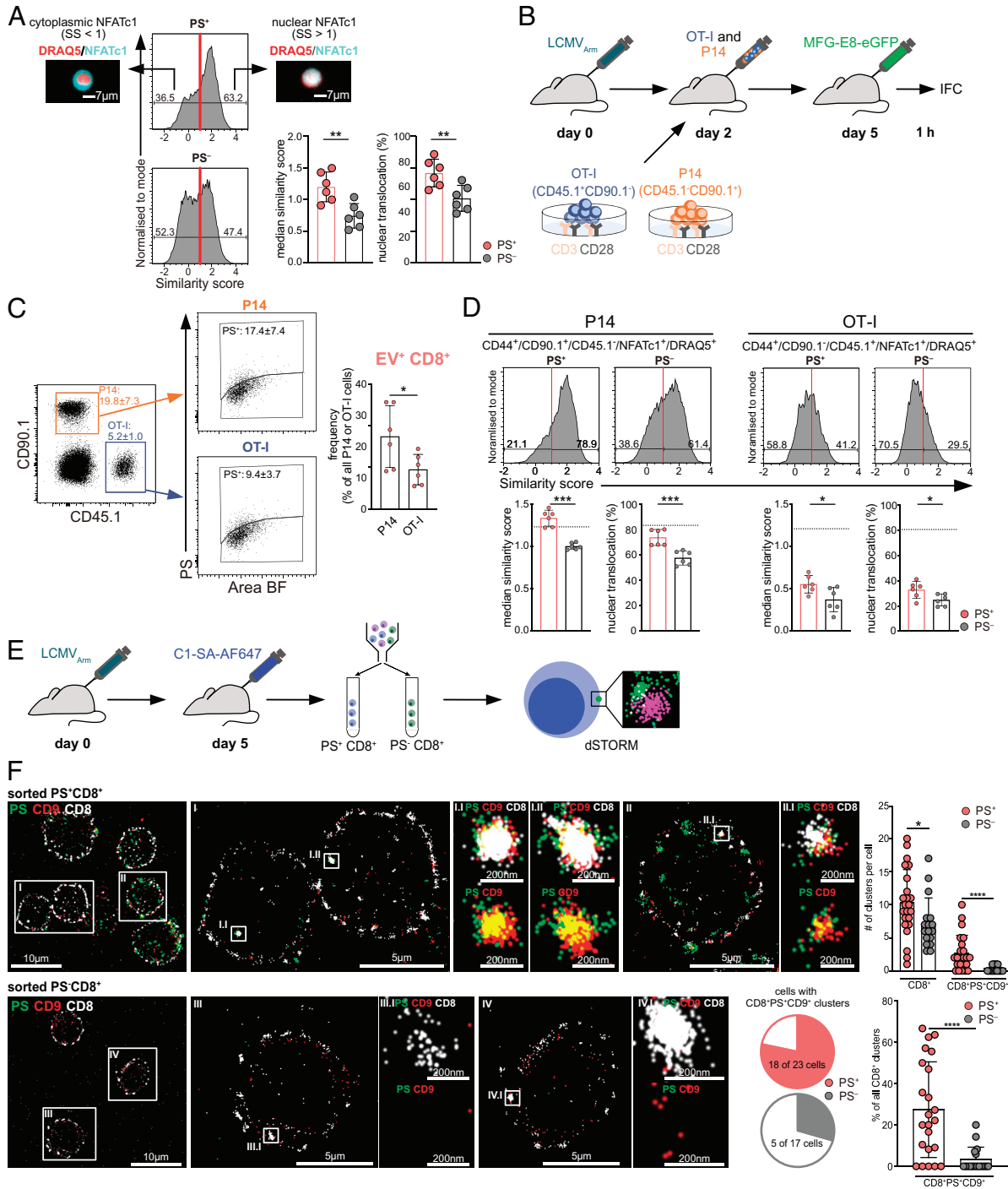


Fig. 2. Increased nuclear translocation of NFATc1 in EV⁺CD44⁺CD8⁺ T cells. Mice were infected with LCMV_{Arm} (n = 6, pooled from two independent experiments), on day five p.i., naturally occurring PS⁺ EVs were stained in vivo by injecting MFG-E8-eGFP (100 µg/mouse). Isolated splenocytes were stained for surface markers, NFATc1 and DRAQ5 (DNA dye) and analyzed by IFC. (A) Nuclear translocation of NFATc1 in Draq5⁺NFATc1⁺PS⁺ and PS⁻CD44⁺CD8⁺ T cells (gating strategy *SI Appendix, Fig. S2*) was determined using the similarity feature of the IDEAS software. Cells with a similarity score (SS)>1 have nuclear NFATc1, cells with a SS<1 have cytoplasmic NFATc1. Representative histograms show median SS of PS⁺ and PS⁻CD44⁺CD8⁺ T cells and frequencies of cells with cytoplasmic and nuclear NFATc1. Representative IFC images display cells with cytoplasmic NFATc1 (Left) and nuclear NFATc1 (Right). (Scale bar 7 µm.) Bar graphs show the median SS ±SD (Left) and the frequencies ±SD (Right) of PS⁺ and PS⁻CD44⁺CD8⁺ T cells. Representative results from four independent experiments are shown. For statistical analysis, unpaired Student's *t* test was used with **P* < 0.05, ****P* < 0.01, and *****P* < 0.001. (B) Experimental setup for analyzing NFATc1 translocation in transferred CD45.1⁺CD90.1⁺ P14 and CD45.1⁻CD90.1⁻ OT-I CD44⁺CD8⁺ T cells. (C) Splenic P14 and OT-I CD8⁺ T cells were stimulated in vitro and transferred into day two LCMV-infected mice. After 3 d, MFG-E8-eGFP was injected, and NFATc1 translocation was analyzed. Dot plots show gating of PS⁺ and PS⁻ CD90.1⁺CD45.1⁺ P14 and PS⁻ CD45.1⁻CD90.1⁻ OT-I T cells with average percentages ±SD (n = 6). Bar graph displays average frequencies ±SD of PS⁺ P14, OT-I cells. (D) Representative histograms show SS of PS⁺ and PS⁻ CD44⁺ P14 and CD44⁺ OT-I T cells with frequencies of cells with a SS>1 and <1. Bar graphs show frequencies of cells with nuclear NFAT and median SS ±SD. Results from six mice were pooled from two independent experiments. Dotted horizontal lines represent the SS of in vitro-activated P14 and OT-I before transfer into mice (n = 1). (E) Experimental setup for (F): infected mice were injected with 50 µg C1-SA-AF647 to stain PS⁺ EVs in vivo. One hour later, spleens were removed and stained with CD8-CF488 and CD9-CF568. After fixation, PS⁺ and PS⁻ CD8⁺ T cells were sorted and analyzed by dSTORM superresolution microscopy. (F) Upper and Lower panels show representative superresolution images of PS⁺ and PS⁻ CD8⁺ T cells, respectively (PS green, CD9 red, CD8 white). Areas labeled with I, II, III, and IV are shown with higher magnifications in the micrographs labeled accordingly. Total CD8⁺ clusters and CD8⁺CD9⁺PS⁺ triple-positive clusters were quantified using the cluster analysis tool of the CODI software (Oxford Nanoimaging). Upper bar graph shows the number of total CD8⁺ and triple-positive clusters per sorted PS⁻ (n = 17) or PS⁺ (n = 23) cell. Each datapoint represents one cell. Lower bar graph shows the percentage of triple-positive clusters of all CD8⁺ clusters per cell. Pie charts indicate the number of cells with triple-positive clusters. For statistical significance, unpaired Student's *t* test was used with **P* < 0.05, ****P* < 0.01, and *****P* < 0.001.

Upper bar graph). While more than 75% of the sorted PS⁺CD8⁺ T cells had CD8⁺CD9⁺PS⁺ triple-positive clusters (Fig. 2 F, Lower, pie chart), approximately 30% of all observed CD8⁺ clusters of each cell were CD8⁺CD9⁺PS⁺ triple positive and therefore colocalized with CD9 and PS. (Fig. 2 F, Lower, bar graph). The few PS⁺ triple-positive clusters on PS⁻ cells were of low intensity and likely due to sort impurities. These data show that CD8⁺ T cells associated with PS⁺ EVs had i) more aggregated CD8⁺ clusters as compared to PS⁻ CD8⁺ T cells and ii) that PS⁺ EVs locate to the CD8/TCR-complex on the T cell surface, making EV-mediated TCR-signaling a likely event.

Transcriptional Profiling Reveals Increased Proliferation, Effector Function, and Reduced Memory Potential of EV⁺ CD8⁺ T Cells.

For an in-depth comparison of EV⁻ and EV⁺ CD8⁺ T_E cells, we performed RNAseq analysis of these cells sorted from LCMV-infected mice at days five and 10 after infection. We were specifically interested in whether EV-binding to CD8⁺ T cells influences specific CD8⁺ memory or effector differentiation programs. For this, we performed gene expression analyses (RNAseq, data available at GEO accession number GSE201507) and subsequent gene set enrichment analyses (GSEA) against 10 well-described gene clusters (39). These clusters define gene-expression signatures of naive, short-term, early, and late effector cells, as well as memory precursor, and memory CD8⁺ T cells. On day five, three gene sets (cluster I—initial cytokine or effector response, cluster II—preparation for cell division, and cluster III—cell cycle and cell division; Fig. 3A) were significantly enriched in EV⁺ CD8⁺ T cells (Fig. 3A and B). All differentially expressed genes (DEGs) on day five (Fig. 3B and C and SI Appendix, Fig. S4) and day 10 (SI Appendix, Fig. S5) with a false discovery rate (FDR) of <0.05 are highlighted in fold change plots. Expressions of the main CD8⁺ T_E cell cytokine *Ifng* and the orphan nuclear receptor *Nra4a1* (encoding for NUR77), which is induced by TCR signals in a dose-dependent manner (40) were significantly up-regulated in EV⁺ CD8⁺ T cells (Fig. 3C and SI Appendix, Fig. S4A).

Also, EV⁺ CD8⁺ T cells showed significantly elevated *Irf4* and *Irf8* transcription factors, which are both crucial for CD8⁺ T cells to develop effector functions (41, 42) (Fig. 3C and SI Appendix, Fig. S4A). Hence, we conclude that EV⁺ CD8⁺ T cells receive additional TCR signals for proliferation and effector cytokine production than their EV⁻ counterparts. In addition, EV⁺ CD8⁺ T cells showed five significantly down-regulated gene sets (cluster IV—naive and late memory, cluster VI—short-term effector and memory, cluster VII—memory precursor, cluster VIII—naive or late effector or memory, and cluster X—late effector or memory) and therefore may have a reduced potential to differentiate into memory T cells (Fig. 3A–C and SI Appendix, Fig. S4B)—a process that is normally initiated around days four to six p.i. (43, 44). Specifically, genes such as the transcriptional repressors *Id2* (cluster VI, SI Appendix, Fig. S4B) and *Id3* (cluster II, Fig. 3C and SI Appendix, Fig. S4B), which regulate memory differentiation (45), the transcription factor TCF1 (cluster VII, encoded by *Tcf7*) which is essential for the formation of central memory CD8⁺ T cells (46–48), and *Il7r* (cluster VII), which is highly expressed on memory cells (49), were significantly down-regulated in EV⁺ CD8⁺ T cells (Fig. 3C and SI Appendix, Fig. S4B).

We then assessed differences between EV⁺ and EV⁻ CD8⁺ T cells on day 10 of the LCMV infection and performed a GSEA analysis against the same gene sets (Fig. 3A and SI Appendix, Fig. S5). Also, on day 10, clusters I, II, and III showed clear enrichment in EV⁺ CD8⁺ T cells, indicating that these cells are still proliferating and have effector phenotypes with *Irf4*, *Irf8*, and *Nra4a1*, but not *Ifng* being significantly up-regulated (Fig. 3A and SI Appendix,

Fig. S5A). However, at this later point and in contrast to day five, cluster IV (naive and late memory) was also enriched in EV⁺CD8⁺ T cells (Fig. 3A and SI Appendix, Fig. S5A). Clusters VI, VII, VIII, and X were, as seen on day 5, down-regulated in day 10 EV⁺CD8⁺ T cells (Fig. 3A and SI Appendix, Fig. S5B). In contrast to *Id2* and *Id3*, essential memory signature genes, such as *Il7r* and *Tcf7*, were not significantly reduced on day 10 (SI Appendix, Fig. S5A and B). Overall, EV⁺CD8⁺ T cells on day five and day 10 showed a very similar gene signature indicative of proliferating effector cells. However, one must consider that a much smaller number of EV⁺CD8⁺ T cells were present on day 10 than on day five (Fig. 1B). Therefore, the potential influence of EVs during the immune response probably fades after the early peak of T cell expansion and would therefore primarily influence critical amounts of CD8⁺ T_E cells early during adaptive immune responses.

As gene clusters regulating cell cycle and cell division were enriched in PS⁺ cells (Fig. 3A–C), we set out to confirm these results by assessing cell cycle stages of PS⁺ and PS⁻ CD44⁺CD8⁺ cells in LCMV_{Arm}-infected mice on day five using nuclear staining with DRAQ5. Cells with the highest DNA content represent cells in G₂/M stage. In line with the transcriptome analysis, T cells carrying in vivo stained PS⁺ EVs showed significantly higher DRAQ5 levels than EV-free T cells. While approximately 19 ± 6% of PS⁺ CD44⁺CD8⁺ T cells were in G₂/M stage, only approximately 5 ± 2% of their PS⁻ counterparts were in G₂/M stage (Fig. 3E), confirming that EV⁺ T cells show more proliferation.

BMDC-Derived EVs Stimulate Activated T Cells Independently of DCs in an Ag-Dependent Manner.

The above results demonstrate that T cells that bind Ag-specific EVs have increased TCR signaling as demonstrated by more NFAT translocation to the nucleus. Furthermore, EV⁺ T cells show a more robust effector phenotype than EV⁻ T cells. However, it still remains to be clarified if EVs cause these changes by directly triggering the TCR and/or costimulatory receptors on T cells or whether a specific T_E subset, e.g., one that has just recently been activated by APCs, is particularly good at binding EVs. Although many studies in the past have aimed to demonstrate T cell stimulation or even priming of naive T cells by EVs (14, 50), clear and convincing evidence for such a scenario is still lacking (2, 3). Considering the negligible binding of EVs to naive T cells found during viral infection (Fig. 1D), we decided to concentrate on activated T cells and wanted to convincingly determine if these are directly modulated by EV binding in vivo. To do so, we set up the following experiment: We adoptively transferred in vitro activated TCR-transgenic OVA-specific OT-I and LCMV-specific P14 CD8⁺ T cells into H2-K^{bm1} mice (Fig. 4A). These recipient mice cannot present the cognate OT-I peptide OVA₂₅₇₋₂₆₄ on MHC-I (51), ruling out participation of endogenous APCs in specific OT-I TCR triggering. After the adoptive transfer, we injected PKH26-labeled EVs derived from OVA-pulsed BMDCs (Fig. 4A). We measured DC activation markers by flow cytometry and confirmed successful activation of EV-producing BMDCs (SI Appendix, Fig. S7A). We also determined the presence of molecules needed for T cell stimulation (MHC-I, CD86, and CD54) on EVs using IFC (SI Appendix, Fig. S7B and C). The cotransferred P14 cells do not recognize the OT-I peptide and thus served as an internal control. To test whether T cells received a stimulatory signal from the EVs, we analyzed PKH26⁺ EV⁺ and EV OT-I and P14 cells 1 h after the EV injection for nuclear translocation of NFATc1 (Fig. 4A). To exclude that PKH26 aggregates forming during the preparation bind to activated CD8⁺ T cells and render them falsely PKH26⁺, we followed the EV staining protocol using PKH26 without adding EVs and injected the same fractions as PKH26

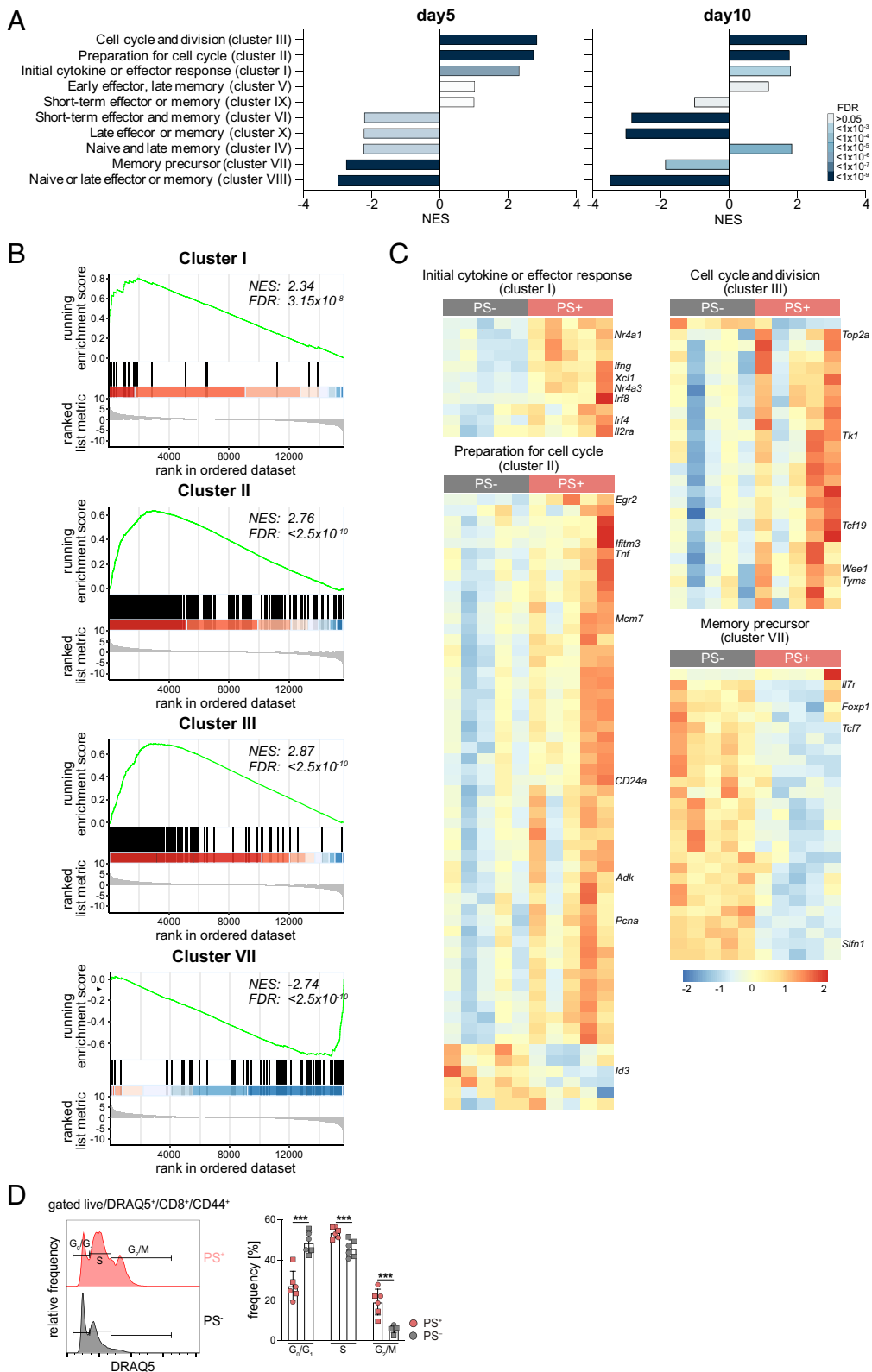


Fig. 3. EV⁺ CD8⁺ T cells have a gene signature of proliferating effector cells. PS⁻ and PS⁺ CD44⁺CD62L⁻ CD8⁺ T cells were sorted from LCMV_{Arml}-infected mice on day five after infection (sorting strategy see *SI Appendix, Fig. S3*). Transcriptomic analysis was performed by RNAseq on sorted cells. (A) Gene set enrichment analysis (GSEA) was performed against 10 gene clusters characterizing different CD8⁺ effector and memory subsets during infection and memory formation (39). Bar graph shows summary of GSEA results. x axis shows normalized enrichment score, color code indicates adjusted *P* values. (B) Heat maps show differentially expressed genes (DEGs, padj < 0.05) between PS⁻ and PS⁺ CD8⁺ T cells from clusters I, II, III, and VII using Pearson correlation as distance measure. Color code indicates z score. (C) GSEA plots from clusters I, II, III, and VII. (D) Cells carrying PS⁺ EVs from LCMV_{Arml}-infected mice were stained in vivo by injecting MFG-E8-eGFP on day five p.i. (D) G₀/G₁, S, and G₂/M cell cycle stages of PS⁺ and PS⁻ CD44⁺CD8⁺ T cells were analyzed using the DNA dye DRAQ5. Representative histograms of PS⁺ (upper histogram) and PS⁻ (lower histogram) CD44⁺CD8⁺ are shown. Bar graphs show frequencies of cells in G₂/M stage of PS⁺ (red) and PS⁻ (gray) CD44⁺CD8⁺ T cells from nine mice pooled from three independent experiments. Samples from the same experiment are shown with the same symbol. Student's *t* test was used to determine statistical significance, with ***P* > 0.01, *****P* < 0.0001.

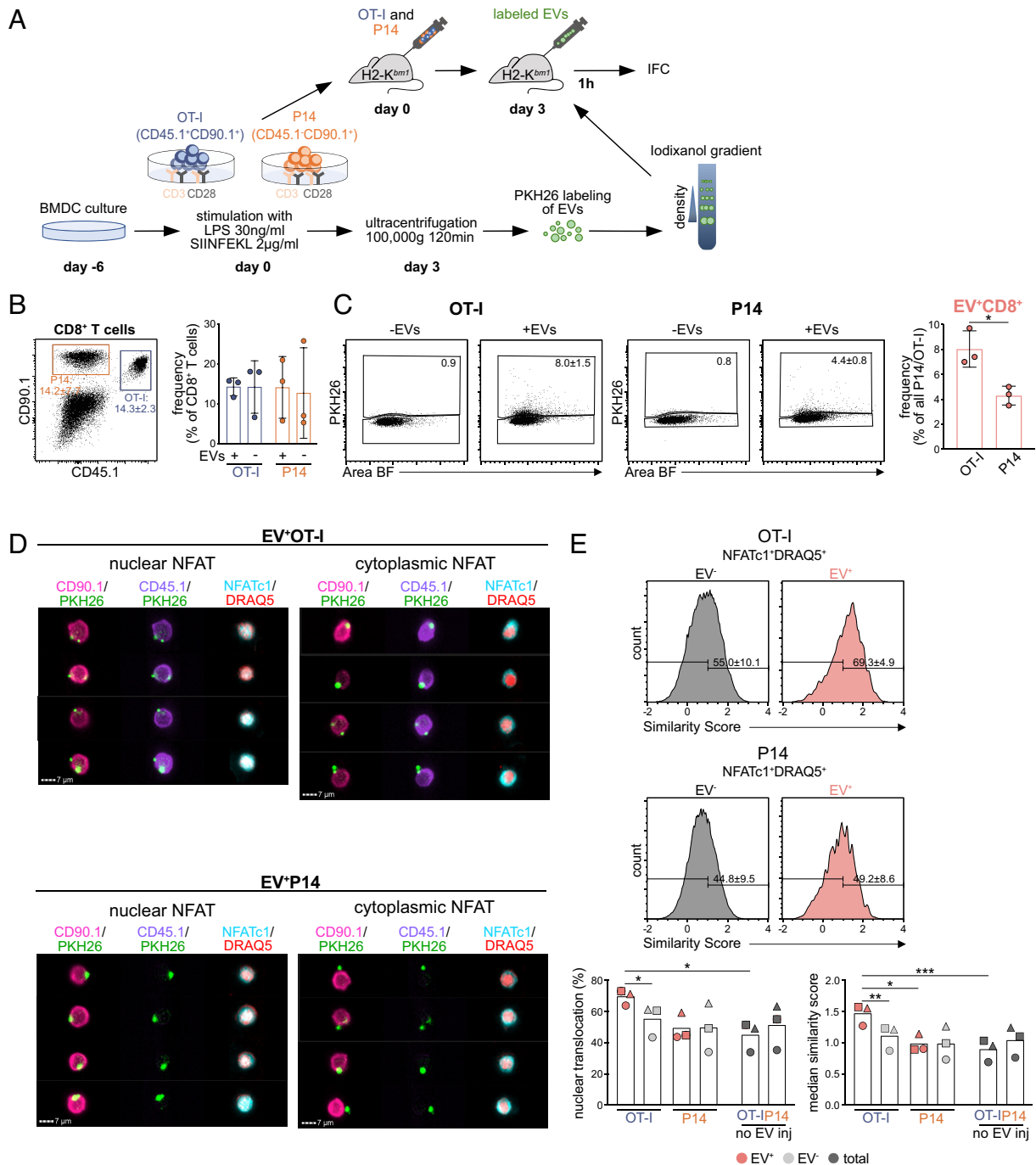


Fig. 4. Ag-dependent stimulation of CD8⁺ T cells by BMDC-derived EVs. (A) Illustration of experimental setup. At day six of the culture, BMDCs were stimulated with LPS and pulsed with SIINFEKL peptide. PKH26-labeled EVs from BMDCs and injected into H2K^{bm1} mice that had received in vitro activated OT-I and P14 cells 3 d earlier. One hour later, isolated splenocytes were stained for surface markers, NFATc1 and DRAQ5, and analyzed by IFC. (B) Dot plots show gating of transferred CD90.1⁺CD45.1⁺ P14 and CD90.1⁺CD45.1⁺ OT-I CD8⁺ T cells with average percentages ±SD (n = 3). The bar graph displays average frequencies ±SD of P14 and OT-I CD8⁺ T cells in H2K^{bm1} mice injected with BMDC-derived EVs (+) or noninjected (-). (C) Dot plots show gating of EV*P14 and EV*OT-I CD8⁺ T cells with average percentages ±SD (n = 3). Bar graph displays average frequencies ±SD of EV*P14 and EV*OT-I CD8⁺ T cells in H2K^{bm1} mice injected with BMDC-derived EVs. (D) Representative images depict CD90.1/PKH, CD45.1/PKH, and NFATc1/DRAQ5 overlays of EV*OT-I and EV*P14 cells. (E) Representative histograms show the SS of EV* OT-I and P14 CD8⁺ T cells with average frequencies ±SD of cells with a SS>1. The bar graphs show the frequencies and the median similarity scores ±SD of EV*, EV- OT-I and P14 T cells. Results from OT-I and P14 cells from mice that did not receive EVs are labeled “no EV inj”. Individual mice in different graphs are represented by the same symbol. Results from three mice were pooled from three independent experiments. For statistical significance paired t test was used with *P < 0.05, **P < 0.01, and ***P < 0.001.

only controls into LCMV-infected mice. No aggregate binding occurred by CD8⁺ T cells (SI Appendix, Fig. S7D).

Both, OT-I and P14 T cells were present in similar frequencies of approximately 15% of all CD8⁺ T cells (Fig. 4B). This frequency was irrespective of whether mice had received EVs or not, indicating that EVs could neither induce specific T cell proliferation,

expansion, nor survival during this 1-h in vivo incubation (Fig. 4B). However, when we analyzed OT-I and “Bystander” P14 T cells for EV-binding, about twofold more OT-I T cells were associated with OVA-EVs than nonspecific P14 T cells (Fig. 4C). This observation indicates a contribution of cognate TCR-peptide/MHC interaction to EV-binding, corroborating our findings in Fig. 2C.

To determine if EV association could induce TCR signaling, we next analyzed nuclear NFATc1 translocation in the T cells by IFC (Fig. 4D and *SI Appendix*, Fig. S8). Bystander P14 cells had comparable frequencies of nuclear NFATc1 (Fig. 4D and E), regardless of whether they were bound to EVs or not or were isolated from control mice that had not received EVs (Fig. 4E). This suggested that activated T cells which bind EVs with unpeptide/MHC complexes do not receive TCR-downstream signals via the NFAT-signaling pathway. However, in marked contrast to P14 cells, we observed statistically significant NFATc1-translocation from the cytoplasm to the nucleus in EV⁺ vs. EV⁻ OT-I T cells and relative to OT-I T cells in mice that had not received EVs at all. (Fig. 4E). This clearly indicated that recognition of peptide/MHC complexes on EVs indeed triggered Ag-specific TCR signaling in OT-I T cells. Moreover, the strength of the NFATc1 signal in EV⁺ OT-I cells was much higher than in EV⁻ OT-I cells, as measured by the colocalization (similarity) score with DRAQ5 (ss of 1.5, Fig. 4E). These results demonstrate that TCR stimulation as assessed by NFAT translocation is strongly enhanced when cognate Ag is present on EVs. Importantly, this TCR stimulation was independent of DCs since the OT-I peptide cannot be presented on MHC-I of *H2-K^{bm1}* mice. To our knowledge, this is the first direct demonstration of Ag-dependent TCR signaling by EVs in vivo. Direct TCR stimulation by EVs is also supported by our demonstration of PS⁺CD9⁺ EVs colocalizing with the TCR complex (Fig. 2E).

Discussion

Especially activated CD8⁺ T cells associate with naturally occurring EVs during viral infection. These EVs induced TCR signaling in Ag-specific CD8⁺ T cells in vivo. As a result, CD8⁺ T cells receiving signals from EVs had enhanced T_E cell gene signatures, while T cells without EVs showed more memory T cell gene signatures. Our data suggest that EVs attached to the surface of CD8⁺ T cells act as adjuvants for virus-specific activated CD8⁺ T function to enhance antiviral T effector cell responses.

Our approach of staining naturally occurring EVs is limited to PS⁺ EVs. The presence of PS in the membrane of EVs is very common (4, 5), and PS-affinity based methods are used to isolate almost all EVs from bodily fluids, suggesting that the PS⁺ EVs represent the majority of all EVs. Yet, PS⁻ or PS^{low} EVs seem to exist as a minor fraction and a recent study showed that injected PS⁻ EVs persist longer in the blood circulation of mice than PS⁺ EVs (52). However, in our own analysis of serum-derived EVs from healthy and infected mice, virtually all EVs (>95%) were PS⁺. Additionally, we confirmed our result with a PS-independent EV-detection approach using PKH26-labeled BMDC-derived EVs.

We initially developed our in vivo PS-labeling approach to detect apoptotic cells in vivo but realized that >90% of the stained cells were not apoptotic but live cells with EVs attached to their surface (27). To identify the rare apoptotic cells, we used a deep learning-assisted image interpretation approach. However, PS-staining of cells is not limited to apoptotic or EV⁺ cells. Highly phagocytic cells may also become PS⁺ by our method, although most of the eGFP signal is quenched after phagocytosis of the MFG-E8-eGFP-stained material. We also excluded that MFG-E8-eGFP is bound via integrins, as MFG-E8 constructs lacking the RGD-motif gave identical results (27). While there are also reports that B cell receptor and TCR signaling induces transient PS exposure on the cell surface (53, 54), our results from this and previous studies (27) suggest that this rather increases their capacity to bind PS⁺ EVs and that they therefore become PS⁺.

Previous publications using in vitro generated exosomal EVs from APC such as B cells or DCs reported activation of naive CD4⁺ (6, 16) and naive CD8⁺ T cells (7). However, in these landmark studies, naive T cells were not activated by direct exosome-T cell interactions but instead required bystander DCs, which indirectly presented specific exosome-borne Ag (16, 20). During LCMV infection, most T cell-bound EVs were of APC origin as they carried the corresponding surface molecules MHC-II, CD54, and CD86 and exosome markers CD9 and CD63 (27). These EVs caused NFATc1 nuclear translocation in activated EV⁺ but not EV⁻ CD8⁺ T cells arguing for direct effects rather than a role for DCs in this setting. As we found that EVs associated with CD44⁺ activated CD8⁺ T_E cells but not naive CD8⁺ T cells, it is, therefore, rather unlikely that EVs can activate naive CD8⁺ T cells through direct interaction in vivo, confirming previous findings (50).

These findings correlate with reports that activated LFA1 expressed by T cells (11) and CD54 on EVs (55) mediate T cell-EV interaction. As activated LFA-1 is not present on naive CD8⁺ T cells, it is likely that they neither can bind CD54⁺ EVs nor get activated directly by EVs generated in vivo. Due to the widespread usage of in vitro generated EVs in most previous studies, it remained unclear whether one could also transfer these findings to EVs in vivo (reviewed in refs. 1–3). Possible contributions of the amount, purity, Ag-density, bioavailability, and half-life of artificially generated EVs from cell cultures could not be excluded and might have influenced these former studies. We show for the first time the kinetics of EV interaction with CD8⁺ T cells in vivo during acute viral infection, which correlated roughly to the expansion kinetics of CD8⁺ T cells and peaked between day 5 and 10 p.i. (30, 56). Such EV-CD8⁺ T cell association is likely not dependent on a temporal increase in generation of EVs as observed in various types of pathogen infections such as HIV (57), SARS-CoV-2 (58), mycobacteria (59), or plasmodium (60). On the contrary, we found a significant drop in EV serum numbers in LCMV-infected mice. However, LCMV-associated destruction of the splenic microarchitecture, including the marginal zone (61) might lead to increased EV influx into the spleen and hence facilitate EV binding by T cells resulting in the reduction of serum EV numbers.

TCR specificity did contribute to EV-T cell binding, as activated specific CD8⁺ T cells bound higher frequencies of EVs in vivo than activated nonspecific T cells. This is also supported by the superresolution microscopy data showing clear colocalization of EVs with CD8, which is part of the TCR complex. Furthermore, EVs carry CD86 and CD54 and could engage costimulatory molecules and therefore facilitate EV binding by all activated CD8⁺ T cells, independently of TCR specificity.

The continuous stimulation of T cells and NFAT activation by EVs might lead to T cell exhaustion in certain settings. Indeed, NFAT has been shown to induce exhaustion in CD8⁺ T cells, when not complexed with the transcription factor AP-1 (62). Indeed, the MAP kinase pathway is sensitive to tuning by persistent Ag and overexpression of its target c-Jun makes CAR-T cell products more resistant to exhaustion (63–65) Such unbalanced TCR signaling is unlikely to happen during an acute viral infection like LCMV_{Arm}, as we have observed a rapid drop of EV binding after viral clearance. However, it is conceivable that EVs could contribute to T cell exhaustion in other settings, such as chronic viral infections and cancer. There is considerable evidence that specifically tumor-derived exosomal EVs carry PD-L1 on their surfaces and can thereby suppress both activation and proliferation of CD8⁺ T cells in an Ag-independent way (66–73). As PD-1 signaling attenuates T cell activation by interfering with TCR/

MHC and CD28/CD86 signaling pathways, tumor-derived PD-L1⁺ EVs also inhibited PD-1⁺ CD8⁺ T cells with other TCR specificity than for tumors (66). Therefore, it is unlikely that the TCR needs to receive direct signals from MHC on tumor-derived EVs in this setting.

In marked contrast, we show that APC-derived exosomal EVs influence T cell function and differentiation during antiviral immune responses by directly engaging the TCR. The extent to which costimulatory pathways are necessary for these positive effects is unknown, however CD28 and ICOS induce sustained PI3K activity, leading to the upregulation of NFATc1 transcription (74). But it is unclear, whether costimulatory molecules alone have the potential to increase nuclear NFATc1 translocation, as unique, TCR-independent roles for CD28 have been challenging to dissect (75). It has been shown that CD28 signals alone can inhibit the kinase GSK3 β , which promotes NFAT export from the nucleus (76, 77), causing trapping of NFAT in the nucleus. Potentially, such NFAT-trapping may cause slight effects on NFATc1 translocation, as we have observed in nonspecific EV⁺ T cells in LCMV-infected mice.

NFATc1 positively regulates cell proliferation and represses cell death (78), and EV⁺ CD8⁺ T cells showed upregulation of corresponding gene clusters II (preparation for cell cycle) and III (cell cycle and division), linking NFATc1 translocation to gene expression of EV⁺ CD8⁺ T cells. Among known genes regulated by NFATc1, we found upregulation of *Egr2*, *Ifng*, *Irf4*, *Tnf*, and *Nr4a1* in EV⁺ CD8⁺ T cells. Especially the effector cytokines IFN- γ and TNF- α are NFATc1 dependent (79). CD8⁺ T_E cells are central to fight viral infection by cytotoxic lysis of infected cells (80). In addition, non-cytocidal effector mechanisms mediated by CD8⁺ T cell-derived IFN- γ and TNF- α critically contribute to viral clearance of LCMV and other viruses (81–86). Therefore, a potential boost of such effector cytokine gene expression in EV⁺ CD8⁺ T cells suggests an additional, previously unrecognized EV/exosome-mediated adjuvant effect for Ag-specific effector CD8⁺ T cells.

Materials and Methods

Mice. All mice were housed and bred under specific pathogen-free conditions at the Core Facility Animal Models of the Biomedical Center of the Ludwig-Maximilians-University, Munich. All protocols were approved by the Government of Oberbayern. Age and sex-matched mice of both sexes were used at 6 to 12 wk of age. C57BL/6NRj mice were bred in-house or purchased from Janvier (strain C57BL/6), P14/CD90.1 (B6-Tg (TcrLCMV)327Sdz-Thy1⁺) mice express a transgenic Va2/Vb8.1 TCR that is specific for specific for the LCMVgp33-41 peptide, presented by H-2D^b (36LCMV). OT-I/CD45.1 and OT-I/CD90.1 (B6-Tg (TcrTcrb)1100Mjb-ptprc³) express a transgenic V α 2/V β 5 TCR recognizing the OVA peptide SIINFEKL (OVA257-264) by H-2K^b (37). To reduce the number of mice needed for this study and to apply the 3R principles, OT-I mice used were either CD45.1⁺CD90.1⁻ (Fig. 2) or CD45.1⁺CD90.1⁺ (Fig. 4). H-2K^b^{bm1} mice carrying a mutant H-2K allele are incapable of presenting the OVA₂₅₇₋₂₆₄ peptide (51). To keep animal numbers at a minimum and to determine the optimal sample size, the software G*Power (87) was used.

Antibodies/Reagents. See *SI Appendix, Table S1*.

LCMV. Mice were infected with 2 \times 10⁵ p.f.u. LCMV Armstrong intraperitoneally. Virus was propagated in L929 cells. Viral titers were determined by focus-forming assays on Vero cells followed as described previously (88).

Preparation of Single-Cell Suspensions. Single-cell suspensions of the spleen were prepared by meshing the organs through a nylon mesh followed by erythrocyte lysis or by centrifugation of cells through Pancoll (PAN Biotech). For NFAT translocation experiments, cells were immediately fixed after organ removal by preparing the single-cell suspension using ice-cold FACS buffer (PBS+2% FCS) and 4% PFA mixed 1:1 as described previously (65).

Serum EV Isolation. Serum samples were diluted with PBS + Protease inhibitors (Complete tablets, EDTA-free, Roche). After centrifugation (1,500 g and 10,000 g, 10', RT), serum was loaded onto qEV 35-nm columns (Izon Science) and the flow through was collected (500 μ L fractions). Fractions 2 to 7 were pooled and concentrated to 300 μ L. Particle number and size distribution of serum EVs were determined by NTA using the ZetaView PMX110 instrument (ParticleMetrix). Eleven positions were measured with three reading cycles. Preacquisition parameters were sensitivity = 75, shutter speed = 50, frame rate = 30 fps, trace length = 15. Postacquisition parameters were minimum brightness = 20, pixels size = 5 to 1,000. For ImageStream analysis serum, EVs were stained with mC1 for 1 h at RT followed by the addition of 5% (v/v) NP-40 to detergent controls or the corresponding volume of filtered PBS. Prior to analysis, EV samples were fixed with 2% (v/v) filtered PFA. All data were acquired at 60 \times magnification at low flow rate and with the removed beads option deactivated, as described previously (89).

Adoptive Transfer. For adoptive transfer of OT-I and P14 CD8⁺ T cells, single-cell suspensions of the spleen were prepared. Non-CD8⁺ T cells were removed using the CD8⁺ T cell negative selection isolation kit (Miltenyi Biotech). Isolated CD8⁺ T cells were activated in vitro for 2 d using 10 μ g/mL anti-CD3 and anti-CD28 mAbs coated 96-well plates (Sarstedt) and then 3.0 to 3.5 \times 10⁶ cells were adoptively transferred into recipient mice and analyzed 3 d later (90).

Flow Cytometry/IFC/FACS Sort. First, 1 \times 10⁶ and 5 \times 10⁶ cells were stained for flow cytometry of IFC, respectively, with appropriate antibody mixes (20 min on ice) and analyzed on a FACSCanto (BD Biosciences) or an ImageStream^{MX} MKII imaging flow cytometer (Luminex). For digitally sorting PS⁺ cells into apoptotic and EV⁺ subsets, a CAE was used as described in ref. 27.

For sorting PS⁺ CD8⁺ T cells for dSTORM microscopy, mice injected with 50 μ g C1-SA-AF647 to stain PS in vivo. For C1-SA-AF647 conjugation, C1 monomers (Apo-Monomer, Cat. #480157, Biolegend) were mixed with Streptavidin-AF647 in a 1:5 ratio. Mice were killed 1 h after the injections. Spleens were removed and surface staining with CD8-CF488 and CD9-CF586 (antibodies were labeled in-house with dSTORM compatible dyes using Mix-n-StainTM CFTM488 and CFTM568 kits according to the manufacturer's instructions) was performed on splenocytes. To exclude unwanted and dead cells, LIVE/DEADTM violet, CD11c-BV421, IgM-BV421, and CD4-BV421 were added to the dump channel. After fixation with 4% PFA (20 min), cells were sorted on a FACSAriaIII cell sorter (BD Biosciences) using a 130- μ m nozzle and low flow rate to minimize shearing forces resulting in EV loss.

For sorting PS⁺ CD8⁺ T cells for RNAseq analysis, spleens from mice injected with 100 μ g MFG-E8-eGFP were stained with LIVE/DEADTM violet anti-CD8 PE-Cy7, anti-CD44 APC/Fire750, and anti-CD62L PE mAbs. Cells were sorted on a FACSAriaIII cell sorter (BD Biosciences) using a 130- μ m nozzle. After sorting cells were lysed in Trizol.

dSTORM Superresolution Microscopy. For dSTORM, sorted and labeled cells (see section *Flow cytometry/IFC/FACS sort*) were immobilized on 0.1% (w/v) poly-L-lysine (P8920, Sigma-Aldrich)-coated 76 \times 26 mm slides (03-0001, Langenbrinck) with a 22 \times 22 mm 1.5H cover glass (80-2222/5, Marienfeld). Freshly prepared BCubed STORM-imaging buffer (ONI, Oxford Nanoimaging) was added prior to image acquisition on a temperature-controlled Nanoimager S Mark II microscope from ONI. Images were taken in dSTORM mode acquired sequentially using the total reflection fluorescence (TIRF) illumination (calculated evanescent field penetration depth was >200 nm). Before imaging, channel mapping was calibrated using 0.1 μ m TetraSpeck beads (T7279, Thermo Fisher Scientific). Superresolution images were filtered using the NimOS software (v.1.18.3, ONI) and data have been further processed with the Collaborative Discovery (CODI) online analysis platform from ONI.

RNAseq. RNA from sorted cells was isolated by Vertis Biotechnology AG (Freising, Germany) with Monarch RNA Cleanup Kit (New England Biolabs). First-strand cDNA was synthesized using an oligo(dT)-adapter primer and M-MLV reverse transcriptase. The Illumina TruSeq sequencing adapter was ligated and the cDNA was PCR amplified to about 10 to 20 ng/ μ L using a high-fidelity DNA polymerase followed by cDNA purification. Samples were pooled in approximately equimolar amounts. The cDNA pool in the size range of 300 to 400 bp was eluted from an agarose gel and sequenced in four runs on an Illumina NextSeq 500 system using 1 \times 75 bp read length. Sequencing reads were aligned to the mouse reference genome (version GRCh38.99) with STAR (version 2.6.1d). Expression

values (TPM) were calculated with the software package RSEM (version 1.3.0). Post-processing was performed in R/bioconductor (version 4.0.0) using default parameters if not indicated otherwise. Differential gene expression analysis was performed with "DESeq2" (version 1.26.0). An adjusted *P* value (FDR) of less than 0.1 was used to classify significantly changed expression. GSEA were conducted with "clusterProfiler" (version 3.18.1) on the statistic reported by DESeq2. Data are available at Gene Expression Omnibus GSE201507.

Production of BMDC-derived EVs. Bone marrow cells from femur and tibia were seeded at a density of 1×10^6 /mL in RPMI 1640 Glutamax (Fisher Scientific) medium with 10% EV-free FCS, 1% penicillin/streptomycin, 20 ng/mL GM-CSF (produced in-house, centrifuged at 100,000 g at 4 °C for 18 h to remove EVs), and 0.05 mM 2-mercaptoethanol. EV-free FCS was produced as described (91). In short, FCS was diluted 1:1 with pure RPMI and centrifuged at 100,000 g at 4 °C for 18 h. The supernatant was filtered (0.2 µm and stored at -20 °C).

After 6 d, adherent cells were stimulated with 30 ng/mL LPS (Sigma-Aldrich) and 2 µg/mL SIINFEKL peptide (NeoBiotec) for 72 h. Then, the supernatant from activated BMDCs was collected (from approximately 70 T175 bottles per experiment), debris was removed (2,000 g, 20 min), filtered (0.2 µm), and centrifuged [90 min, 100,000 g, 4 °C using a type 45 Ti fixed-angle rotor (Beckman Coulter)]. EV-containing pellet was resuspended in PBS containing protease inhibitors (Complete tablets, EDTA-free, Roche), pooled, and concentrated using Amicon spin columns. For PKH26 labeling, Diluent C and PKH26 were incubated for 5 min. Staining was stopped by adding 2 mL of sterile-filtered 1% BSA. Excess dye was removed using Amicon spin columns. After washing, labeled EVs were mixed with iodixanol (Optiprep) (60%) and layered onto the bottom of ultraclear centrifuge tubes (Beckman Coulter; Cat no 344062). Another layer of 30% iodixanol diluted in PBS was placed on top, followed by a final layer consisting of filtered PBS. The discontinuous density gradient was then centrifuged for 160,000 g at 4 °C for 18 h in an SW 55 Ti swinging-bucket rotor (Beckman Coulter).

Then, 500 µL fractions were collected from the top of the gradient. Fractions 3 to 8 were pooled, washed, and concentrated using Amicon spin columns. Concentration of EVs was determined using Nanoparticle Tracking Analysis (NTA). Then, 2 to 7×10^{11} EVs were injected into recipient mice. For PKH26-only controls, PKH26 and Diluent C were added to PBS, containing protease inhibitor, without EVs. Subsequently, the same protocol as for the EV-containing samples was adhered to and fractions 3 to 8 were pooled after the iodixanol gradient ultracentrifugation. Concentrated fractions were injected into recipient mice at day five of LCMV infection.

Statistical Analysis. For statistical analysis, the PRISM software (GraphPad Software) was used. Significance was analyzed using Student's *t* test or one-way ANOVA test unless stated otherwise, with **P* < 0.05, ***P* < 0.01, and ****P* < 0.001. Bar graphs show average ± SD.

Data, Materials, and Software Availability. RNAseq data have been deposited in Gene Expression Omnibus (GSE201507) (92).

ACKNOWLEDGMENTS. We acknowledge Anne-Sophie Neumann for technical support, the Core Facility Flow Cytometry at the Biomedical Center, Ludwig Maximilian University of Munich, for providing the ImageStream[™] MKII imaging flow cytometer, cell sorters, and services. T.B., R.O., V.R.B., and J.K. are supported by the Deutsche Forschungsgemeinschaft (German Research Foundation)–Project-ID 210592381–SFB 1054 (TP B03; TP B07; TP B15; TP Z02).

Author affiliations: ^aFaculty of Medicine, Institute for Immunology, Biomedical Center, Ludwig Maximilian University of Munich, 82152 Martinsried-Planegg, Germany; ^bInstitute for Medical Microbiology, Immunology and Hygiene, Technical University of Munich, 81675 Munich, Germany; and ^cCore Facility Bioinformatics, Faculty of Medicine, Biomedical Center, Ludwig Maximilian University of Munich, 82152 Martinsried-Planegg, Germany

- M. F. S. Lindenbergh, W. Stoorvogel, Antigen presentation by extracellular vesicles from professional antigen-presenting cells. *Annu. Rev. Immunol.* **36**, 435–459 (2018).
- A. G. Yates *et al.*, In sickness and in health: The functional role of extracellular vesicles in physiology and pathology in vivo: Part II: Pathology. *J. Extracell. Vesicles* **11**, e12190 (2022).
- A. G. Yates *et al.*, In sickness and in health: The functional role of extracellular vesicles in physiology and pathology in vivo: Part I: Health and Normal Physiology. *J. Extracell. Vesicles* **11**, e12151 (2022).
- G. van Niel, G. D'Angelo, G. Raposo, Shedding light on the cell biology of extracellular vesicles. *Nat. Rev. Mol. Cell Biol.* **19**, 213–228 (2018).
- C. Théry *et al.*, Minimal information for studies of extracellular vesicles 2018 (MISEV2018): A position statement of the international society for extracellular vesicles and update of the MISEV2014 guidelines. *J. Extracell. Vesicles* **7**, 1–47 (2018).
- G. Raposo *et al.*, B lymphocytes secrete antigen-presenting vesicles. *J. Exp. Med.* **183**, 1161–1172 (1996).
- L. Zitvogel *et al.*, Eradication of established murine tumors using a novel cell-free vaccine: Dendritic cell-derived exosomes. *Nat. Med.* **4**, 594–600 (1998).
- E. Segura *et al.*, ICAM-1 on exosomes from mature dendritic cells is critical for efficient naive T-cell priming. *Blood* **106**, 216–223 (2005).
- E. Segura, S. Amigorena, C. Théry, Mature dendritic cells secrete exosomes with strong ability to induce antigen-specific effector immune responses. *Blood Cells Mol. Dis.* **35**, 89–93 (2005).
- F. Aligne, D. Bout, S. Amigorena, P. Roingeard, I. Dimier-Poisson, Toxoplasma gondii antigen-pulsed-dendritic cell-derived exosomes induce a protective immune response against T. gondii infection. *Infect. Immun.* **72**, 4127–4137 (2004).
- E. N. Nolte-'t Hoen, S. I. Buschow, S. M. Anderton, W. Stoorvogel, M. H. Wauben, Activated T cells recruit exosomes secreted by dendritic cells via LFA-1. *Blood* **113**, 1977–1981 (2009).
- S. Hao *et al.*, Mature dendritic cells pulsed with exosomes stimulate efficient cytotoxic T-lymphocyte responses and antitumor immunity. *Immunology* **120**, 90–102 (2007).
- S. Utsugi-Kobukai, H. Fujimaki, C. Hotta, M. Nakazawa, M. Minami, MHC class I-mediated exogenous antigen presentation by exosomes secreted from immature and mature bone marrow derived dendritic cells. *Immunol. Lett.* **89**, 125–131 (2003).
- I. Hwang, X. Shen, J. Sprent, Direct stimulation of naive T cells by membrane vesicles from antigen-presenting cells: Distinct roles for CD54 and B7 molecules. *Proc. Natl. Acad. Sci. U.S.A.* **100**, 6670–6675 (2003).
- C. Admyre, S. M. Johansson, S. Paulie, S. Gabrielsson, Direct exosome stimulation of peripheral human T cells detected by ELISPOT. *Eur. J. Immunol.* **36**, 1772–1781 (2006).
- C. Théry *et al.*, Indirect activation of naive CD4+ T cells by dendritic cell-derived exosomes. *Nat. Immunol.* **3**, 1156–1162 (2002).
- H. Vincent-Schneider *et al.*, Exosomes bearing HLA-DR1 molecules need dendritic cells to efficiently stimulate specific T cells. *Int. Immunol.* **14**, 713–722 (2002).
- A. Montecalvo *et al.*, Exosomes as a short-range mechanism to spread alloantigen between dendritic cells during T cell allorecognition. *J. Immunol.* **180**, 3081–3090 (2008).
- A. E. Morelli *et al.*, Endocytosis, intracellular sorting, and processing of exosomes by dendritic cells. *Blood* **104**, 3257–3266 (2004).
- F. Andre *et al.*, Exosomes as potent cell-free peptide-based vaccine. I. Dendritic cell-derived exosomes transfer functional MHC class II peptide complexes to dendritic cells. *J. Immunol.* **172**, 2126–2136 (2004).
- J. Marino *et al.*, Donor exosomes rather than passenger leukocytes initiate alloreactive T cell responses after transplantation. *Sci. Immunol.* **1**, aaf8759 (2016).
- O. B. Herrera *et al.*, A novel pathway of alloantigen presentation by dendritic cells. *J. Immunol.* **173**, 4828–4837 (2004).
- B. Hugel, M. C. Martinez, C. Kunzelmann, J.-M. Freyssinet, Membrane microparticles: Two sides of the coin. *Physiology (Bethesda)* **20**, 22–27 (2005).
- A. Lorente *et al.*, Molecular lipidomics of exosomes released by PC-3 prostate cancer cells. *Biochim. Biophys. Acta* **1831**, 1302–1309 (2013).
- M. C. Martinez, J. M. Freyssinet, Deciphering the plasma membrane hallmarks of apoptotic cells: Phosphatidylserine transverse redistribution and calcium entry. *BMC Cell Biol.* **2**, 20 (2001).
- C. Théry, L. Zitvogel, S. Amigorena, Exosomes: Composition, biogenesis and function. *Nat. Rev. Immunol.* **2**, 569–579 (2002).
- J. Kranich *et al.*, In vivo identification of apoptotic and extracellular vesicle-bound live cells using image-based deep learning. *J. Extracell. Vesicles* **9**, 1792683 (2020).
- L. Rausch *et al.*, Binding of phosphatidylserine-positive microparticles by PBMCs classifies disease severity in COVID-19 patients. *J. Extracell. Vesicles* **10**, e12173 (2021).
- R. Kaiser *et al.*, Procoagulant platelet sentinels prevent inflammatory bleeding through GPIIb/IIIa and GPVI. *Blood* **140**, 121–139 (2022).
- C. L. Althaus, V. V. Ganusov, R. J. De Boer, Dynamics of CD8+ T cell responses during acute and chronic lymphocytic choriomeningitis virus infection. *J. Immunol.* **179**, 2944–2951 (2007).
- E. J. Wherry, J. N. Blattman, K. Murali-Krishna, R. van der Most, R. Ahmed, Viral persistence alters CD8 T-cell immunodominance and tissue distribution and results in distinct stages of functional impairment. *J. Virol.* **77**, 4911–4927 (2003).
- K. Murali-Krishna *et al.*, Counting antigen-specific CD8 T cells: A reevaluation of bystander activation during viral infection. *Immunity* **8**, 177–187 (1998).
- F. Macian, NFAT proteins: Key regulators of T-cell development and function. *Nat. Rev. Immunol.* **5**, 472–484 (2005).
- S. Klein-Hessling *et al.*, NFAT1 controls the cytotoxicity of CD8(+) T cells. *Nat. Commun.* **8**, 511 (2017).
- P. G. Hogan, L. Chen, J. Nardone, A. Rao, Transcriptional regulation by calcium, calcineurin, and NFAT. *Genes Dev.* **17**, 2205–2232 (2003).
- H. Pircher, K. Burki, R. Lang, H. Hengartner, R. M. Zinkernagel, Tolerance induction in double specific T-cell receptor transgenic mice varies with antigen. *Nature* **342**, 559–561 (1989).
- K. A. Hogquist *et al.*, T cell receptor antagonist peptides induce positive selection. *Cell* **76**, 17–27 (1994).
- J. G. Borger, R. Zamojska, D. M. Gakamsky, Proximity of TCR and its CD8 coreceptor controls sensitivity of T cells. *Immunol. Lett.* **157**, 16–22 (2014).
- J. A. Best *et al.*, Transcriptional insights into the CD8+ T cell response to infection and memory T cell formation. *Nat. Immunol.* **14**, 404–412 (2013).
- A. E. Moran *et al.*, T cell receptor signal strength in Treg and iNKT cell development demonstrated by a novel fluorescent reporter mouse. *J. Exp. Med.* **208**, 1279–1289 (2011).
- F. Miyagawa *et al.*, Interferon regulatory factor 8 integrates T-cell receptor and cytokine-signaling pathways and drives effector differentiation of CD8 T cells. *Proc. Natl. Acad. Sci. U.S.A.* **109**, 12123–12128 (2012).
- M. Grusdat *et al.*, IRF4 and BATF are critical for CD8(+) T-cell function following infection with LCMV. *Cell Death Differ.* **21**, 1050–1060 (2014).

43. L. Kretschmer *et al.*, Differential expansion of T central memory precursor and effector subsets is regulated by division speed. *Nat. Commun.* **11**, 113 (2020).
44. S. Grassmann *et al.*, Early emergence of T central memory precursors programs clonal dominance during chronic viral infection. *Nat. Immunol.* **21**, 1563–1573 (2020).
45. C. Y. Yang *et al.*, The transcriptional regulators Id2 and Id3 control the formation of distinct memory CD8+ T cell subsets. *Nat. Immunol.* **12**, 1221–1229 (2011).
46. G. Jeannot *et al.*, Essential role of the Wnt pathway effector Tcf-1 for the establishment of functional CD8 T cell memory. *Proc. Natl. Acad. Sci. U.S.A.* **107**, 9777–9782 (2010).
47. X. Zhou *et al.*, Differentiation and persistence of memory CD8(+) T cells depend on T cell factor 1. *Immunity* **33**, 229–240 (2010).
48. D. Pais Ferreira *et al.*, Central memory CD8(+) T cells derive from stem-like Tcf7(hi) effector cells in the absence of cytotoxic differentiation. *Immunity* **53**, 985–1000.e11 (2020).
49. E. J. Wherry *et al.*, Lineage relationship and protective immunity of memory CD8 T cell subsets. *Nat. Immunol.* **4**, 225–234 (2003).
50. K. Coppieters *et al.*, No significant CTL cross-priming by dendritic cell-derived exosomes during murine lymphocytic choriomeningitis virus infection. *J. Immunol.* **182**, 2213–2220 (2009).
51. S. R. Clarke *et al.*, Characterization of the ovalbumin-specific TCR transgenic line OT-I: MHC elements for positive and negative selection. *Immunol. Cell Biol.* **78**, 110–117 (2000).
52. A. Matsumoto *et al.*, Phosphatidylserine-deficient small extracellular vesicle is a major somatic cell-derived sEV subpopulation in blood. *iScience* **24**, 102839 (2021).
53. S. R. Dillon, A. Constantinescu, M. S. Schlissel, Annexin V binds to positively selected B cells. *J. Immunol.* **166**, 58–71 (2001).
54. K. Fischer *et al.*, Antigen recognition induces phosphatidylserine exposure on the cell surface of human CD8+ T cells. *Blood* **108**, 4094–4101 (2006).
55. W. Zhang *et al.*, ICAM-1-mediated adhesion is a prerequisite for exosome-induced T cell suppression. *Dev. Cell* **57**, 329–343.e7 (2022).
56. E. A. Butz, M. J. Bevan, Massive expansion of antigen-specific CD8+ T cells during an acute virus infection. *Immunity* **8**, 167–175 (1998).
57. A. Hubert *et al.*, Elevated abundance, size, and microRNA content of plasma extracellular vesicles in viremic HIV-1+ patients: Correlations with known markers of disease progression. *J. Acquir. Immune Defic. Syndr.* **70**, 219–227 (2015).
58. E. Campello *et al.*, Longitudinal trend of plasma concentrations of extracellular vesicles in patients hospitalized for COVID-19. *Front. Cell Dev. Biol.* **9**, 770463 (2021).
59. P. P. Singh, V. L. Smith, P. C. Karakousis, J. S. Schorey, Exosomes isolated from mycobacteria-infected mice or cultured macrophages can recruit and activate immune cells in vitro and in vivo. *J. Immunol.* **189**, 777–785 (2012).
60. F. M. Campos *et al.*, Augmented plasma microparticles during acute Plasmodium vivax infection. *Malar. J.* **9**, 327 (2010).
61. B. Odermatt, M. Eppler, T. P. Leist, H. Hengartner, R. M. Zinkernagel, Virus-triggered acquired immunodeficiency by cytotoxic T-cell-dependent destruction of antigen-presenting cells and lymph follicle structure. *Proc. Natl. Acad. Sci. U.S.A.* **88**, 8252–8256 (1991).
62. G. J. Martinez *et al.*, The transcription factor NFAT promotes exhaustion of activated CD8+ T cells. *Immunity* **42**, 265–278 (2015).
63. S. Han, A. Asoyan, H. Rabenstein, N. Nakano, R. Obst, Role of antigen persistence and dose for CD4+ T-cell exhaustion and recovery. *Proc. Natl. Acad. Sci. U.S.A.* **107**, 20453–20458 (2010).
64. R. C. Lynn *et al.*, c-Jun overexpression in CART cells induces exhaustion resistance. *Nature* **576**, 293–300 (2019).
65. A. Trefzer *et al.*, Dynamic adoption of anergy by antigen-exhausted CD4(+) T cells. *Cell Rep.* **34**, 108748 (2021).
66. G. Chen *et al.*, Exosomal PD-L1 contributes to immunosuppression and is associated with anti-PD-1 response. *Nature* **560**, 382–386 (2018).
67. Y. Yang *et al.*, Exosomal PD-L1 harbors active defense function to suppress T cell killing of breast cancer cells and promote tumor growth. *Cell Res.* **28**, 862–864 (2018).
68. J. Monypenny *et al.*, ALIX regulates tumor-mediated immunosuppression by controlling EGFR activity and PD-L1 presentation. *Cell Rep.* **24**, 630–641 (2018).
69. F. L. Ricklefs *et al.*, Immune evasion mediated by PD-L1 on glioblastoma-derived extracellular vesicles. *Sci. Adv.* **4**, eaar2766 (2018).
70. M. N. Theodoraki, S. S. Yerneni, T. K. Hoffmann, W. E. Gooding, T. L. Whiteside, Clinical significance of PD-L1(+) exosomes in plasma of head and neck cancer patients. *Clin. Cancer Res.* **24**, 896–905 (2018).
71. Y. Fan *et al.*, Exosomal PD-L1 retains immunosuppressive activity and is associated with gastric cancer prognosis. *Ann. Surg. Oncol.* **26**, 3745–3755 (2019).
72. D. H. Kim *et al.*, Exosomal PD-L1 promotes tumor growth through immune escape in non-small cell lung cancer. *Exp. Mol. Med.* **51**, 1–13 (2019).
73. M. Poggio *et al.*, Suppression of exosomal PD-L1 induces systemic anti-tumor immunity and memory. *Cell* **177**, 414–427.e13 (2019).
74. R. I. Nurieva *et al.*, A costimulation-initiated signaling pathway regulates NFATc1 transcription in T lymphocytes. *J. Immunol.* **179**, 1096–1103 (2007).
75. J. H. Eesensten, Y. A. Helou, G. Chopra, A. Weiss, J. A. Bluestone, CD28 costimulation: From mechanism to therapy. *Immunity* **44**, 973–988 (2016).
76. M. Diehn *et al.*, Genomic expression programs and the integration of the CD28 costimulatory signal in T cell activation. *Proc. Natl. Acad. Sci. U.S.A.* **99**, 11796–11801 (2002). Erratum in: *Proc. Natl. Acad. Sci. U.S.A.* **99**, 15245 (2002).
77. M. Pan *et al.*, Enhanced NFATc1 nuclear occupancy causes T cell activation independent of CD28 costimulation. *J. Immunol.* **178**, 4315–4321 (2007).
78. B. K. Robbs, A. L. Cruz, M. B. Werneck, G. P. Mogno, J. P. Viola, Dual roles for NFAT transcription factor genes as oncogenes and tumor suppressors. *Mol. Cell Biol.* **28**, 7168–7181 (2008).
79. G. P. Mogno, F. R. Carneiro, B. K. Robbs, D. V. Faget, J. P. Viola, Cell cycle and apoptosis regulation by NFAT transcription factors: New roles for an old player. *Cell Death Dis.* **7**, e2199 (2016).
80. J. T. Harty, A. R. Twinnereim, D. W. White, CD8+ T cell effector mechanisms in resistance to infection. *Annu. Rev. Immunol.* **18**, 275–308 (2000).
81. L. G. Guidotti *et al.*, Noncytotoxic clearance of lymphocytic choriomeningitis virus from the hepatocyte. *J. Exp. Med.* **189**, 1555–1564 (1999).
82. T. P. Leist, M. Eppler, R. M. Zinkernagel, Enhanced virus replication and inhibition of lymphocytic choriomeningitis virus disease in anti-gamma interferon-treated mice. *J. Virol.* **63**, 2813–2819 (1989).
83. U. Muller *et al.*, Functional role of type I and type II interferons in antiviral defense. *Science* **264**, 1918–1921 (1994).
84. H. G. Zhang *et al.*, Inhibition of tumor necrosis factor alpha decreases inflammation and prolongs adenovirus gene expression in lung and liver. *Hum. Gene Ther.* **9**, 1875–1884 (1998).
85. A. Nansen *et al.*, Compromised virus control and augmented perforin-mediated immunopathology in IFN-gamma-deficient mice infected with lymphocytic choriomeningitis virus. *J. Immunol.* **163**, 6114–6122 (1999).
86. C. Bartholdy, J. P. Christensen, D. Wodarz, A. R. Thomsen, Persistent virus infection despite chronic cytotoxic T-lymphocyte activation in gamma interferon-deficient mice infected with lymphocytic choriomeningitis virus. *J. Virol.* **74**, 10304–10311 (2000).
87. F. Faul, E. Erdfelder, A. G. Lang, A. Buchner, G*Power 3: A flexible statistical power analysis program for the social, behavioral, and biomedical sciences. *Behav. Res. Methods* **39**, 175–191 (2007).
88. M. Pellegrini *et al.*, IL-7 engages multiple mechanisms to overcome chronic viral infection and limit organ pathology. *Cell* **144**, 601–613 (2011).
89. A. Görgens *et al.*, Optimisation of imaging flow cytometry for the analysis of single extracellular vesicles by using fluorescence-tagged vesicles as biological reference material. *J. Extracell. Vesicles* **8**, 1587567 (2019).
90. H. Rabenstein *et al.*, Differential kinetics of antigen dependency of CD4+ and CD8+ T cells. *J. Immunol.* **192**, 3507–3517 (2014).
91. M. Albanese *et al.*, MicroRNAs are minor constituents of extracellular vesicles that are rarely delivered to target cells. *PLoS Genet.* **17**, e1009951 (2021).
92. J. Kranich, T. Brocker, L. Rausch, RNAseq analysis of PS+ vs. PS- effector CD8 T cells sorted from spleen of LCMV-Armstrong infected mice. Gene Expression Omnibus. <https://www.ncbi.nlm.nih.gov/geo/query/acc.cgi?acc=GSE201507>. Deposited 25 April 2022.